Measurements of the atmospheric muon rate with the ANTARES neutrino telescope

Messungen der atmosphärischen Myonrate mit dem ANTARES Neutrinoteleskop

Der Naturwissenschaftlichen Fakultät
der Friedrich-Alexander-Universität Erlangen-Nürnberg
zur Erlangung des Doktorgrades Dr. rer. nat.

vorgelegt von
Klaus Geyer
aus Forchheim

Als Dissertation genehmigt
von der Naturwissenschaftlichen Fakultät
der Friedrich-Alexander-Universität Erlangen-Nürnberg
Tag der mündlichen Prüfung: 10.07.2015

Vorsitzender des Promotionsorgans: Prof. Dr. Jörn Wilms

Gutachter/in: Prof. Dr. Gisela Anton
Prof. Dr. Uli Katz

Contents

Chapter 1

Introduction

Cosmic rays were discovered by Victor Hess in 1912. He used balloon experiments to show that the signal measured in ionization chambers is a function of the altitude. He concluded that the increase of the ionization with height comes from radiation from space. Since then a lot has been learned about this radiation. Experiments have measured the chemical and energetic composition of these so called cosmic rays [1]. They also showed that the energy spectrum of the cosmic rays decreases over several orders of magnitude. Ultra-high-energy cosmic rays have been measured with energies more than 10^{20} eV [2] [3].

A particle of the cosmic rays interacts with nuclei of the atmosphere and creates a cascade of secondary particles called air shower. If the energy of the secondary particles is high enough, the particles can be measured at sea level. One type of the secondary particles is the muon which is created by decays of pions and kaons. In chapter 2 the theory of the cosmic rays, their sources and the air showers are described.

The muons of air showers can be used to measure the anisotropy in the arrival direction of the muons as done by the IceCube collaboration [4] [5]. The angular size and shape of the anisotropy then can be used to determine the sources of the anisotropy. For example the existence of magnetic fields or the presence of the Compton-Getting effect which can cause a dipolar anisotropy derived by the fact that a detector located on Earth travels trough the reference frame where the cosmic rays are isotropic [6]. The sources and the theory of measuring the large scale anisotropy are described in chapter 3.

Chapter 3.2 shows that the data taking of the detector and influencing variables on the muon rate must be well understood to measure the large scale anisotropy. This includes the seasonal variation of the muon rate. The effect of the effective temperature of the atmosphere on the muon rate is discussed in chapter 4. The effective atmospheric temperature is calculated by using the atmospheric data from the ECMWF [7]. The seasonal variation of the muon rate has already been seen by different experiments [8] [9] [10] showing that the muon rate follows the variation of the atmospheric temperature.

The muon rate can be determined by detectors like ANTARES by counting the muons that were able to penetrate deep underground because of their high energy. The ANTARES detector is located at the Mediterranean Sea at a depth of about 2500 m. It uses the Cherenkov effect to reconstruct the trajectory of the muons. The ANTARES experiment is described in chapter 5. There the detection principle, the layout of the detector, the data acquisition and track reconstruction is explained.

The signal of the seasonal variation of the muon rate is expected to be larger than the signal of the large scale anisotropy. The search for the variation of the muon rate is used in this work to determine whether the stability in data taking and interpretation of the data allows to see the signal of the large scale anisotropy.

To study the variation of the muon rate of ANTARES it is necessary to understand the parameters that affect the efficiency and the properties of the detector. This includes the analysis of the efficiency of the detector over time, the consideration of different setups of the detector, the influence of the trigger and the effect of the optical background to the reconstruction algorithm and the muon rate. Chapter 10 summarizes the steps made in this work to study the muon rate of ANTARES.

Chapter 2

Cosmic rays

Investigating the universe consists in the search for signals coming from miscellaneous sources. Someone can easily see the stars spread out all over the sky. The photons coming from these point sources are part of the cosmic rays. Like the sun, the other stars do not only emit photons, but other particles too. But they are not the sources for high energetic cosmic rays. Cosmic rays with energies up to 10^{21} eV are neither meant to be accelerated within our solar system nor in our galaxy. The sources that are believed to be able to create high energetic cosmic rays are supernovae, active galactic nuclei or gamma-ray bursts.

Searching for the sources of the cosmic rays and detecting the different types of particles allows to deduce the acceleration process and the properties of the source. Understanding the interaction of the particles with matter and knowing their path through space helps understanding the processes and objects in space.

The detection of the cosmic rays can be done by satellites, balloon experiments, ground based detectors and underwater detectors like ANTARES. For the latter, the detected cosmic rays have already traversed the atmosphere of the earth what must be taken into account for the measurements. In this chapter a brief description of the cosmic rays, their composition and their interaction with the atmosphere of the earth is given.

2.1 Composition of cosmic rays

Cosmic rays are particles traveling through space coming from different sources. Particles that hit the atmosphere of the earth interact with the particles of the atmosphere and are called primary particles or primaries in the following. Their energy range varies from a few GeV up to more than 10^{20}eV while the energy dependent flux spans several orders of magnitude. The higher the energy, the lower the flux of the particles. The primaries are hitting the Earth's atmosphere all the time at a rate of about 1000 per

square meter and second [6]. They consist of particles, where there are about 79% protons and 15% alpha particles. The rest consists of electrons, photons, neutrinos and heavier nuclei[11]. Most of the particles are relativistic and their energy can be up to 10^{20} eV. Figure 2.1 shows the flux of the cosmic rays over the energy of the primary particles measured by different experiments and for different primary particle species.

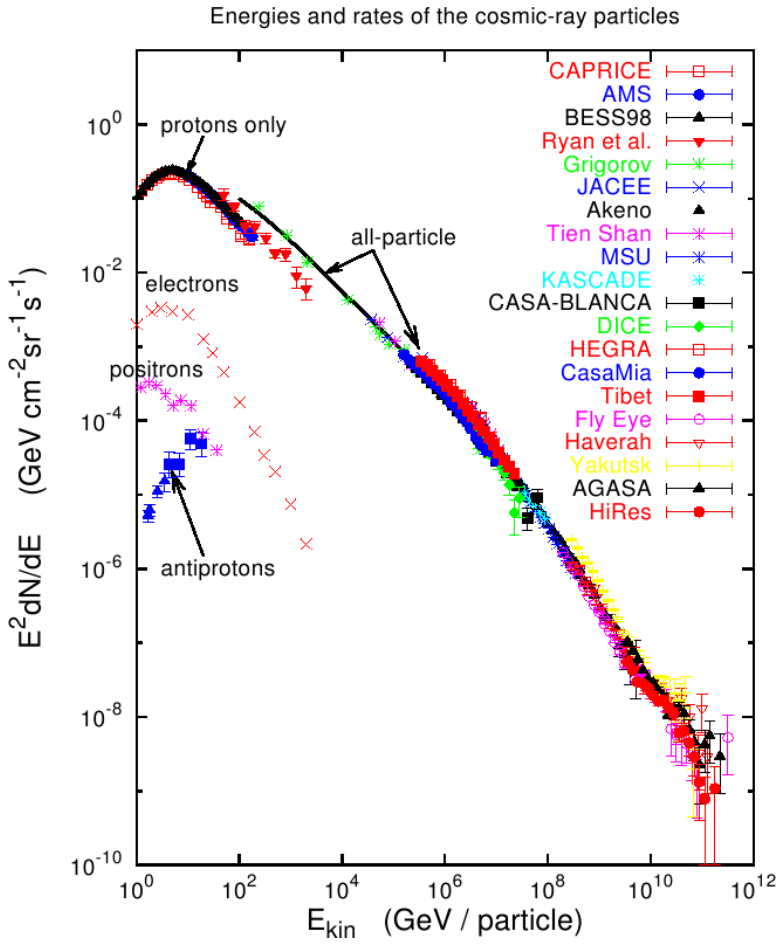

Figure 2.1: *Compilation of measurements of the energy spectrum of charged cosmic rays [12].*

The differential flux of the cosmic rays can be described by an inverse power law in energy by:

$$\frac{dN}{dE} \approx E^{\gamma} \tag{2.1}$$

where γ is about -2.7 for energies in the range of 10^{10} eV to the so called knee at about $10^{15.5}$ eV. Above that energy the power law steepens where γ is about -3.1 and recovers beyond the so called ankle at about 10^{18} eV [12] [13].

The explanation for the knee and the ankle is not well known up to now. For the knee several explanations exist. Some of them make the acceleration process responsible for

the effect while other expect a leakage of cosmic rays from the Galaxy, an interaction with background particles in the Galaxy or the air shower development [13].

Some of the fluxes measured by experiments in figure 2.1 only count for a specific type of particles like the protons and electrons. These experiments need to be located outside of the atmosphere of the Earth to be able to measure the particles before they interact with the particles of the atmosphere. The detectors are mounted on balloons or satellites and are able to measure the composition of the cosmic ray flux and the flux for each primary particle. The flux for single primaries above $10^{14}eV$ is too low for the different particles to measure them directly with such experiments, but the total flux of all particles can be measured by air shower experiments (see section 2.4). The detectors are located on the ground or below like ANTARES and measure the particles of the air shower or at least a specific component. There are two different types of air showers that can be distinguished by detectors on earth. The ones induced by photons, electrons or positrons and those where heavier particle like protons hit the Earth's atmosphere. See section 2.4 for the explanation on the difference.

2.2 Acceleration of cosmic rays

Up to now the question about the acceleration processes which are able to generate such high energies is not fully answered. Additionally it isn't known yet where the acceleration takes place. Two possibilities can be thought of. The major acceleration process occurs at the point of their creation where the particles get their maximum energy or the acceleration occurs on large scales in the Galaxy. Solar flares emitted by the sun are able to accelerate particles to energies about GeV and are an example for acceleration at the point of creation. On the other hand, planetary shock waves (e.g. at the Earth's bow shock or shocks associated with the solar wind) are able to accelerate particles too. Both examples do not explain the higher energies viewed in Figure 2.1 and it is clear that there must be sources and mechanisms that can do that. As local sources like the Sun are not able to provide higher energies, the cosmic rays with higher energies are meant to come from galactic sources. The cosmic rays with very high energy (above 10^{18} eV) may be accelerated at active galactic nuclei, in gamma ray bursts or in other powerful astrophysical systems [6].

2.2.1 Fermi mechanism

The principle of the Fermi mechanism is that charged particles gain energy from a moving magnetized plasma to many times of their origin energy. For this the particle encounters the plasma many times getting a macroscopic amount of kinetic energy with each iteration. The probability for a particle to escape from acceleration per

encounter is P_{esc} and the probability for the particle of still being in the accelerator after n encounters is $(1 - P_{esc})^n$. The energy after n encounters is $E_n = E_0(1 + \xi)^n$, where the amount of energy ΔE, that a particle gets from each encounter, is $\Delta E = \xi E$. This leads to [14]:

$$N(> E) \approx \frac{1}{P_{esc}} \left(\frac{E}{E_0} \right)^{-\gamma}, \tag{2.2}$$

where E is the energy the particle has after escaping the accelerator and $\gamma \approx \frac{P_{esc}}{\xi}$.

The Fermi mechanism leads to the power law spectrum of energies as desired. Taking time into account it can be said that particles with higher energies take longer to be accelerated than low energy particles. Furthermore, if an accelerator has a specific lifetime, the maximum energy particles can achieve is limited by that.

2nd order Fermi mechanism

The second-order Fermi mechanism (illustrated in Figure 2.2) describes the acceleration of relativistic particles by means of their collision with interstellar clouds. For the particles, these randomly moving clouds act as magnetic mirrors, where they are reflected by them. The particles then gain energy from the scattering within the cloud, while these scatterings are not to be understand as interactions or collisions where the particle would loose energy. The energy gain for the second-order Fermi mechanism for a particle going in and out of the cloud once is:

$$\left(\frac{\Delta E}{E} \right) \approx \frac{4}{3} \beta^2, \tag{2.3}$$

where $\beta = V/c$ and V the velocity of the cloud. However, the density of such clouds is low [15] and because of that, this model can not explain the energy of the cosmic rays shown in Figure 2.1.

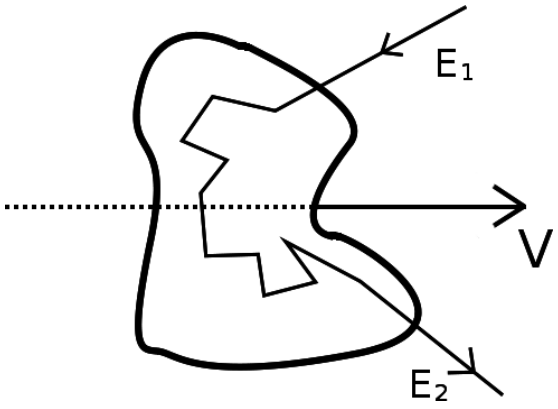

Figure 2.2: *Illustration of the second-order Fermi mechanism. A Particle is accelerated by an partially ionized and moving gas cloud.*

1st order Fermi mechanism

The first-order Fermi mechanism is illustrated in figure 2.3. Here a strong shock wave (e.g. produced by supernova explosions, active galactic nuclei, etc.), which can reach supersonic velocities (10^3 times the velocity of an interstellar cloud) [15], accelerates the particles as follows. With $-v_1$ as the velocity of the the shock front, v_2 is the velocity of the shocked gas relative to the shock front and $|v_2| < |v_1|$. The gas behind the shock front moves with velocity $V = -v_1 + v_2$. Now $\beta = V/c$ is interpreted as the velocity of the shocked gas relative to the unshocked gas (downstream: behind the shockfront and upstream: in front of the shock). It can be shown [14] that the average energy gain for particles that have been back and forth across the shock front is given by:

$$\left(\frac{\Delta E}{E}\right) \approx \frac{4}{3}(\beta) \tag{2.4}$$

where $\beta = V/c$ refers to the relative velocity of the plasma flow not to the cosmic rays.

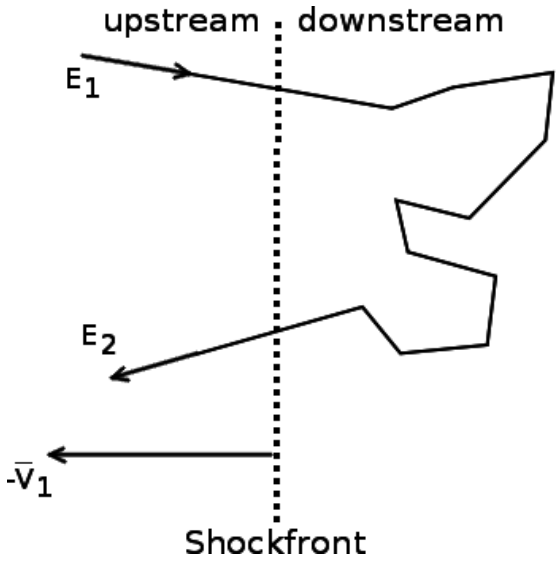

Figure 2.3: *Illustration of the first-order Fermi mechanism. A Particle is accelerated by a shock front.*

2.3 Propagation of cosmic rays

The cosmic rays are accelerated and created by different sources like the Sun or a supernova. The particles with energy about MeV and GeV can be created by nearby sources, but for those with higher energy the sources are believed to be in the space

of the Galaxy or even larger scale. The experiments measuring the flux of the particles are located on Earth and the cosmic rays have to travel from the sources and accelerators to the detectors to be measured. The information on the direction and the energy of the particles at which they arrive at Earth can be used to determine the processes on how they have been created and accelerated. But this can be difficult if the existence of interstellar magnetic fields, material clouds and other obstacles are taken into account. Charged particles like protons and electrons are distracted by such objects. Additionally the information about their arrival direction at Earth does not need to be the direct path from their source. This effect becomes larger the higher the energy of the particles is, if the particles are not created within our solar system or even our Galaxy. The only particles that can traverse even large masses without interacting with nuclei or being distracted by magnetic fields are the neutrinos. This advantage has the down side that the neutrinos are hard to detect and large arrays are needed to do so. For that purpose ANTARES was built. Due to the design of the detector (see section 5) it is also possible to measure the muons of the air showers produced by the cosmic rays in the atmosphere of the Earth that are described in the following.

2.4 Air showers

Air showers are induced by the cosmic rays when they hit particles of the Earth's atmosphere. The particles that are created afterwards can be detected by experiments on Earth. An air shower is made up of different types of particles and the detectors have to be specialized for the type of the particles and the altitude of the position of the detector itself. This Chapter gives an overview on the development of air showers.

If a particle of the cosmic rays collides with a particle of the atmosphere of the earth at an altitude of about 10 - 40 km, it will create a cascade of different reactions emitting secondary particles to the ground. This cascade is called an air shower [16]. There are two types of air showers to distinguish. The first type is introduced by a photon, electron or positron hitting the Earth's atmosphere. For the second type, the primary particle is a proton or heavier nuclei. These two types differ by the particles of the cascade and their development. An air shower introduced by a photon, electron or positron mainly consists of the electromagnetic component while the second type has three components (electromagnetic, hadronic and muonic) [14] which are described in the following.

The secondary particles of the shower can interact with other particles of the atmosphere or decay. The probability for interacting and decay depends on the energy and the density of the atmosphere. Downwards the air shower the average energy of all particles at depth X decreases. Starting with a single particle from the cosmic ray the number of particles in the shower first multiplies, then reaches it's maximum and

decreases again as the secondary particles fall below the threshold for further particle production. Figure 2.4 illustrates the creation of different particles in the air shower and shows how the number of particles evolves. In this thesis data from ANTARES

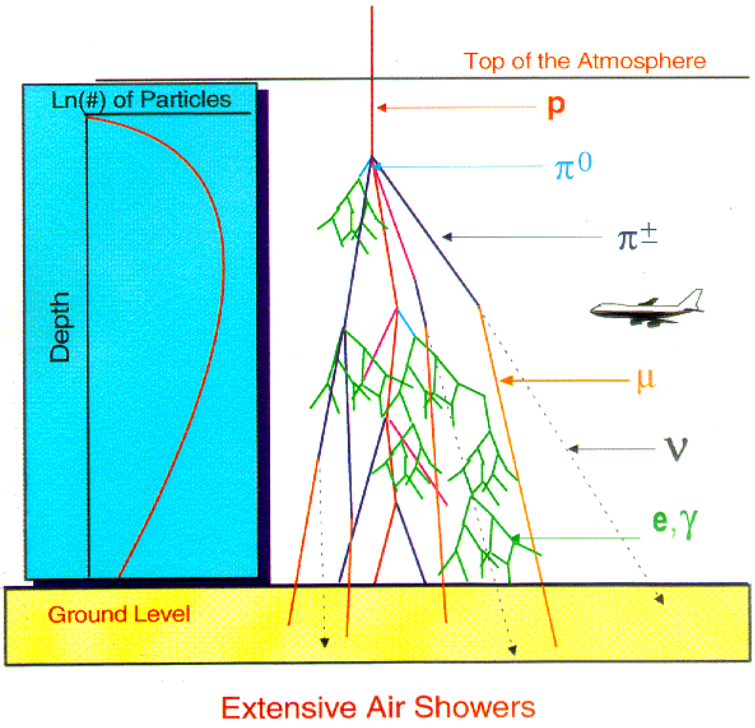

Figure 2.4: *A diagram of the propogation of an extensive air shower showing the particles produced [17].*

(see chapter 5) is used to get information about the directions of the muons from the air showers. The detector is an under water array of photo multipliers, detecting the Cherenkov light emitted by the muons. Atmospheric muons detected by ANTARES have to travel down to about 2400m below sea level and need to have an energy higher than the critical threshold energy (see section 9.1) to be still able to create Cherenkov light. With increasing depth the intensity of the underground muons is decreasing, which is shown in figure 2.5.

2.4.1 Electromagnetic component

A high energetic photon interacting with matter creates pairs of electrons and positrons (pair production). Photons are created by Bremsstrahlung and as long as the energy of the photon is large enough, additional electrons and positrons are created by pair production again. For lower energies the Compton effect becomes more important. Electrons and positrons also lose energy by Cherenkov radiation. As long as the photons have enough energy for pair production each of them will create an electromagnetic

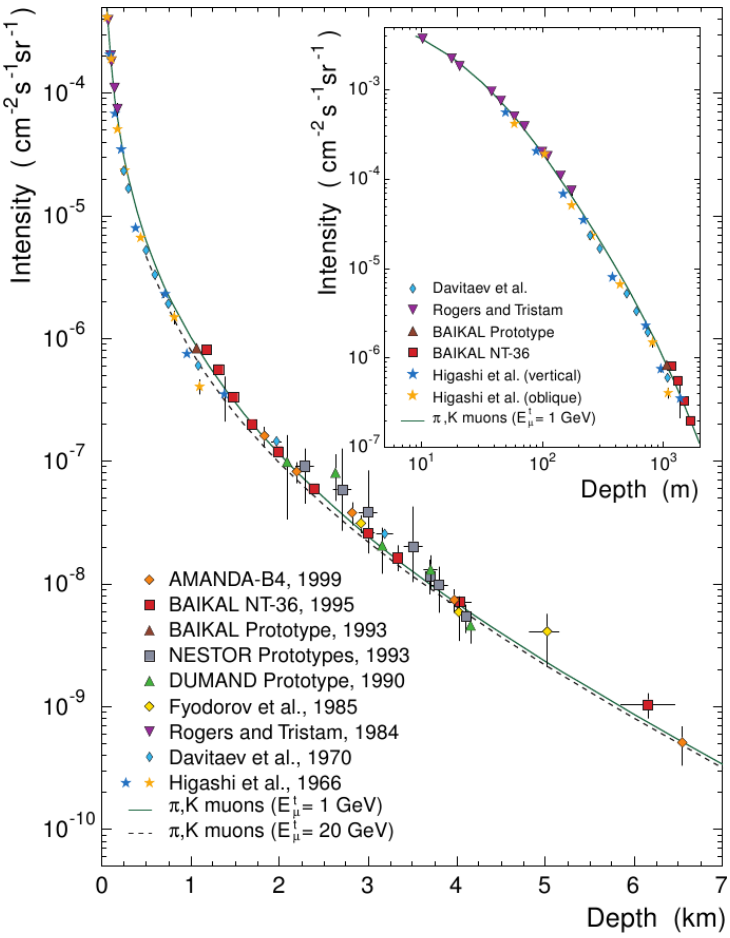

Figure 2.5: Muon intensity vs depth in water (linear and log-scale) for different experiments (dots) and calculated depth-intensity relation (curves) for the muon threshold energy 1GeV and 20GeV. [18]

subshower alternating pair production and Bremsstrahlung. For the primary particles photon, electron and positron this is the main component. Air showers introduced by other particles of the cosmic rays also have this component while the electromagnetic component is mainly driven by the high energetic hadrons that feed this component primarily by photons from decay of neutral pions. This component contains the largest number of particles.

2.4.2 Hadronic component

The hadronic component is produced by interactions of hadrons like protons, neutrons and pions from the primary or secondary particles of the air shower with molecules of the atmosphere. The number of charged particles produced in the interaction is called multiplicity. It increases with energy E_0 of the primary particle. The hadrons produced by the interactions are mainly pions [6]. The neutral pions of the cascade decay into two

γ ($\pi^0 \rightarrow \gamma\gamma$) feeding the electromagnetic component of the shower. The charged pions decay by the weak interaction into muons and neutrinos as shown in equation 2.5. The $\pi^{\pm}$ can decay or interact with nuclei of the atmosphere. The probability for the decay and interaction depends on the energy of the pions and the density of the atmosphere the pion is traversing. The higher the energy of the pion the higher the probability to interact with nuclei of the atmosphere because of the Lorentz factor. Pions with low energy will decay more probably. The density of the atmosphere is lower for higher altitudes. Therefore the probability for the pions to decay is more likely for the higher levels of the atmosphere. If a pion interacts, additional hadrons are produced. This process continues until the hadron energy falls below an interaction threshold.

2.4.3 Muonic component

The muons of the muonic component are created by decays of the pions and kaons of the hadronic component shown by the following equations.

$$\begin{aligned} K^+ &\rightarrow \mu^+ + \nu_\mu \\ K^+ &\rightarrow \pi^+ + \pi^0 \\ K^0 &\rightarrow \pi^+ + \pi^- \\ \pi^+ &\rightarrow \mu^+ + \nu_\mu \\ \pi^- &\rightarrow \mu^- + \bar{\nu}_\mu \end{aligned} \tag{2.5}$$

The density of the atmosphere affects the probability for the pions and kaons to interact with nuclei of the atmosphere. This will be discussed in more detail in section 4.

The muonic component is the most penetrating component and can reach to several thousands of kilometers into the ground. It was said that the probability for the decay of a pion increases with lower energies. A critical energy E_{cr} exists where the decays become more probable than interactions when going to lower energies. The critical energy is reached after $\bar{n}$ interactions and can be written as [6]:

$$\bar{n} = \frac{ln(E_0/E_{cr})}{ln(n_h)} \tag{2.6}$$

With n_h is the number of produced hadrons. Muons can have energy high enough to reach the ground. The flux of the muons with energy greater than 1 GeV is about 200 particles/$(m^2 s)$ at sea level [6]. The reason for this is the small energy loss of about 2 GeV when crossing the atmosphere.

Underground detectors are not time restricted like a balloon experiment and normally have a large effective area. The depth-intensity relation $I_\mu^0(h)$ is used to determine the energy spectrum of the muons at sea level by measuring the muon intensity $I_\mu(h, \theta)$

with the underground detector at different zenith angles θ. For high energies ($E_\mu >$ TeV) and $\theta \leq 60°$ the relation of $I^0_\mu(h)$ and $I_\mu(h,\theta)$ can be written as [6]:

$$I_\mu(h,\theta) = I^0_\mu(h)/cos\theta \tag{2.7}$$

Using this relation, the muon intensity measured at different values of θ with an underground detector can be translated into an estimate of the vertical flux. The vertical flux of the muon intensity as a function of the depth can be seen in figure 2.5.

Chapter 3

Anisotropy of the cosmic ray flux

Assuming that the sources of the cosmic rays are isotropically distributed and the cosmic rays will find their way more or less directly to Earth, one could expect that the arrival direction of the cosmic rays is isotropic over the sky too. The particles can be redirected e.g. by strong magnetic fields located in the inner or outer galaxy. This means that the particles may be distracted in the manner that they arrive anisotropic on the Earth. Another possibility for the source of the anisotropy in the arrival direction of the cosmic rays is described by the Compton-Getting effect which is described in the following section. The first assumption, that the sources of the cosmic rays are isotropic, is not necessarily true and the anisotropy at the arrival direction seen on Earth can originate in that fact too.

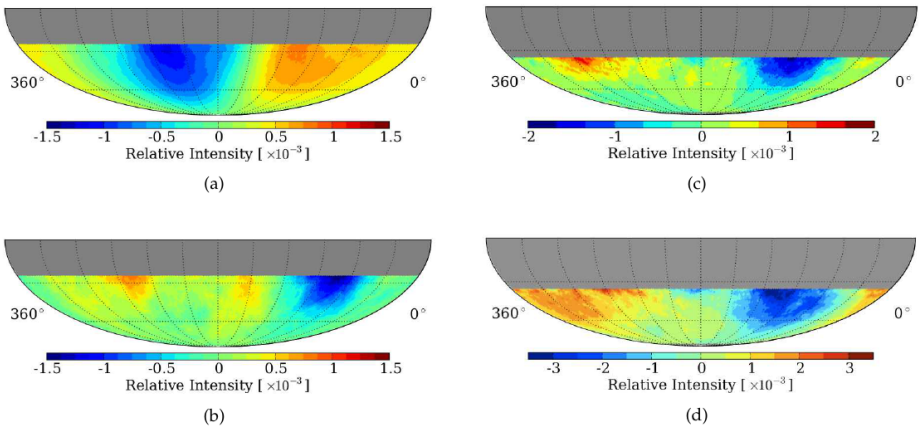

Figure 3.1: *Statistical significance sky maps of the muon rate from IceCube [4]. IC79 (in-ice), with median energies of 20 TeV (a) and 400 TeV (b) and IT73 (IceTop) with median energies of 400 TeV (c) and 2 PeV (d).*

Figure 3.1 shows the large scale anisotropy seen by IceCube for different median energies using the in-ice and IceTop detector. This chapter will give an overview at the sources of the anisotropy and will describe how to measure the effect.

3.1 Compton-Getting effect

In 1930 Arthur Compton and Ivan A. Getting [19] explained the anisotropy in the arrival directions of the cosmic rays by the fact, that an observer at speed $\vec{v}$, that equals a significant fraction of the speed of the cosmic rays, sees an excess of the CR's in the direction of travel. In the case that the cosmic rays in the reference frame are isotropic and at rest compared to the moving detector. The observer then sees an underrun for the opposite direction. This leads to an dipolar pattern for the distribution of the arrival direction of the cosmic rays measured by the moving observer. This is called the Compton-Getting Effect. The arrival direction of a cosmic ray particle relative to the direction of travel of the detector is defined by the polar angle θ where $\theta = 0°$ equals the direction of travel. In analogy to the relativistic Doppler effect the energy E' of a particle measured by a moving detector can be written as:

$$E' = E\frac{\sqrt{1-\beta^2}}{1-\beta cos\theta} \tag{3.1}$$

where $\beta = v_{det}/c$, with v_{det} as the velocity of the detector in the moving frame, c the speed of light and E the energy of the particle measured by the detector at rest depending on the incident direction of the particle. If $\beta \ll 1$, E' can be written as:

$$E' = \frac{E}{1-\beta cos(\theta)} \tag{3.2}$$

As seen in equation 3.2 the Energy E of the particle will be overestimated for incident directions with $\theta < 90°$ and underestimated for incident directions with $\theta > 90°$ by the moving observer. Compton and Getting showed that the ratio of the flux of the cosmic ray particles observed in the moving frame Φ and the flux of the frame at rest Φ' is:

$$\frac{\Phi\prime}{\Phi} = \frac{1}{(1-\beta cos(\theta))^3} \xrightarrow{\beta<<1} 1 + 3\beta cos(\theta) \tag{3.3}$$

which is the basic formula of a dipole with the amplitude of 3β. Taking into account the power-law spectrum of equation 2.1 the total dipole amplitude D as a function of β is approximately [19]:

$$D \approx (\gamma + 2)\beta \tag{3.4}$$

With that an experiment measuring the amplitude and direction of the anisotropy of the cosmic rays can confirm or exclude certain scenarios. Here the question about where the moving and the resting frame is located might be answered, or in which

frame the cosmic rays are isotropic.

3.1.1 Different scenarios of the Compton-Getting effect

The Compton-Getting effect as described above just characterizes the principle on how an Anisotropy can be seen by a moving observer through a resting frame. But where the resting frame is and in which frame the observer is located was not treated. It is possible that the cosmic rays are isotropic in the resting frame of the galaxy. Then, the motion of our solar system would cause a dipole in the arrival directions of the cosmic rays. If the extragalactic cosmic rays were isotropic and our galaxy now was the moving frame with the observer on Earth, an anisotropy could also bee seen. In another scenario the isotropic extragalactic cosmic rays correspond to the cosmic microwave background, which is the resting frame and our solar system is the moving frame. Each scenario would have its own energy region. Higher energies, around the angle (see figure 2.1), are expected to be produced by extragalactic sources. Therefore looking for different bands of energies and the direction of the anisotropy would give different amplitudes, see equation 3.4, with respect to the value of γ within the energy region.

Magnetic fields as source for the anisotropy of cosmic rays

Beside the Compton-Getting effect, which predicts the anisotropy of the arrival direction of the cosmic rays is caused by the observers frame in motion relative to the frame resting, the interstellar magnetic fields can give another explanation for the anisotropy.

Pointsources as source for the anisotropy of cosmic rays

From effects causing the anisotropy of the cosmic rays described up to now one can conclude that the cosmic rays are isotropic in the rest frame and only the motion of the observer or some influence is responsible for the anisotropy seen. It is also possible that the sources of the cosmic rays are not evenly spread over the sky leading to an anisotropic behavior.

3.2 Measuring the large scale anisotropy

A detector on Earth is able to measure the anisotropy of the cosmic rays as described above due to the rotation of the Earth scanning the sky in right ascension. This chapter will give a mathematical description on that [20] [21].

Defining $\Phi_i(\delta, \alpha, E_0)$ as the differential spectrum of the primary particles $i = p, He, \gamma, ...$, depending on the direction of those as declination δ and right ascension α, the function for anisotropy can be defined as :

$$\delta_i^{dir}(\delta, \alpha, E_0) = \frac{\Phi(\delta, \alpha, E_0}{\bar{\Phi}_i(E_0)} - 1 \tag{3.5}$$

Here $\bar{\Phi}_i$ is the mean differential spectrum of the primary particles and is defined as:

$$\bar{\Phi}_i(E) = \frac{1}{4\pi} \int_{-\pi/2}^{+\pi/2} d\delta cos(\delta) \int_0^{2\pi} d\alpha \Phi_i(\delta, \alpha, E) \tag{3.6}$$

The ideal detector has a life time of 100%. This is of course not the case for the most detectors and must be taken into account when searching for anisotropy. The anisotropy is measured in equatorial coordinates that depend on sidereal time t_s and the lifetime of the detector. The lifetime distribution as a function of sidereal time can be written as :

$$\Gamma(t_s) = \int dt L(t) \delta_{Dirac}(\Upsilon_s(t) - t_s) \tag{3.7}$$

$L(t)$ is 1 for times t when the detector was ready and has measured events and 0 for times when the detector was shutdown or no data was taken. $\Upsilon_s(t)$ transforms a given time t to the sidereal time t_s and δ_{Dirac} is the Dirac's δ-function. The expected number of measured muons per steradian as dependency of the direction (δ, α) with the energy greater than E_c at the surface can be written as:

$$N_\mu(\delta, \alpha, E_c) = \sum_i \int_0^\infty dE \int_0^{2\pi} dt_s \Phi_i(\delta, \alpha, E) \Gamma(t_s) A_i(\delta, [\alpha - t_s], E_c) \tag{3.8}$$

$A_i(\delta, h_n, E_c)$ is the efficiency distribution on how sensitive the detector is measuring muons with energy greater then E_c with the direction given by declination δ and the negative hour angle $h_n = \alpha - t_s$. It also contains the effective area of the detector for the given energy and direction.

Φ_i can be written as the sum of an isotropic and an disturbing part causing the anisotropy:

$$\Phi_i(\delta, \alpha, E) = \bar{\Phi}_i(E) + \Phi_i^\delta(\delta, \alpha, E) \tag{3.9}$$

According to 3.5 and 3.6 $\Phi_i^\delta(\delta, \alpha, E)$ can be written as:

$$\Phi_i^\delta(\delta, \alpha, E) = \bar{\Phi}_i(E) \cdot \delta_i^{dir}(\delta, \alpha, E) \tag{3.10}$$

Using equation 3.8 separately on the elements of equation 3.9, the total number of detected muons $N_{\mu i}$ can be written with the two components $N_{\mu i}^{iso}$ (isotropic compo-

nent) and $N^{\delta}_{\mu i}$ (anisotropic component) for particle type i:

$$N_{\mu i} = N^{iso}_{\mu i} + N^{\delta}_{\mu i} \tag{3.11}$$

Now the total number of measured muons for the isotropic part can be written as :

$$N^{iso}_{\mu}(\delta, \alpha, E) \equiv \sum_i N^{iso}_{\mu i}(\delta, \alpha, E) = \int_0^{2\pi} dt_s \Gamma(t_s) \tilde{A}(\delta, [\alpha - t_s], E) \tag{3.12}$$

and

$$\tilde{A}(\delta, h_n, E) = \sum_i \int_0^{\infty} dE \bar{\Phi}_i(E) A_i(\delta, h_n, E) \tag{3.13}$$

The total function for the anisotropy can now be written as:

$$\bar{\delta}^{dir}(\delta, \alpha, E) = \frac{\sum_i \int_0^{\infty} dE \cdot \delta^{dir}_i(\delta, \alpha, E) \cdot N^{iso}_{\mu,i}(\delta, \alpha, E)}{\sum_i \int_0^{\infty} dE \cdot N^{iso}_{\mu i}(\delta, \alpha, E)} \tag{3.14}$$

using equation 3.12, 3.5 can be written as:

$$\bar{\delta}^{dir}(\delta, \alpha, E) = \frac{N_{\mu}(\delta, \alpha, E)}{N^{iso}_{\mu}} - 1 \tag{3.15}$$

Now there is a formula that would allow to determine the anisotropy. The problem here is, that for this purpose $\tilde{A}(\delta, h_n, E)$ must be known very accurate as the expected anisotropy is smaller than 1/1000 [22]. Using $\tilde{N}_{\mu}(\delta, h_n, E)$, the distribution of the detected muons in equatorial coordinates defined as:

$$\tilde{N}_{\mu}(\delta, h_n, E) = \tilde{A}(\delta, h_n, E) \int_0^{2\pi} dt_s (1 + \bar{\delta}^{dir}(\delta, [t_s + h_n])) \Gamma(dt_s) \tag{3.16}$$

and $\tilde{A}$ becomes

$$\tilde{A}(\delta, h_n, E) = \frac{1}{L_t} \tilde{N}_{\mu}(\delta, h_n, E) \tag{3.17}$$

in the case that the anisotropy function is zero ($\delta^{dir}_i = 0$) and $L_t = \int_0^{2\pi} dt_s \Gamma(t_s)$, the total livetime, $\tilde{A}$ represents the direction dependent detection rate.

For the case that the anisotropy function is not zero ($\delta^{dir}_i \neq 0$) and $\Gamma(t_s) = \frac{L_t}{2\pi} = const.$ equation 3.16 can be written as:

$$\tilde{N}_{\mu}(\delta, h_n, E) = L_t \tilde{A}(\delta, h_n, E) \int_0^{2\pi} dt_s (1 + \bar{\delta}^{dir}(\delta, t_s)) \tag{3.18}$$

and therefore:

$$\tilde{A}(\delta, h_n, E) = \frac{2\pi \tilde{N}_{\mu}(\delta, h_n, E)}{L_t \int_0^{2\pi} dt_s (1 + \bar{\delta}^{dir}(\delta, t_s))} \tag{3.19}$$

For fixed declinations δ_j the number of detected muons $\tilde{N}_\mu(h_n)$ and the distribution of $\tilde{A}(h_n)$ can be set into relation as:

$$\frac{\tilde{A}(\delta_j, h_n, E)}{\int_0^{2\pi} dh_n \tilde{A}(\delta_j, h_n, E)} = \frac{\tilde{N}_\mu(\delta_j, h_n, E)}{\int_0^{2\pi} dh_n \tilde{N}_\mu(\delta_j, h_n, E)} \tag{3.20}$$

With equation 3.11 and taking into account a constant livetime distribution, the distribution of measured muons can be written as:

$$N_\mu(\delta, \alpha, E) = (1 + \bar{\delta}^{dir}(\delta, \alpha)) L_t \int_0^{2\pi} dt_s \tilde{A}(\delta, t_s, E) \tag{3.21}$$

where the integral part is independent of the right ascension and the shape of the distribution of $N_\mu(\alpha)$ is the same as the first part of equation 3.21, for fixed declination it can be written as:

$$\frac{1 + \bar{\delta}^{dir}(\delta_j, \alpha)}{\int_0^{2\pi} d\alpha (1 + \bar{\delta}^{dir}(\delta_j, \alpha))} = \frac{N_\mu(\delta_j, \alpha, E)}{\int_0^{2\pi} d\alpha N_\mu(\delta_j, \alpha, E)} \tag{3.22}$$

Equations 3.22 and 3.20 show that it is possible to measure the amplitude of the anisotropy in the direction of right ascension even if the uncertainties of $\tilde{A}$ and therefore the deviations of the isotropy is larger than the signal of the anisotropy. The only factors that matter are the statistics and the stability in time of the direction dependent efficiency. The latter can be improved if only the right ascension is of interest while the declination will be neglected. The function for anisotropy 3.15 can then be written as:

$$\tilde{\delta}^{dir}(\alpha) = \frac{\int_{-\pi/2}^{\pi/2} d\delta \bar{\delta}^{dir}(\alpha, \delta) \int_0^{2\pi} dh_n \tilde{A}(\delta, h_n)}{\int_{-\pi/2}^{\pi/2} d\delta \int_0^{2\pi} dh_n \tilde{a}(\delta, h_n)} \tag{3.23}$$

Now, if the distribution of $\tilde{A}(h_n)$ approximately has the shape of the Dirac delta function, the right ascension can be identified with the sidereal time. At the same time the distribution of the events in right ascension is given by the detection rate as a function of the sidereal time. Here the arrival direction of the events is not used. This can be made if the fluctuations (as function of α) of the anisotropy which wants to be detected is much larger than the absolute value of α of the detected events. It is also possible to divide the sky into several frames in declination with respect to the horizontal reference frame. For this a high statistic is mandatory.

With this in hand there is the possibility to measure the amplitude of the large scale anisotropy by using the number of muons detected, taking into account side effects that come from detector geometry, uptimes, changing efficiency over time, etc. .

Chapter 4

Atmospheric effects on the muon rate

For air showers induced by cosmic ray particles (protons and nuclei) the density of the atmosphere has a great influence on the production and path length of the secondary particles. The production of muons by decays of secondary particles of the air shower is a function of the energy of the particles and the density of the atmosphere. The first has to exceed the critical energy where the probability for interactions is higher than for decays. Then, the density and the temperature of the atmosphere affects the average free path length of the particles. Pions and kaons can interact with nuclei of the atmosphere creating again pions and kaons. This process can continue until the critical energy is reached and decays become more probable. The pion (kaon) flux rises from zero at the top of the atmosphere to a maximum at about 140 (160) g/cm^2 [14]. A higher temperature of the atmospheric levels will decrease the average free path length of the particles and therefore increase the interaction probability of the pions and kaons with nuclei of the atmosphere. Thus, the production of muons depends on the temperature in the way that a variation of the muon rate can be measured. In this chapter the production of the muons and the influence of the atmospheric temperature on the muon rate will be discussed. The figures 4.1 and 4.2 show measurements of the dependency of the muon rate to the atmospheric temperature as done by the IceCube Collaboration [10] and the MINOS Collaboration [8].

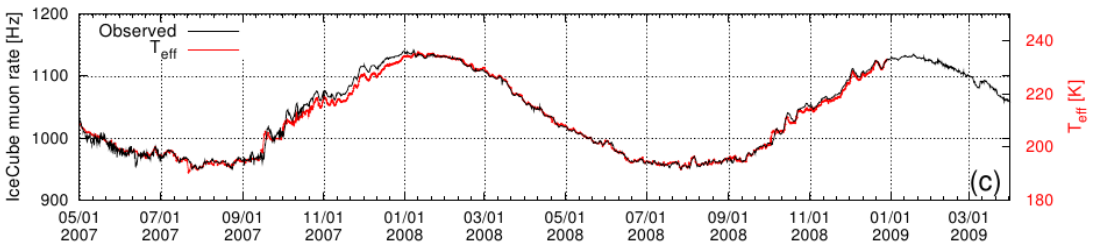

Figure 4.1: *Atmospheric temperature (red) and IceCube muon trigger rate (black). Taken from [10].*

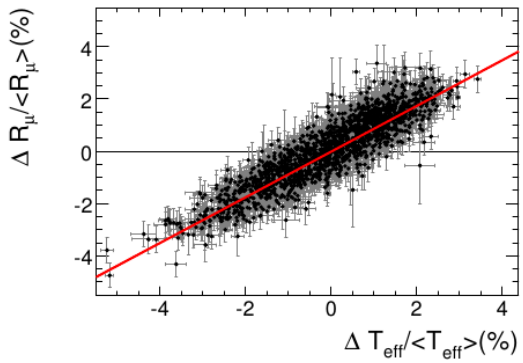

Figure 4.2: $\Delta R_\mu / < R_\mu >$ *as a function of* $\Delta T_{eff} / < T_{eff} >$ *shown by the MINOS collaboration [8].*

4.1 Dependency of muon production on the atmospheric temperature

As described in section 2.4.3, muons are generated by decays of charged pions π and kaons K created as secondary particles in an air shower. According to [14], the differential intensity of muons is a function of energy at the surface and can be written as:

$$\frac{dI_\mu}{dE_\mu} = \int_0^\infty P_\mu(E_\mu, X)\, dX \tag{4.1}$$

where P_μ is the production spectrum of muons, X the atmospheric depth and E_μ the energy of the muon at the surface. $P_\mu(E_\mu)$ applies for particle trajectories less than 60° in zenith. In that case the curvature of the Earth can be neglected. For the case that decays can be neglected ($E_\mu \gg \epsilon_\mu$) and the attenuation length Λ_i is much shorter than the depth that the particles can travel, which is the case because the size of the atmosphere is larger than the attenuation length ($X_{max} \gg \Lambda_i$), equation 4.1 can be written as:

$$\frac{dI_\mu}{dE_\mu} \approx 0.14 E^{-2.7} \left(\frac{1}{1 + \frac{1.1 \cdot E_\mu \cdot cos(\theta)}{\epsilon_\pi}} + \frac{0.054}{1 + \frac{1.1 \cdot E_\mu \cdot cos(\theta)}{e_K}} \right) \tag{4.2}$$

where ϵ_i are the critical energies for pion and kaon interactions.

When it comes to an experiment like ANTARES (see chapter 5), the muon flux can be measured and the intensity can be written as:

$$I_\mu = \int_0^\infty dE_\mu \frac{dI_\mu}{dE_\mu} \tag{4.3}$$

The muon intensity depends on the interaction and decay processes in the pion and

kaon cascades within the atmosphere. If interactions dominate, which is the case at higher energies, the variations of the temperature of the atmosphere depends directly on the production of muons and therefore on the intensity of the muons. Lower energies do not have this dependency. To separate the two energy ranges, the critical energy for the pion ϵ_π and kaon ϵ_K decay is used [23].

$$E_\mu \gg \epsilon_i = \frac{m_i \cdot c^2 \cdot H(T)}{c \cdot \tau_i},\ i = \pi\ or\ K \tag{4.4}$$

where m_i is the mass, $c \cdot \tau_i$ is the decay length of the pion and kaon and $H(T) = RT/Mg$ is the atmospheric scale height for an isothermal, exponential atmosphere.

Looking at equation 4.1, the temperature dependence is in the function P, which can be written as:

$$\begin{aligned} P_\mu(X, E_\mu, T_0 + \Delta T) &= P_\mu(X, E_\mu, T_0) + (\partial P_\mu/\partial T)_{T_0} \Delta T(X) \\ &= P^0_\mu(X, E_\mu) + \eta^0(X, E_\mu)\Delta T(X) \end{aligned} \tag{4.5}$$

while the functions with superscript 0 are the interpretation of the temperature sensitive functions at $T = T_0$. Then, using 4.3 and 4.1 amounts to:

$$\begin{aligned} I_\mu(E_\mu, T_0 + \Delta T) &= \int_0^\infty dE_\mu \int_0^\infty dX \left(P^0_\mu(X, E\mu) + \eta^0(X, E_\mu)\Delta T(X)\right) \\ &= I^0_\mu + \int_0^\infty dX \Delta T(X) \int_0^\infty dE_\mu \eta^0(X, E_\mu) \end{aligned} \tag{4.6}$$

When using $\Delta I_\mu = I_\mu(T_0 + \Delta T) - I^0_\mu$, the dependence of the muon intensity variations on the temperature of the atmosphere can be written as [24] :

$$\frac{\Delta I_\mu}{I^0_\mu} = \int_0^\infty dX \alpha(x) \frac{\Delta T(X)}{T(X)} \tag{4.7}$$

where $\alpha(X)$ is the temperature coefficient:

$$\alpha(X) = \frac{T(X)}{I^0_\mu} \int_0^\infty dE_\mu \eta^0(X, E_\mu) \tag{4.8}$$

with $W(X) = \int_0^\infty dE_\mu \eta^0(X, E_\mu)$ 4.8 becomes:

$$\alpha(X) = \frac{T(X)}{I^0_\mu} W(X) \tag{4.9}$$

The temperature coefficient is hard to determine experimentally because the variations of the temperature for different atmospheric depths is not known. The integral can be simplified when defining an effective temperature T_{eff} [24]:

$$T_{eff} = \frac{\int_0^\infty dX T(X) \int_0^\infty dE_\mu \eta^0(X, E_\mu)}{\int_0^\infty dX \int_0^\infty dE_\mu \eta^0(X, E_\mu)} \tag{4.10}$$

and the effective temperature coefficient α_T

$$\alpha_T = \frac{T_{eff}}{I_\mu^0} \int_0^\infty dX \int_0^\infty dE_\mu \eta^0(X, E_\mu) \tag{4.11}$$

Using equation 4.8 and defining ΔT_{eff} analog to T_{eff} shown in equation 4.10, the intergral in 4.7 can be transformed to:

$$\int_0^\infty dX \alpha(x) \frac{\Delta T(X)}{T(X)} = \alpha_T \frac{\Delta T_{eff}}{T_{eff}} \tag{4.12}$$

which can be written as:

$$\frac{\Delta I_\mu}{I_\mu^0} = \alpha_T \frac{\Delta T_{eff}}{T_{eff}} \tag{4.13}$$

This function describes the dependence of muon intensity fluctuations and atmospheric temperature fluctuations.

To evaluate the value of α_T it is necessary to calculate the effective temperature and the muon intensity which can be written as:

$$I_\mu = \frac{\frac{N_i}{t_i}}{\varepsilon \cdot A_{eff} \cdot \Omega} \tag{4.14}$$

where N_i is the number of muon events measured by the detector, t_i the lifetime in which they were detected, A_{eff} the detector effective area and Ω the total solid angle viewed by the detector. For the following calculation it is important that the effective area A_{eff}, Ω and ε are constant over time. Then equation 4.13 can be transformed as follows:

$$\frac{\Delta I_\mu}{I_\mu} = \frac{\left(\frac{\Delta N_i/t_i}{\varepsilon \cdot A_{eff} \cdot \Omega}\right)}{\left(\frac{\Delta N_i/t_i}{\varepsilon \cdot A_{eff} \cdot \Omega}\right)} = \frac{\Delta N_i/t_i}{N_i/t_i} = \frac{\Delta R_\mu}{R_\mu} \approx \frac{R_\mu - \bar{R}_\mu}{\bar{R}_\mu} \tag{4.15}$$

where $R_\mu = N_i/T_i$ is the rate of the muons detected during lifetime t_i and $\bar{R}_\mu = \sum_i N_i / \sum_i t_i$ is the avarage muon rate over the period of time taking data $\sum_i t_i$. Inserting this into equation 4.13, it becomes:

$$\frac{\Delta R_\mu}{\bar{R}_\mu} = \alpha_T \frac{\Delta T_{eff}}{\bar{T}_{eff}} \tag{4.16}$$

With this formula it is possible to study the effect of the variations of the atmospheric

temperature with a detector with the characteristics described above. The rate of measured muons over time gives the R_μ and $\bar{R}_\mu$.

4.2 Effective temperature of the atmosphere

The pressure and temperature are changing continuously through the atmosphere. The production of the muons with higher energies than the critical energy (ϵ_π, ϵ_K) depends on that temperature. The production of the muons usually takes place at an altitude of about 10-40 km above sea level. The effective temperature as defined in 4.10 considers the different production probabilities for muons at different altitudes by the weights $W(X)$ as defined for equation 4.9. These weights consist of two main parts that are responsible for the muon production in the air shower and can be written as: $W(X) = W^\pi + W^K$, representing the contribution of pions and kaons to the overall variation in muon intensity and can be written as [14] [25]:

$$W^{\pi,K}(X) \approx \frac{(1 - X/\Lambda'_{\pi,K})^2 e^{-X/\Lambda_{\pi,K}} A^1_{\pi,K}}{\gamma + (\gamma+1) B^1_{\pi,K} K(X) (\langle E_{th} \rangle / \epsilon_{\pi,K})^2} \tag{4.17}$$

with

$$K(X) \equiv \frac{(1 - X/\Lambda'_{\pi,K})^2}{(1 - e^{-X/\Lambda'_{\pi,K}})\Lambda'_{\pi,K}/X} \tag{4.18}$$

where the parameter $A^1_{\pi,K}$ includes the amount of inclusive meson production in the forward fragmentation region, masses of mesons/muons and the muon spectral index. $B^1_{\pi,K}$ indicates the relative atmospheric attenuation of mesons, E_{th} is the energy required for a muon to survive to a specific depth (where the detector is located) and can be detected by the detector. $\Lambda'_{\pi,K}$ is defined by the attenuation lengths for the cosmic rays primaries Λ_N, pions Λ_π and kaons Λ_K as $1/\Lambda'_{\pi,K} \equiv 1/\Lambda_N - 1/\Lambda_{\pi,K}$. γ is the muon spectral index and $\epsilon_{\pi,K}$ is the critical energy. The temperature as function of the atmospheric depth is not easy to estimate. However it is possible to determine the temperature for discrete pressure levels. Such data sets are provided by the European Centre for Medium-Range Weather Forecasts (ECMWF) [7]. Then, the integral in 4.10 can be written as a sum over the different atmospheric levels X_n. Taking into account the two parts of $W(X)$ for pions and kaons as mentioned above, the effective temperature can be written as:

$$T_{eff} \approx \frac{\sum_{n=0}^{N} \Delta X_n T(X_n)(W^\pi(X_n) + W^K(X_n))}{\sum_{n=0}^{N} \Delta X_n (W^\pi(X_n) + W^K(X_n))} \tag{4.19}$$

Chapter 5

The ANTARES experiment

ANTARES is a neutrino detector that uses the emission of Cherenkov light to detect the particles created by neutrinos interacting with the surrounding matter. One of these particles is the muon coming from the muon neutrino. This principle allows to detect the muons created by the air showers of the cosmic rays. The information can be used to determine the anisotropy of the cosmic rays and the muonic component of the air showers. This section will give an overview on the detection principle, the layout and data taking of the ANTARES detector.

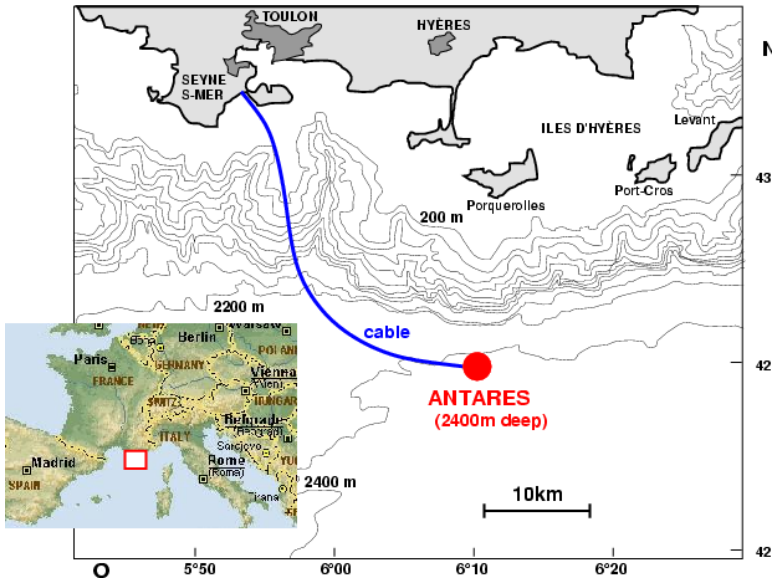

Figure 5.1: *The location of the ANTARES detector. The cable which connects the detector with the shore is illustrated [26].*

Figure 5.2: *Optical Module of the ANTARES detector [27].*

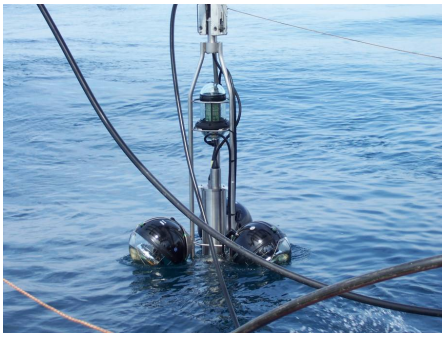

Figure 5.3: *A storey of ANTARES still above sea level [28].*

5.1 Detector layout

ANTARES is located in the Mediterranean Sea, about 40 km south-east off the coast from Toulon, France. Picture 5.1 gives an overview of the position. The detector is located at a depth of about 2.5 km, shielded from light sources like the sun. An electro-optical cable connects the detector to the shore from where the power and the high voltage are supplied and the data coming from the detector is saved.

The optical modules (OM's) are the basic devices responsible for detecting Cherenkov light emitted by high energetic particles in water (see figure 5.2). It is a sphere of glass with 43 cm of inner diameter and 15 mm thickness so it can withstand the pressure of up to 600 atm under water. It houses the photomultiplier tube (PMT) which is sensitive for single photons for wavelength from 300 to 600nm, and the electronics board.

Figure 5.3 shows a storey which is built of 3 OMs and a frame. The OMs are positioned at equidistant angles around the frame, pointing downwards at 45°. The frame is a titanium cylinder and holds the electronics for data transmission, calibration and monitoring.

The storeys are connected serially at a vertical distance of about 14 meters to the lines. Each line holds 25 storeys (except the last, which has only 20 storeys) and are connected to the junction box. Each line is anchored in the sea ground and is strained by a buoy at the top. There are 12 lines overall which makes the complete detector with the additional 13 th line, the instrumentation line. The last 5 storeys of the 12 th line and the instrumentation line are equipped with instruments for environmental parameters and acoustic neutrino detection. Figure 5.4 shows a scheme of the alignment of the lines and the dimensions of the detector. The total amount of OMs is 885 and the instrumented volume is about $1.1 \cdot 10^7 m^3$. The junction box receives the data from each line and sends it to the shore station. It provides the lines with power and passes control signals from the shore to the lines.

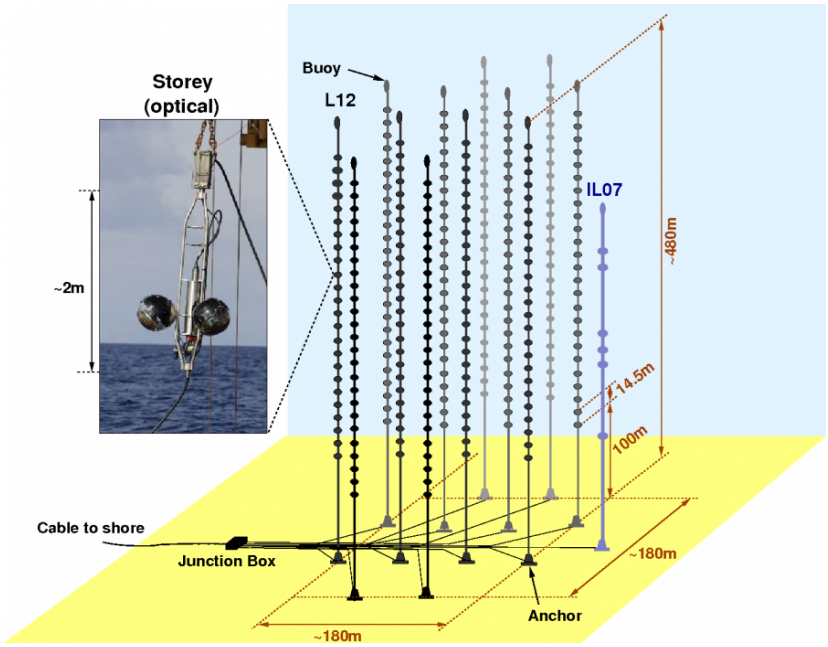

Figure 5.4: *Schematic scheme of the ANTARES detector. On the left, a story is shown [28].*

5.2 Detection principle

Charged particles like Muons can be measured with detectors like ANTARES because of the Cherenkov effect. For that, the velocity of the particles has to be greater than the speed of light in the matter. Then, these particles not only lose energy by bremsstrahlung etc. but also by the Cherenkov effect, emitting electro-magnetic radiation. Because of the speed of the particle the Cherenkov radiation occures at a characteristic emission angle Θ_C, resulting in a cone of light directed along the trajectory of the particle. For sea water that surrounds the ANTARES detector the emission angle is about 42° [29]. Figure 5.5 illustrates the cone of Cherenkov light for a muon traveling through ANTARES. The sea water has an absorption length of $60m \pm 10m$ and an effective scattering length of $270m \pm 30m$ for the wavelength of 473 nm [30].

Then the photons from the Cherenkov effect can be detected by the OMs of ANTARES. With the knowledge of the position of each OM, the specific time when the photons were measured and with respect to the emission angle it is possible to reconstruct the direction and the energy of the traversing particles.

5.3 Optical background

Beside the photons emitted by Cherenkov radiation the location of ANTARES in the Mediterranean sea is responsible for optical background from different sources having

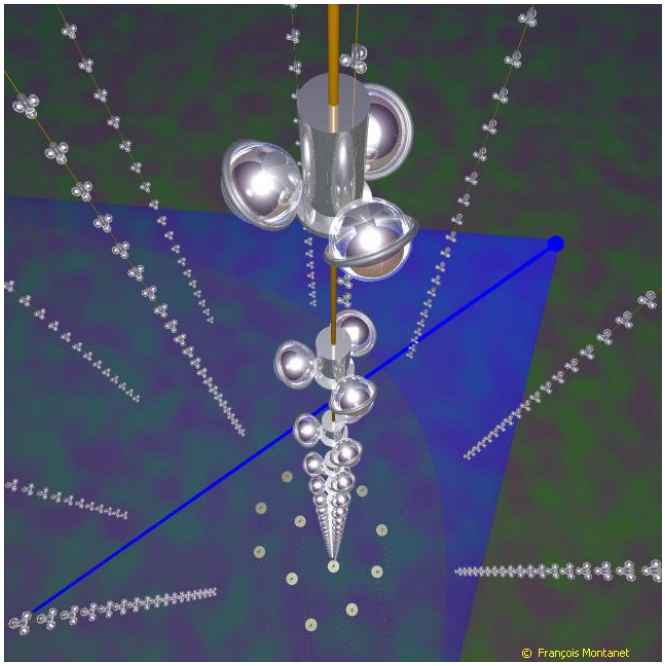

Figure 5.5: *Principle of a muon traversing the ANTARES detector [28].*

a direct influence on the counting rate of the PMTs. Picture 5.6 shows an example of the hit rate of one PMT of ANTARES. The baseline here is about 50 – 60 kHz. Bursts can lead to much higher rates. In the example they go up to several MHz. Both, the baseline and the bursts are highly depending on the current circumstances of the sea water like temperature, velocity and the activity of bacteria. The picture only shows one PMT but it counts for the other PMT throughout ANTARES too. Bacteria and

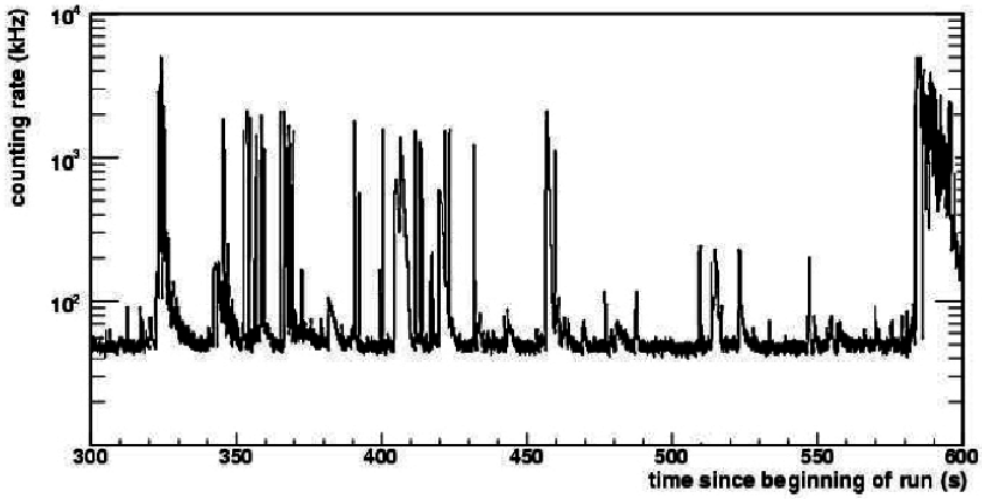

Figure 5.6: *Example of the hit rate of one PMT of ANTARES. The spikes are called bursts and are mainly caused by bioluminescence [31].*

other life forms that are able to emit light and radioactive decays of K^{40} are responsible for the baseline part of the hit rate. While the K^{40} decays are constant over time, the optical background caused by bacteria can vary up to several hundreds of kHz. Bursts as seen in picture 5.6 are meant to be caused by multi-cellular organisms emitting light as short flashes. The optical background can be different within the detector e.g. the floors positioned at the top of the detector have a higher baseline and bursts as the floors at the bottom.

Reconstruction algorithms have to make a hit selection to identify hits on optical modules caused by optical background or the Cherenkov effect. In the case where a muon traverses the detector photons are emitted because of the Cherenkov effect at a cone along the trajectory of the muon at an angle of about 42°. Beside this effect the information on the intensity of the hits measured in photo-electrons is used to distinguish background and signal hits [32]. Using this information the reconstruction algorithms of ANTARES can reduce the influence of the optical background to reconstructed trajectories of the muons.

5.4 Trigger

The baseline which represents the hit rate of each OM of the detector can vary over a range from about 50 kHz up to several hundreds of kHz. It is necessary to filter the data sent to the shore station in the way, that only the data which does include an event caused by a particle has to be recorded. For that purpose triggers are applied online to the hits of the OMs.

There are different triggers that have different purposes and different sensitivities. To be able to react on the varying optical background these triggers are turned off and on according to trigger rates and baseline. This is done manually by people of the ANTARES collaboration called shifters. The triggers can be combined and are organized by run setups to make it easier for the shifters to decide which trigger should be turned off or on and to have similar circumstances for different time ranges.

The basic concept of data taking in ANTARES is that all data will be transferred to the shore station. If one or more off-shore triggers have detected a coincidence in the hits of some OMs, all data in a defined time slice is recorded and send to the onshore station. In sum there are six different triggers available. In this analysis only two triggers are used and will be explained in the following [33].

A photon that hits an PMT will create a signal. The strength of that signal is expressed in photo-electrons (p.e.). The PMTs have a dark noise which also can lead to a singal. To avoid this a 0.3 p.e. threshold is set. If a signal exceeds that threshold the hit is called L0. That is the lowest requirement for signals to be considered a signal

from a particle.

L0 hits can be interpreted as L1 hits if the signal exceeds 3p.e. or 10p.e. (depending on the period of time) or if at least two L0 hits from different OMs of the same storey inside a window of 20ns are coincident with respect to different position of the OMs and scattering effects. These hits are the basis for the triggers.

The 3T trigger is fired if two L1 hits in a time window of 80ns or 160ns are found. If there are two 3T trigger events, the trigger 2T3 is fired. The 3DScan trigger requires at least five L1 hits in a specific time window corresponding to a muon track. It is possible that data chosen to be sent to the shore station could have been triggered by multiple triggers. Reconstructed tracks do not lose the information which trigger has fired and can be checked within the analysis.

Picture 5.7 shows a screen shot of the actual trigger rates as viewed at a computer at the control station of ANTARES. The triggers that have a counting rate of zero Hz are turned off, the other are online and send data to the shore station. The rates differ from 0.1 Hz to about 12 Hz for the trigger named TRIGGER-3D. This work uses events triggered by T3 and 3DScan which can be seen in the figure.

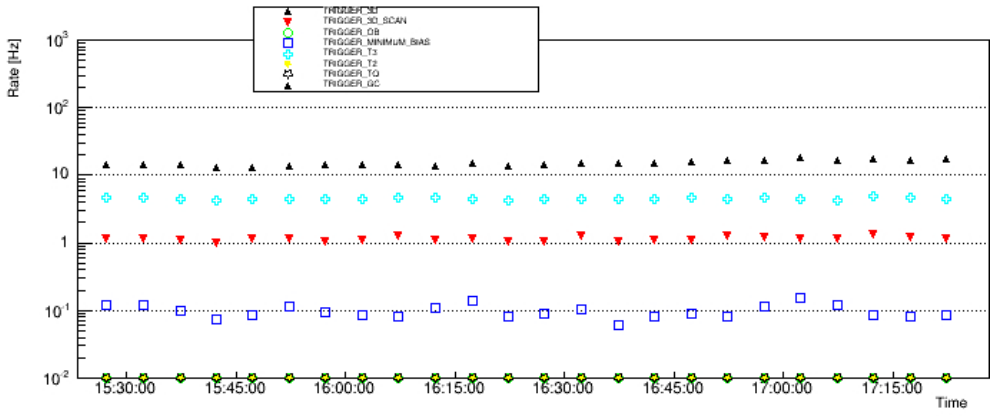

Figure 5.7: *A screenshot of the online monitor for the trigger rates of ANTARES.*

Beside the precise time when a photon hits an PMT of ANTARES, the position and direction of the OM is important for the reconstruction of the tracks of the particles. The lines are anchored in the sea ground while the position was determined by GPS from the ship that has deployed the lines. The lines themselves are flexible structures hold up by a buoy for each line but the sea current may change the position of the buoy and therefore the position of the OMs for several meters. To get the current position and direction of the OMs, five hydrophones are equipped to each line, distributed over the 25 floors. They can receive acoustic signals send from the bottom string socket and so the position of the floors where the hydrophones are mounted can then be calculated. For the orientation of the OMs tilt meters and compasses are available. With that, the position of each OM can be determined within a 10 cm range [34]. The graphs in 5.8

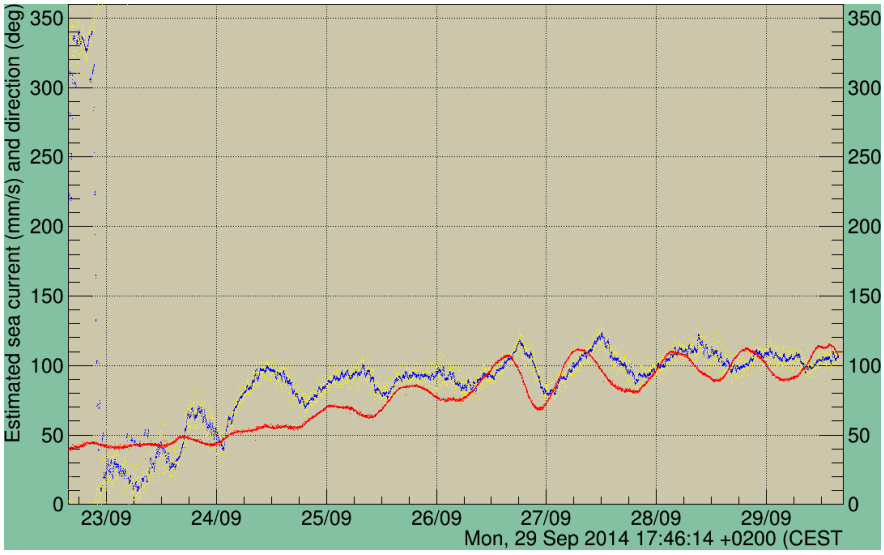

Figure 5.8: *A screenshot of the online monitor for the sea current (red, mm/s) and direction (blue/yellow, degree) at the ANTARES site over time.*

show the sea current (red) in mm/s and the direction in deg measured by the sensors described above. It can be seen that the direction and current can change rapidly and with them the circumstances of data taking. Here the shift people need to decide wether to change the run setup or not.

5.5 Data acquisition, storing and quality

The data sent to the shore station by the detector is saved in files referred to as runs. Each run has a unique run number and is saved as a root tree [35]. A program named Runcontrol is responsible for the used triggers. As described above, the triggers are chosen by the shifters based on different circumstances like the mean hit rate of the OMs and trigger rates. The time one run covers has changed over the time from a few ($\approx 2h$) to several hours ($\approx 8h$). If the conditions are stable, the Runcontrol automatically starts a new run at the end of the time or if the file exceeds a specific size. The run number will be increased, the current file will be closed and a new file will be started. The shifters always have the possibility to pause, restart and stop the current run to start a new one. This should be avoided to get the maximum uptime for the detector but is necessary if the conditions like the hit rate changed and triggers need to be enabled or disabled. Beside the data runs, different types of calibration runs exist. The data from that runs are used to calibrate the charge and time properties of the OMs.

Every analysis made with the data of ANTARES needs to make selections on the runs. Different circumstances for different runs like the baseline or active OMs for the

run make it useful to have a quality parameter. Each analysis has different requirements to that quality parameters. To provide a basis to which anybody has access a quality parameter called quality basic (QB) is available. It differs 4 cumulative characteristics as shown below. For a precise list see [36]

- QB=1: this makes very basic checks for each run where the data will be checked for misbehavior of the electronics and the data acquisition system. All runs that match these criteria will get at least this value.
- QB=2: additionally to QB=1: runs, where at least 80% of the OMs are in status OK get this value.
- QB=3: additionally to QB=2: makes a cut on the baseline and the burstfraction (baseline $\leq 120kHz$, burstfraction $\leq 40\%$)
- QB=4: additionally to QB=3: baseline $\leq 120kHz$, burstfraction $\leq 40\%$

The baseline and the burstfraction can be described using figure 5.6 when a histogram is made out of the values of the hit rate. The median of Gaussian fit to the corresponding histogram will give the baseline. The burstfraction corresponds to the fraction of time during that the OM counting rates are larger than 20% above the value of the baseline [37].

5.6 Track reconstruction

The OMs of ANTARES with their PMTs give the time and the intensity of the photons measured. Track reconstruction is the search for signals caused by Cherenkov light emitted by a particle traversing the detector and to retrace the trajectory of that particle. A straight line refered to as track that represents the way of the particle through or near the detector is the basic model of a track reconstruction. Picture 5.5 shows this principle. As already mentioned the hits from optical background can not be distinguished from the hits caused by Cherenkov light but by their timing. While the background hits are randomly distributed throughout the detector it is possible to identify the hits from Cherenkov light, if the light cone and the timings of the corresponding hits are considered. A reconstructed track is then given by the absolute time of occurrence, the position $\overrightarrow{p} = (x, y, z)$ with respect to the center of the detector and the direction $\overrightarrow{d} = (\theta, \phi)$. This section shortly describes the two main reconstruction algorithms used for ANTARES.

BBFit [38] has been designed for fast and robust reconstruction. It uses coincidence L1 hits just like the T3 trigger to select hits. To make this algorithm fast some simplifications were made: The lines of the detector are supposed to be straight and appear

to be vertical. Another simplification is that the three OMs of one floor are merged to one point that lies on the line and different timings from the OMs that lie in a time window of 20ns of one floor are therefore lost. The same accounts for the charge of the hits. To estimate an error on the reconstructed track an error function is used and its value is available for all tracks reconstructed by BBFit. Find more information in [38].

Because the method used for this algorithm is fast enough the data sent to shore is analyzed online with BBFit. This allows a look on events currently detected. An online display shows a selection of incoming events. Picture 5.9 shows a single line event reconstructed online with BBFit. Each graph corresponds to one line where the charge of the hits (dots) is masked with colors. The line is the reconstructed track and marks the times where hits on the OMs of that line could also have occurred.

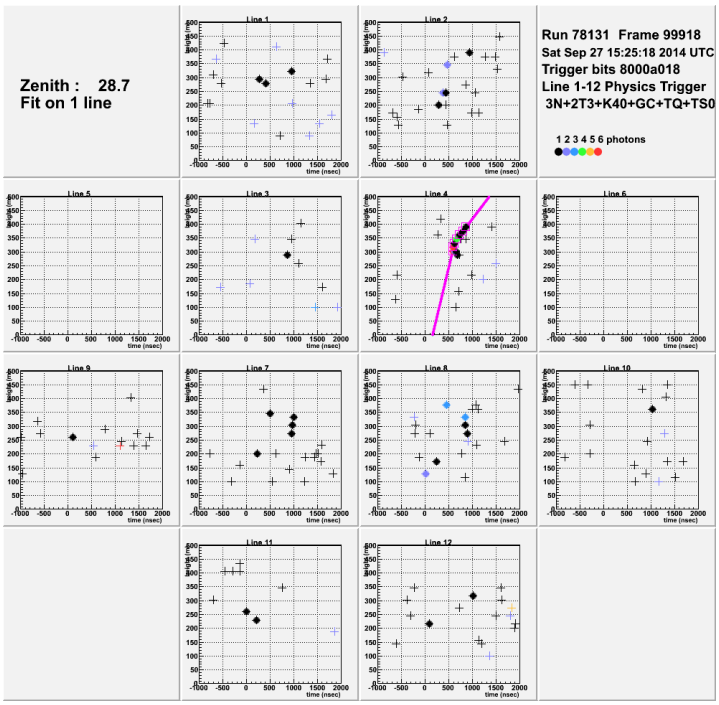

Figure 5.9: *The online display of ANTARES for events.*

The second reconstruction algorithm is AAFit [39]. Here precise information on the position of the single OMs are taken into account. A first fit with L1 hits is made to provide a stable starting point for the maximum likelihood algorithm where all hits (not only those which have caused a trigger) are considered and may be used with respect to their timing on the muon track. If a track could be reconstructed for the given data the reliability is given by the parameter λ. This algorithm is more time consuming than BBFit and is not used for online reconstruction.

5.7 Monte Carlo simulations

Monte Carlo simulations are useful to check the reliability of the used algorithms. In ANTARES different packages and approaches are used to cover all information expected to come from the detector. For the various signals (e.g. muons, neutrinos, optical background) different programs are available. All simulated signals are then merged together with respect to their lifetime and are available as data just like the data coming directly from the detector. This section gives an overview of some of the used programs.

GENHEN [40] is a neutrino Monte Carlo simulator where the user can define different input parameters like the flavour of the neutrinos, the energy range, charged and neutral current interactions, the model of neutrino interaction and the neutrino flux which defines the lifetime of the simulation. Each simulated event has a weight with which the number of events in one simulation file can be adapted to the lifetime of that file. The muons induced by neutrinos are simulated inside of a surface surrounding the instrumented volume (the detector) called the can. Figure 5.10 shows the dimensions of the can in relation to the instrumented volume, which is also defined cylindrical in shape just like the can. The size of the can is defined by the radius of the detector plus about 3 times the absorption length of the Cherenkov light in water.

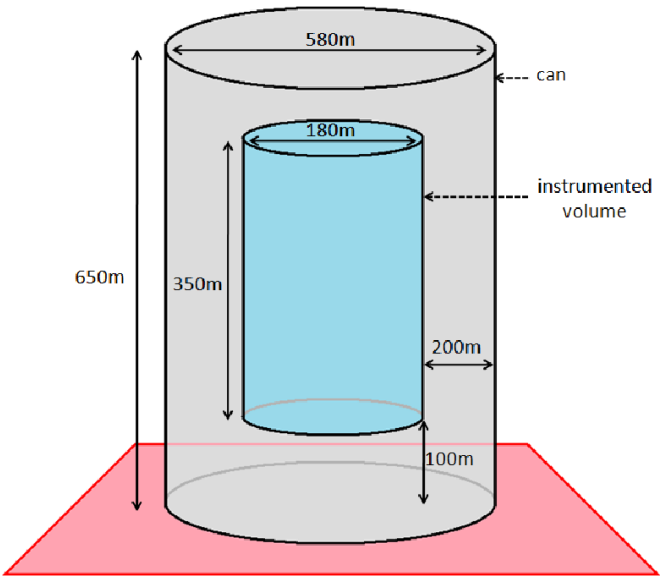

Figure 5.10: *The dimensions of the can used by Monte Carlo simulations [41].*

GEASIM [42] uses the output files from GENHEN and simulates particles and showers including their propagation and the radiation produced by the particles along their trajectory.

For the simulation of atmospheric Muons created by airshowers MUPAGE [43] is

used. Other than Corsika [44], which is the other tool for simulations of airshowers in ANTARES, MUPAGE does not trace down the whole process starting by a particle hitting the Earth's atmosphere, creating secondary particles until the muons arrive at the detector, but starts directly at the can (see figure 5.10). MUPATE uses formulas computed by a full Monte Carlo simulation and is much faster. It allows muon simulations up to 5.0 km w.e. that makes it suitable for simualtions for ANTARES. The program takes different parameters, such as the shower multiplicity and energy, the range for the zenith angle to be simulated and the properties of the water like the density and optical absorption length.

For the optical background two different approaches are available. For the first, a fixed background rate is specified and is added to the simulated hits according to a Poisson distribution. The rate can be defined for each run by the user. The second approach is called run-by-run (rbr) and is designed to produce more realistic conditions concerning the data taken from the detector. The conditions for optical background, lifetime of the run, position and orientation of the OMs and the calibrations are taken from the actual data and are included into the Monte Carlo simulation. After that the same algorithms for track reconstruction are applied to that data, leading to Monte Carlo data that suits one data run. The enumeration of the Monte Carlo data is the same as the data taken as runs from the detector. That makes it easier to identify the associating run.

For this analysis the run-by-run Monte Carlo data V2.0 is used when data and MC were compared. This analysis only looks for Muons coming from air showers above the detector. The neutrinos that come through the Earth are not of interest in this work and are excluded by a cut on the zenith of the arrival direction of the detected muons.

Chapter 6

Data selection

The measurement of the anisotropy in the arrival direction of the cosmic rays by atmospheric muons is a matter of statistics and therefore the number of events that can be detected as described in chapter 3.2. In the same chapter some assumption like a fully known efficiency in time of the detector were made. This leads to equations 3.23 and 3.22. Both methods can be used to detect the anisotropy but they differ in detail. This chapter will summarize the two principles and how they can be applied to the data taken by ANTARES.

6.1 Constraints for the search of the anisotropy

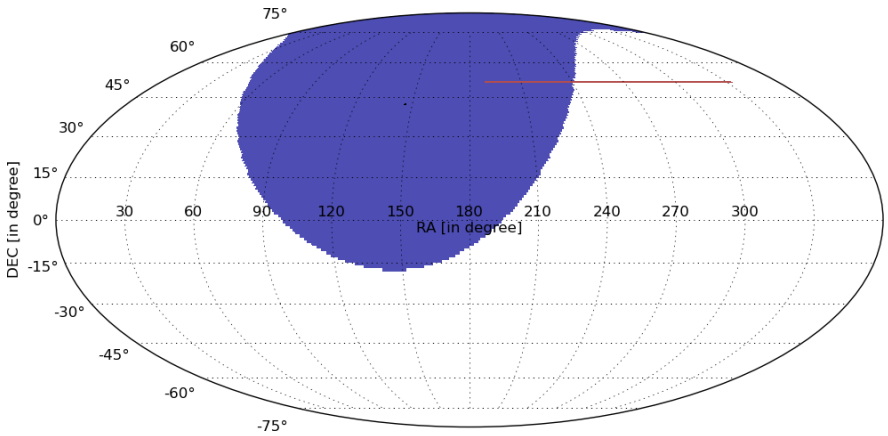

Figure 6.1: *A Skyplot in equatorial coordinates showing the visible area (blue) for ANTARES for events, where the zenith is less then* 60°*, for a specific time. The red line shows how events are evolving over time, if they come from a constant direction of* 30° *for zenith and azimuth (left to right).*

Figure 6.1 shows a skyplot in equatorial coordinates and gives a feeling on how data taking is evolving over time and what area can be seen at a specific time by ANTARES. The right ascension (RA) is identified with the hour angle and both, RA and declination (DEC), are binned over the whole sky. The black dot at about 148° RA

and 42° DEC marks the center of the detector for October 24th 2011 0:00 am, where the event would have come from directly above the detector (zenith = 0°). The blue area also counts for the same time and marks the sector from where events count for that time. It is effectively a circle in the local coordinate system, where the maximum zenith angle is 60°. Events with an angle less than this would survive this cut and would be counted. In the equatorial coordinate system, this circle appears distorted because of the transformation and projection. The whole area would travel to the right for later times until it starts again at 0° RA. The red line masks a time period from October 24th 2011 0:00am until October 24th 2011 4:48pm (the start and end times are chosen at random to illustrate the principles). The start point at the left is for an event with 30° in zenith and azimuth in the local coordinate system. The position in local coordinates of the event is kept while the time evolves and creates that line. It can be seen, that the declination is constant over time and only the right ascension increases. The whole northern sky (down to −15° dec) can be seen by ANTARES when time is evolving using the described cut on zenith angle. The right ascension is scanned completely during one sidereal day.

An anisotropy in the arrival direction of the cosmic rays is expected to be visible in the direction of right ascension as described in section 3.2 and ANTARES is capable to investigate this by scanning the visible sky. Because of the low amplitude of the large scale anisotropy a high number of events is required (see section 3. ANTARES is a ground based detector, that takes data all the time. The visible direction is fixed in local coordinates and changes only because of the rotation of the earth. Because of maintenance and the optical background, the detector is not taking data all the time. There are time periods where the detector was disabled or where data was taken that was not used in this work. This periods can be a few hours up to several days, for example if illuminating bacteria is very active at spring time. The lifetime distribution $\Gamma(t_s)$ as defined in equation 3.7 is considered in the equations in chapter 3.2 but still has influence on the measurement of the anisotropy. A lack of data in the sidereal day, where the detector does not take data, can change the information significantly. Based on the blue area in figure 6.1, where the visible area for one specific time is shown, figure 6.2 accumulates the visible area over the time from 2011 October 24th 07:12:00 until 2011 October 25th 04:48:00. The time period was chosen at random, covering nearly a whole sidereal day. The values of the bins are the time in seconds for how long a single bin was seen by the detector. The black line shows how the middle of the detector (events coming from above, zenith=0.0, azimuth=0.0) evolves over that time and illustrates how the centre position of the detector will be projected in equatorial coordinates. The gab in that line marks the time where the detector was simulated to be turned off. It can be seen, that this single gab in the time of data taking does have an influence on the measurement in the way, that an anisotropy would have been introduced. A measurement for the anisotropy has to deal with that. In figure 6.3 the same data is shown except that the bins do not show the absolute value of the time in

seconds for each bin but the absolute value $t_{i,j}$ divided by the mean of each declination band. The mean time for the declination band $< t_{\delta_i} >$ is calculated in the following way:

$$< t_{\delta_i} >= \sum_j t_{i,j} \tag{6.1}$$

where δ_i is the $i'th$ declination band and j is identified with the right ascension band. The relative value of a bin $\tilde{t}_{i,j}$ is:

$$\tilde{t}_{i,j} = \frac{t_{i,j}}{< t_{\delta_i} >} \tag{6.2}$$

In this illustration smaller differences are easier to recognize. The area where the detector was turned off virtually is darker, showing that the detector has seen that area less seconds in comparison to the other areas. The small artifacts visible for the declination band at about $-16°$ are statistical fluctuations coming from the simulation and binning. The white bins in the same declination band were not seen at all in this simulation because of the gab in the sidereal day.

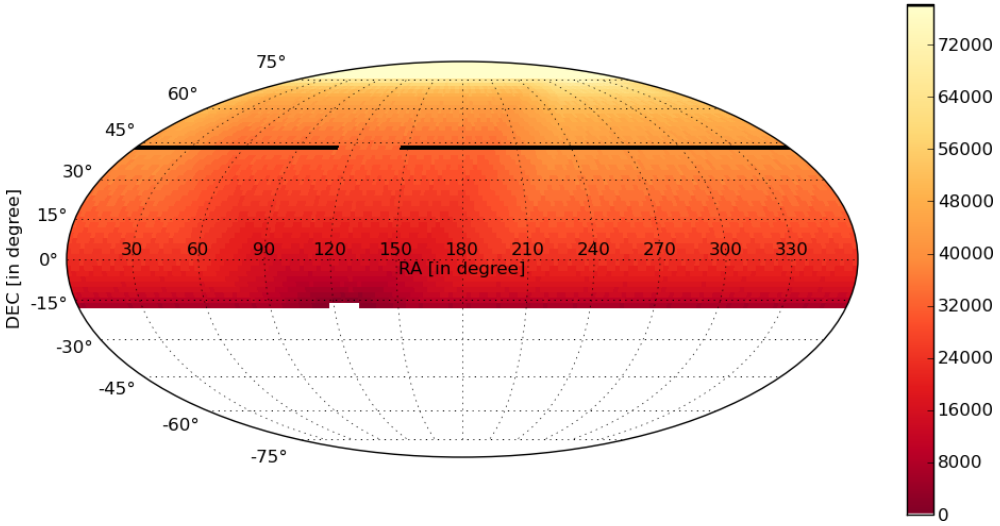

Figure 6.2: *A Skyplot in equatorial coordinates showing the influence of the lifetime of the detector. The color shows the time in seconds for which the bins where visible to the detector, and the zenith angle is less than 60° in the local coordinate system. The black line is the position of detector (zenith=0.0, azimuth=0.0) through the time.*

In practice the total lifetime will be of about a year or more and it is very unlikely that there is a complete lack in the skyplot where no data was taken at all. The optimum, where the detector took data a whole year, is on the other hand very unlikely too and the lifetime for each bin has to be taken into account to avoid interferences with the signal of the anisotropy.

How many times each bin was seen by the detector is defined by circumstances like

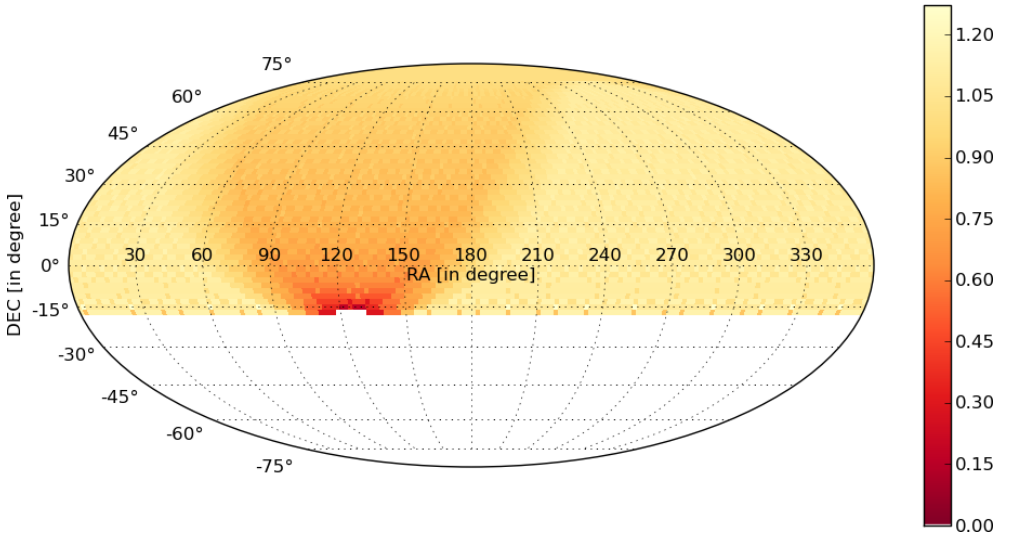

Figure 6.3: *This plot roughly shows the same data as in figure 6.2 except that the values of the bins do not show the absolute time in seconds but the relative time (see text).*

down times as described in chapter 5 and the selection of runs used for the analysis. Some runs, like calibration runs, are not appropriate for the analysis and will not be used.

The search for the large scale anisotropy depends on many features and they have to be understood and taken into account. For example the size of the bins in δ and α depends on the total number of events. The effect of the anisotropy is expected to be about 0.2 ‰[22] and each bin has to have an amount of events large enough to reduce the statistical error so that the effect of the anisotropy can be detected. This may define the bin size to larger values if the statistics of the events decreases. If the bins become too large, the number of data points may be too little to fit a dipole/sinus function. If the efficiency of the detector changes on different time scales during data taking, the muon rate will be affected. The understanding of the factors and properties that have an affect on the muon rate is mandatory for the search of the large scale anisotropy. In the following chapters the variation of the muon rate and the influence of different parameters and circumstances on the muon rate are discussed.

6.2 Detector lifetime and periods with similar characteristics

The first data was taken by ANTARES in 2006. Only one line was deployed at this time. About one year later the detector was equipped with five lines and first results were made. It took until May 2008 when the whole detector was completed, now consisting of all 12 lines.

In the following years some lines were redeployed for maintenance and repair. The duration where one or more lines were missing ranges from some days to several months and the efficiency of the detector changes for all these periods because of the loss or gain of optical modules on that lines. This work uses data starting with May 2008 when all 12 lines were deployed until the end of 2013. Time periods are identified where the number of lines of the detector is kept constant. A TimeSlice identifies such a time period with increasing ID, see table 6.1.

Reference name	Lines lost/available	Time period
TimeSlice1:	All lines running	29 May 2008 - 11 Mar 2009
TimeSlice2:	Line 12 missing	13 Mar 2009 - 1 Jul 2009
TimeSlice3:	Line 12, 9 missing	3 Jul 2009 - 26 Oct 2009
TimeSlice4:	Line 9, 6 missing	14 Nov 2009 - 10 Feb 2010
TimeSlice5:	Line 12, 9, 6 missing	12 Feb 2010 - 27 Oct 2010
TimeSlice6:	All lines running	3 Nov 2010 - 31 Dec 2011
TimeSlice7:	All lines running	1 Jan 2012 - 31 Dec 2012
TimeSlice8:	All lines running	1 Jan 2013 - 31 Dec 2013

Table 6.1: *Defintion of TimeSlices. The start and end of the time periods are inclusive.*

There is a gap between the end of TimeSlice3 and the start of TimeSlice4 of about 3 weeks. Within this time range the communication with line 10 was malfunctioning and the whole time range was skipped for that analysis. For the other time periods mostly only one day is lost (for example between TimeSlice1 and TimeSlice2). That is the day where the corresponding lines were lost or reconnected. Within the last three TimeSlices all lines were available. This period is divided for reasons concerning the processing and the fact that Monte Carlo data is not available for later time intervals.

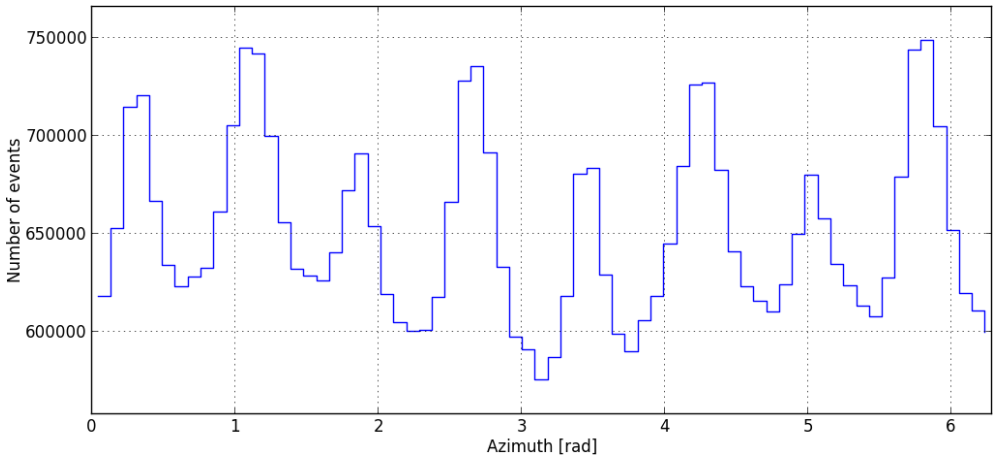

Figure 6.4: *Distribution of the azimuth for reconstructed events of TimeSlice1.*

The geometric shape of the detector does have an influence on the angular acceptance. The angular acceptance for azimuth direction for the full 12 line detector is

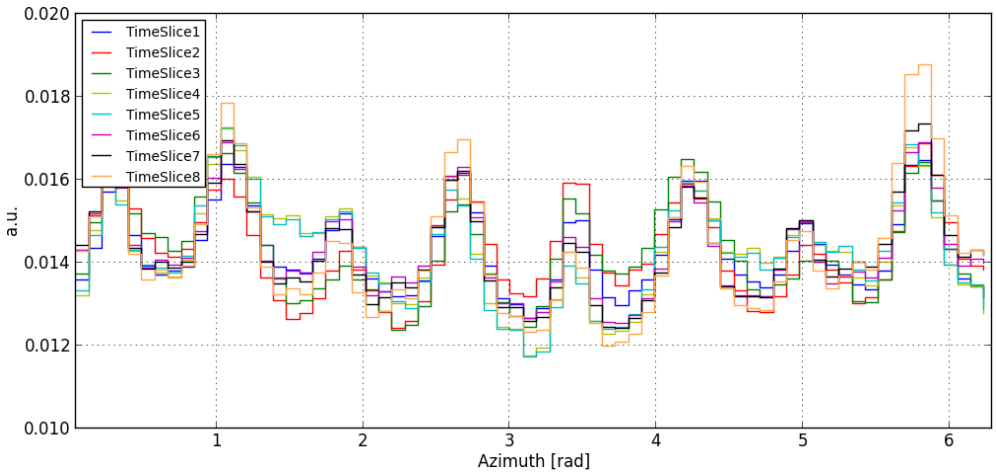

Figure 6.5: Distribution of the azimuth of the reconstructed events for all TimeSlices.

shown in figure 6.4. It was created with data from TimeSlice1. The bins in the histogram count the events with the corresponding value in azimuth while the zenith is ignored as long as its value does not exceed 60° as requested in chapter 4. The formation seen in that histogram comes directly from the geometric shape shown in figure 5.4 which has an influence on the used reconstruction algorithm.

The characteristics of the spikes are different for the other TimeSlices because the geometric properties change if one or more lines are missing. For comparison the histograms for the other TimeSlices are shown in figure 6.5. It should be remembered, that the lifetime for the periods differs and therefore the total number of events. The histograms shown are normed for that reason. It can be seen that the absence of some lines has an influence on the shape of the histograms. The variation of the number of events depending on the azimuth of the events is about 10% and is larger than the expected signal of the large scale anisotropy and seasonal variation of the muon rate. To prevent side effects when a skyplot in equatorial coordinates is created, each event gets a weight depending on its azimuth value to flatten the distribution. The average number of events is calculated based on the histograms shown in figure 6.5 for each TimeSlice. Then the events get a weight as a function of the azimuth calculated by the distributions shown with respect to the average number of events and the azimuth of the event.

The angular acceptance in zenith direction has two main effect: the path length for a muon from sea level to the detector and the detector layout. Muons with lower energy (but still higher than the threshold energy) coming from above can reach the detector, while muons with the same energy may fall below the energy threshold for greater angles in zenith because of their longer path through the surrounding water. The higher the zenith the less muons will be detected.

The second aspect is the angular acceptance of the detector. The optical modules

are equipped with 45° with respect to the line, looking downward. Muons coming from above the detector are hardly visible. The higher the zenith angle, the higher the probability for detecting a muon. A distribution of the angular acceptance for the zenith angle for TimeSlice6 is shown in figure 6.6. It has its maximum at a zenith value of about 0.5 rad. Events with a zenith of 60° or more were rejected. The last bin seems to be very low in comparison to the values of the former bins. This is because the cut off lies within that bin.

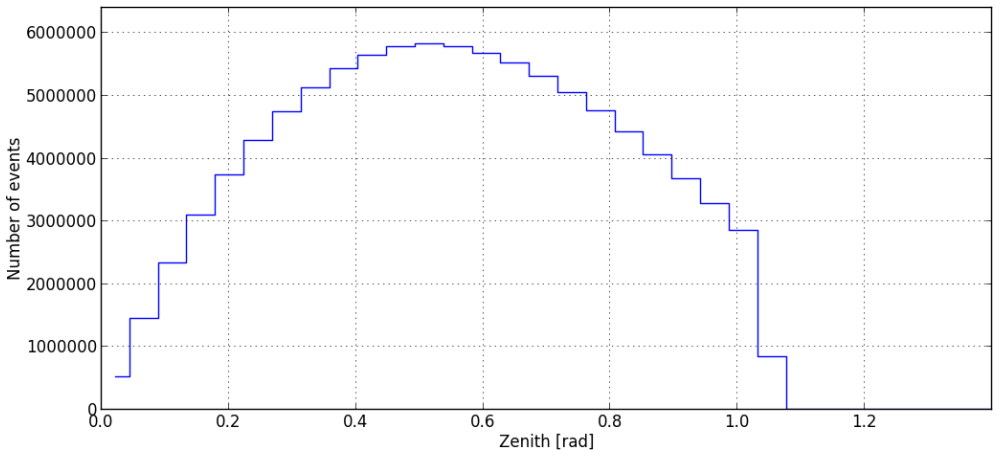

Figure 6.6: *Distribution of the zenith for reconstructed events.*

This work only uses reconstructed events. Another method could use the trigger signal and could count how often a trigger has fired in a specific period of time (for example the duration of a run or a day). With this method, no information on the direction of an event is given. Furthermore, not every triggered event can be reconstructed to a track or will survive other cuts like the quality cut on λ (for the AAFit reconstruction method) or χ (for the BBFit reconstruction method). For the plots in figures 6.5 and 6.6, only events that could be reconstructed with AAFit and with a value of $\lambda > -6.6$ are used. The threshold value for that quality parameter will be explained in section 8. It is mentioned here for completeness. Furthermore, a selection on the runs was applied which is described in section 6.3.

6.3 Run setup selection

The data of ANTARES is organized in runs with increasing ID over time. Some runs were made to define the calibration for timing and the optical properties and can not be used for physical analysis.

Physics runs can differ from another by their size (= number of events), time, the used triggers and other circumstances like the optical background. The shifters are responsible for the used triggers and have access to a set of rules on how and when

to change the run setups. That and the fact that these rules have changed over time lead to the situation where many different cases are imaginable concerning the different properties of the runs.

The search for the large scale and seasonal anisotropy depends on the available statistics. This means the number of events where the more events are used the higher the possibility for seeing a signal. Table 6.2 shows how many triggers were fired during the time periods of the different TimeSlices. The triggers used by this work are listed separately.

Name of period of time	Total days	Lifetime of runs (days)	Counted triggers	Number of runs
TimeSlice1:	286	3DScan: 149 T3: 149	3DScan: 47,137,902 T3: 121,768,454	3DScan: 1937 T3: 1937
TimeSlice2:	110	3DScan: 48 T3: 29	3DScan: 23,150,742 T3: 36,912,107	3DScan: 382 T3: 243
TimeSlice3:	115	3DScan: 95 T3: 87	3DScan: 26,615,605 T3: 63,785,728	3DScan: 577 T3: 521
TimeSlice4:	88	3DScan: 69 T3: 69	3DScan: 19,090,700 T3: 44,871,141	3DScan: 575 T3: 575
TimeSlice5:	257	3DScan: 200 T3: 198	3DScan: 48,019,432 T3: 131,131,183	3DScan: 1824 T3: 1790
TimeSlice6:	423	3DScan: 357 T3: 348	3DScan: 127,427,104 T3: 291,017,745	3DScan: 4131 T3: 4003
TimeSlice7:	366	3DScan: 280 T3: 246	3DScan: 103,480,636 T3: 230,468,093	3DScan: 2935 T3: 2496
TimeSlice8:	365	3DScan: 214 T3: 188	3DScan: 108,354,298 T3: 143,951,693	3DScan: 981 T3: 962

Table 6.2: *The total days are the time periods in days that each TimeSlice covers. The lifetime is given in days and accumulates the actual time where data was taken with these triggers. Counted triggers give the number on how often one trigger has fired during that time period.*

The data for table 6.2 consists of all runs available which are marked as physics runs. Parameters like the quality basic (QB), baseline, burstfraction or the number of active OMs were not taken into account. The difference of the total days of the time periods and the sum of the lifetime of the selected runs is sometimes more than 50%. This is because the detector has to be turned off during some periods due to the high optical background. Other aspects are calibration runs or maintenance. The lifetime of the selected runs will decrease even more if other cuts e.g. for the baseline are made. The numbers in the column for the counted triggers are not reflecting the reconstructed events but only the triggered ones. These numbers will decrease too if the reconstruction is made and quality cuts are applied. The counters for the trigger 3DScan are lower than for the trigger T3, even if the trigger T3 has lower lifetimes. The trigger 3T has higher rates on average and the shifters can turn it off if its rate exceeds a defined limit. In figure 6.7 a histogram of the values of the baseline for each

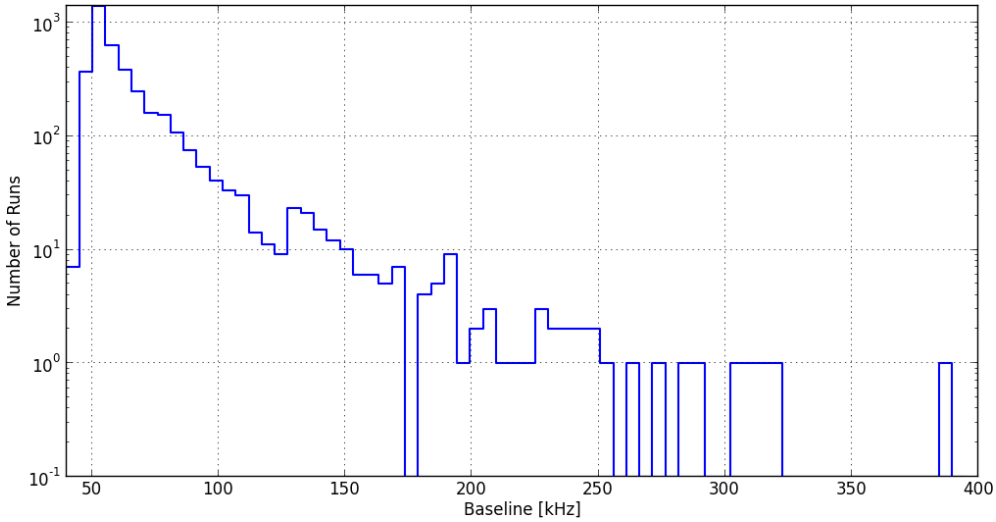

Figure 6.7: *Histogram of the values of baseline for TimeSlice6.*

run in TimeSlice6 is shown. The number of runs decreases for an increasing baseline with a maximum at about 60kHz. The higher the baseline gets, the less triggers are active. It is possible that the detector took data with a specific trigger setup which should have changed based on the baseline and other parameters. This can happen during the night after the shift crew has done their last check and the conditions have changed rapidly afterwards. Runs with higher baseline rates do have more background

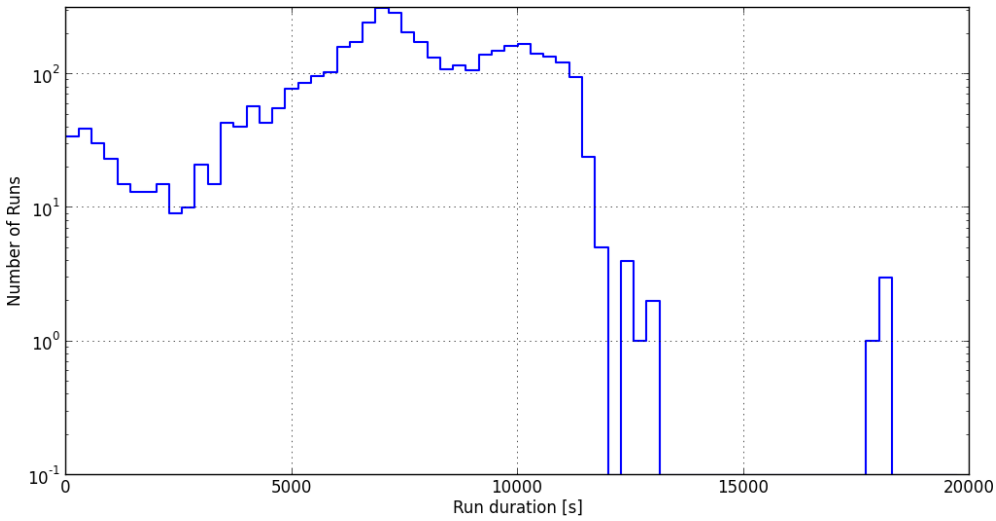

Figure 6.8: *Histogram of the duration for the runs of TimeSlice6.*

hits which can decrease the quality of the track reconstruction. It will be shown that the baseline has an influence on the number of reconstructed events. This dependency must be taken into account but a cut on the baseline can not be defined with the information shown so far without further investigation and inclusion of other factors

like the quality parameters of the reconstruction methods. This point will be discussed in chapter 8.2.

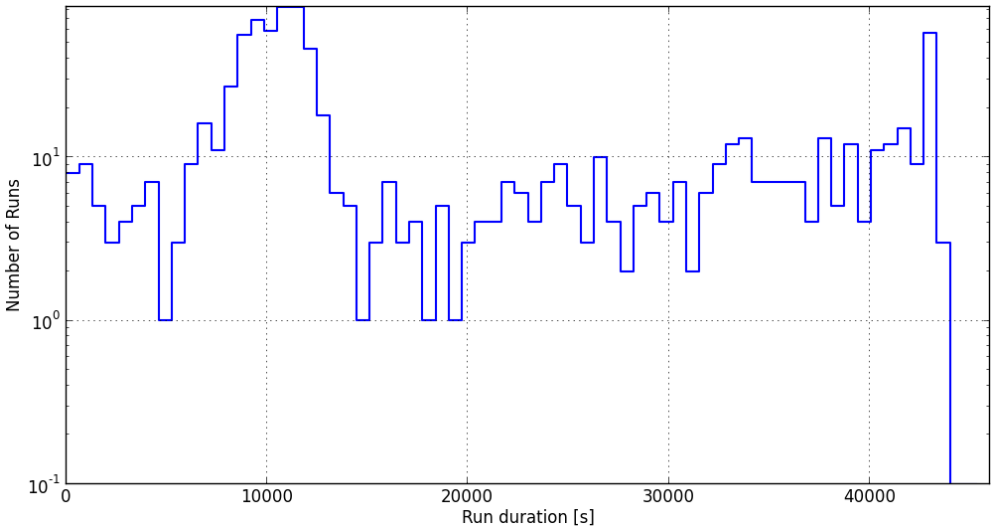

Figure 6.9: *Histogram of the duration for the runs of TimeSlice8.*

The distribution of the duration of the runs of TimeSlice6 can be seen in figure 6.8. The duration is given in seconds. As already mentioned the runs can be stopped and started manually by the shifters. If they don't do anything the run control will start a new run after a specific time is reached or the file size exceeds a defined limit. Both changed during the five year period of data taking used in this work. In the year 2013 the maximum file size and duration were increased drastically which can be seen in figure 6.9. The longer a run takes data, the more time is covered with the same detector configuration. A length of zero is never reached for the runs shown. However,

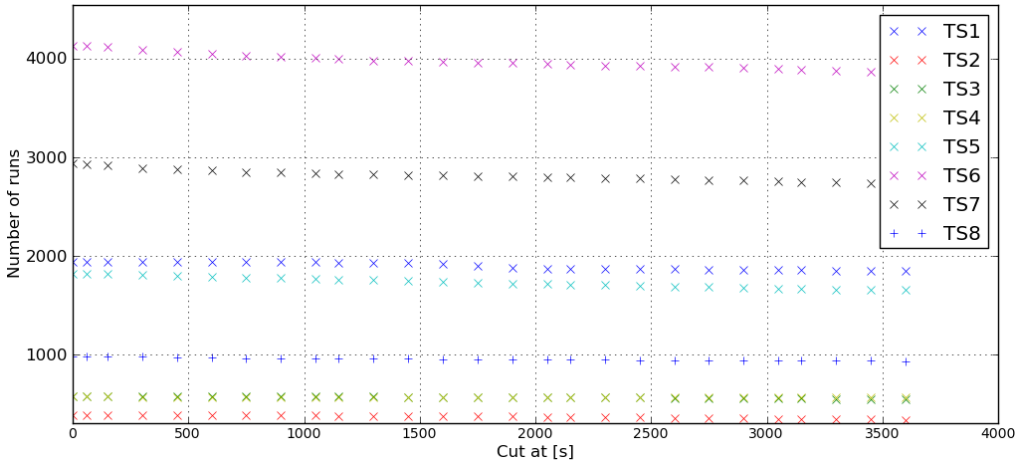

Figure 6.10: *Number of runs over the cut on the run duration for all TimeSlices.*

runs with a minimum time of about 1 minute do exist. These runs were most probably stopped by the shifters to change the run setup because the conditions have changed.

Runs can be shorter than the desired run duration or size if the conditions have changed but the run setup was not. In that case it is possible that more or less data (caused by the frequencies of the triggers) is written and the run was stopped because of the size limit or the time limit.

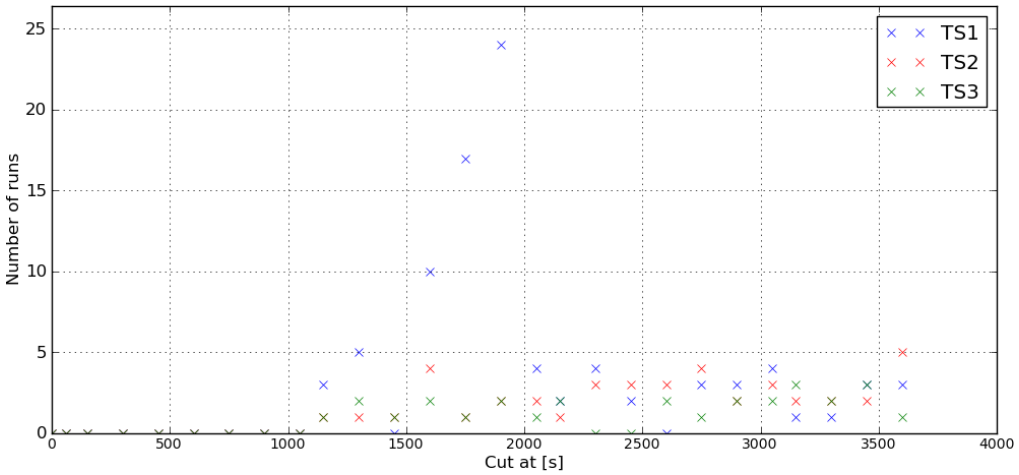

Figure 6.11: *Difference of the number of surviving runs compared to the previous cut (see text).*

A cut on a minimum run duration is reasonable to get runs with stable conditions. However, every run that gets rejected reduces the statistics. In figure 6.10 the number of runs which would stay available after the cut on the duration in seconds is shown for all TimeSlices. Here runs with a duration less than the definition of the cut are rejected. The cut start at zero seconds and goes until about an hour. The number of the surviving runs decreases with higher cuts. In figure 6.11 the difference $\Delta N_i = N_{i-1} - N_i$ is shown for the first three TimeSlices, where N is the number of surviving runs with cut i and every cross illustrates a cut i. For the shown three time periods, no runs with a duration of less than about 1000 seconds exist. This is not the case for the other TimeSlices. For TimeSlice1, the difference has its maximum at a cut of about 1900s. Detailed plots are shown in appendix B. A cut of 900 seconds was chosen in this work to get rid of the runs that were stopped manually and to not lose more statistics than necessary.

A cut on the parameter QB (= quality basic, see section 5.5) is reasonable and will be set to 1 for the upcoming chapters (used runs have a QB of one or higher). The cut on $QB \geq 1$ only excludes runs which are not physics runs and if there were some problems with the electronics. Applying the cut on the duration and the parameter QB, the table 6.2 becomes:

Name of period of time	Total days	Lifetime of runs (days)	Counted triggers	Number of runs
TimeSlice1:	286	3DScan: 149 T3: 149	3DScan: 47,137,902 T3: 121,768,454	3DScan: 1937 T3: 1937
TimeSlice2:	110	3DScan: 48 T3: 29	3DScan: 23,150,742 T3: 36,912,107	3DScan: 382 T3: 243
TimeSlice3:	115	3DScan: 95 T3: 87	3DScan: 26,615,605 T3: 63,785,728	3DScan: 577 T3: 521
TimeSlice4:	88	3DScan: 69 T3: 69	**3DScan: 19,088,290** **T3: 44,865,592**	**3DScan: 572** **T3: 572**
TimeSlice5:	257	3DScan: 200 **T3: 197**	**3DScan: 47,857,635** **T3: 130,674,727**	**3DScan: 1776** **T3: 1745**
TimeSlice6:	423	**3DScan: 351** **T3: 342**	**3DScan: 123,482,840** **T3: 282,882,565**	**3DScan: 3945** **T3: 3827**
TimeSlice7:	366	**3DScan: 270** **T3: 238**	**3DScan: 101,470,006** **T3: 226,433,759**	**3DScan: 2745** **T3: 2385**
TimeSlice8:	365	**3DScan: 208** **T3: 186**	**3DScan: 86,002,746** **T3: 141,673,400**	**3DScan: 919** **T3: 838**

Table 6.3: *The total days are the time periods in days that each TimeSlice covers. The lifetime is given in days and accumulates the actual time where data was taken with these triggers. Counted triggers gives the number on how often one trigger has fired in that time period. The used runs are selected by their duration and on QB (see text). Values shown bold have changed compared to table 6.2.*

Chapter 7

Detector efficiency over time

The efficiency of the detector is decreasing over time which can be seen by the decrease of the muon rate. This effect might be due to sedimentation of bacteria and other lifeforms onto the spheres of glass holding the PMTs. The detector is calibrated several times a year to compensate this effects but it can not completely be avoided. The decreasing efficiency of the detector has to be compensated to avoid side effects for the analysis.

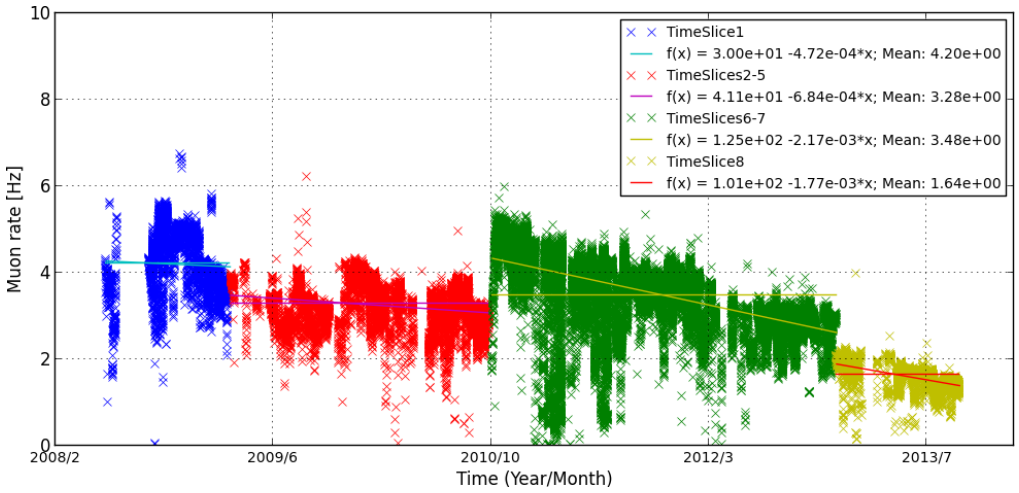

Figure 7.1: *Muon rate over time and the fitted functions and mean values to the data.*

In figure 7.1 the muon rate for reconstruced muons with AAFit, λ-cut -6.6 and events with zenith $< 60°$ is shown over the time from may 2008 until december 2013. Each cross represents the muon rate for one run. The different colors separate the intervals used to calculate the weights withdrawing the decreasing efficiency of the detector over the time. The data points shown in blue are for the TimeSlice 1 where the whole detector was available. The red data points are for the TimeSlices 2 - 5. During that period some lines were removed and again connected. The green points show the muon rate for the TimeSlices 6 - 7 where the whole detector was available again. The yellow crosses show the data of the year 2013 (TimeSlice8). It can be seen that the average

muon rate for the time period of the year 2013 has dropped. The reason for that can be a recalibration in combination with the used trigger.

The effect of decreasing efficiency can be seen very clearly for the green data points. The spreading of the muon rate is quite large even for smaller time scales. That is because of the different baselines and used run setups. The gaps are coming from the definition of the TimeSlices, the down time of the detector and the run selection. For example, the steps within the blue data points are introduced by different run setups and circumstances during data taking like the baseline. Different run setups with different calibrations result in different muon rates which have to be taken into account for further investigation on the muon rate.

To compensate the decreasing efficiency of the detector it is mandatory to choose large periods to avoid effects introduced by the different run setups and baseline. Because of that the whole data from may 2008 until December 2013 is only divided into four sections as shown. The decreasing efficiency of the OMs within the time period of TimeSlice1 (blue crosses) is meant to be very low. At this time the detector was quite new. The steps within the data points for the first time period do not come from the decreasing efficiency but from other aspects like the run setup and baseline. The red dots combine the TimeSlices 2 - 5 for reasons just described.

The fit function and the mean value for the muon rate in the time periods are shown in the legend of figure 7.1. The parameter x of the fit functions $f(x)$ is the time in the format of the Modified Julian Date (MJD). The weight calculated with the help of the fit functions consist of two components. $W_{T,i} = W^1_{T,i} \cdot W^2_T$, with T standing for the time period, i identifies the run and

$$W^1_{T,i} = \frac{f^T(x(i))}{< R >_T} \tag{7.1}$$

$$W^2_T = \frac{< R >}{< R >_T} \tag{7.2}$$

where $f^T(x(i))$ is the fitted function for the time period T, $x(i)$ the start time of the run i in MJD, $< R >_T$ the mean value of the muon rate as shown in figure 7.1 for TimeSlice T and $< R >= \sum_{T=1}^{4} < R >_T$ the total mean over the whole time calculated by the mean rates of each time period T.

Applying the weights to the data shown, the decreasing efficiency is compensated as shown in figure 7.2. The colors were kept and are the same as in figure 7.1. The solid line shows the relative value of the weights applied.

It can be seen that the rate now is much more constant over the time while the variations on small scales were kept. The upcoming discussion will make use of that

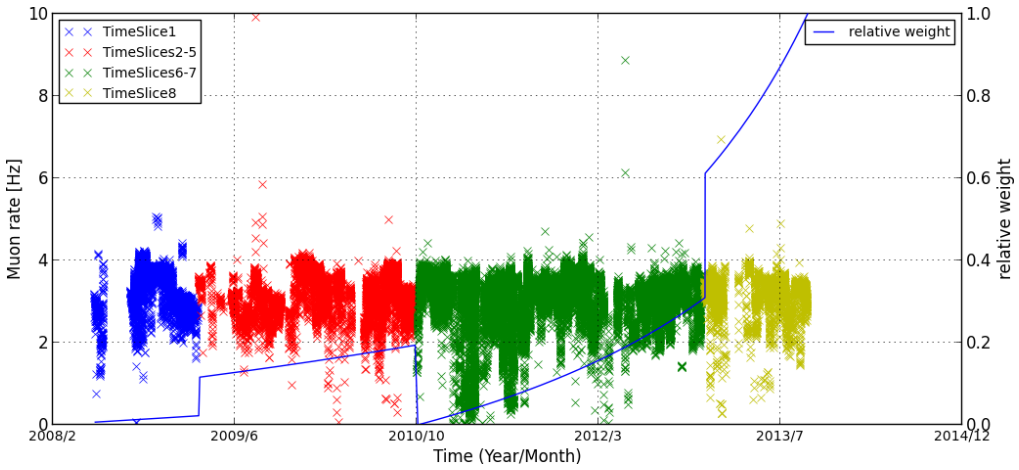

Figure 7.2: *Weighted muon rate (crosses) over time and the corresponding weight (solid line).*

weights to compensate the decreasing efficiency of the detector over the time. The events used to find the weights were triggered by T3 only and were reconstructed with AAFit in this example. In appendix H and I it can be seen that the used trigger does have an influence on the muon rate and to weights calculated this way. This is because of the different amount of hits (including the coincidences) used by the different triggers. In the following chapters two different trigger will be used and the weights for the decreasing efficiency of the detector introduced in this chapter, will be recalculated.

Chapter 8

Dependencies of the muon rate of ANTARES

In this chapter, the dependency of the muon rate on the baseline, the number of active OMs and the quality parameter of the reconstruction algorithm is studied. The steps made to define the cuts are described in detail using the reconstruction method AAFit. In the later chapters, the reconstruction method BBFit will also be used to determine the muon rate. The steps described here are then repeated and the results will be shown in the chapters and the appendix mentioned in the corresponding section.

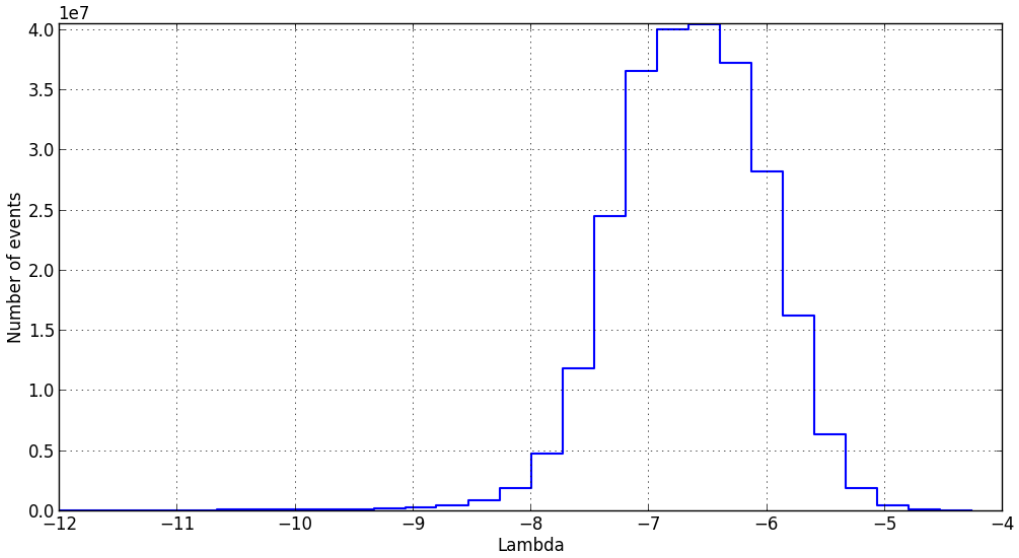

Figure 8.1: *Histogram of the number of events that were reconstructed with the value of lambda shown.*

The reconstruction method AAFit gives a quality parameter called λ for each reconstructed event. A lower cut on that parameter (the value of lambda is less than zero) will give more events which is the aim for the measurement of the large scale anisotropy, see figure 8.1. Here the number of events from data with a specific λ-cut is shown. From right to left, the quality of the events is decreasing (identified with lambda). Very few events do have values of -5 or higher. The maximum is at about -6.9 and the number of events with a lesser value of λ decreases again. Lambda can

also have a value of NaN (not a number), what is not shown in the graph. The average error on the reconstruced events is increasing for lower values of λ.

The baseline and the number of active OMs also do have an influence on the quality and number of the reconstructed events with AAFit. In this chapter the lambda cut used in this work is defined. Side effects on the quality and number of events with respect to the baseline and the number of active OMs are shown. The error on the reconstructed events is determined by the use of Monte Carlo files.

8.1 Monte Carlo – Data comparison

For ANTARES Monte Carlo Data is available for down going muons (zenith $< 90°$). The flux of simulated events in the Monte Carlo is 1/3 of the expected flux. All events do therefore have the same weight. Muons simulated with Monte Carlo do make simulated hits on the OMs of the detector. Triggers are applied and have to fire in order to find that event. After that the reconstruction algorithms do have the same information as for data events coming from the detector and try to reconstruct the track of the detected muon. In the case of a perfect simulation chain where all systematic effects are considered there should be no difference between Monte Carlo events and data events. Actually this is not the case for the Monte Carlo used in this work. Table 8.1 shows the number of reconstructed events from data, the ratio of the reconstructed events from data and Monte Carlo and the λ-cut used for TimeSlice6. The ratio between data events and Monte Carlo events increases for lower cuts on λ. That means that more events can be found in data than in the Monte Carlo. It can be seen that the number of events do increase with looser cuts on λ. The difference from one cut to the other has its maximum for $-7.1 < \lambda < 6.1$ which is what it is expected when looking at figure 8.1.

Lambda cut	Data / MC	Number of events in million
-9.1	1.261	141
-8.1	1.260	140
-7.1	1.227	130
-6.6	1.159	90
-6.1	1.145	50
-5.9	1.153	20
-5.5	1.140	4.5

Table 8.1: *Reconstructed events for TimeSlice6 for specific cut on lambda. The column Data/MC gives the ratio of the reconstructed events for data and Monte Carlo for the same TimeSlice.*

In order to get the maximum statistics a higher cut on λ seems reasonable. The difference in the reconstructed events for Monte Carlo and data increases and is about 11% compared to the minimum and maximum cut on λ. The number of reconstructed

(a): λ-cut: -5.5

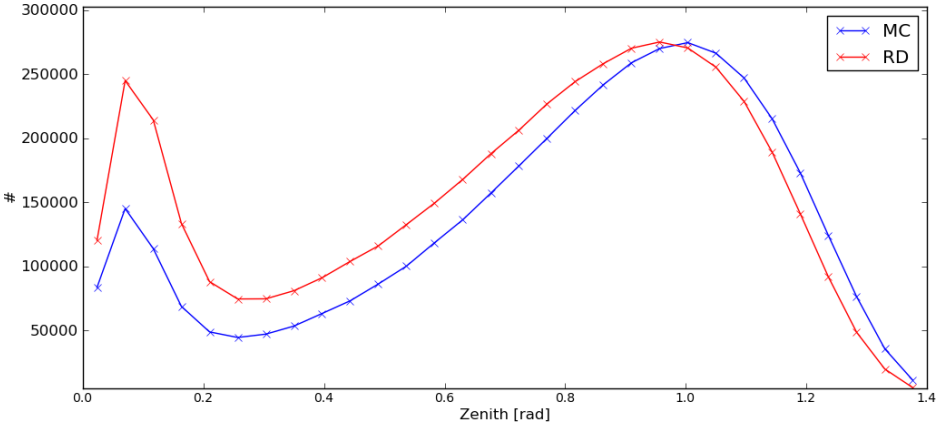

(b): λ-cut: -6.6

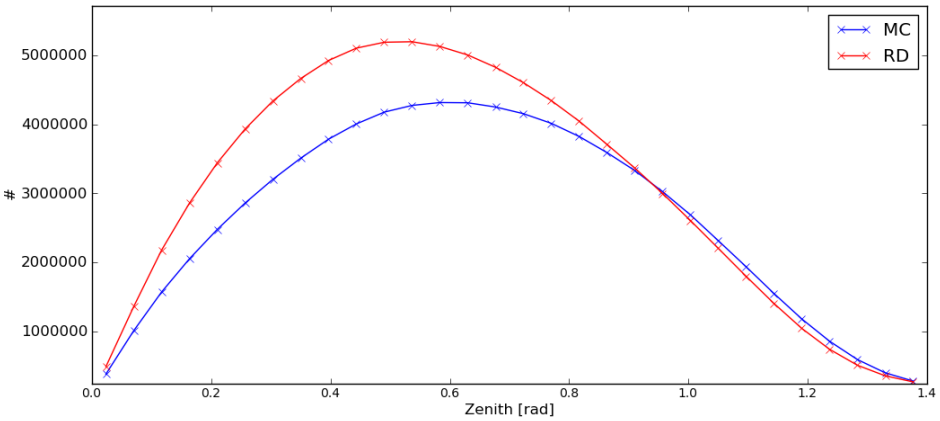

(c): λ-cut: -7.1

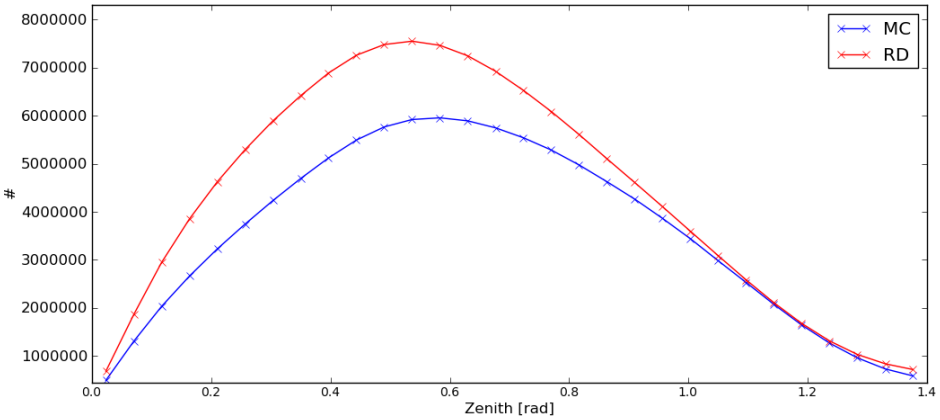

Figure 8.2: Distribution of zenith angle of reconstructed events for three different cuts on lambda using Monte Carlo (blue) and data (red).

events increases by a factor of about 30 at the same scheme.

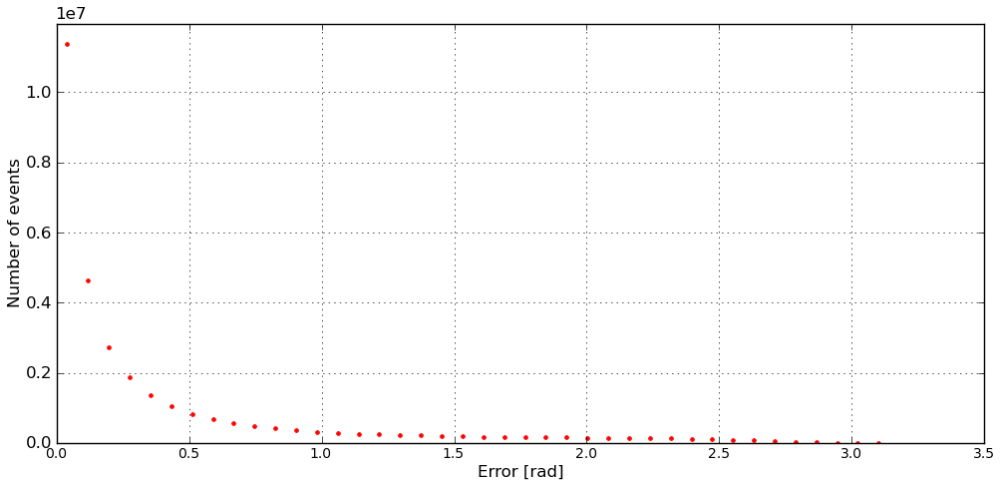

Figure 8.3: Number of events with an angular distance to Monte Carlo truth in radians for TimeSlice6.

Looking at the distribution of the zenith angle of the reconstructed events showed in figures 8.2 it can be seen that a cut on λ changes this distribution. Here an example of three cuts on lambda is given. Events with a value for lambda higher than the value showed under the plots have survived the cut. From plot (a) to (c) the number of events increases and with them the shape of the plot. Events of (a) are included in (b) and (c) (and (b) is included in (c)). The spike for zenith values of about 0.1 rad in (a) and the following minimum is a characteristic of the reconstruction method with that cut. With lower cuts the shape of the plots becomes what is expected by the layout of the detector and the surrounding water.

8.1.1 Error on reconstructed tracks

The recontruction method AAFit uses the likelihood method to get the best fit for the track for the given hits. The reconstructed tracks can therefore differ in the direction in comparison to the Monte Carlo truth. To investigate the influence of the λ-cut on the error of the reconstruction the runs of TimeSlice 6 were used. The cut on zenith was set to 60° as described above. The error is the angular distance between the Monte Carlo track and the reconstructed track and is shown in figure 8.3 for a λ-cut of -6.6. The plot ends on the value of π, which is the maximum error for the reconstructed tracks. The number of events within the last bin (3.06 - π) actually is zero.

To the data in figure 8.3 a Gauss function can be fitted. The sigma of that fit gives a value for the quality of the reconstruction. For some cuts on lambda the sigma was calculated and is shown in table 8.2. With reference to table 8.1 some higher cuts on lambda were omitted. The number of events for that cuts were too low to be usable. It can be seen that the quality of the reconstruction depends on the λ-cut. A lower cut on Lambda leads to more events with a higher angular distance between the reconstructed

Lambda cut	Data / MC	Number of events in million	Sigma in °
-9.1	1.261	141	9.2
-8.1	1.260	140	9.1
-7.1	1.227	130	8.8
-6.6	1.159	90	7.1
-6.1	1.145	50	6.2

Table 8.2: *The error of the track reconstruction for different λ-cuts.*

track and the Monte Carla information.

It was mentioned that a cut on the zenith for the events was set to 60°. An error on the reconstructed track of an event can lead to the situation where the zenith of the true track would be within that cone but the reconstructed track is not and vice versa. The table 8.3 gives the percentage of

- False in cone: Number of events where the reconstructed events lie within the cone (zenith $< 60°$) but the MC truth does not, divided by the total number of events within the cone (reconstructed).
- False out of cone: Number of events where the reconstructed events do not lie within the cone but the MC truth does, devided by the total number of events within the cone (reconstructed).
- In cone MC/Fit: Number of event that lie within the cone for MC truth divided by the number of events that lie within the cone for reconstructed events.

Period of time	False in cone	False out of cone	In cone MC/Fit
TimeSlice1	0.95%	6.96%	106.01%
TimeSlice2	1.05%	7.52%	106.47%
TimeSlice3	0.99%	7.71%	106.72%
TimeSlice4	0.90%	7.09%	106.19%
TimeSlice5	1.01%	7.50%	106.49%
TimeSlice6	0.98%	6.83%	105.85%

Table 8.3: *Comparison of data and MC events reconstructed with a zenith less than* 60° *(cone).*

It can be seen that the percentage of events that would be reconstructed with a zenith angle $< 60°$ where the truth of the angle is larger for all TimeSlices is about 1%. On the other hand, the percentage of the events that get lost because of the reconstruction (False out of cone) is about 7% which is reflected in the last column. For all TimeSlices the number of reconstructed events within the cone was underestimated for about 6%. This means that the cut on zenith and the error on the reconstruction (sigma = 7.1°) is not expected to have a high influence on the muon rate. In addition more events are getting lost than gained because of the error of the reconstruction.

The size of the signal of the large scale anisotropy in right ascension is large in comparison to the values of the sigma for all cuts shown (see figure 3.1 and chapter 6). In order to get high statistics the parameters shown so far would lead to a relatively low cut on lambda. The shape of distribution of the zenith angle would suggest to use a low cut on lambda too. The following section will use parameters of the runs to qualify the lambda cut.

8.2 Dependency on baseline and number of active OMs

It was shown that the lambda cut has an influence on the number of events usable for the search for the large scale and seasonal anisotropy. The runs hold data collected under different circumstances like optical background which is reflected in the baseline. The number of active OMs counts the OMs which are in state OK[1]. The optical modules can be in one of different conditions caused by different events. A lost line will decrease the amount of active OMs. This is why the TimeSlices were introduced. Beside this it is possible that some optical modules were disabled manually because of misbehavior or if the frequency with which the optical module sent data was too high. In all these cases the OM loses its OK status. The latter is in some way connected to the baseline. That is why this two aspects (baseline and number of active optical modules) are tested together for their influence on the data quality and stability in this section.

In the last sections the number of events were used. This was possible because of the fact that the covered time always was a whole TimeSlice and the data used does not depend on the actual size of the run. For the test on how the lambda cut and the number of events are affected by the baseline and the active OM single runs have to be observed. The runs have different durations and the number of events in one run depend on that. For that reason the rate of the muons in Hz is calculated for each run by counting the events surviving the cut set for the parameter λ divided by the time of the run.

The runs have a start and end time written to the database of ANTARES. These times are defined by the data acquisition system (DAQ) at the very moment the run has started or ended (automatically or manually by the shifters). The difference of these times would give the duration of the run. In a matter of fact data is not taken right away from the beginning of the run and the duration calculated this way can lead to an error. Runs with a quality basic (QB) of 1 or higher already have passed some tests concerning the accuracy of the time properties of the run. The difference of the total time (described above) and the effective time still can be up to 450s [36]. For this

[1]Optical modules are in state OK if the hit rate is below 200 kHz. This rate mainly consists of optical background. The hits mostly do not have a coincidence with other OMs and do not invoke a trigger.

(a): λ-cut: -6.1

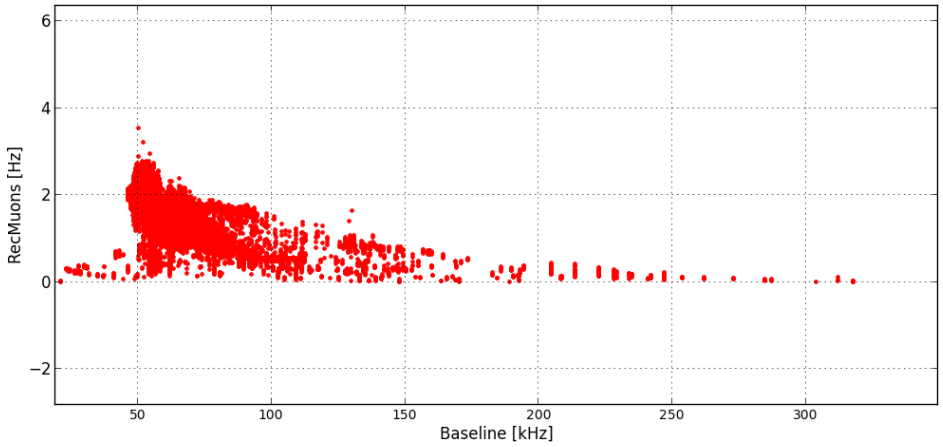

(b): λ-cut: -6.6

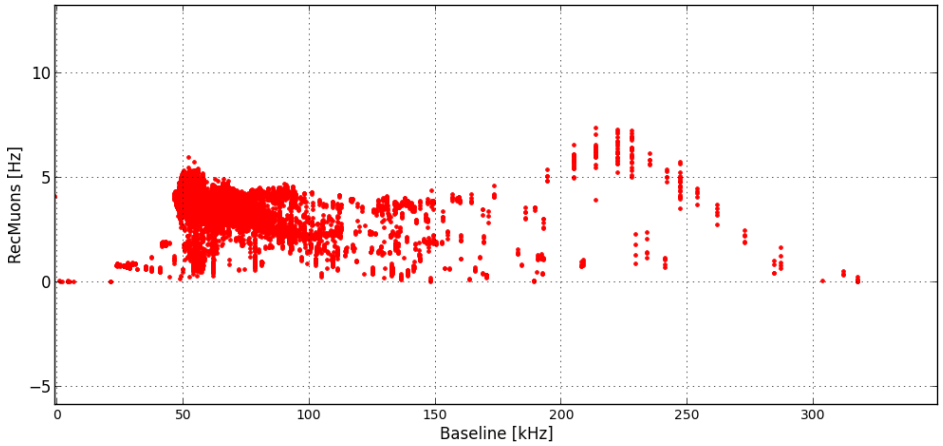

(c): λ-cut: -7.1

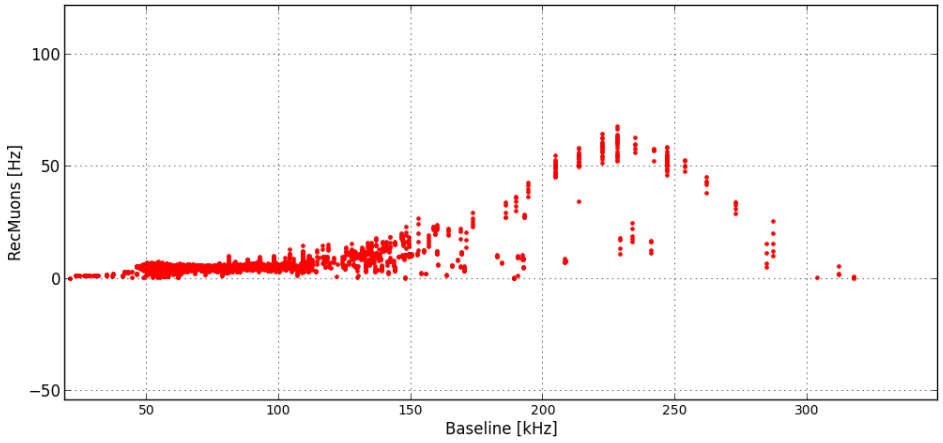

Figure 8.4: Muon rate over the baseline for different cuts on λ for TimeSlice5.

analysis the effective time is used as the duration of the run. The data is sent to the shore organized into frames. These frames have a defined duration and the effective time is calculated by multiplying the number of the frames of one run with the time of one single frame.

The figures in 8.4 and 8.5 show the dependency of the rate of the muons from the baseline for different cuts on λ. The zenith angle of all events is less than 60°. They were triggered by T3 and reconstructed by AAFit. Every dot in the graphs is the rate of the reconstructed muons for one run in the time period. The higher the λ-cut the higher the muon rate becomes due to the increasing number of reconstructed muons. At the same time the spread of the muon rate of the data points increases too. The number of runs with higher baselines ($>$ 200 kHz) decreases.

Find the plots for the other TimeSlices in appendix C. Based on the plots in 8.4 and 8.5 the spreading of the muon rate is too wide to make any corrections depending on the baseline. For that the muon rates are sorted by the used run setup described below.

For the purpose of this analysis the number of reconstructed muons should be as high as possible. In chapter 8.1 it was shown that lower cuts on lambda would better fit for that. Here the opposite is the case. The compromise chosen here is to use the cut of -6.6 for lambda (with AAFit reconstruction method).

In figure 8.4(b) the muon rate reaches its maximum at about 220kHz for the baseline. The quality cut on lambda can prevent this but at the same time the muon rate decreases to nearly 0.2Hz. The lower λ-cut would decrease the total amount of reconstructed muons more than we would gain from using that range. Therefore, a cut on the baseline is used at 160kHz. In figure 8.4(b) this is the point where the spread of the muon rate is still constant in comparison to lower baseline rates.

The runs shown as data points in the figures above by their muon rate are taken with different run setups. Different triggers were turned on or off during data taking. In figure 8.6 only runs with the same run setup were taken into account (name of the run setup as used for describing the run: Line 1-12 Physics Trigger 3N+2T3+K40+TS0 June2011). Again different λ-cuts are shown. It can be seen that this run setup was not used for higher baselines. For the cut of -7.1 the muon rate is spreading again for baselines higher than 90kHz. Other run setups for TimeSlice6 can be seen in appendix D. Some of the run setups were used only for very low rates of the baseline ($\approx 50 - 60kHz$).

In most cases the muon rate decreases with increasing baseline. The baseline itself can change very quickly as described in chapter 5.3. Consecutive runs can have different run setups. To get a more constant muon rate over the time weights are applied runwise with respect to the baseline and the used run setup. For that a polynomial curve was

(a): λ-cut: -6.1

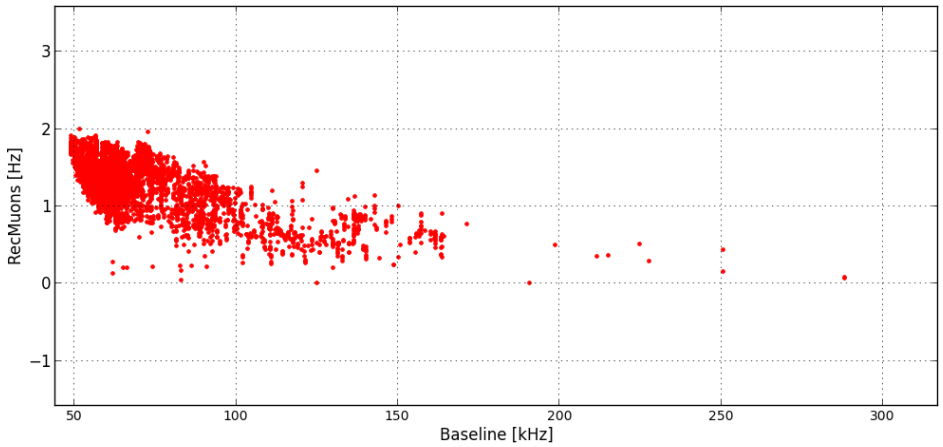

(b): λ-cut: -6.6

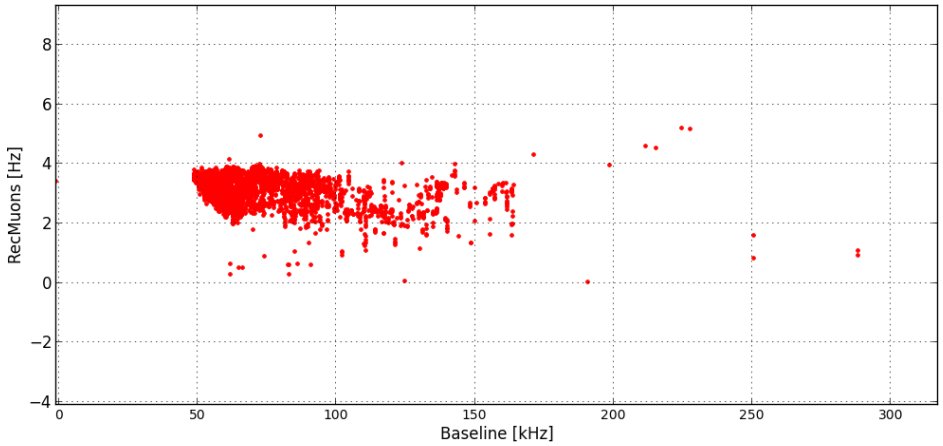

(c): λ-cut: -7.1

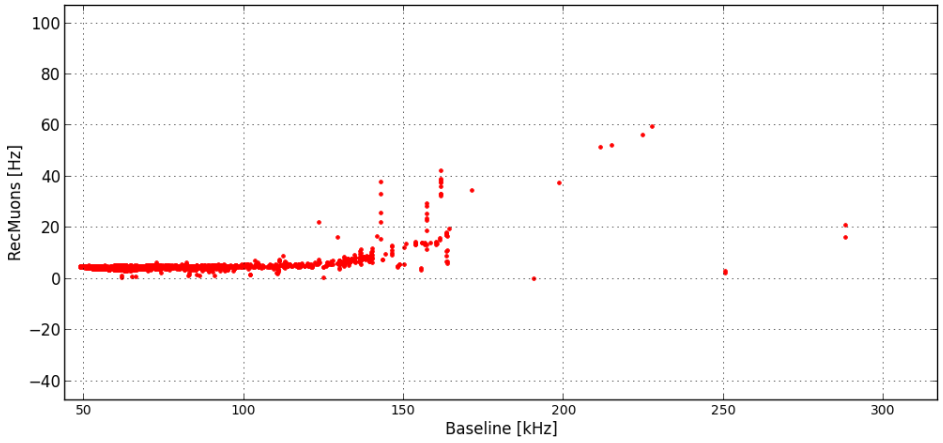

Figure 8.5: Muon rate over baseline for different cuts on λ for TimeSlice5.

(a): λ-cut: -6.1

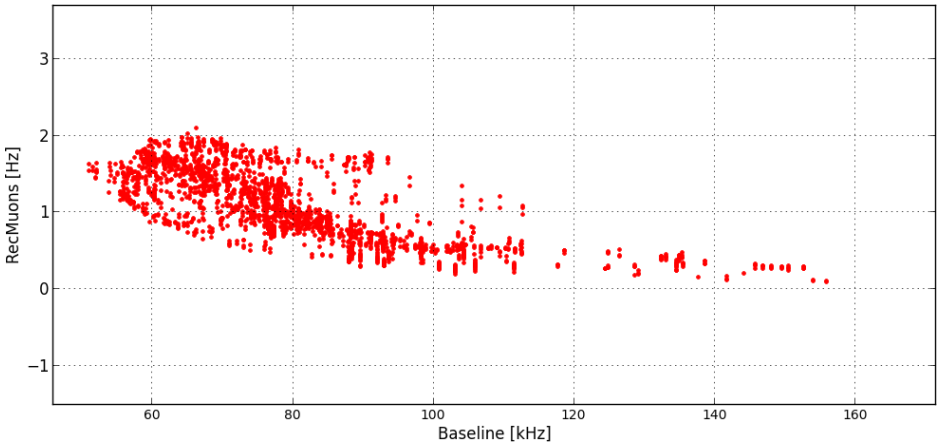

(b): λ-cut: -6.6

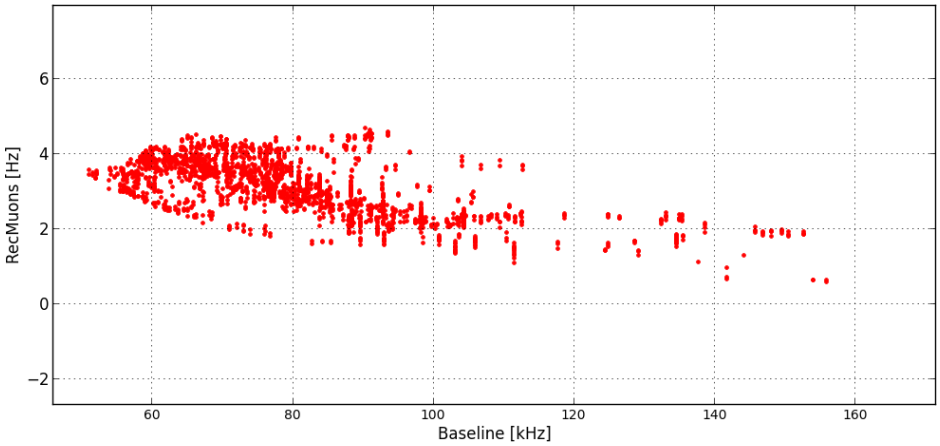

(c): λ-cut: -7.1

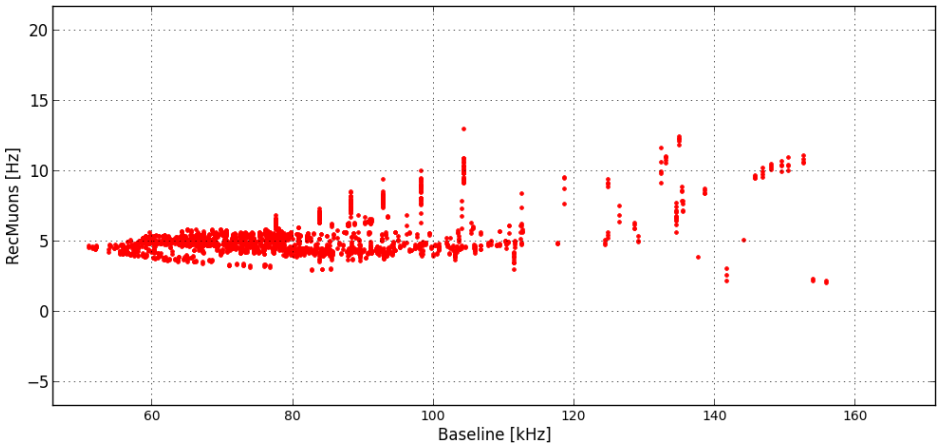

Figure 8.6: Muon rate over the baseline for different cuts on λ using runs of TimeSlice6 with the run setup name 'Line 1-12 Physics Trigger 3N+2T3+K40+TS0 June2011'.

fitted to the data points(= muon rate for a run). Data points which lay out of the boundaries for the baseline were not used. Some other points which make a fit difficult or impossible have also been removed. The plots in 8.4 have shown the combination for all run setups while the method just described uses only the runs taken with a specific run setup.

At the beginning of that chapter it was mentioned that the number of active OMs has an influence on the number of reconstructed events. In figure 8.7 the muon rate depending on the number of active OMs is shown. The less OMs are in state OK the lower the corresponding muon rate becomes. The state if the OMs is defined by the hit rate of the OMs. This hit rate is used to calculate the baseline and dependencies of the muon rate on the baseline and the number of active OM are not independent. It turned out that applying the weights for active OMs first and for the baseline second works best. Find the plots for each runsetup in TimeSlice6 with a λ-cut of -6.6 with different weights applied in appendix E.

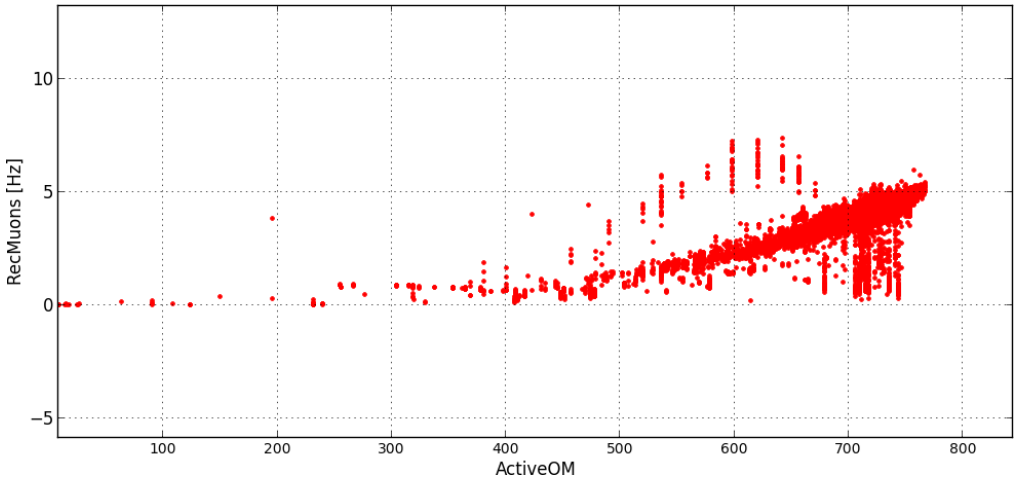

Figure 8.7: *Muon rate over the number of active OMs for all runs of TimeSlice6.*

To get the weights depending on the number of active OMs and the run setup the same steps as for the weights for the baseline were made. The bow in figure 8.7 at around 600 (active OMs) with muon rates above 5 Hz comes from the same data points as the bow in figure 8.4(b) and will be cut off by the cut on the baseline as described above.

Data points which are cut off by one of the procedures described above will not be taken into account for calculating the weights for the other. The process is incrementing that means that if in step two (e.g. search for the weights on baseline) some runs were excluded step one (in this example the search for the weights in the number of active OMs) has been repeated.

Figures 8.8 and 8.9 show how the different weights change the characteristics of the

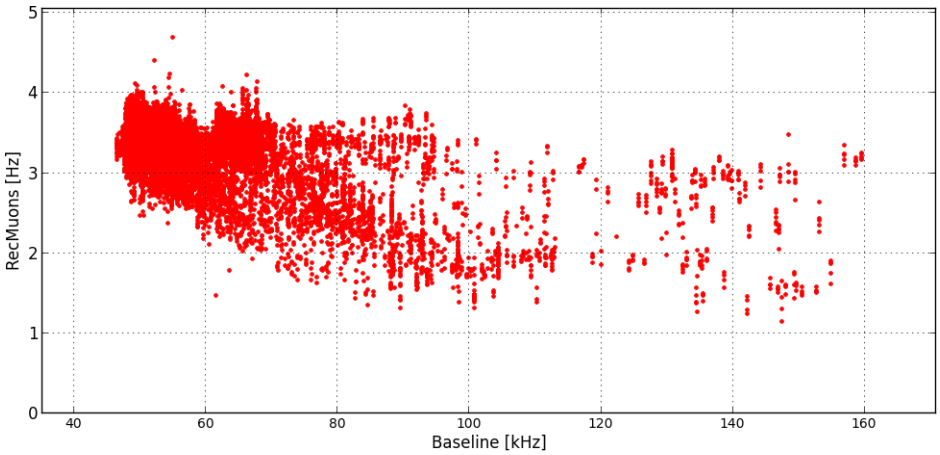

(a): Weights compensating the decreasing efficiency are applied.

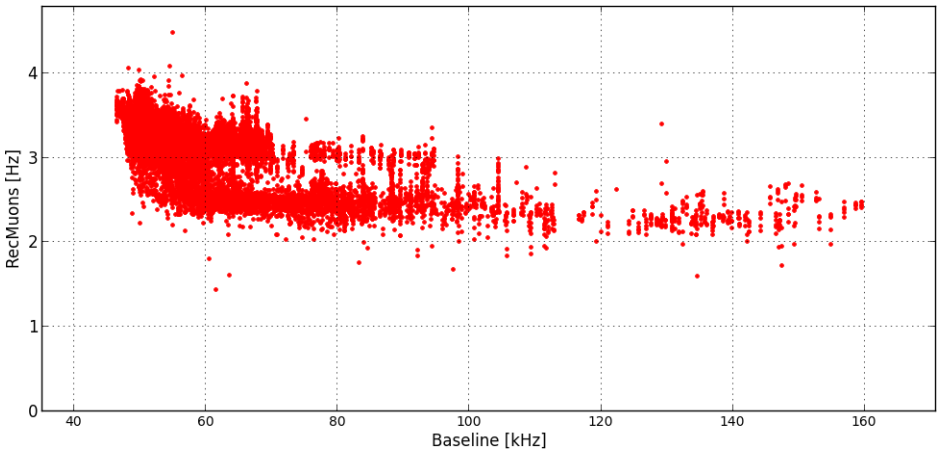

(b): Weights for active OMs applied.

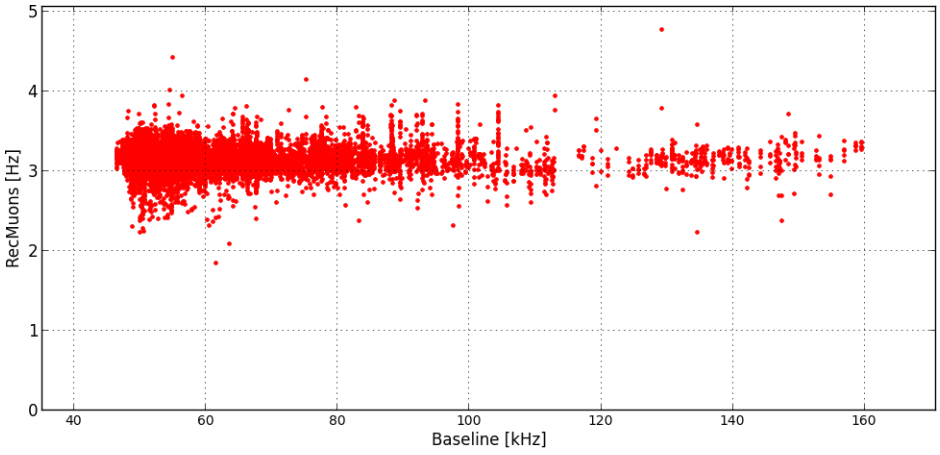

(c): Weights for active OMs and baseline applied.

Figure 8.8: Muon rate over the baseline with different weights applied.

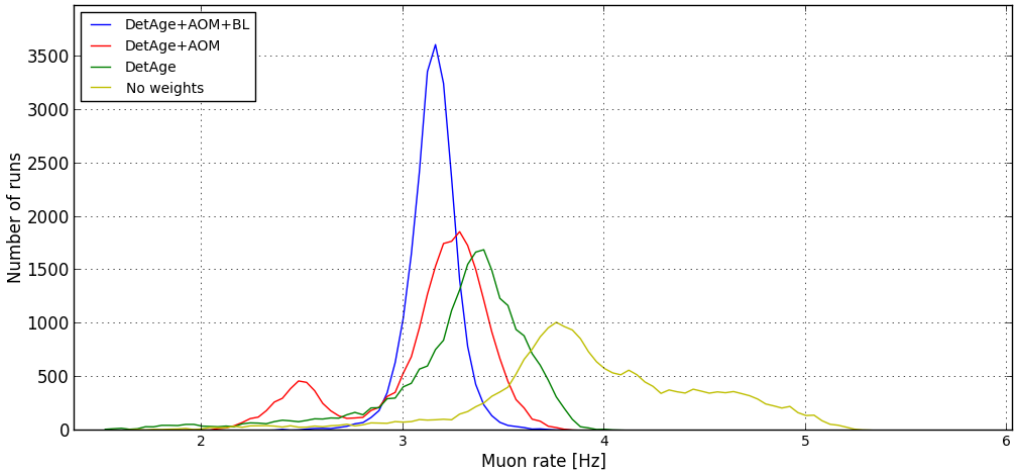

Figure 8.9: Histograms of the muon rate with different weights applied.

distribution of the rates of the reconstructed muons. The plots show the muon rates for TimeSlice6 using all run setups. The weights were calculated for each run setup. In 8.8(a) no weights except that for compensating the decreasing efficiency were applied. A cut on the number of active OMs was specified where all runs taken with less than 400 OMs in status OK were not used. Figure 8.8(b) shows the muon rates after the weights for the number of active OMs were applied. For 8.8(c) the weights of both, active OMs and baseline, were applied. The weights applied with respect to the used run setup concentrate the muon rates which was intended to increase the stability of the rates. Figure 8.9 shows a histogram of the muon rates and the effect of the weights to the spread. With no weights applied (yellow line) the spreading is higher than with all weights (blue line). The red and green lines show the intermediate steps (applied weights for compensating the decreasing efficiency of the detector over the time and the number of active OMs). The distribution of the muon rate and how it is changed by the weights shown in figure 8.9 for the other TimeSlices can be seen in appendix G.

In this chapter the λ-cut for the AAFit reconstruction method was defined to be -6.6. The need for a high statistic and the distribution of the zenith for reconstructed events lead to even lower cuts. On the other hand it was shown that a low cut increases the spreading of the muon rate. This decreases the stability in reconstruction which is necessary and would lead to a higher cut on lambda. The cut chosen is a reasonable compromise. Some data runs were rejected due to their corresponding value of baseline or the number of active OMs. Some run setups were completely rejected because they have not yet been calibrated (e.g. run setups marked with 'scan').

Chapter 9

Seasonal anisotropy of the muon rate of ANTARES

In the last chapters the selection of the available data and the definition of the λ-cut for the AAFit reconstruction method used by ANTARES was defined. This was done to get stable conditions for the search of the large scale anisotropy. It was shown that the muon rate calculated for each run is affected by the baseline and the number of active OMs. Weights were introduced to compensate their influence on the muon rate.

The stability of the data is mandatory for the search for the large scale anisotropy (see section 3.2). In chapter 4 it was shown that the temperature of the different pressure levels in the atmosphere have an influence on the muon rate measured with a detector like ANTARES. These effects should be analyzed. The existence of the effect in the data would give a good hint on the stability of the muon rate. The effect too influences the measurement of the large scale anisotropy and has to be considered. The effect of the large scale anisotropy is expected to be about 0.2 ‰[22] as described in section 6.1. The effect of the seasonal variation of the muon rate is expected to be about 2% as described in section 4. This chapter will use the selected data to search for the seasonal anisotropy.

9.1 Effective atmospheric temperature

The temperature of the different pressure levels of the atmosphere is considered as effective temperature. Weights are calculated for each pressure level and summed up to get the effective temperature as described in chapter 4 equation 4.19. The constants used to calculate the weigths $W^{\pi,K}(X)$ are summed up in table 9.1.

In figure 9.1 the relative weights and the average temperature for the different pressure levels for the time period May 2008 until December 2013 is shown. The height was calculated with the help of the barometric formula to get a feeling for the different pressures. The red dots are the average temperature for the corresponding pressure

Parameter	Value
A_π^1	1 [25]
A_K^1	$0.38 \cdot r_{K/\pi}$ [25]
$r_{K/\pi}$	0.149 [14]
B_π^1	1.460 [25]
B_K^1	1.740 [25]
Λ_N	120 g/cm^2 [14]
Λ_π	180 g/cm^2 [14]
Λ_K	160 g/cm^2 [14]
$< E_{th} >$	0.773 TeV
γ	1.7 [14]
ϵ_π	0.114 TeV [25]
ϵ_K	0.851 TeV [25]

Table 9.1: *Constants for calculating the weights of the effective atmospheric temperature.*

level over the mentioned time period. The blue dots are the relative weights for the pressure levels using the sum of the weights for pions and kaons ($W^\pi + W^K$).

The European Centre for Medium-Range Weather Forcasts (ECMWF) [7] provides the temperature of the pressure levels ranging from 1hPa up to 1000hPa. The data set used is called ERA-Interim (ERAIN). The data is organized in data files for each pressure level in GRIB format (GRIdded Binary) [45]. Each file holds the temperatures for a single pressure level over the whole earth binned with 0.7° in longitude and latitude. The temperature for the corresponding pressure level is calculated four times a day by ECMWF.

In this work only the bin right above the ANTARES detector is used as information about the temperature. The cut where no events with a zenith greater than 60° is used leads to the case where the size of the grid of the ERAIN data is larger than the sector seen by ANTARES. This is true for the most pressure levels. Only the highest levels (low in pressure) would see up to four bins of the ERAIN data. The average temperature over these bins minus the temperature for the bin above ANTARES is less than 0.25K for these pressure levels and is small in comparison to the change of the temperature during the day and the influence on T_{eff} of equation 4.19. Therefore, only the bin above ANTARES is used to determine the effective temperature.

In equation 4.17 the threshold energy of the detector is used to calculate the weights for the production of the muons in the atmosphere. To determine this energy figure 9.2 is used. The histogram shows the energy spectra of the reconstructed events. The energy values come from the Monte Carlo simulations. The threshold energy is defined as the median of the energy spectrum and is 0.773 TeV. Muons with lower energy than the left limit in figure 9.2 can not be seen by ANTARES according to the simulations.

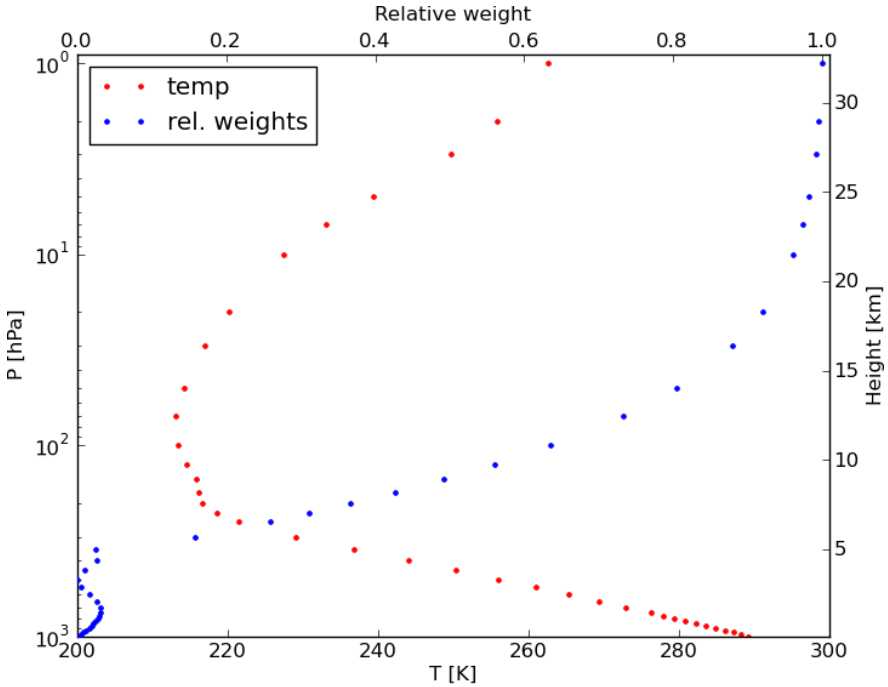

Figure 9.1: *Calculated average temperature and relative weights for different pressure levels.*

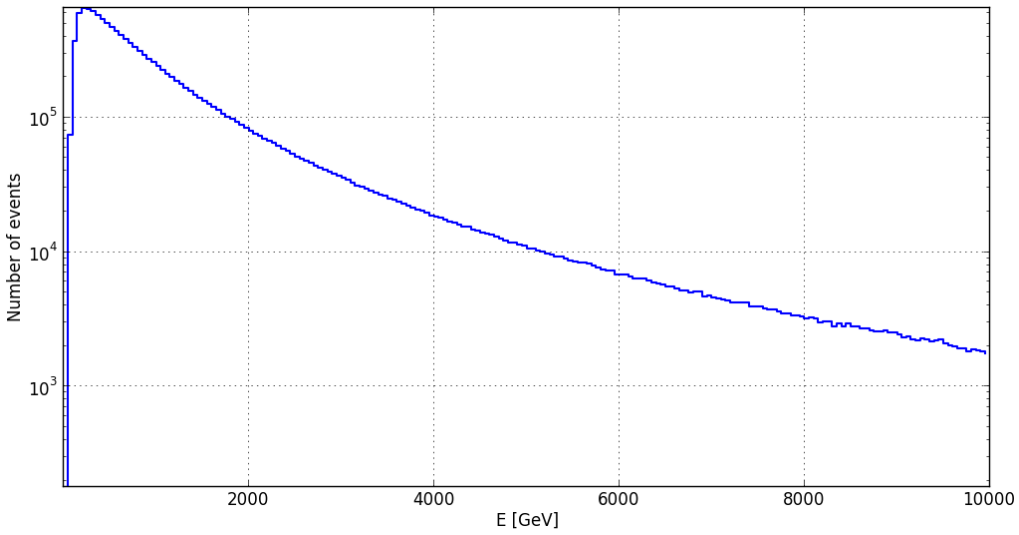

Figure 9.2: *Muon energy spectrum for ANTARES Monte Carlo.*

9.2 Variation of the muon rate using AAFit and T3 trigger

The run selection and weights for the baseline and number of active OMs as described in the former sections are used to determine the muon rate for each run. The lifetime used is shown in figure 9.3. It shows the fraction of each hour covered by the data used. On the y axis the year and month can be identified. Each month starts at the left side and counts the hours to the right in that month. On the left bottom January 2008 starts. The line above is February 2008 and so on. The color shows the coverage of the hours as a fraction in time. The maximum value naturally is 1.0. White areas were not used because of the run selection or downtime of the detector.

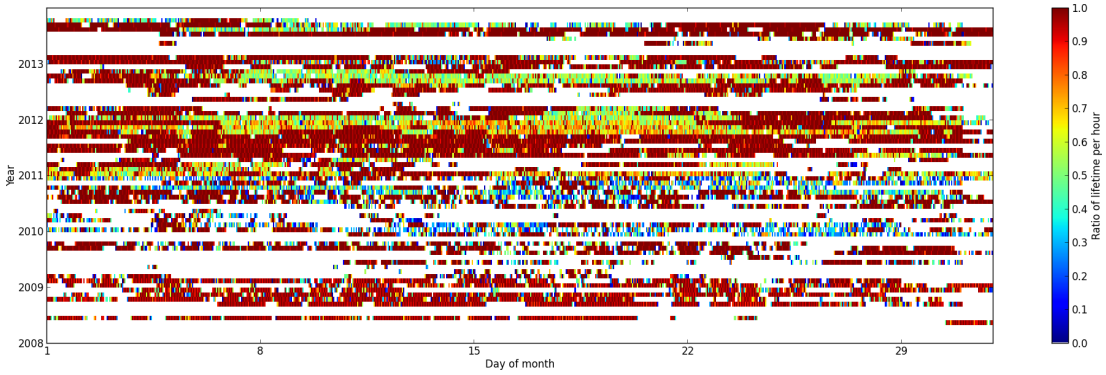

Figure 9.3: *Lifetime of the data used after the run selection. The ratio (color bar) gives the fraction of time for each hour used.*

The ratio $dT_{eff}/ < T_{eff} >$ with $dT_{eff} = T_{eff} - < T_{eff} >$ over the time can be seen in figure 9.4. The data points are the average temperature for one day with statistical error bars divided by the average effective temperature over the whole time period of about $< T_{eff} >= 228K$. It can be seen that the maximum is achieved every year at about July and August. For some dates no temperature is given in that plot like spring of the years 2012 and 2013. For this times no runs were selected as it can be seen in the plot 9.3 showing the lifetime.

Looking at the muon rates $dR/ < R >$ shown in figure 9.5 for the same time period it can be seen that the spreading of the rates is still high. Especially in the beginning of year 2012. Within that time periods the number of used run setups are less than in year 2011. This leads to the situation where the same run setup was used over a wider range of baseline and optical background. In year 2013 the maximum run time and hits for each data file was extended from about 2 hours to 8 hours. This has a similar effect where the same run setup was used over a longer time covering different baselines and optical backgrounds while in the previous year the used run setups have been adjusted to such differences.

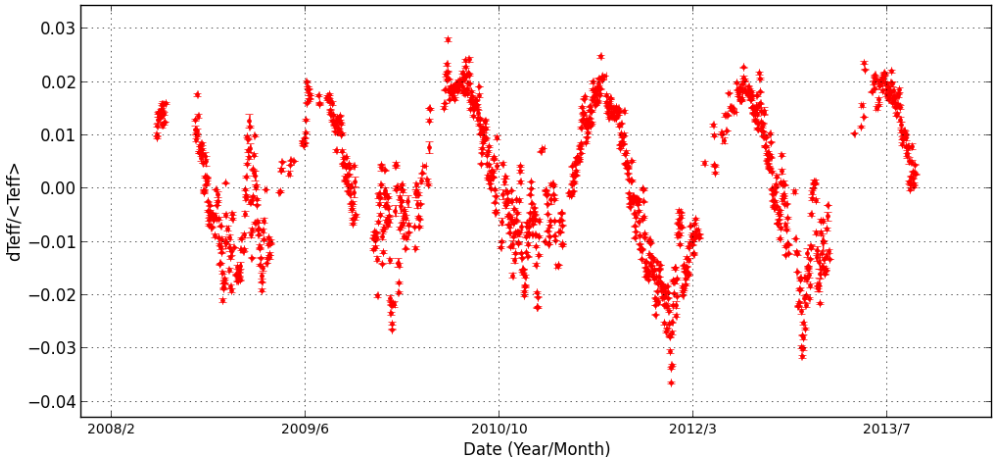

Figure 9.4: *Effective atmospheric temperature over time with statistical errors.*

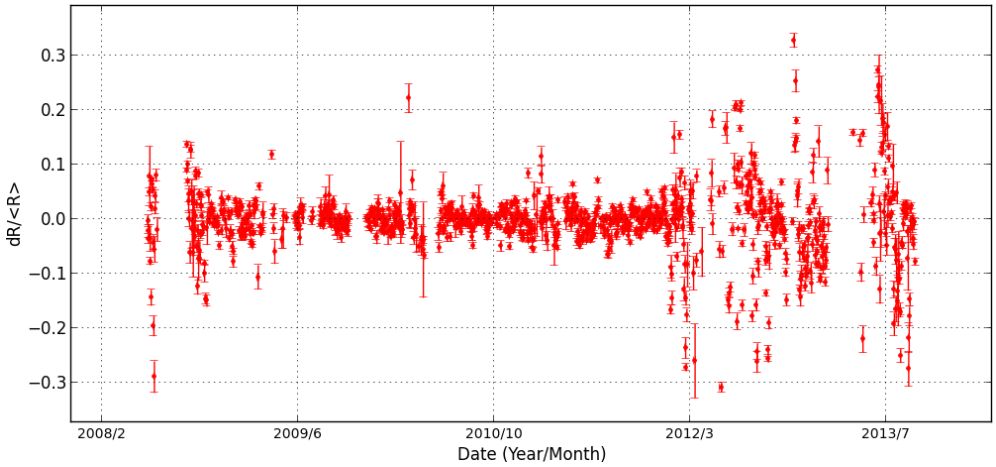

Figure 9.5: *Muon rate over time with statistical errors.*

The equation 4.16 shows that the ratio $\tilde{R} = dR/ < R >$ for the muon rates and $\tilde{T}_{eff} = dT_{eff}/ < T_{eff} >$ depend linear to each other by the factor α. In the case that the muon rate follows the temperature in the atmosphere α can be determined directly if $\tilde{R}$ is plotted over $\tilde{T_{eff}}$ and a linear function is fitted to the data. In figure 9.6 the theoretical value for α over the depth mwe is shown.

For the ANTARES detector at a depth of about 2400m under sea water α is expected to be about 0.9. The variation of the muon rate expressed in $\tilde{R}$ therefore has the same order as the variation of the temperature expressed in $\tilde{T_{eff}}$. From figure 9.4 it can be seen that the variation of $\tilde{T_{eff}}$ is about 2% with respect to the average effective temperature. The variation for $\tilde{R}$ should be around 2% too when $\alpha = 0.9$. The rate in figure 9.5, however, varies more than that on much shorter intervals. That shows that the stability of the detector does not allow the determination of α experimentally with the data and parameters used. Additional cuts on the baseline where only a defined

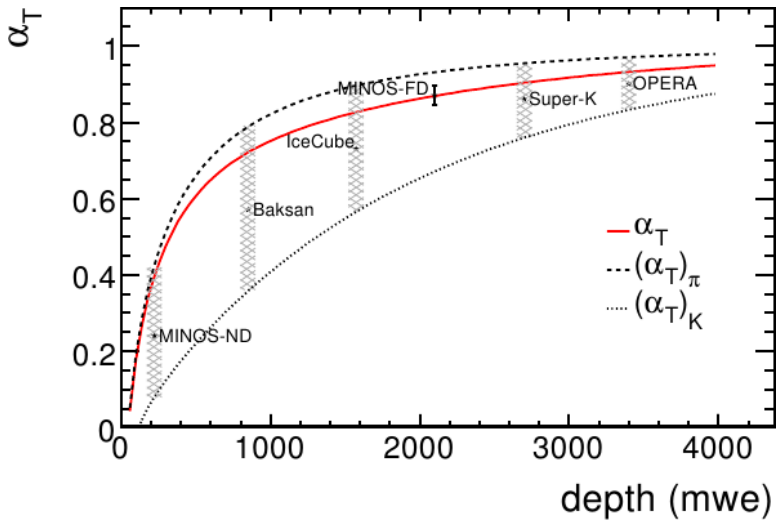

Figure 9.6: *Theoretical values of α_T over the depth in mwe (solid). The measurements from different experiments are shown with the sensitivity indicated (cross-hatched regions). The dashed and dotted curves show the value of α when using only pion and kaon decays [25].*

range (e.g. 60 kHz - 80 kHz) was used and only runs where a specified number of triggers were enabled also did not allow to determine α based in the data. Figure 9.7 shows $\tilde{R}$ over $\tilde{T_{eff}}$ only for TimeSlice6. Here the spreading of $\tilde{R}$ is within the expected range. The data points calculate the average for the muon rate and the effective temperature over 21 days. However, neither is a dependence visible there.

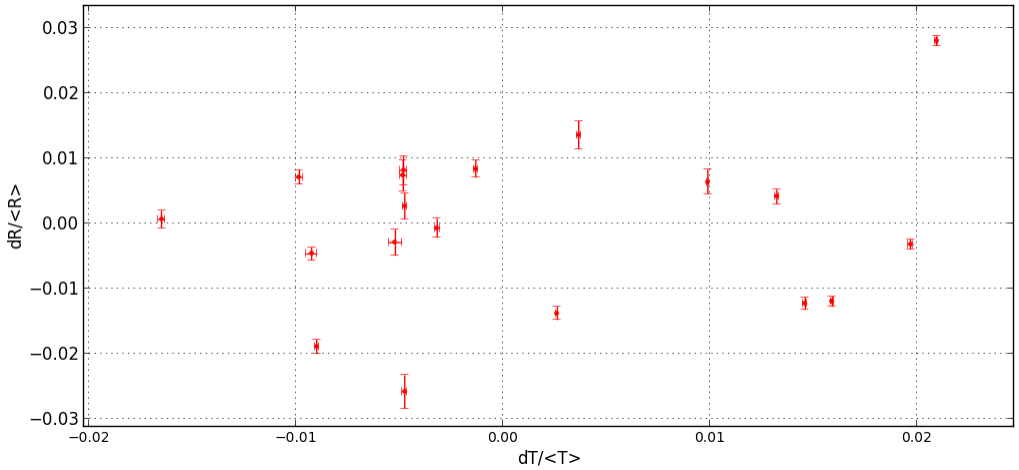

Figure 9.7: *$dR/ < R >$ as a function of $dT_{eff}/ < T_{eff} >$ using the average over 21 days for the muon rate and the effective temperature for data within TimeSlice6.*

9.3 Variation of the muon rate using AAFit and 3DScan trigger

The analysis of the data using the cuts described in the former chapters did not show any correlation of the muon rate to the atmospheric temperature. There only events that were found by the trigger T3 were used. In this chapter the triggers will be changed and only events triggered by 3DScan are used. For more information about the trigger see chapter 5.4. The trigger 3DScan has a slightly lower rate and was turned off less times in comparison to the trigger T3. The muon rate therefore is lower than compared to the former chapters.

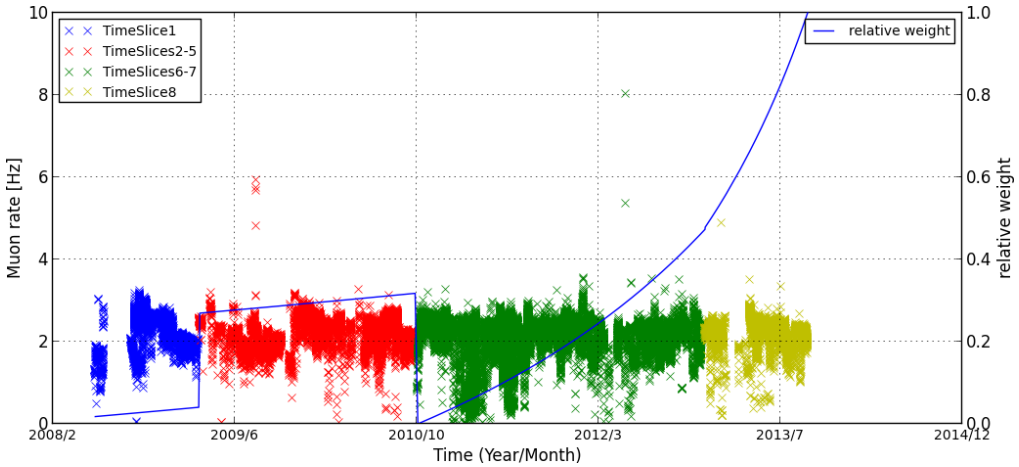

Figure 9.8: *Weighted muon rate (crosses) over time and the corresponding relative weights (solid line).*

In figure 9.8 the weights for compensating the decreasing efficiency of the detector over the time (see chapter 7) are applied. The relative weight is shown by the blue line. The different colors of the crosses illustrate the four time periods chosen as it was done in chapter 7. The structures in the muon rate over the time stay the same as in figure 7.2. Find a plot of the muon rate over the time without weights in appendix H.

Figure 9.9 shows $\tilde{R} = dR/ < R >$ over time. Only events triggered by 3DScan are used. The λ-cut is -6.6 and the weights for baseline, number of active OMs and the decreasing efficiency are applied to reduce the spreading of the data. The corresponding lifetime of the data used for the plot and histograms showing the effect of the weights for the distribution of the muon rate are shown in appendix H. A plot showing the muon rate $\tilde{R}$ over time without the weights for baseline and active OMs can also be found in that appendix. There it can be seen that the spreading of the muon rate has been reduced by applying the weights.

The muon rate does not show any correlation to the effective temperature as shown in picture 9.4 which is also valid for that plot. The factors of the fitted functions to

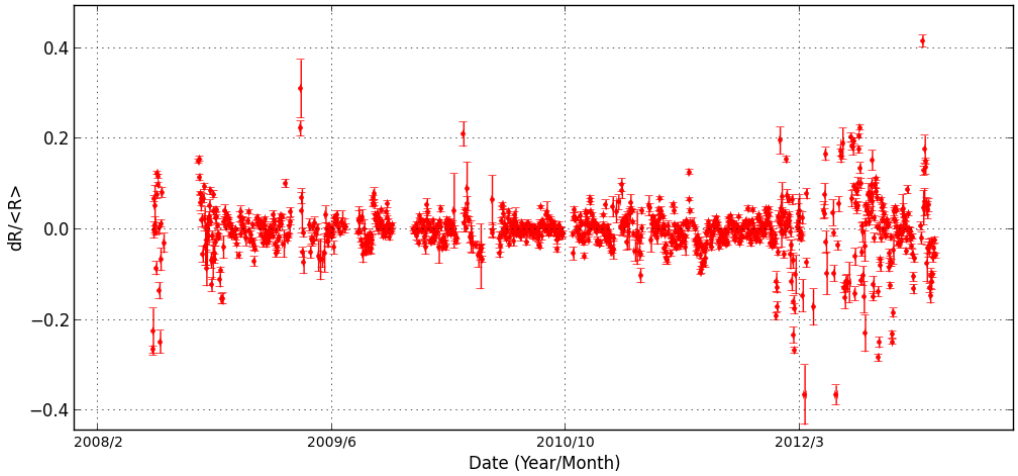

Figure 9.9: *Muon rate over time. The error bars give the statistical error on the muon rate.*

get the weights for the muon rate depending on the baseline and the number of active OM can be found in appendix F

It can be said that the characteristics of the detector do not allow to determine the change of the muon rate by the temperature in the atmosphere when using the AAFit strategy and the shown principle in weighting of the data. The effect is expected to be about 2% of the average muon rate and it can be seen that the spreading of the data even for short time scales is about the same range without following the atmospheric temperature.

Several aspects are possible which create that spreading in the muon rate. The optical background which is represented by the value of the baseline is rapidly changing during data taking. The burst created by bioluminescence are creating extra hits that may survive the cuts of the reconstruction algorithm and also influence data taking. With that the shifters have to change the run setup by turning off and on different triggers. Different run setups have also an effect on the muon rate as shown in chapter 8.2.

Using only one specific run setup (the same triggers enabled) did neither show any correlation of the muon rate to the atmospheric temperature. A cut on the baseline only using the runs within a specific range and a cut on the burstfraction did neither reduce the spreading that much that a correlation could be seen. The figures in 9.10 and 9.11 show the relative muon rate and temperature over time with the following cuts applied:

- Baseline < 80 kHz
- Burstfraction < 0.2
- Only runs with the following trigger set: 3N+2T3+GC+K40+TS0

Comparing the variation of the relative atmospheric temperature in figure 9.11 with the variation of the relative muon rate in figure 9.10 no correlation can be seen. The data points showing the data at the end of the year 2012 seem to follow the temperature, but the variation of the muon rate is too large to be identified as the effect of the seasonal variation. Furthermore the variation of the muon rate for previous dates show contrary behavior.

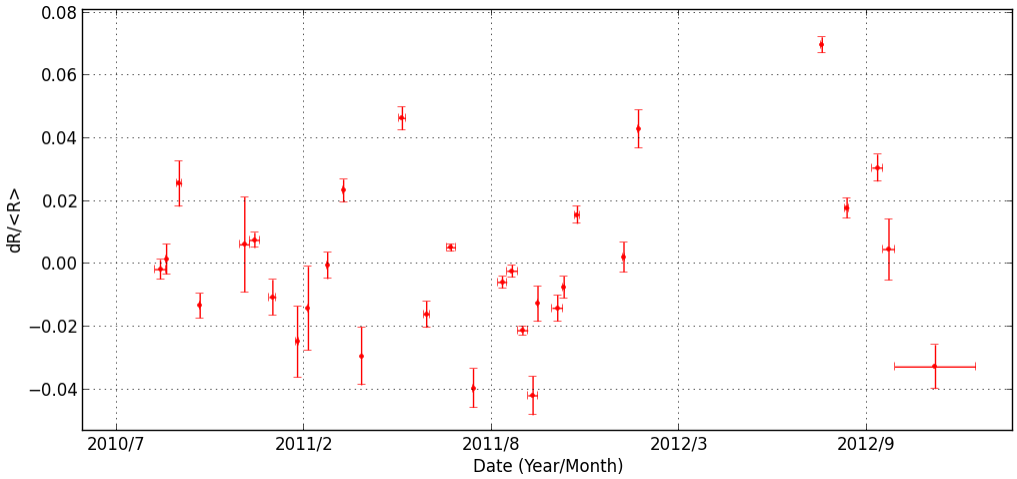

Figure 9.10: *Relative muon rate over time. The error bars give the statistical error on the relative muon rate.*

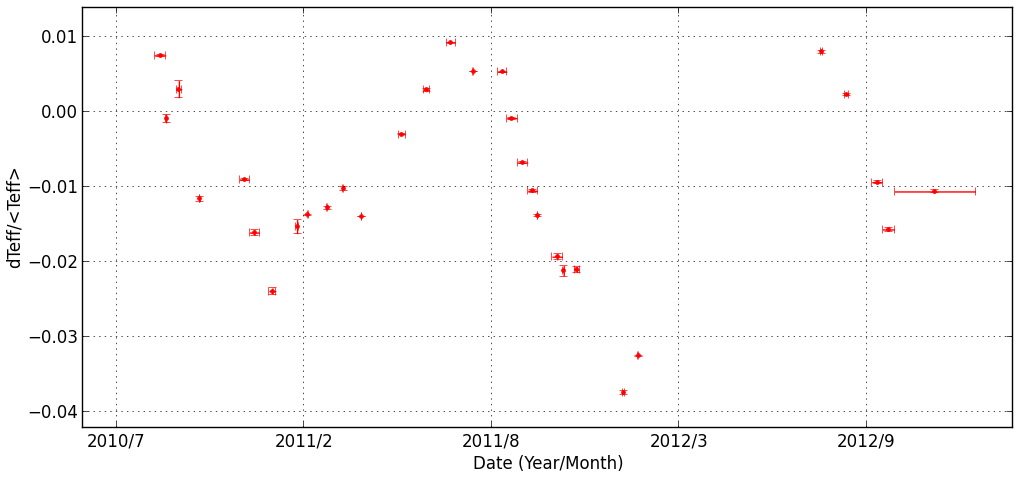

Figure 9.11: *Relative temperature over time. The error bars give the statistical error on the relative temperature.*

9.4 Variation of the muon rate with run-by-run Monte Carlo

The run-by-run (rbr) approach of ANTARES creates Monte Carlo data that uses the circumstances of data runs as basis for the simulation. This includes the information available for each data run saved in the database of ANTARES. The optical underground is added based on the information about baseline, mean rate and other parameters of the data runs. Optical modules that were turned off during data taking were disabled for the rbr files too. The reason to create these rbr Monte Carlo is to have a simulated input as close to the truth as possible. For this work only files that simulate atmospheric muons are used. The muons are simulated by the package MUPAGE. The rbr files are organized similar to the data files by run numbers. This ID makes it easy to identify the simulation and data files that belong together. Find more information about the rbr files in chapter 5.7.

The rbr files use a constant muon flux over time. With a precise Monte Carlo simulation based on that approach it is possible to extract not simulated information from the data taken by the detector. This chapter will use this principle to search for the seasonal anisotropy. For that the muon rate is calculated per file.

The properties like the duration and the baseline of the files with the same ID should be the same and the ratio of the muon rate of the rbr and the data file should show the information that has not been simulated like the seasonal Anisotropy.

In chapter 8.2 it was shown that the data and especially the reconstruction method is influenced by the baseline and the number of active OMs. Weights were calculated to minimize the influence of that parameters to the muon rate. The same was made for the rbr data. A whole new set of fitting functions was created of which the parameters can be seen in appendix F. The muon rates calculated from the simulation files do not depend that much on the baseline or the number of active OMs as the muon rate calculated from the data files.

The decline of the efficiency of the detector over the time as discussed in chapter 7 is not simulated for the rbr files and was taken into account only for the data.

The reconstruction method used is AAFit. The λ-cut was set to -6.6 as described in chapter 8. The maximum zenith angle for the reconstructed events to be counted is $60°$. For the rbr files only the reconstructed events were used. The Monte Carlo truth was ignored. For a basic comparison of the data and the rbr files concerning the reconstruction algorithm see section 8.1. A cut on the baseline was made for 160kHz as described in section 8.2. The time period used for the plots shown in this chapter is TimeSlice6 as defined in table 6. This period was chosen because it is the most stable period concerning data taking and spreading of the whole 5 year period that is used in

the former chapters.

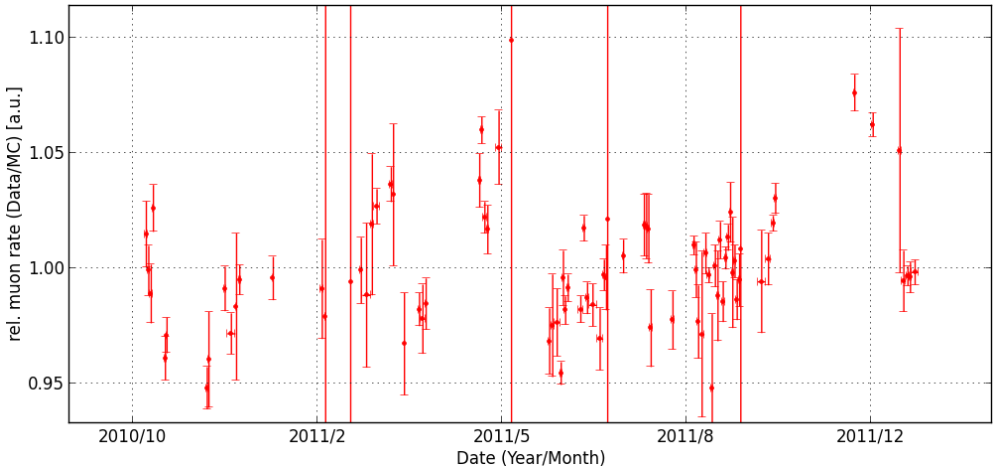

Figure 9.12: *Relative muon rate $\tilde{R}$ over the time.*

The weights for the dependency on the number of active OM and the baseline were applied to the muon rates that were calculated for the data files and the rbr files separately. The relative muon rate $\tilde{R}$ was calculated by $\tilde{R}_{id} = R_{data,id}/R_{rbr,id}$. The id here is the run number by which the files can be identified and matching files for data and rbr can be found. Picture 9.12 shows $\tilde{R}$ as the relative muon rate over time. The error bars are statistical errors. The maximum time range for one data point is one day. For some days only very few data is available which makes the error bars that big. For comparison figure 9.14 shows the effective temperature as defined in section 9.1 over time. According to figure 9.6 and 9.7 the muon rate should vary about 2%, following the effective temperature. As it can be seen the variation of the relative muon rate $\tilde{R}$ is higher than expected and not correlated to the effective temperature.

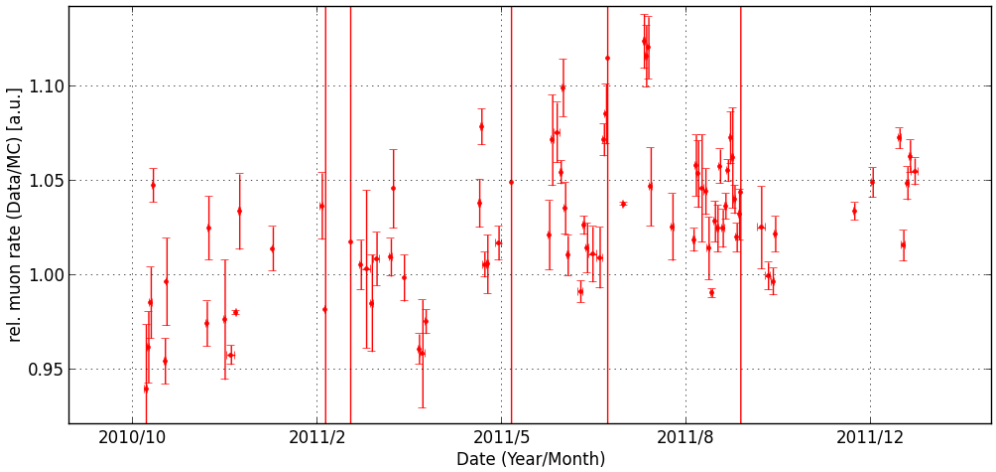

Figure 9.13: *Relative muon rate $\tilde{R}$ over time. No weights applied.*

The run-by-run simulation seems not to cover all characteristics of the detector in

order of the desired accuracy for that method. The spread in the plot shown here is about the same order as shown in chapter 9.2. The change of the characteristics of the detector during time, the influence of the changing baseline and different run setups as described at the end of chapter 9.3 don't seem to be sufficiently included within the simulation. Figure 9.13 shows $\tilde{R}$ without weights applied for the baseline and the number of active OMs for both, muon rates calculated from the Monte Carlo and data. The muon rates from data were only weighted to compensate the reduction of the efficiency of the detector over time. For that the weights described in chapter 7 are used. It can be seen that the spreading of the data points is even larger compared to figure 9.12 where all weights have been applied. If the simulation used would fit the data exactly (this includes the dependency of the reconstruction algorithm on the baseline and the number of active OMs) figures in 9.12 and 9.13 should look the same. It can be seen that the used Monte Carlo simulation does not fit to the data perfectly. Therefore, the Monte Carlo can not be used to determine the seasonal anisotropy because of the differences shown. The weights got by the study on the dependency of the muon rate on the baseline and the number of active OMs (see appendix F) also show a disagreement between data and Monte Carlo.

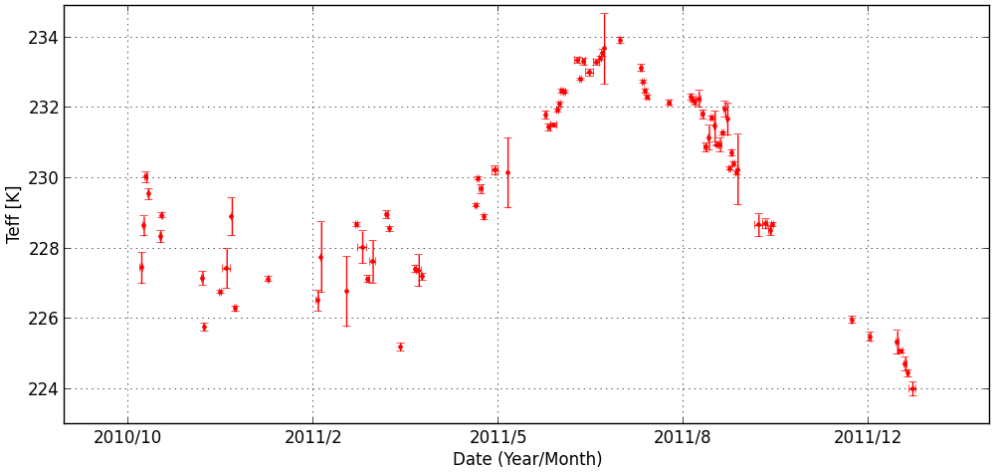

Figure 9.14: *Effective temperature over time.*

9.5 Variation of the muon rate using BBFit

This chapter will repeat the steps described in the former chapters 8 and 9 with the BBFit reconstruction method. Events used in the following sections are reconstructed only by BBfi. Some parameters defined in the former chapters will be the same here and are shortly summarized.

- The maximum zenith angle for reconstructed events is 60°.
- The used trigger to select the events is T3. The use of the trigger 3DScan did not show any different systematics concerning the dependence of the atmospheric temperature as shown in chapter 9.3 and will be neglected.
- The runs selected in chapter 6 will be used for that method too.

The reconstruction method BBFit defines a quality parameter too. This chapter explains how the cut on that parameter was defined and why. After that the dependency of the muon rate determined by the reconstructed events with BBFit for each data run on the baseline and the number of active OMs will be analyzed and weights are calculated as described in chapter 8. Then the variation of the muon rate with respect to the effective atmospheric temperature is studied.

9.5.1 Definition of the quality parameter

The quality parameter used for the events reconstructed by BBFit algorithm is called $T - \chi^2$. The distribution of the reconstructed events with no cuts applied can be seen in figure 9.15. In contrary to the λ-cut used by AAFit the parameter $T - \chi^2$ for BBFit is positive. A cut on that parameter selects events with a lower value as the defined value of $T - \chi^2$.

The cut for λ in chapter 8 was defined by characteristics of the reconstruction method. The distribution of the zenith of the reconstructed events and the performance depending on the baseline and the number of active OMs have defined the λ-cut. The zenith distribution for different cuts on $T - \chi^2$ can be seen in figure 9.16. The run by run Monte Carlo simulation was used to generate that distribution. The two lines that are labeled with MC use the Monte Carlo truth of the reconstructed events. They are shown for two different cuts on $T - \chi^2$. The other lines show the distribution of the zenith of the events reconstructed by BBFit with different cuts on $T - \chi^2$. For all cuts the reconstruction algorithm overestimates the direction with zenith equal to zero. It can be seen that the distribution of reconstructed tracks follows the Monte Carlo truth better for higher cuts of $T - \chi^2$.

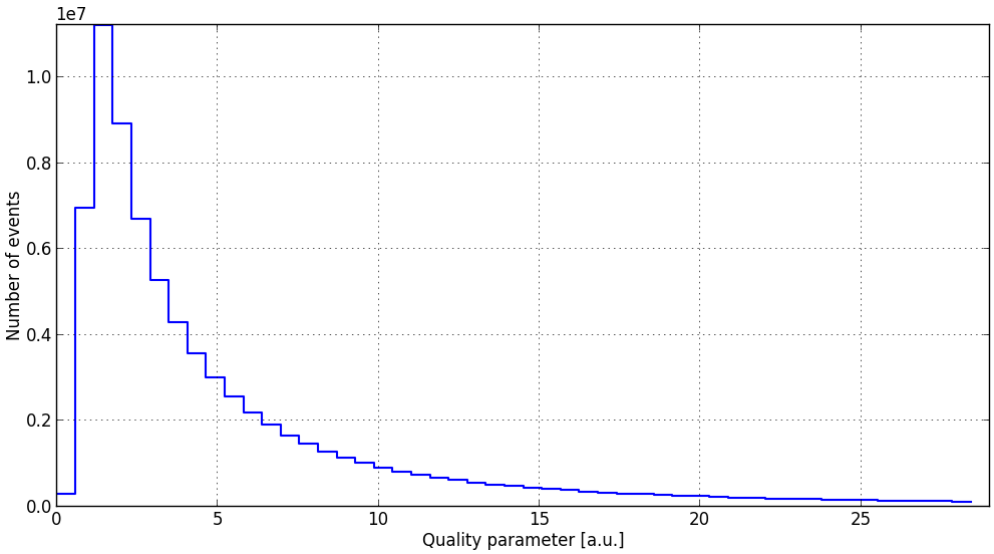

Figure 9.15: *Distribution of the events for values of the quality parameter for BBFit.*

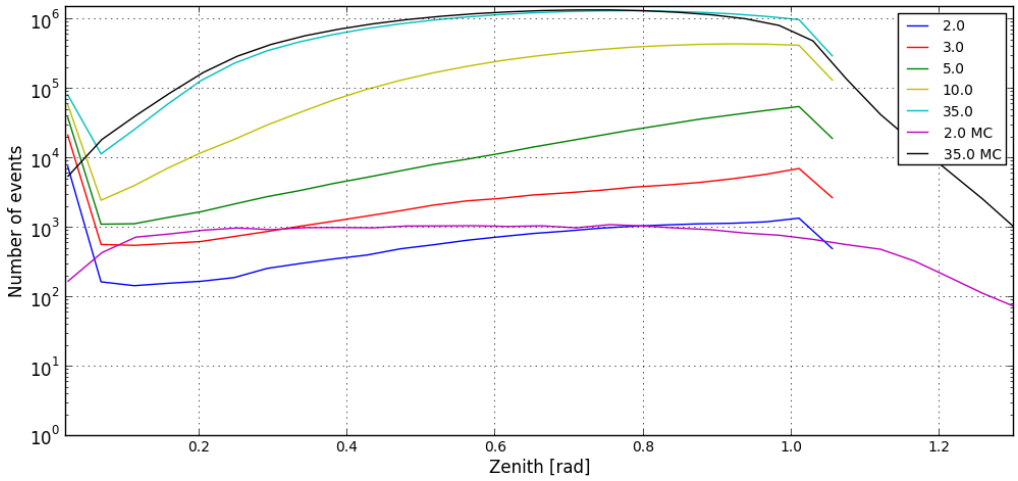

Figure 9.16: *Distribution of reconstructed events over zenith angle for different quality cuts (legend). The black and the violet lines show the distribution of the Monte Carlo truth of the reconstructed events for two cuts.*

A cut on the zenith angle of 60° was applied to the reconstructed events. The plots showing the Monte Carlo truth do not have these cut due to the error on the zenith angle for the reconstruction method. The lines for the reconstructed events in that plot shows a decrement after a value of zenith greater than 1.0 rad. This is because of the binning where the end of the last bin is higher than the cut on zenith made. As for the AAFit reconstruction method looser cuts on $T - \chi^2$ change the distribution of the zenith angle to shapes it is expected (see chapter 8.1).

The table 9.2 shows the sigma of the errors for different cuts on $T - \chi^2$ as it is described in section 8.1.1. It can be seen that higher cuts will add more events where the

$T-\chi^2$ cut	Sigma in °
2.0	81.7
3.0	67.9
5.0	22.5
10.0	8.9
20.0	7.22
35.0	7.14

Table 9.2: *Error of the track reconstruction for different cuts on the quality parameter.*

angular distance between the reconstructed events and the Monte Carlo truth decreases by the mean. Therefore, the sigma of the fitted Gauss function to the angular distance decreases for higher cuts.

From figure 9.16 someone could expect that the events with a zenith of a few degrees are wrongly reconstructed events from higher zenith angles until about 0.8 rad. This was tested by counting the number of events with a zenith angles less than 60° for reconstructed events and the corresponding Monte Carlo information on the direction of the event as it was done in section 8.1.1 and table 8.3. Table 9.3 shows the ratio in percent of the number events reconstructed by BBFit and the Monte Carlo information with a zenith less than 60° ("In cone MC/Fit") for two different cuts on $T-\chi^2$. The information from Monte Carlo is used to determine the number and the percentage of events that have been wrongly reconstructed into the cone ($< 60°$) or with greater zenith angle (out of the cone). Additionally, the number of events fitted by BBFit with a zenith $< 60°$ is shown.

$T-\chi^2$-cut	False in cone	False out of cone	In cone MC/Fit	Number of events fitted
2.0	8.3%	594.2%	686.0%	22597
35.0	1.3%	10.1%	108.8%	18323579

Table 9.3: *An estimation of the percentage of miss reconstructed events with respect to the cone defined by the cut on zenith.*

For the low cut of 2.0 the ratio of the number of events in the cone is about 686%. This means that the events from the first bin in figure 9.16 around 0.0 rad do not come mainly from events nearly with the same angle concerning the information of the Monte Carlo. The value of the error of the reconstruction in table 9.2 agrees with that.

This fact will define the cut on $T-\chi^2$ to higher values where the comparison between data and Monte Carlo is better and the reconstruction error is less than for lower cuts. To withdraw the overestimation of the reconstruction algorithm for events with a zenith angle around zero the events with a lower zenith of 0.03 rad ($\approx 1.7°$) are rejected for the upcoming discussion.

Figure 9.17 shows the influence of that cut on the distribution in zenith for two different cuts on $T-\chi^2$. It can be seen that the peak in figure 9.16 for events with

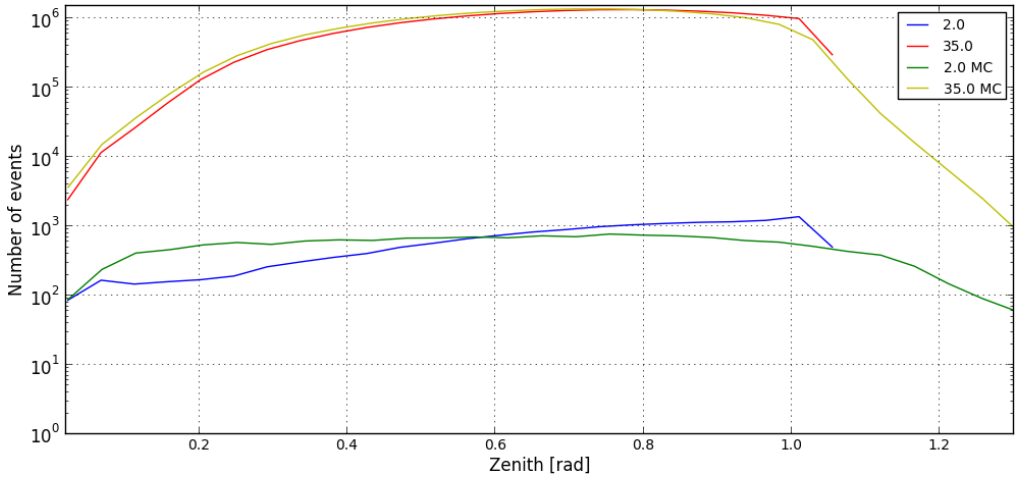

Figure 9.17: *Distribution of reconstructed events over zenith angle for different quality cuts for BBFit. The legend gives the cut on $T-\chi^2$ used. Events with a angle in zenith < 0.03 rad ($\approx 1.7°$) are rejected.*

a zenith of about zero now is gone and that the distribution follows the Monte Carlo better in that range. The fact that the plot does not drop to zero because of the cut is again the binning of the data. Calculating the error on the angle of the reconstructed events to the Monte Carlo information the sigma shown in table 9.2 is reduced for a $T-\chi^2$-cut of 2.0 to $\sigma = 55.6°$. The average error for the $T-\chi^2$-cut of 35.0 keeps constant as the number of events with a zenith $< 1.7°$ is about an order of magnitude smaller than the maximum of the zenith distribution.

The other aspect that has defined the cut on λ for the AAFit reconstruction method in chapter 8 was the distribution of the muon rate over the baseline and the number of active OMs. A loose cut has increased the spreading of the muon rates depending on the baseline and the number of active OMs. The cut for the AAFit reconstruction method was therefore limited in two directions and it was set to -6.6. In this section it was shown by the zenith distribution for the BBFit reconstruction algorithm and the error on the reconstruction angle that a higher (looser) cut is better. This is the same as for the AAFit reconstruction method. Figure 9.18 shows histrograms of the muon rate with different weights applied for a $T-\chi^2$-cut of 35.0. By the yellow line it can be seen that the BBFit reconstruction method does not increase the spreading for the loose cut on the quality parameter. The muon rates calculated based on the AAFit reconstruction algorithm have shown an excess for lower cuts and the quality parameter was constricted by that. This is not the case here and the cut at 35.0 for the quality parameter $T-\chi^2$ was chosen.

Figure 9.18 also shows the influence of the weights that were applied for baseline (BL), number of active OM (AOM) and the decreasing efficiency of the detector over time (DetEff). The weights are described in detail in section 8.2. The distribution of the muon rates is shown for no weights (yellow), decreasing efficiency of the detector

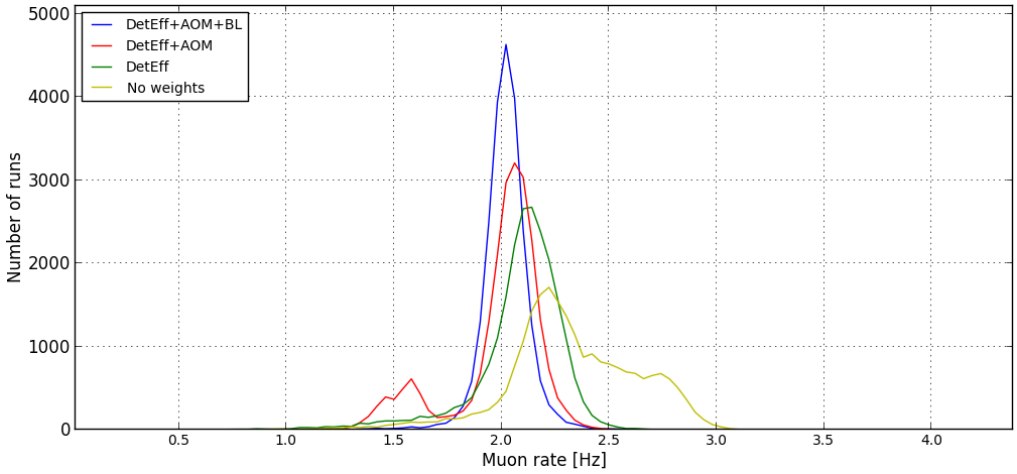

Figure 9.18: *Distribution of the muon rates with different sets of weights applied.*

over time (green), additionally applied weights for the number of active OMs (red) and the baseline (blue).

A new set of weights concerning baseline, number of active OMs and the decreasing efficiency of the detector over the time was created based on the events reconstructed by BBFit over all TimeSlices. Find the parameters of the functions used to calculate the weights in appendix F. The influence of the weights on the muon rate for the other TimeSlices and the used weights for the decreasing efficiency of the detector can be found in appendix I.

It was shown that the cut on the quality parameter $T - \chi^2$ of BBFit can be chosen very loose. The comparison of the Monte Carlo simulation and the reconstructed events have shown better agreement for the chosen cut than for lower values. Like the AAFit reconstruction method the BBFit algorithm also shows a dependency on the baseline and the number of active OMs.

9.5.2 Time dependent variation of the muon rate

The BBFit reconstruction method is now used to calculate the muon rate for each data run within the time period used in this work. Weights will be applied to the muon rate based on the baseline, the number of active OMs and the decreasing efficiency of the detector over time. Analog to chapter 9.2 the muon rate $\tilde{R}_i = (dR_i - < R >)/ < R >$ over time is shown in figure 9.19. Where dR_i is the muon rate within the time interval i used for one data point and $< R >$ is the mean muon rate over all times shown in the figure. The figure 9.20 shows the progress of $\tilde{T}_{eff}$ defined analog to $\tilde{R}$ using the effective temperature (see section 9.1) instead of the muon rates.

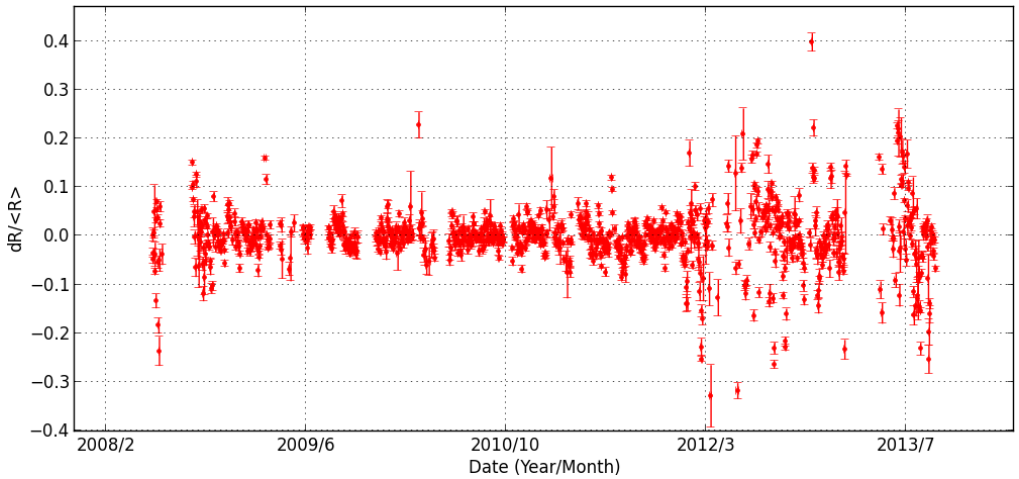

Figure 9.19: *Relative muon rate over time shown as the one day average. The error bars show the statistical error.*

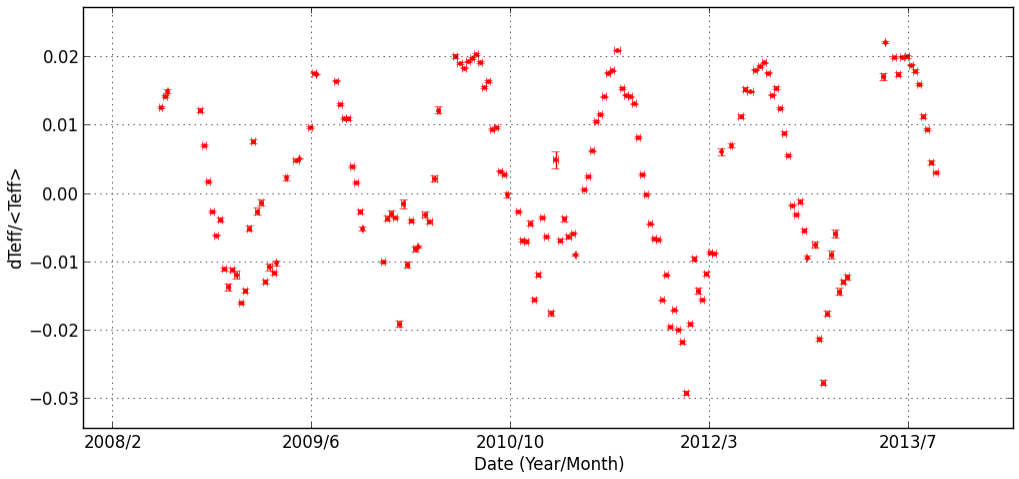

Figure 9.20: *Effective atmospheric temperature over time.*

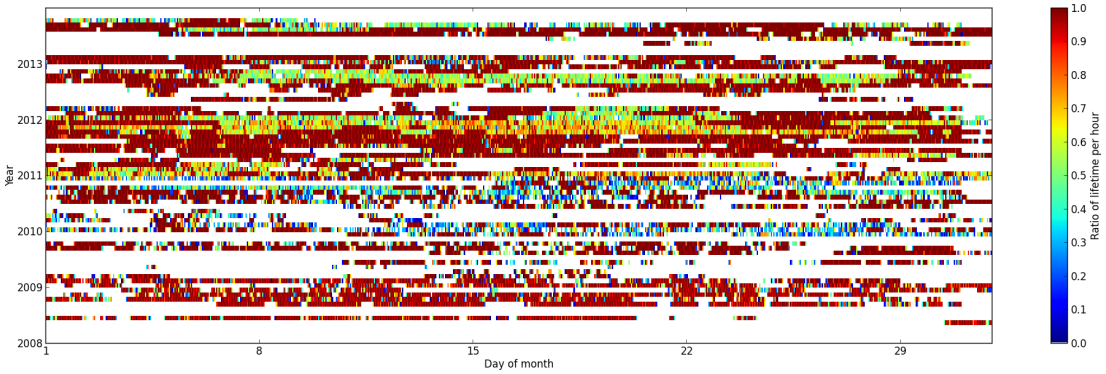

Figure 9.21: *Lifetime on a one hour basis for the data selected.*

The plots show the average of the muon rate and the effective temperature over one day. The error bars show the statistical error. It can be seen that the spreading, especially for the years 2012 and 2013, is higher than the expected effect of the effective temperature on the muon rate (which is about 0.8 multiplied by the variation of the effective temperature as shown in figure 9.20). Figure 9.21 shows the distribution of the lifetime of the used data.

Figure 9.22 only shows the muon rates of TimeSlice6. Stronger cuts for selected data based on the burstfraction and the baseline were made. Where the value of the baseline for one run has to be between 60 kHz and 80 kHz and the value for the burstfraction has to be less than 0.2. With that cuts applied it can be seen that the variation of the muon rate $\tilde{R}$ (about ± 0.2) is less compared to figure 9.19 but still is too high when looking at the variation of the effective temperature for the same run selection (about ± 0.1) seen in figure 9.23.

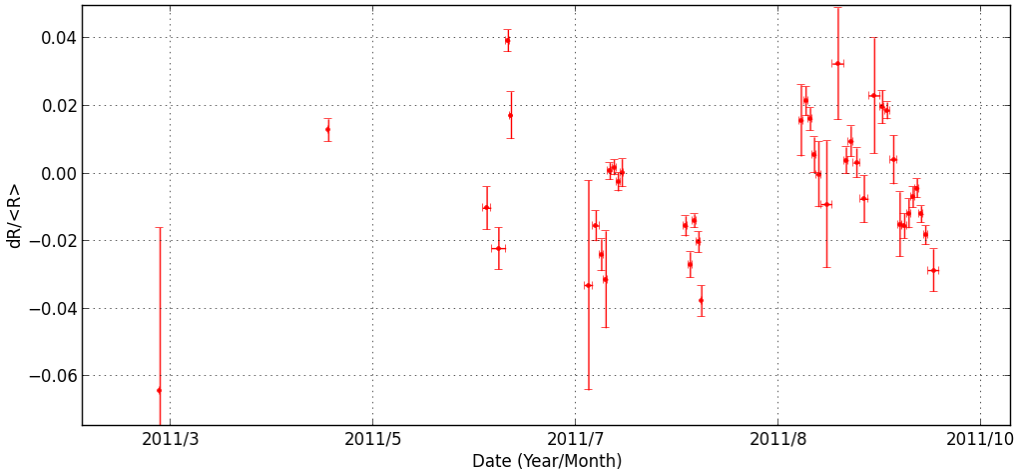

Figure 9.22: *Relative muon rate over time with stronger cuts applied (see text).*

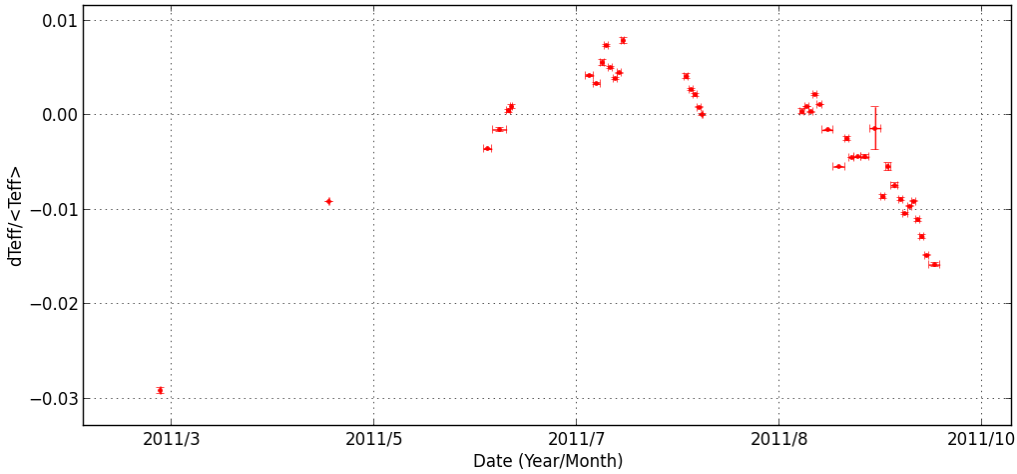

Figure 9.23: *Relative effective atmospheric temperature over time.*

Compared to the AAFit reconstruction method, BBFit has not shown different properties concerning the variation of the muon rate over the time. It has not shown the same characteristics for weaker cuts which was used to increase the total number of events that were reconstructed by the BBFit algorithm but the variation of the muon rate over the time still can not be correlated to the effective atmospheric temperature.

9.6 Variation of the muon rate based on data frames

In the former chapters the muon rate was calculated based on the number of muons and the time of each run. It was shown that the variation of the muon rate is dominated by the characteristics of the detector and the spreading of the muon rate over the time does not have the accuracy necessary to see the relationship to the atmospheric temperature.

In chapter 5.5 the data acquisition of ANTARES is described. The data of ANTARES is organized by run files with a unique id and for each run additional information like the baseline and the working optical modules (OMs) are available. The information used so far were the average over each run file. The parameters like the baseline and the number of active OMs can change within that time rapidly as shown in figure 5.7.

The shortest time interval in which the data is sent to the shore station are the data frames. Each frame has a duration of about 104 ms. For every frame the current counting rate and the current status of each OM of ANTARES is available. An OM can be in one of the following states:

- Off: The OM was turned off and/or does not send anything.
- Other: The OM does not work but the reason is unknown.
- XOff: The OM can be in this state if the rate of the PMT is too high for both ARS boards. This state can be temporally for about a few events.
- Empty: A frame was sent, but no data.
- Partially empty: one ARS does not send data, the other does
- Low: The rate (mean rate of both ARS sent to shore station) of the OM is < 40 kHz.
- High: The rate (mean rate of both ARS the PMT of the OM sees offshore) of the OM is > 200 kHz
- OK: If no other status was set.

The ARS (analog ring sampler) boards are part of the electronics and convert the analog signal from the PMT to its digital equivalent which is sent to the shore station. There are two ARS boards connected to each PMT. As long as one ARS processes an event it is not ready to listen to another hit on that PMT. One ARS has a dead time of about 225 ns. In this time the second ARS takes over waiting for a signal from the PMT. In the case that one ARS is in the state error the OM is in state partially empty (see list above).

Based on the number of hits per time slice ($\approx$ 104 ms) both ARS have a hit rate. Two different hit rates are available for each ARS. The number of hits processed by the ARS which is called the off shore rate and the number of hits actually sent to the shore station.

For the upcoming analysis the off shore rate of one ARS (the first if it works, the second in the other case) is read out for each PMT. In figure 9.24 histograms of the mean rates for one run are shown. One entry in the histogram is the mean of the off shore rates for one timeslice. The blue line shows the distribution of this means for the OMs in status OK (RateOK). The red line uses the OMs in status high (RateHigh) and the green line uses the mean of the OMs in status low, OK and high (Rate). The number on the y-axis gives the number of frames with the corresponding mean rate for that run. The run was chosen by random to show that within each run the mean rates over the detector changes.

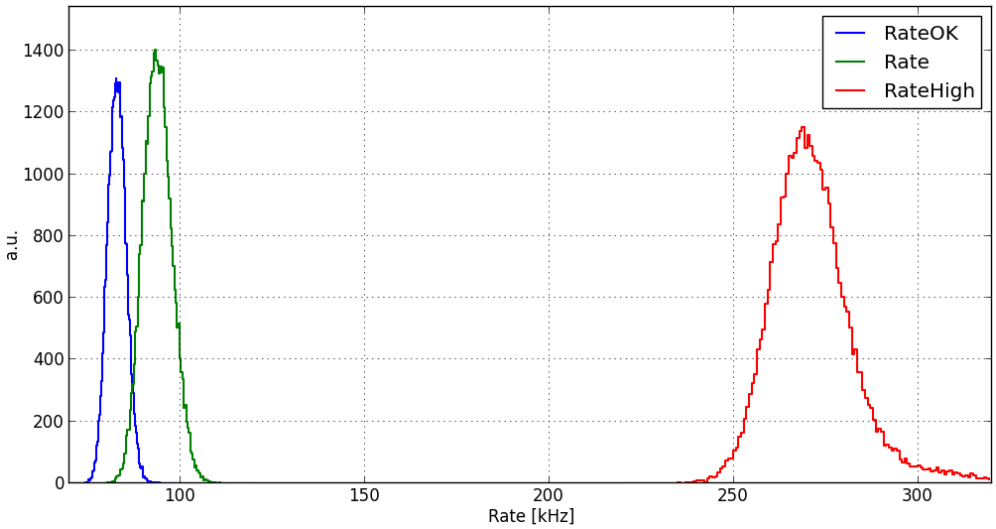

Figure 9.24: *Distribution of the hit rates for one data file (one run).*

9.6.1 Identifying time intervals with equal conditions

In the former chapters a total mean called baseline was calculated for each run. Using the information based on the time frames the current status of the detector can be determined at a time scale of about 104 ms. The intention of these information is to identify time frames with similar circumstances based on the rates shown above. The reconstructed events are organized the way that their relation to one frame can be identified. Time frames and events are used based on cuts on the mean rates for each time frame. It is possible that frames do not have reconstructed events. In this case the time of the frame is counted too if it has survived the cuts. To calculate the muon rate the number of events and the time of each used frame are counted up over one or more days. The muon rate is calculated then based on number of events divided by the time.

The data from TimeSlice6 (November 2010 until December 2011) is used in this section because of the stable conditions of that time period. The muon rate is calculated from the events reconstructed by the AAFit algorithm. By the fact that only a small band of baseline rates based on the frame time is used, the dependency of the reconstruction algorithm to the number of active OMs and the baseline as shown in section 8.2 can be neglected. The only weights applied to the calculated muon rate is the compensation of the loss of the efficiency of the detector over the time as described in section 7.

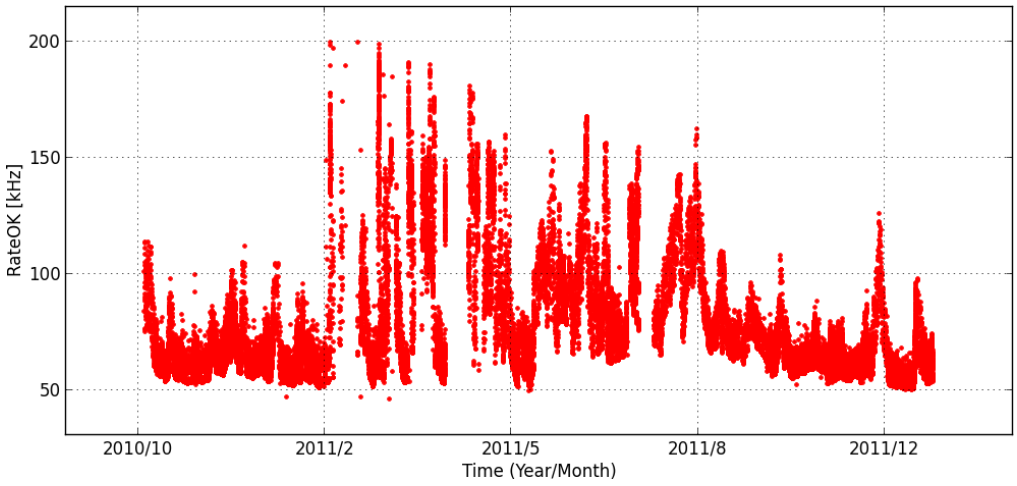

Figure 9.25: *RateOK over time.*

The figure in 9.25 shows the distribution of the mean rate of the OMs which are in status OK (RateOK) over time using the selected runs for the TimeSlice6 (see section 6.2 for the definitions of the TimeSlices). A histogram of the same data would show a maximum for rates of about 60 kHz. It can be seen that a cut for lower rates would not cover all times shown in figure 9.25. August for example would not be selected at

all. Defining the cuts on the RateOK and other parameters must be chosen the way that data points are available over the whole time period shown. Other parameters that are used to define constant detector settings are the RateHigh and the number of OMs which are in status OK/high. Figure 9.26 shows the number of OMs in status OK (CounterOK) over the same time period. It can be seen that a cut on the minimum number of OMs with that status could also lead to a lack of data for weeks or month. Especially at spring time the number of that OMs decreases.

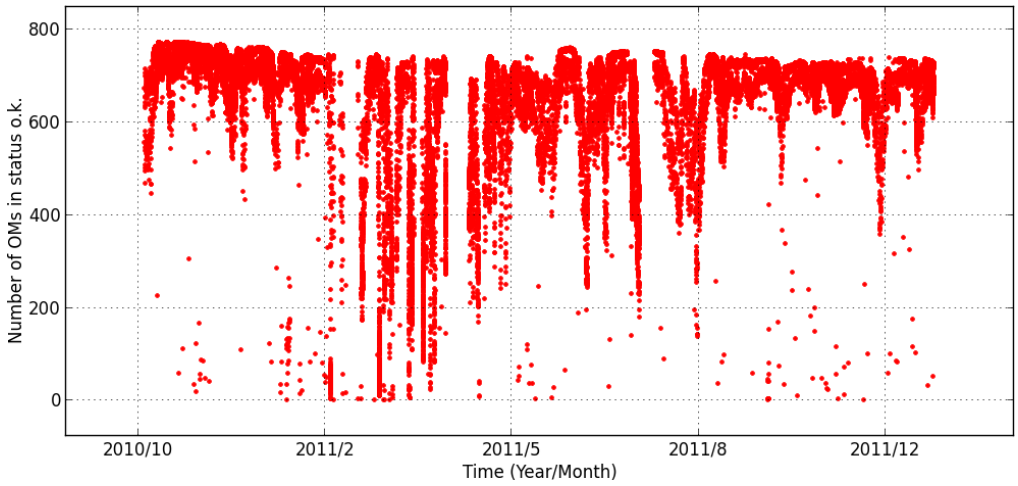

Figure 9.26: *Number of OMs in status OK over time.*

Taking this into account the following cuts were made to test the selection of frames:

- 58 kHz $\leq$ RateOK $\leq$ 65 kHz
- 260 kHz $\leq$ RateHigh $\leq$280 kHz
- 680 $\leq$ CounterOK $\leq$ 700
- Zenith $\leq 60°$
- $\lambda \geq$ -6.6

Each parameter listed above will be calculated and checked once per frame or event (for the cuts on zenith and lambda). A frame survives the cuts if the values of RateOK, RateHigh and CounterOK are all within the specified ranges. The events within one frame are counted only if they fulfill the conditions on the zenith and lambda values specified.

The number of events and the time frames was accumulated over a maximal time period of six days giving the six day average for the muon rate and the effective temperature over the ANTARES detector. The cuts lead to a total amount of 1.9 million events for the whole TimeSlice6. The relative muon rate $\tilde{R}_i = (R_i - \bar{R})/\bar{R}$ and relative effective temperature $\tilde{T}_i$ are shown in figure 9.27. Where R_i is the muon rate calculated

for the ith bin and $\bar{R}$ is the mean of the muon rate over the whole time period shown. $\tilde{T}_i$ is calculated analogically.

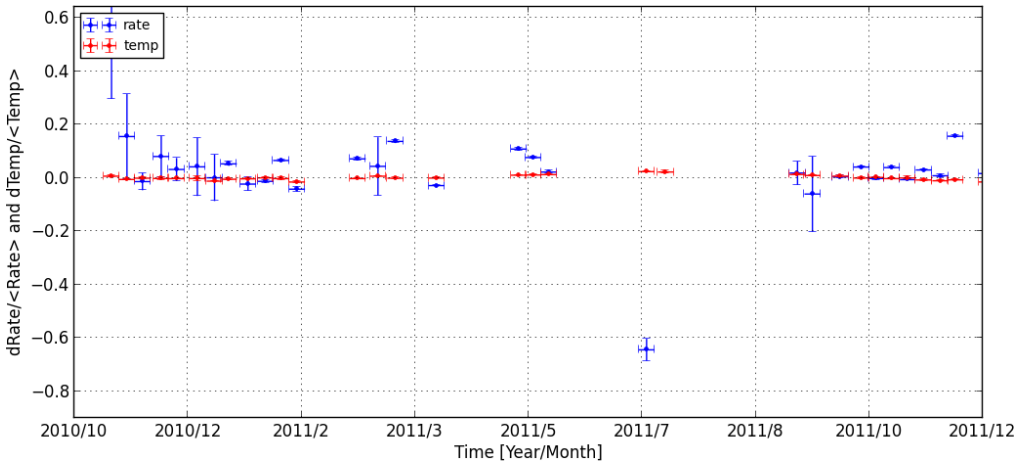

Figure 9.27: *Relative muon rate (blue) and relative effective atmospheric temperature (red) as a six day average over time. The error bars give the statistical error on the data.*

The error bars in y-direction show the statistical error of the data points while the error bars in x-direction show the binning of six days in time. It can be seen that the spreading does not decrease in comparison to the procedure described by the former chapters. The variation of the temperature is hardly to notice because of the variation of the muon rates.

Figure 9.28 shows the muon rate and the temperature like before with the following cuts:

- 55 kHz $\leq$ RateOK $\leq$ 80 kHz
- 260 kHz $\leq$ RateHigh $\leq$280 kHz
- 680 $\leq$ CounterOK $\leq$ 700
- Zenith $\leq$ 60°
- $\lambda \geq$ -6.6

It can be seen that the relative muon rate $\tilde{R}$ changes its sign and the spreading has decreased a little. But the muon rate does still not show a correlation to the effective temperature. That the sign has changed in some cases may come from the new mean muon rate which is calculated with the data used for that plot.

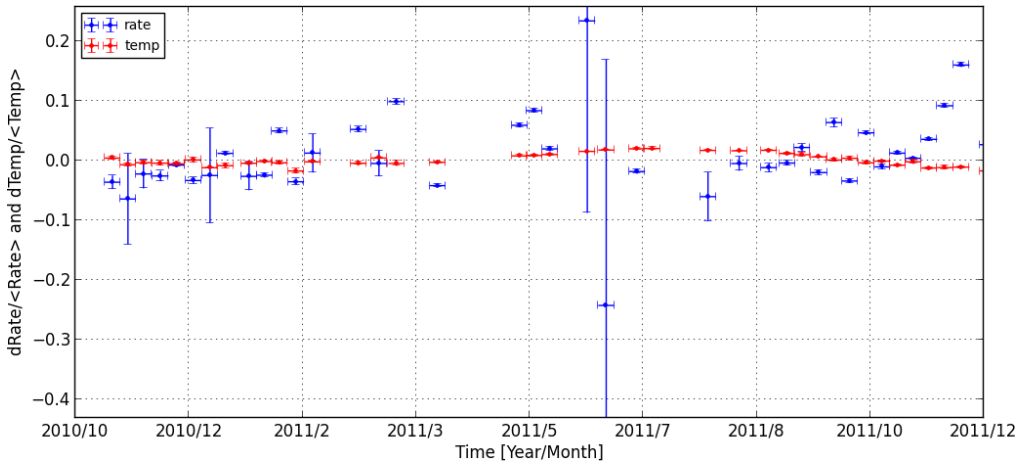

Figure 9.28: *Relative muon rate (blue) and relative effective atmospheric temperature (red) as a six day average over time. The error bars give the statistical error on the data.*

9.6.2 Variation of the muon rate for constant temperature

Figure 9.29 shows the effective temperature over time. It can be seen that there is a plateau for the time period from August 1st 2011 until November 6th 2011 where the variation of the temperature is low. The data points show the effective temperature calculated as described in section 9.1. For each day four datapoints are available. It was tried to search parameters for the RateOK etc. where the variation of the muon rate is of the same order. After some tests the following parameters were found as best:

- 50 kHz $\leq$ RateOK $\leq$ 80 kHz
- 260 kHz $\leq$ RateHigh $\leq$280 kHz
- 680 $\leq$ CounterOK $\leq$ 700
- Zenith $\leq 60°$
- λ-cut $\geq$ -6.6

The relative muon rate for that period as a six day average is shown in figure 9.30. It can be seen that the variation of the effective temperature is around zero while the variation of the relative muon rate keeps high in comparison. The mean of the temperature is calculated by the available data points of that plot. The variation of the relative muon rate (blue points) exceeds the variation of the temperature. Different cuts on the frames were applied to find the most stable condition. A six day average is shown for the temperature and the muon rate. The error bars show the statistical error. For the gabs between the data points no data were available due to the cuts and data selection made.

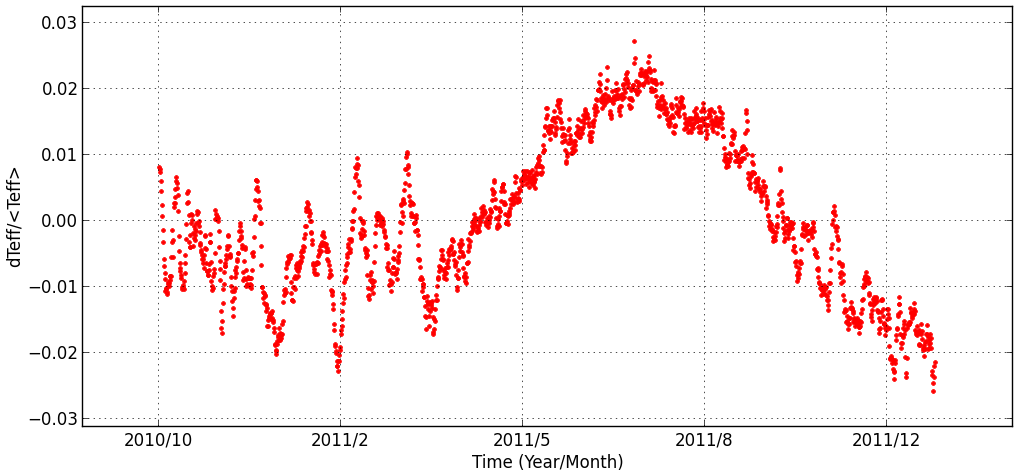

Figure 9.29: *Relative effective temperature over time.*

The fact that the variation of the muon rate is still very high while the mean temperature almost keeps constant shows that the variation with the data used in combination

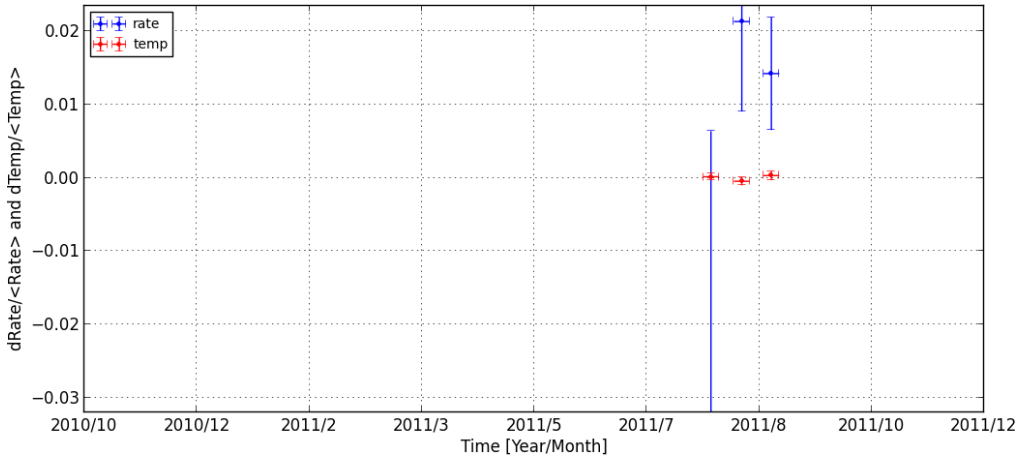

Figure 9.30: *Relative muon rate (blue) and relative effective atmospheric temperature (red) over time*

with the properties of the detector do not allow to see the seasonal anisotropy using the selection of data frames described here.

9.6.3 Event selection by hit rate

The reconstruction algorithm uses a hit selection to identify the detected photons that most probably are created by Cherenkov radiation. Each event that was reconstructed includes the identification number of the used OMs. This information can be combined with the hit rate of each OM in one data frame. With that, it is possible to select events that were reconstructed using OMs with a specific hit rate. Different cuts are thinkable off and are summarized below:

- A minimum number of OMs used for reconstruction.
- A minimum and/or a maximum of the hit rates for the OMs used for reconstruction.
- A percentage or number of OMs that were used for reconstruction that can be out of the former minimum or maximum.
- The mean of the hit rates of all OMs is within specific borders as described in section 9.6.1.

In addition a cut on the quality parameter λ of the AAFit reconstruction method could be changed or completely ignored in the case that the hit rate of the OMs used for reconstruction already has a strict cut.

In figure 9.31 a histogram of the hit rates of the OMs used for reconstruction is shown using the same data as in section 9.6.2. There where no cuts applied to show

that the most hits are within the range of about 50 kHz to 100 kHz. Never the less, a range can be identified to only use events that make use of OMs with a specific range of the hit rate.

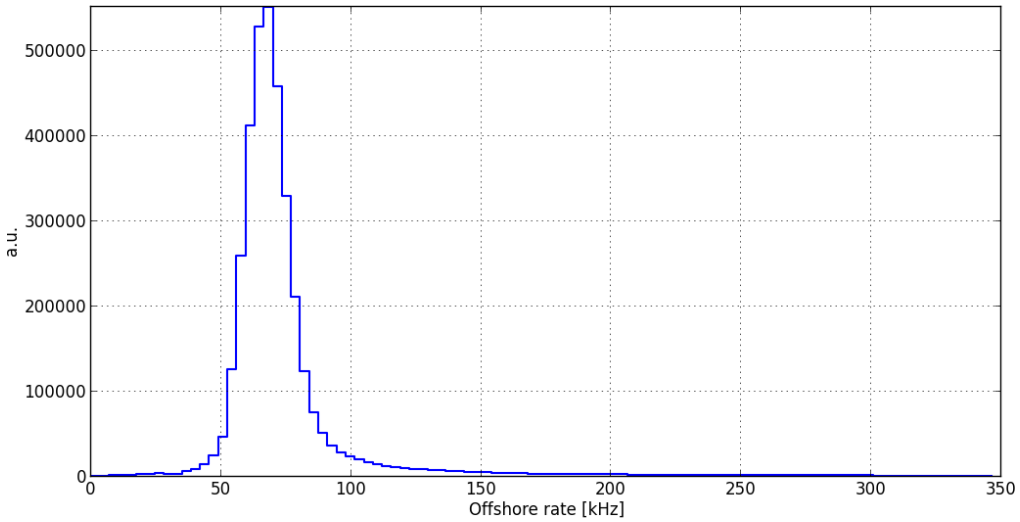

Figure 9.31: *Distribution of the hit rates of the OMs used for reconstruction.*

Different cuts were made to test the effect of the cuts described. The resulting muon rate over time can be seen in figure 9.32. In this case a very strict cut was used on the hit rates of the OMs used for reconstruction. The number of OMs used for the reconstruction had to be greater or equal to eight and the number of OMs with a hit rate out of the range of 55 kHz to 65 kHz is three at a maximum. The error bars in the figure show the statistical error and it can be seen, that only few events have survived this cut by looking at the size of the error bars.

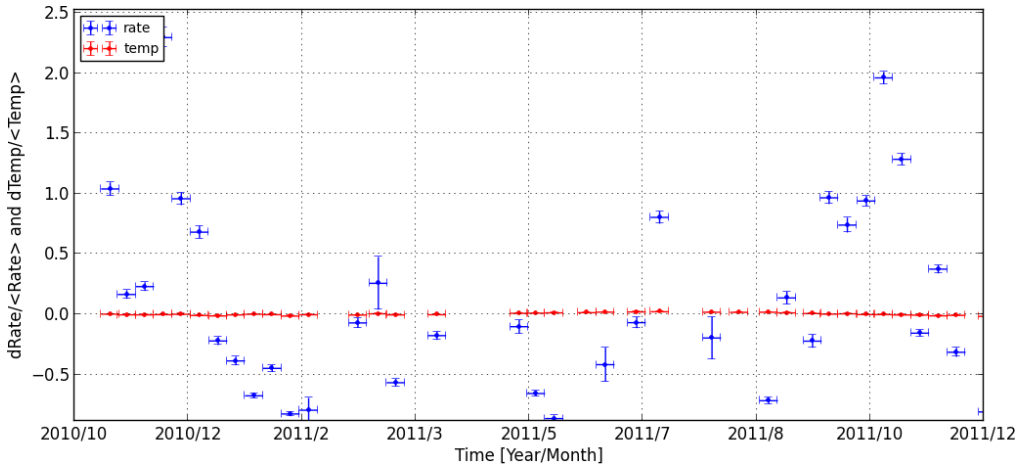

Figure 9.32: *Relative muon rate (blue) and relative effective atmospheric temperature (red) over time.*

The mean muon rate is about 2 mHz over the whole time period shown. This is due to the lack of any cut to the frames used and the strict cut on the events. The

figure 9.33 shows the lifetime of the used data. The data of TimeSlice6 was used in this example. The lack of data taking comes from the run selection and the used trigger (T3).

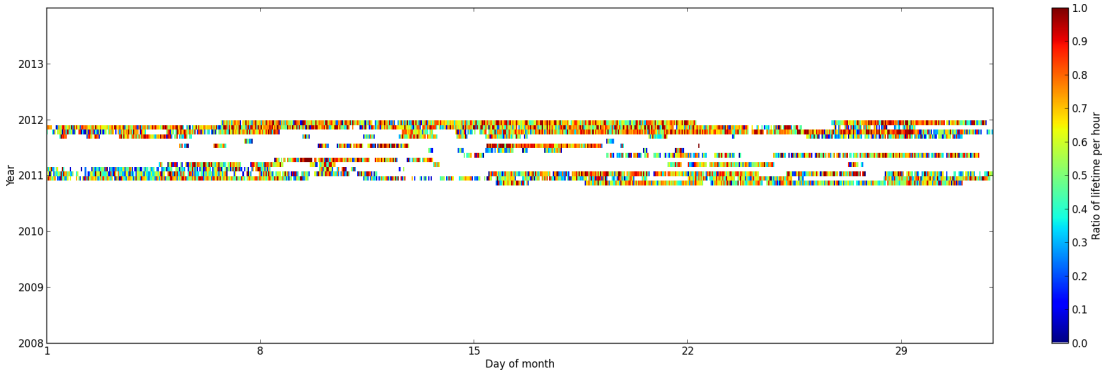

Figure 9.33: *Lifetime of the data used.*

In appendix J some more examples on cuts are shown. It can be seen that a cut on the hit rate of the used OMs for reconstruction does not improve the spreading of the muon rates. Using cuts on the hit rate of the OMs affects the number of events used in the way that the variation increases and it can be seen, that this procedure did not show the desired effect. The stability of the muon rate benefits from larger time intervals as done in former chapters. There, the average over a whole run was used with no cuts on the hits used for reconstruction and frames.

Chapter 10

Summary

The muons of the air shower from interactions of pions and kaons with nuclei of the atmosphere can be used to measure the large scale anisotropy as described in chapter 3.2. The expected signal of the large scale anisotropy is little in comparison to the seasonal variation [4] [9] of the muon rate and the first step was to find this variation of the muon rate following the atmospheric temperature. For both the detector and its properties must be well understood. In this work the variation of the muon rate measured with ANTARES and the influence of different parameters on the muon rate and the reconstruction algorithm were studied.

The setup of the ANTARES detector has changed during time. In chapter 6 these periods of time are identified and the basic selection of the data that was used for this work is explained. Chapter 7 shows how the efficiency of the detector decreases over time and how the weights where calculated to compensate this effect. The two different triggers 3N and 2T3 were used in this work to select the reconstructed events. They are described in chapter 5.4. Their main difference is the number of used hits before the trigger is fired. This leads to the mentioned difference concerning the decreasing efficiency of the detector over time. Only one trigger was used at a time when the muon rate was calculated and with that the corresponding correction for the used trigger.

To be able to calculate the muon rate over time the reconstruction algorithms AAFit and BBFit were used as described in chapter 5. The definition of the quality parameter for the used reconstruction method is important because of its influence on the reliability on the reconstructed tracks. Chapter 8 shows the criteria used to define the quality parameter for the AAFit reconstruction method. Using Monte Carlo the influence of the quality parameter on the reconstruction error and the distributions of events over the zenith angle have been studied. This is one factor that defined the quality cut of the reconstruction algorithm. The selected quality parameter for the BBFit reconstruction algorithm is described in section 9.5.1.

It was shown that the number of active optical modules and the baseline also have an influence on the reconstructed events and the stability in data taking. It was shown

that for both reconstruction methods a higher baseline results in lower muon rates. Chapter 8.2 shows that different run setups also have different characteristics concerning the variation of the muon rate with dependence on the baseline and the number of active OMs. Weights are introduced to compensate the influence of the different characteristics and circumstances during data taking and their effect on the stability of the muon rate is shown.

After the definition of the quality parameters and the weights depending on the decreasing efficiency of the detector the baseline and the number of active OMs the muon rate over the time was calculated. Only one trigger was used at a time to have stable conditions. The results are presented in chapter 9.2. For comparison another trigger was used. The variations of the muon rate show different characteristics concerning the baseline and the active OMs. The weights introduced earlier were again calculated and applied for the events found with that trigger which can be seen in chapter 9.3. The second reconstruction algorithm BBFit was used to analyze the same data and all steps were repeated again including the definition of the quality parameter. The results can be seen in chapter 9.5.

The run-by-run (rbr) Monte Carlo includes the simulation of the availability of the optical modules and the intensity of the optical background is simulated according to the data. The rbr-files are organized the same way as the data that makes it possible to compare single data files with Monte Carlo. The effect of the seasonal anisotropy is not included in the Monte Carlo. In chapter 9.4 it was tested if this effect can be seen by dividing the muon rate calculated from data by the muon rate of the rbr Monte Carlo. For that the characteristics of the reconstruction algorithm depending on different parameters were studied.

For all cases it was shown that the variation of the muon rate is not following the atmospheric temperature. In summary two different reconstruction methods and two different triggers were used. Their dependency on the baseline and the number of active OMs were considered. The data was divided into several parts with respect to the number of available lines and therefore to the different efficiency of the detector. The weights concerning the baseline and the number of active OMs were calculated separately for each run setup which have shown that they also have an influence on the muon rate. Using only one specific set of triggers (run setup) did neither show any dependency of the muon rate to the atmospheric temperature as it is shown in chapter 9.

To find intervals with equal characteristics of the detector and the same properties of the optical background, the smallest time scales available for the data taken with ANTARES (time frames of $\approx$ 104 ms) was used in chapter 9.6. Cuts on the mean of the hit rates for the OMs of each time frame were made to keep the detector in a defined status. The muon rate was calculated based on the accumulated time of the

frames and the number of reconstructed events during that time.

The information of the hit rates of the OMs was used to select events that were reconstructed using OMs with a defined status (see chapter 9.6.3). Again, the muon rate did not show a dependency to the atmospheric temperature.

As described in chapter 9.6.2 a period of time where the atmospheric temperature was nearly constant was used to search for cuts that would reduce the variation of the muon rate in the same time period.

The fact that the seasonal anisotropy could not be seen shows that the search for the large scale anisotropy could not be performed. Here a high stability in the muon rate is required and the efficiency of the detector must be well known.

It was shown that the efficiency of the detector in combination with the characteristics of the used reconstruction methods is varying too much even on short time scales. Using the mean over several days did neither show the desired effect of the seasonal anisotropy. The combination of circumstances of the optical background and the dependency of the efficiency of the detector on the used run setup, trigger and the reconstruction method could not be compensated by the methods presented in this work.

Chapter 11

Results and conclusion

In this work the variation of the muon rate of the ANTARES detector and the influence of different characteristics were studied. The characteristics include the optical background, different reconstruction methods and the efficiency of the detector, which changes during data taking. A more detailed description concerning the used methods can be found in chapter 10.

Different experiments already have shown the seasonal variation of the muon rate [8] [9] [10]. In this work it was tried to detect the signal of the seasonal variation of the muon rate with the ANTARES detector. The muon rate was calculated by different approaches.

The first attempt is based on data files (runs) where each run has different characteristics that have been considered. The runs have a maximal duration and a maximum of events per file which is described in detail in chapter 6.3. The optical background can change during one run which results in lower or higher rates of the optical modules. So called bursts exist where some optical modules or even a whole area of the detector has much higher rates than others. The data used for the first attempt have averaged the values that represent the optical background. It is possible that the timescale of one run is too large to define constant circumstances of the detector comparing one run to another.

The second attempt compared the data to Monte Carlo (run-by-run). It was shown that the simulation used by ANTARES doesn't fit to the data sufficiently enough in the way that the variation could have been seen. For the Monte Carlo the optical background is simulated by randomly distributed hits throughout the detector. The actual optical background measured by the detector could be more complex than simulated due to various sources. This could be different bacteria and higher life forms as well as different sea currents for different layers of the detector which is not considered in the simulation.

The next step used the smallest time scale available for the data of ANTARES

to search for constant properties in data taking. To select the time frames the rate of the optical modules was considered. For each time frame the average rate of the optical modules in a specific state was calculated. In addition the number of the optical modules that are in a specific state was considered. Based on the time of one frame the status of the detector could be determined within a time slice of about 104 ms. Using this selection the muon rate neither showed a correlation to the atmospheric temperature.

The rates of the optical modules used by the reconstruction algorithm were then checked to be within a specific range concerning their hit rates. This was done to ensure that only events with a defined characteristic concerning the optical background were used. This did neither show a correlation of the muon rate to the atmospheric temperature because of the spreading of the muon rate.

It was shown that the efficiency of the reconstruction algorithms also depends on the optical background. It was tried to compensate this behavior in the first steps. The introduced weights for that purpose could not withdraw this dependency completely. The following steps used a more restricted selection of the data where this fact should not have an influence. The spreading of the muon rate calculated as the average of some hours to some days did not decrease. The reason for that could be circumstances concerning the combination of the different systems used like the properties of the electronics, triggers and reconstruction algorithm. The optical background doesn't seem to be understood in the way in that the simulation covers the data. The reconstruction algorithms were tested with this simulated optical background. Here the behavior of the same algorithm could change when used with the optical background in the deep sea. The reconstruction algorithms also depend on the optical background in the way that the detection efficiency changes. The electronics and the optical modules could react to the changing and high optical background in a way where the efficiency of the detector was affected. Furthermore, the used run setup has an influence on the efficiency which could also be connected to the optical background.

The combination of that properties seem to prevent the required stability of the efficiency of the detector to measure the seasonal or large scale anisotropy. The new Monte Carlo simulation V3 may give better results on data to Monte Carlo comparison and may therefore better fit the circumstances of data taking. This also could help investigating the properties of the reconstruction algorithms concerning different circumstances of data taking.

Kapitel 12

Zusammenfassung

Myonen der Luftschauer, die aus der Wechselwirkung von Pionen und Kaonen mit Nukleonen der Atmosphäre entstehen, können zur Messung der großräumigen Anisotropie verwendet werden, wie in Kapitel 3.2 beschrieben. Dieser Effekt ist klein im Vergleich zur saisonalen Anisotropie. Daher war der erste Schritt die Änderung der Myonrate in Abhängigkeit zur atmosphärischen Tempereratur nachzuweisen. In beiden Fällen müssen der Detektor und seine Eigenschaften gut verstanden sein. In dieser Arbeit wurden die Variationen der Myonrate, gemessen mit dem ANTARES Neutrino Teleskop und der Einfluss verschiedener Parameter auf dieser und der verwendeten Rekonstruktionsalgorithmen untersucht.

Im Laufe der Zeit wurden immer wieder Lines des ANTARES-Detektors für Wartungsarbeiten und Reperaturen aus dem Verbund gelöst und zu einem späteren Zeitpunkt wieder versenkt. Im Kapitel 6 werden diese Perioden identifiziert und die grundlegende Strategie zur Auswahl der Daten, die in dieser Arbeit verwendet wurden, wird erläutert. Kapitel 7 zeigt die Abnahme der Effizienz des Detektors über die Zeit und auf welche Weise dieser Effekt berücksichtigt wurde. Dieser Effekt ist vom verwendeten Trigger abhängig. Die ausgewählten Myonereignisse wurden mit Hilfe von zwei verschiedenen Triggern identifiziert und einzeln behandelt. Alle Korrekturen wurden ebenfalls in Abhängigkeit der verwendeten Trigger separat berechnet.

Die Myonrate wurde mit Hilfe von zwei verschiedenen Rekonstruktionsalgorythmen bestimmt. Eine Beschreibung der Algorithmen befindet sich in Kapitel 5. Ein rekonstruiertes Ereignis wird mit einem Qualitätsparameter angegeben. In Kapitel 8 sind die Verfahren am Beispiel von AAFit erläutert, die zur Definition der Qualitätsparameter führten. Mit der Hilfe von Monte Carlo-Simulationen wurde der Rekonstruktionsfehler und der Einfluss des Parameters auf die Verteilung der Ereignisse im Zenithwinkel untersucht.

Desweiteren haben die Anzahl der aktiven optischen Module und die Rate des Untergrunds ebenfalls einen Einfluss auf die Anzahl der Events und die Stabilität der Datennahme. Es wurde gezeigt, dass die Myonrate für beide Rekonstruktionsalgory-

thmen mit zunehmender Untergrundrate sinkt. Im Kapitel 8.2 wird gezeigt, dass unterschiedliche Konfigurationen (run setups) des Detektors die Myonrate verschieden beeinflussen, dies unter Berücksichtigung der Untergrundrate und der Anzahl der aktiven optischen Module. Basierend auf dieser Tatsache wurden Gewichte eingeführt, die diese Charakteristik kompensieren sollen. Der Effekt der Gewichte auf die Stabilität der Datennahme wird anschließend dargestellt.

Nachdem die Qualitätsparamter definiert und die oben beschriebenen Gewichte berechnet waren, wurde die Myonrate in Abhängigkeit der Zeit bestimmt. Die Ergebnisse sind im Kapitel 9.2 dargestellt. Die beiden verwendeten Trigger wurden separat betrachtet, die Ergebnisse sind im darauffolgenden Kapitel zu sehen. Kapitel 9.5 wiederholt die Schritte zur Bestimmung der Gewicht unter Verwendung des zweiten Rekonstruktionsalgorythmus.

Die Monte Carlo-Simulationen von ANTARES wurden unter Berücksichtigung der Anzahl der optischen Module und der Untergrundrate für jede Datendatei erstellt. Auf diese Weise ist es möglich, einzelne Datendateien mit den simulierten Daten zu vergleichen. Da die Simulation kein Signal der saisonalen Anisotropie enthält, ergibt sich die Möglichkeit, dass ein Vergleich zwischen Daten und Simulation die saisonale Variation der Myonrate beobachten lässt. Mit diesem Ansatz beschäftigt sich das Kapitel 9.4, in dem der Einfluss verschiedener Parameter auf die Eigenschaften des Rekonstruktionsalgorythmus untersucht wurden.

In allen oben beschriebenen Variationen konnte aufgrund der Streuung der Myonraten keine Korrelation zwischen dieser und der atmosphärischen Temperatur gesehen werden. Es wurden insgesamt zwei verschiedene Rekonstruktionsalgorythmen und zwei verschiedene Trigger verwendet. In den verschiednene Kombinationen wurde die Abhängigkeit der Myonrate von der Anzahl der aktiven optischen Module und der Untergrundrate berücksichtigt, welche zu diesem Zweck getrennt berechnet wurden. Da gezeigt wird, dass auch die Auswahl der Detektorkonfiguration (run setup) einen Einfluss auf die Myonrate hat, wurde nur eine Konfiguration zur Auswertung heran gezogen, wie in Kapitel 9 dargestellt.

Um die Intervalle mit gleichen Eigenschaften des Detektors und des optischen Untergrunds zu identifizieren, wurde anschließend die kleinste Zeiteinheit (≈ 104 ms) der aufgezeichneten Daten verwendet. In Kapitel 9.6 werden die Auswahl und Definition der Schnitte beschrieben, die die Hit-Raten der einzelnen optischen Module in diesen Zeiteinheiten berücksichtigen, um Zeitintervalle zu indentifizieren, in denen der Detektor gleichen Untergrundraten ausgesetzt war.

Die Information der Hit-Raten einzelner optischen Module wurde anschließend verwendet, um rekonstruierte Ereignisse zu indentifizieren, die unter gleichen Umständen auftraten. Auch hierbei konnte die Schwankung der Myonrate nicht der Schwankung der atmosphärischen Temperatur zugeordnet werden. Das Verfahren und die Ergebnisse

sind in Kapitel 9.6.3 zu sehen.

In Kapitel 9.6.2 wurde ein Zeitintervall verwendet, in dem die atmosphärische Temperatur sehr geringen Schwankungen unterlag. Dieses Zeitintervall wurde verwendet, um nach Parametern der Schnitte auf die Hit-Raten zu suchen, sodass auch die Myonrate im selben Zeitintervall eine ähnlich kleine Schwankung aufweist.

Aufgrund der Tatsache, dass der Effekt der saisonalen Anisotropie nicht nachgewiesen werden konnte, wurde die Suche nach der großräumigen Anisotropie nicht durchgeführt. Für letztere Untersuchung ist es aufgrund der geringen Amplitude des Signals notwendig, eine hohe Stabilität der Myonrate und damit die Effizienz des Detektors genau bestimmen zu können.

Es wurde gezeigt, dass die Effizienz des Detektors in Kombination mit den Eigenschaften der verwendeten Rekonstruktionsalgorythmen selbst auf kleinen Zeitskalen stark schwankt. Der Effekt der saisonalen Anisotropie konnte auch dann nicht nachgewiesen werden, wenn das Mittel der Myonraten über mehrere Tage gebildet wurde. Die Kombination verschiedener Zustände des optischen Untergrunds mit der Abhängigkeit der Effizienz des Detektors von den verwendeten Konfigurationen und Triggern sowie den Rekonstruktionsalgorythmen, konnten mit den Methoden, die in dieser Arbeit vorgestellt wurden, nicht ausgeglichen werden.

Appendix A

Coordinate systems

ANTARES is able to determine the direction of the muons traversing the detector above the critical energy were they emit Cherenkov light. The direction of the primary particle is preserved by about 1° [46] with respect to the direction of the muon. The direction of the muons is taken into account in this work and this section gives an overview on the coordinate systems used.

A.1 Local coordinate system

The local coordinate system or horizontal coordinate system is defined by the observer on Earth, see figure A.1. The directions north, south, east and west lie in the horizontal plane. A direction $\vec{d}$ from where the particle comes from is described by the altitude h and azimuth ϕ. The altitude represents the angular distance between $\vec{d}$ and the horizontal plane. ϕ is the angle between the projection of $\vec{d}$ on the horizontal plane and the north vector measured eastwards. In this work the altitude h is described by the zenith angle θ that is defined as $\theta = 90° - h$. That means, if a particle comes from right above the observer with direction to the observer the zenith angle is zero.

A.2 Equatorial coordinate system

Because of the rotation of the Earth the positions of celestial objects in the local coordinate system can change their direction in azimuth and zenith over time. Another observer located at a different point on Earth has its own horizontal coordinate system and the same object would appear under different coordinates in that system. To describe such an object it is worthwhile to use the equatorial coordinate system shown in figure A.2 which is a spherical system based on the Earth's axis of rotation. Here the plane of the coordinate system is the equatorial plane of the Earth. A direction $\vec{d}$ is then described by the coordinates declination δ and right ascension α. The declination is

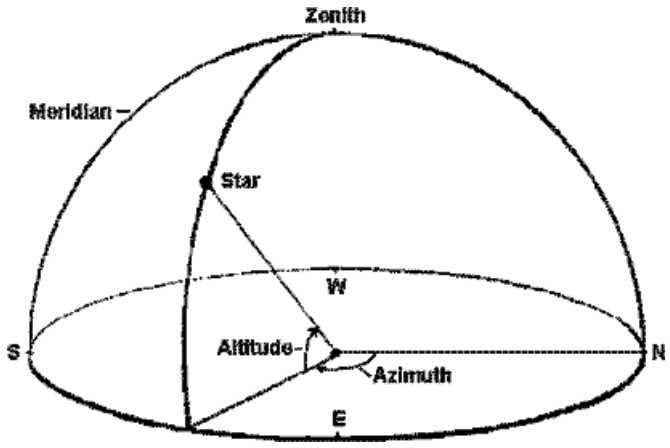

Figure A.1: *Illustration of the local coordinate system. The observer is located in the middle of the plane. The star appears under the direction* $\vec{d}$. [47]

.

the angle between $\vec{d}$ and the equatorial plane. The right ascension is the angle between the projection of $\vec{d}$ on the equatorial plane and some reference point γ. The reference point is usually the position if the Sun at a defined time like the spring equinox. To

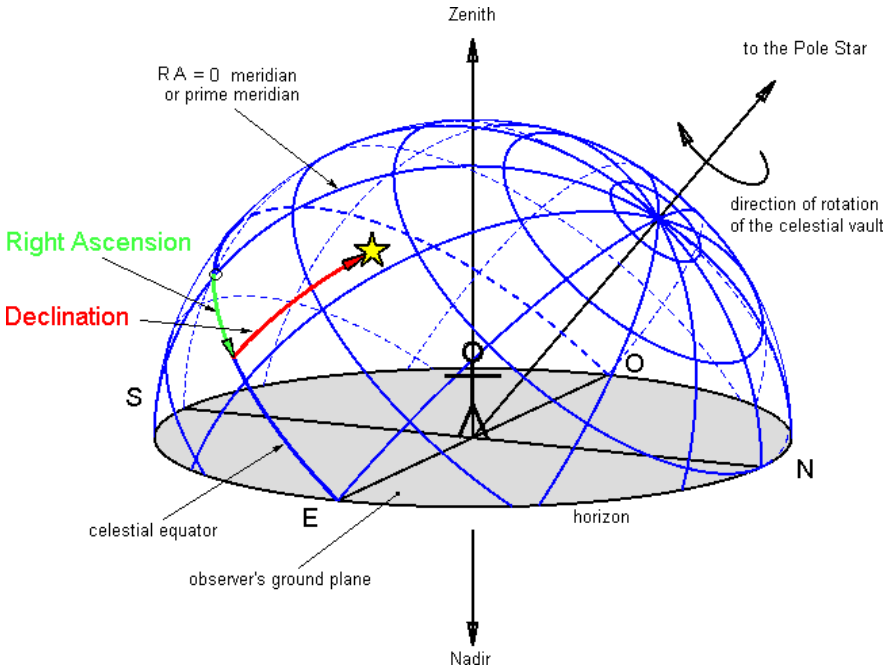

Figure A.2: *Illustration of the equatorial coordinate system. The star appears under the direction* $\vec{d}$ *that is transformed to declination* δ *and right ascension* α. *[47]*

.

transform horizontal coordinates $[\theta, \phi]$ into equatorial coordinates $[\delta, \alpha]$ the first step is to rotate the horizontal system into the local equatorial system. This is also based on the axis of the rotation of the Earth but is fixed with respect to the horizon. The hour

angle (h.a.) is given by the angle of the projection on the equatorial plane between $\vec{d}$ and the south direction, see equation A.2. The declination is shown in equation A.1:

$$\delta = \arccos\Big(\cos(\lambda)\sin(\theta)\cos(\phi) + \sin(\lambda)\cos(\theta)\Big) \tag{A.1}$$

$$h.a. = \arg\Big[-\sin(\lambda)\sin(\theta)\cos(\phi) + \cos(\lambda)\cos(\theta), -\sin(\theta)\sin(\phi)\Big] \tag{A.2}$$

with λ as the geographical latitude of the observer's location. Now the local equatorial system has to be transformed into the equatorial system. This is done by a parity transformation with respect to the vertical north-south plane and a rotation around the axis of the Earth of an angle corresponding to the local sidereal time t_s. The declination keeps the same in both coordinate systems. The right ascension is then calculated by:

$$\alpha = t_s - h.a., \tag{A.3}$$

The brackets mean modulo 2π with respect to the rotation of the Earth and the sidereal time t_s measuring the phase of the rotation of the Earth with respect to the equatorial system. The period of the rotation is a sidereal day, which is $86.164{,}091s$ and therefore less than a solar day (calender day) with the sun as the fixed point.

For completion the galactic coordinate system is mentioned. Here the Sun is the center, the reference point is the center of the Milky Way and the galactic plane is used. The coordinates are expressed in galactic latitude and galactic longitude. Find more information in [48]

Appendix B

Number of runs vs. cut on run duration

The plots in figures 6.11 and 6.10 show combined data for different time periods. Some information is lost because of their common y-axis. Some time periods where not shown in the figure 6.11 at all to avoid too much overlapping dots. Single plots for all time periods are shown here.

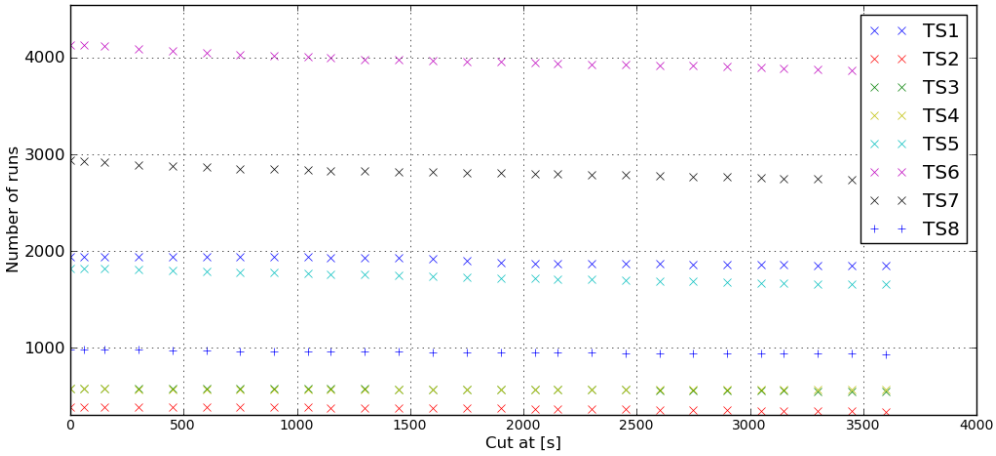

Figure B.1: *The combined plot for the number of runs versus the applied cut on the duration of the runs. This is the same as in 6.10*

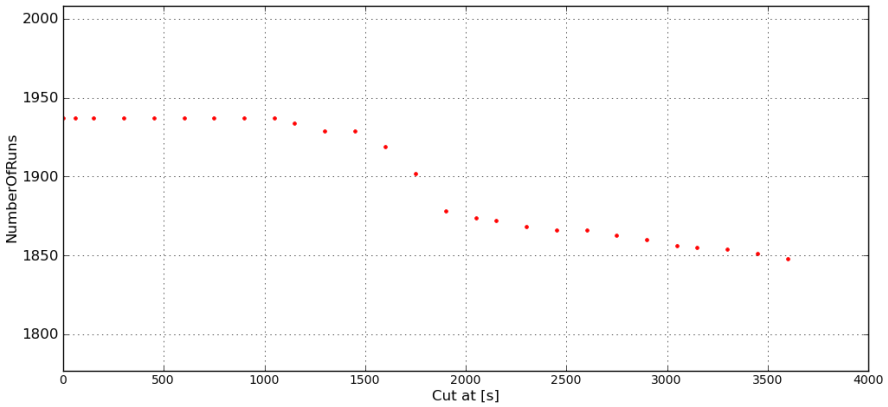

Figure B.2: Detailed view of the cut on duration for TimeSlice1.

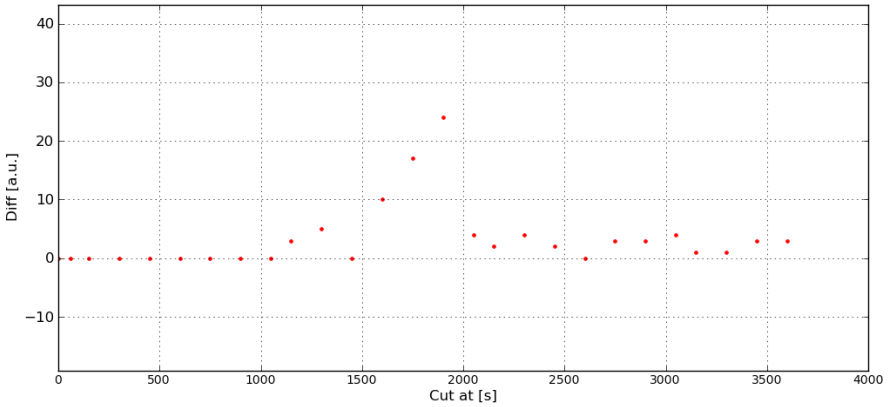

Figure B.3: Detaialed view of the loose of the number of runs versus the cut on duration. Here for TimeSlice1

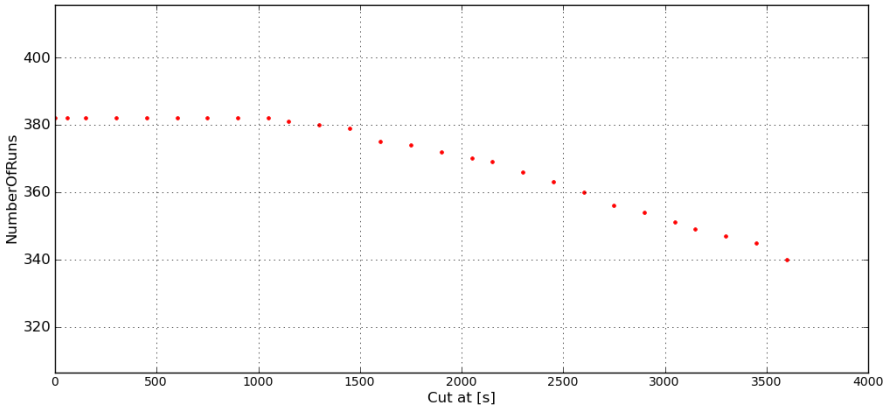

Figure B.4: Detailed view of the cut on duration for TimeSlice2.

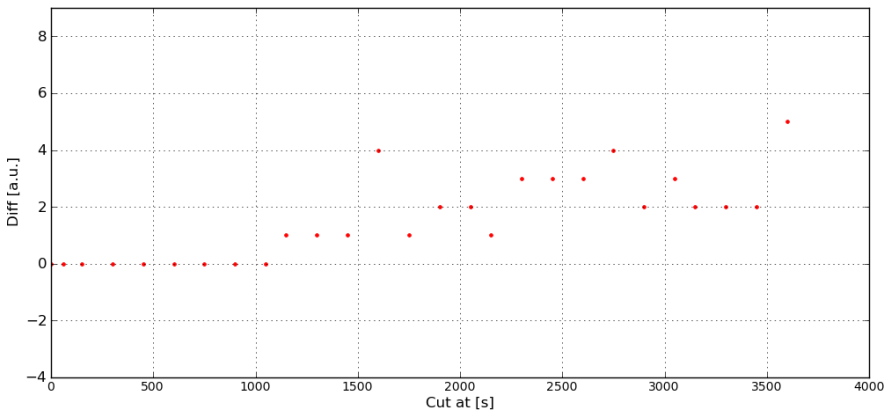

Figure B.5: Detaialed view of the loose of the number of runs versus the cut on duration. Here for TimeSlice2

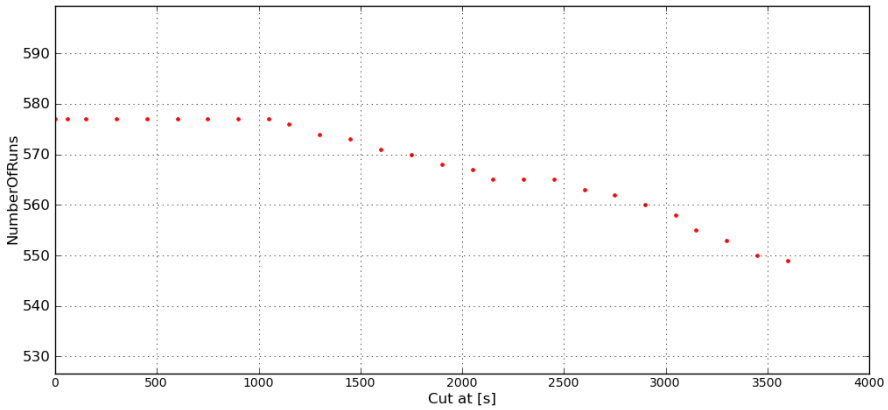

Figure B.6: Detailed view of the cut on duration for TimeSlice3.

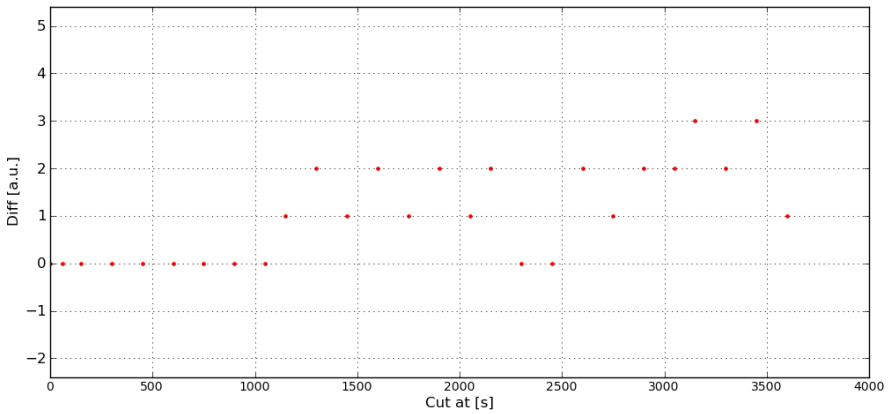

Figure B.7: Detaialed view of the loose of the number of runs versus the cut on duration. Here for TimeSlice3

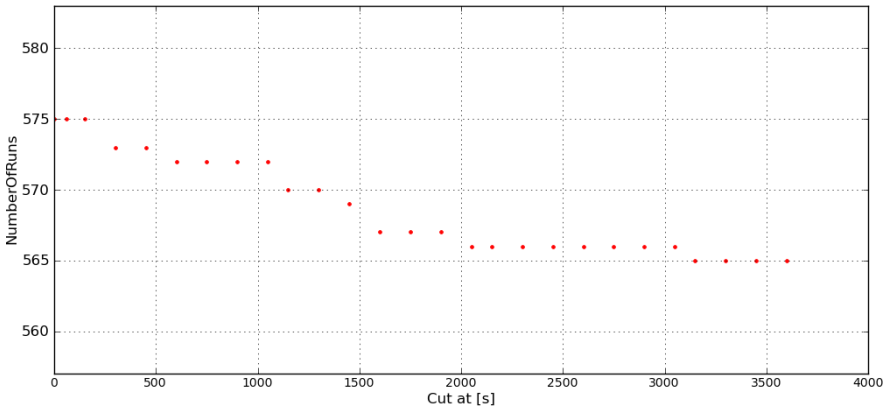

Figure B.8: Detailed view of the cut on duration for TimeSlice4.

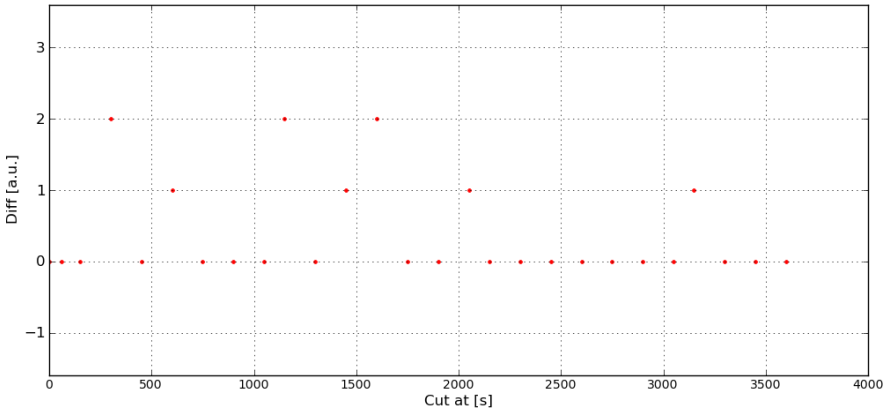

Figure B.9: Detaialed view of the loose of the number of runs versus the cut on duration. Here for TimeSlice4

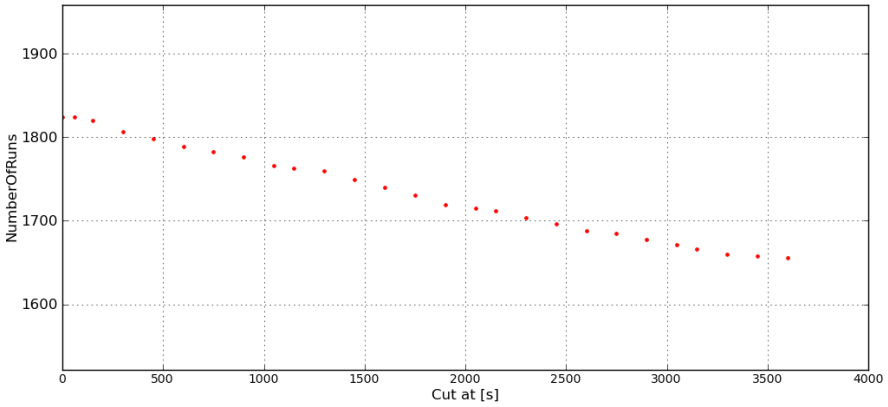

Figure B.10: Detailed view of the cut on duration for TimeSlice5.

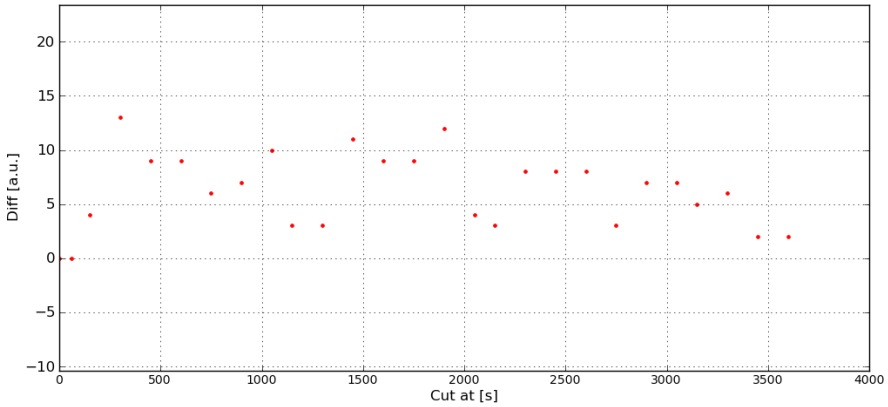

Figure B.11: Detaialed view of the loose of the number of runs versus the cut on duration. Here for TimeSlice5

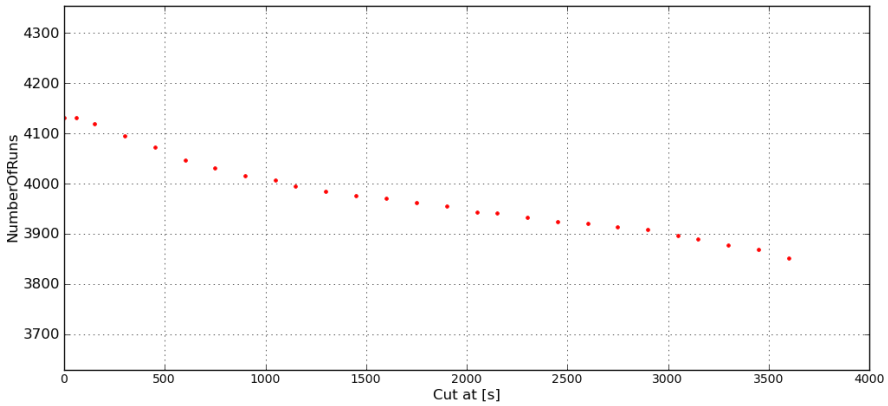

Figure B.12: Detailed view of the cut on duration for TimeSlice6.

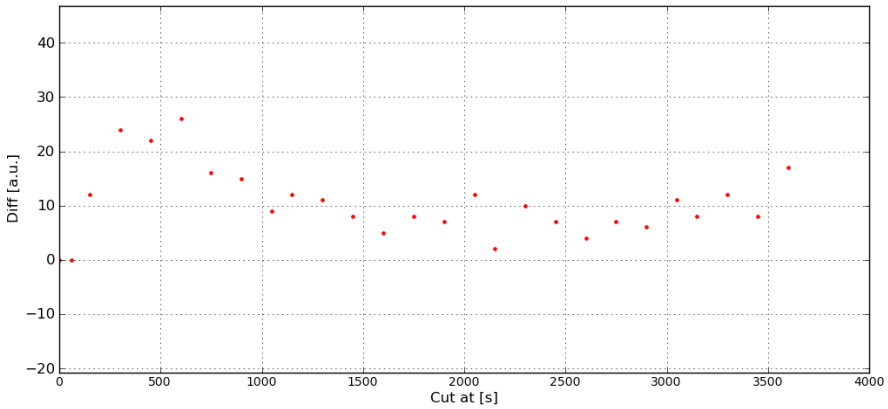

Figure B.13: Detaialed view of the loose of the number of runs versus the cut on duration. Here for TimeSlice6

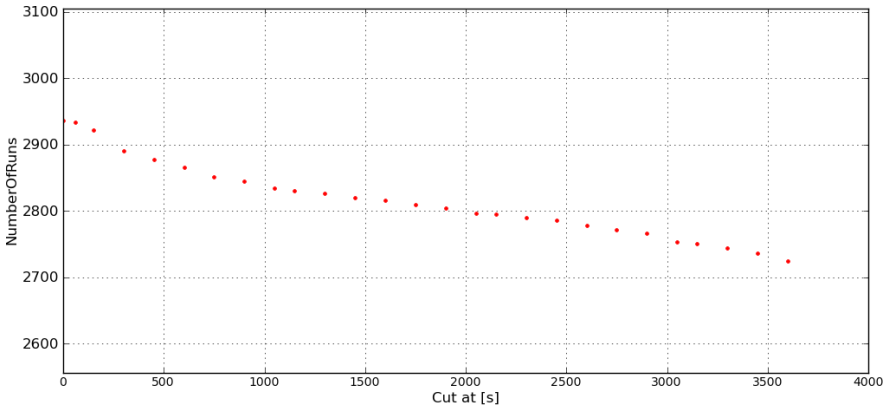

Figure B.14: Detailed view of the cut on duration for TimeSlice7.

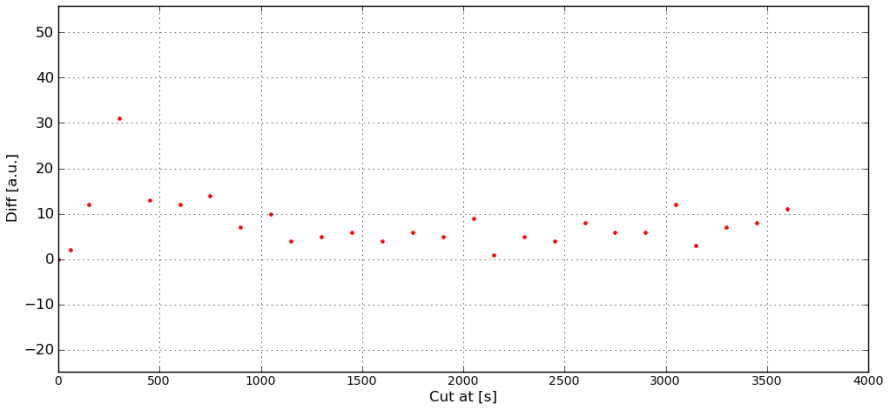

Figure B.15: Detaialed view of the loose of the number of runs versus the cut on duration. Here for TimeSlice7

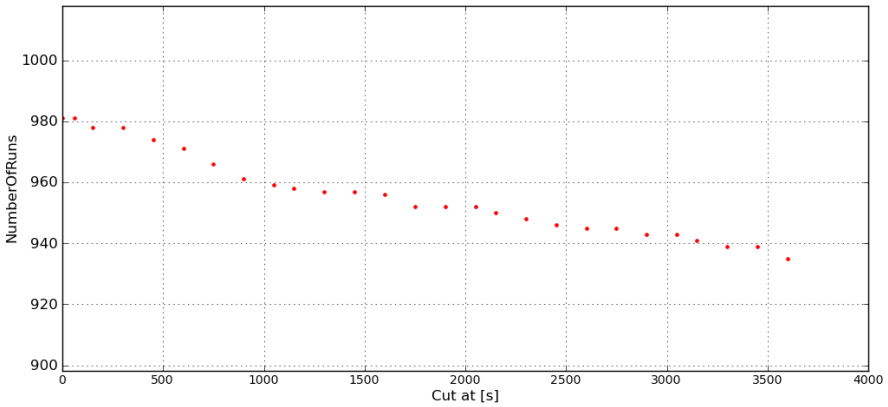

Figure B.16: Detailed view of the cut on duration for TimeSlice8.

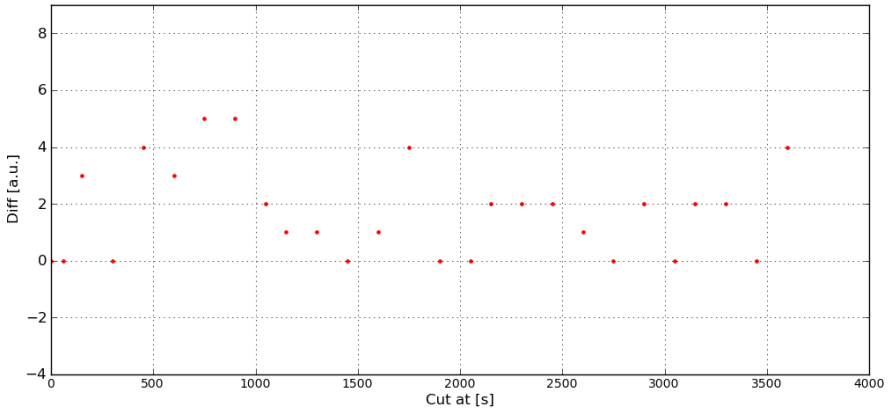

Figure B.17: Detaialed view of the loose of the number of runs versus the cut on duration. Here for TimeSlice8

Appendix C

Muon rate versus baseline and number of active OM

These are plots showing the muon rate for reconstructed muons with zenith $< 60°$. The TimeSlices are analysed seperately. The influence of the λ-cut is shown here for three different cuts (-6.1, -6.6, -7.1). The plots show the data of all runs in one TimeSlice (no separation on run setup name) with the muon rate for one run over the baseline and the number of active optical modules. It can be seen that the spreading is increasing with lower cut on lambda. For detailed describtion see chapter 8.2.

Muon rate for TimeSlice 1, with λ-cut -6.1

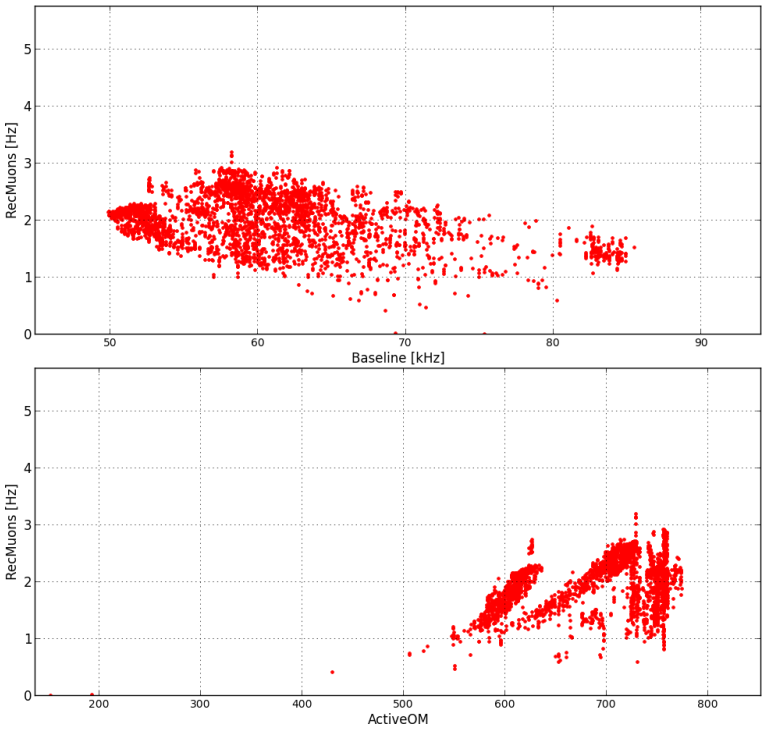

Muon rate for TimeSlice 1, with λ-cut -6.6

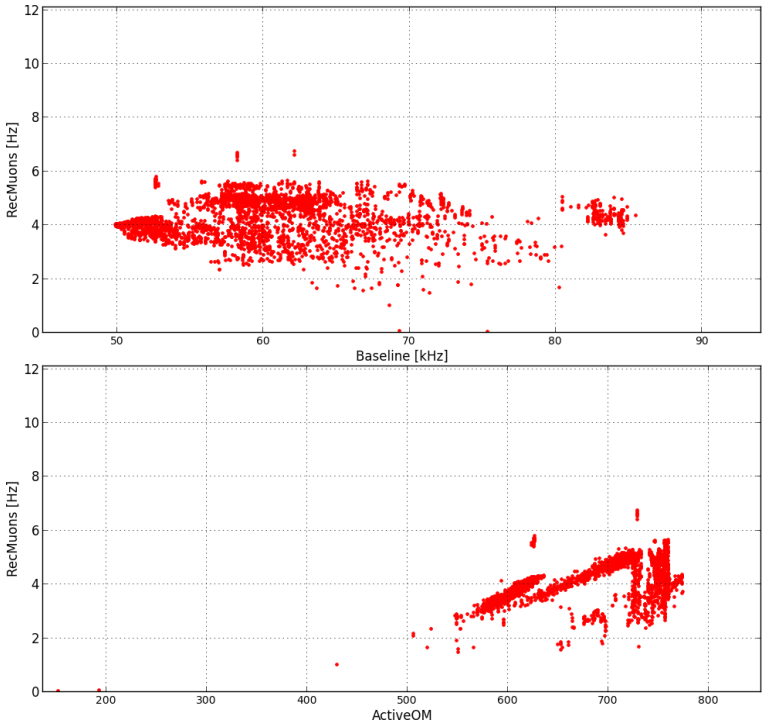

Muon rate for TimeSlice 1, with λ-cut -7.1

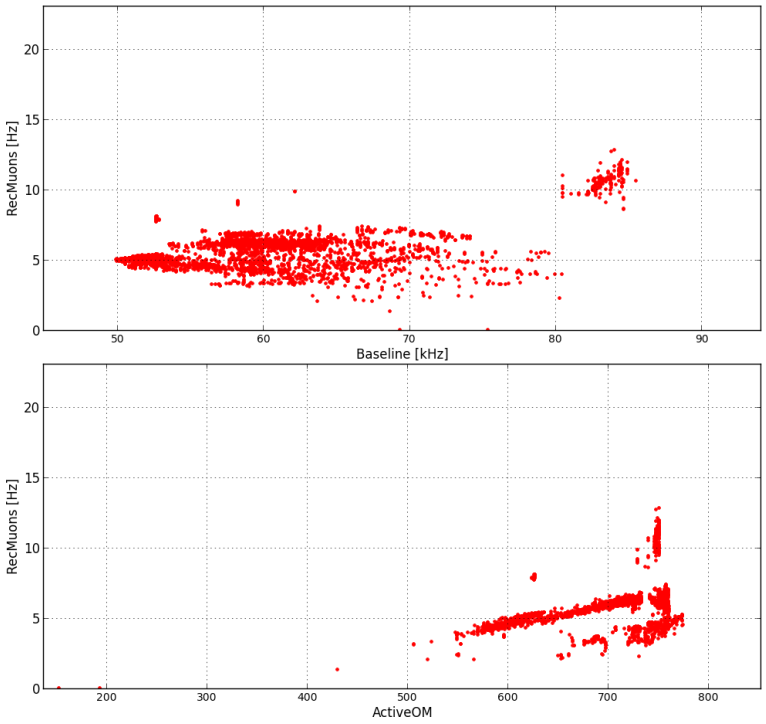

Muon rate for TimeSlice 2, with λ-cut -6.1

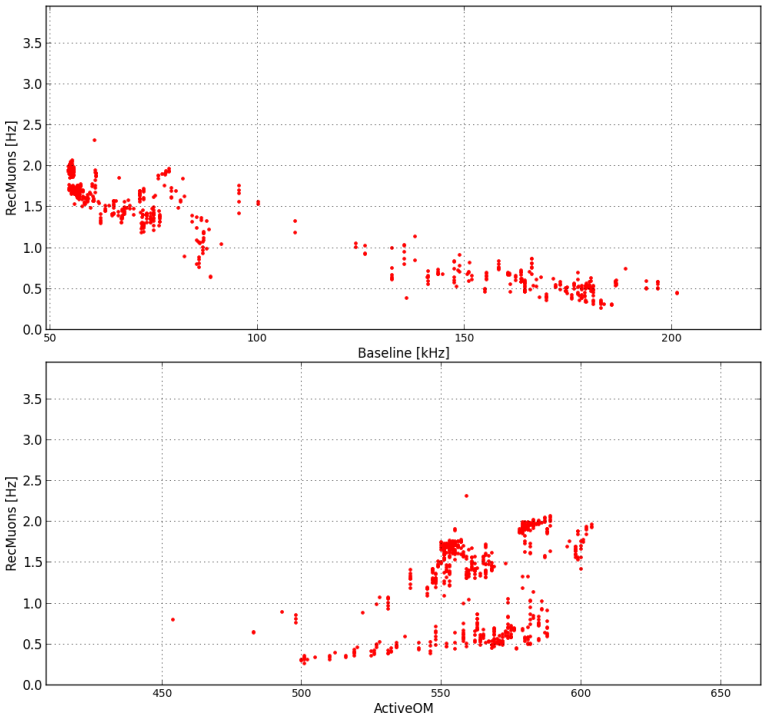

Muon rate for TimeSlice 2, with λ-cut -6.6

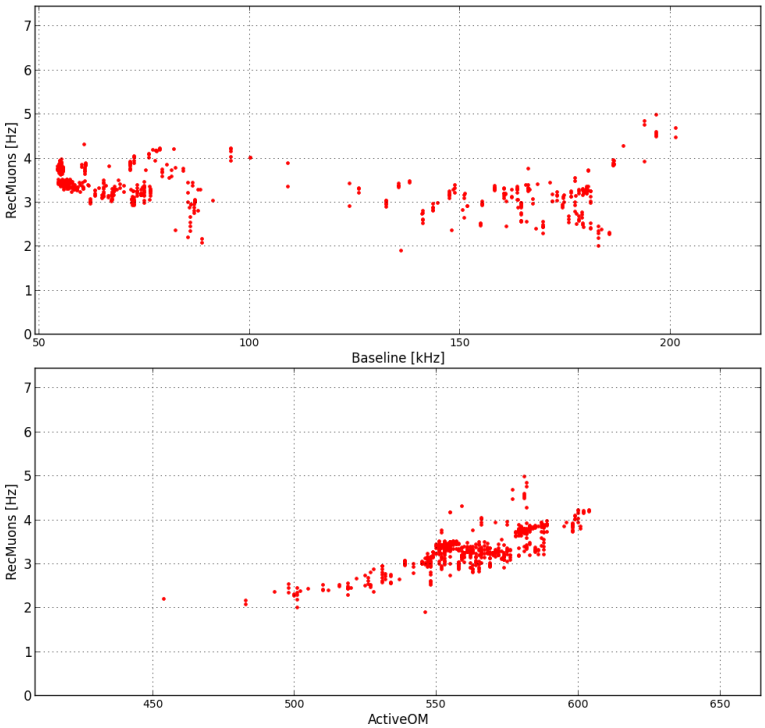

Muon rate for TimeSlice 2, with λ-cut -7.1

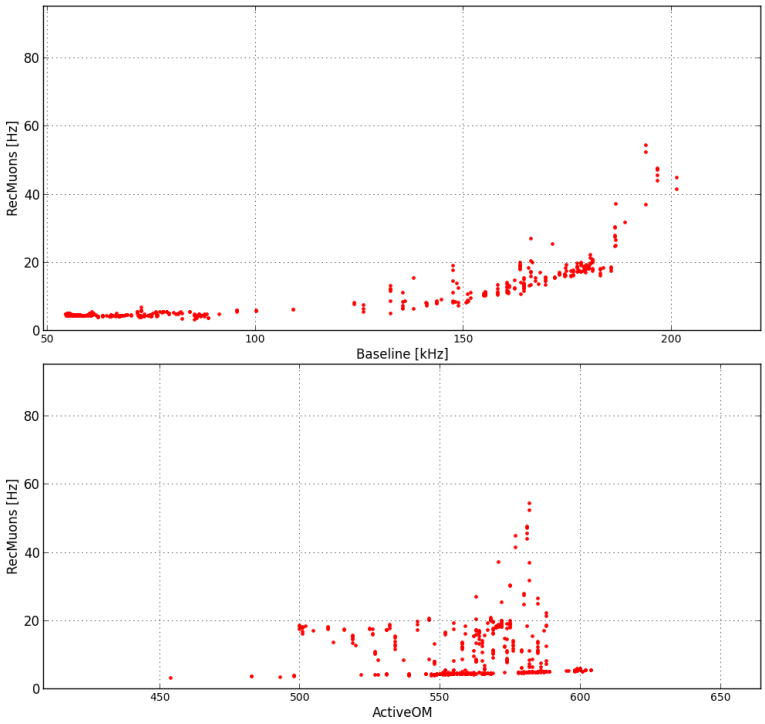

Muon rate for TimeSlice 3, with λ-cut -6.1

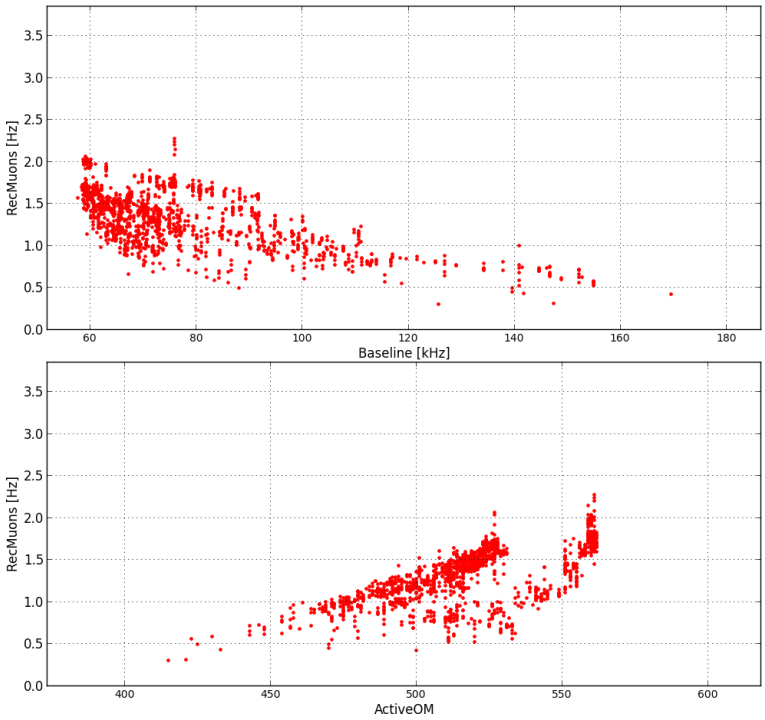

Muon rate for TimeSlice 3, with λ-cut -6.6

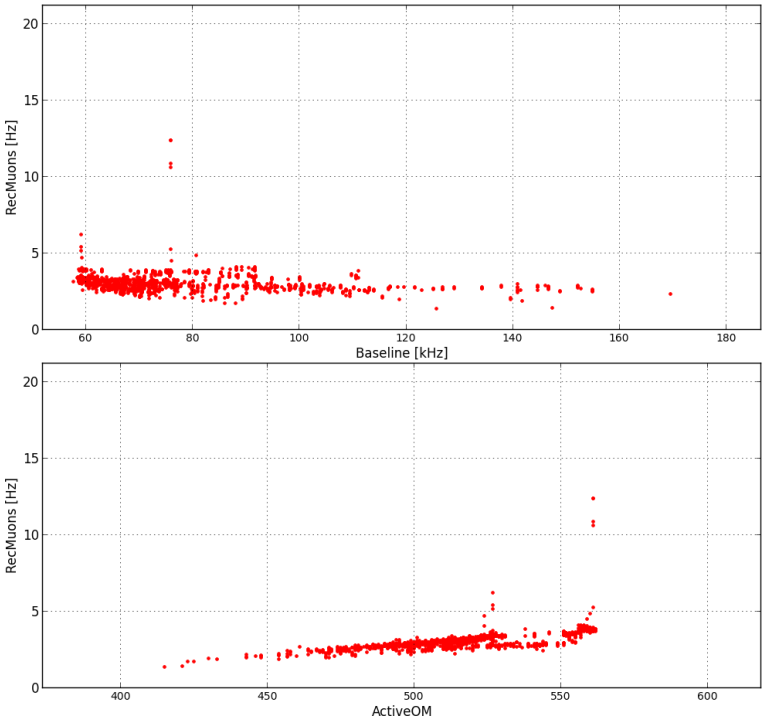

Muon rate for TimeSlice 3, with λ-cut -7.1

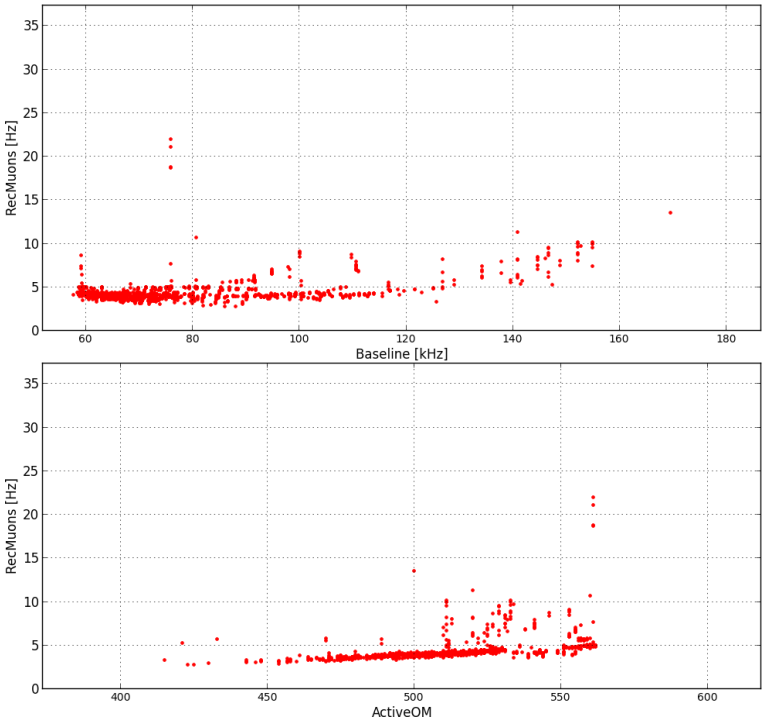

Muon rate for TimeSlice 4, with λ-cut -6.1

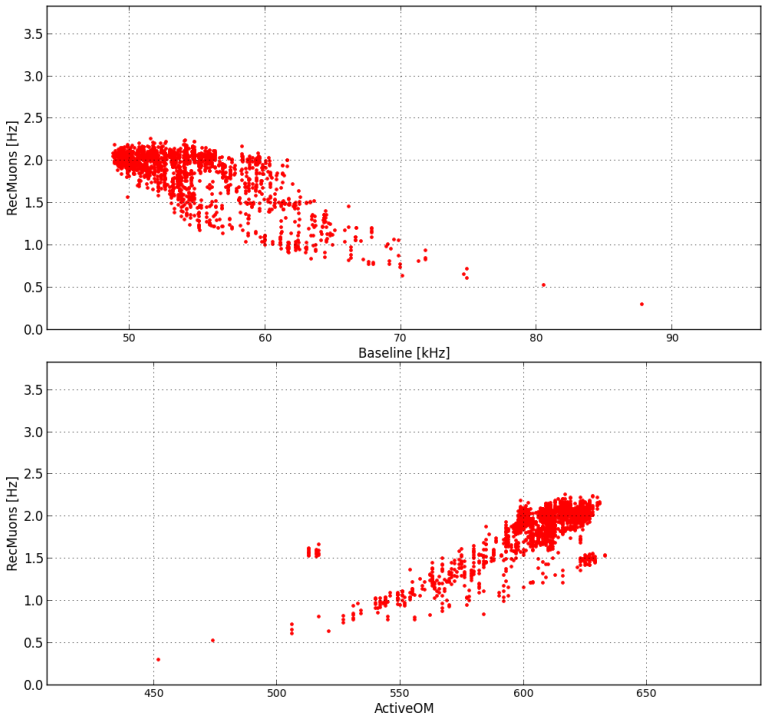

Muon rate for TimeSlice 4, with λ-cut -6.6

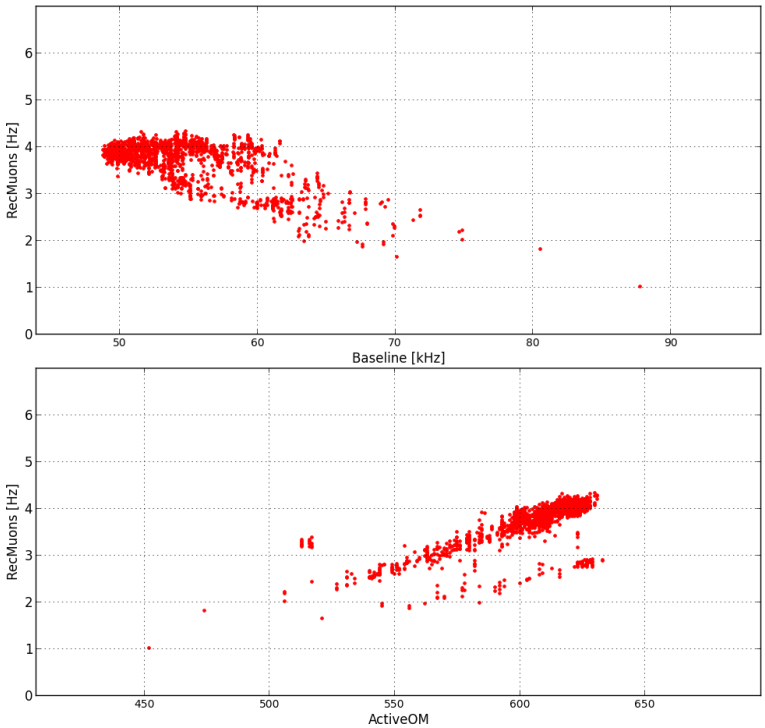

Muon rate for TimeSlice 4, with λ-cut -7.1

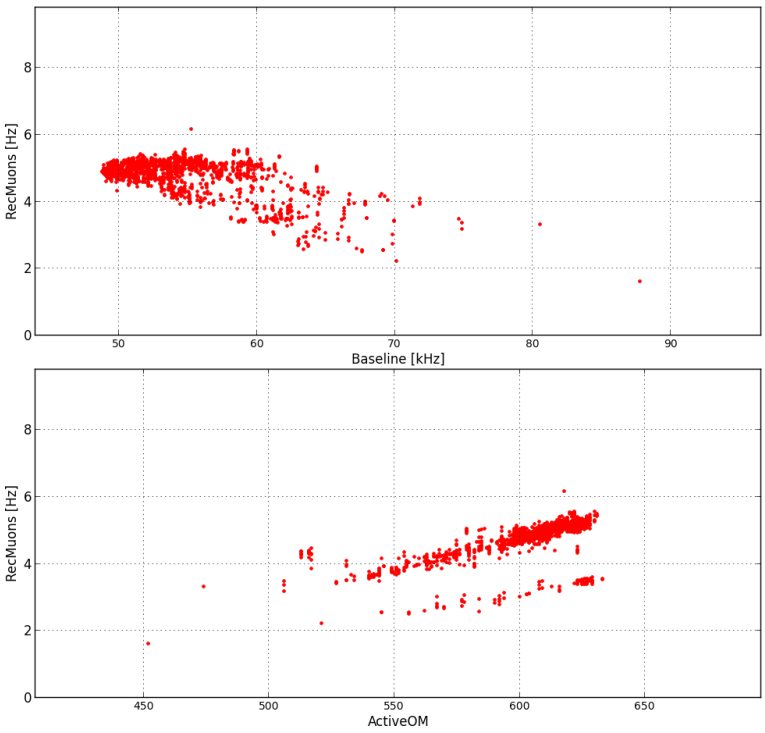

Muon rate for TimeSlice 5, with λ-cut -6.1

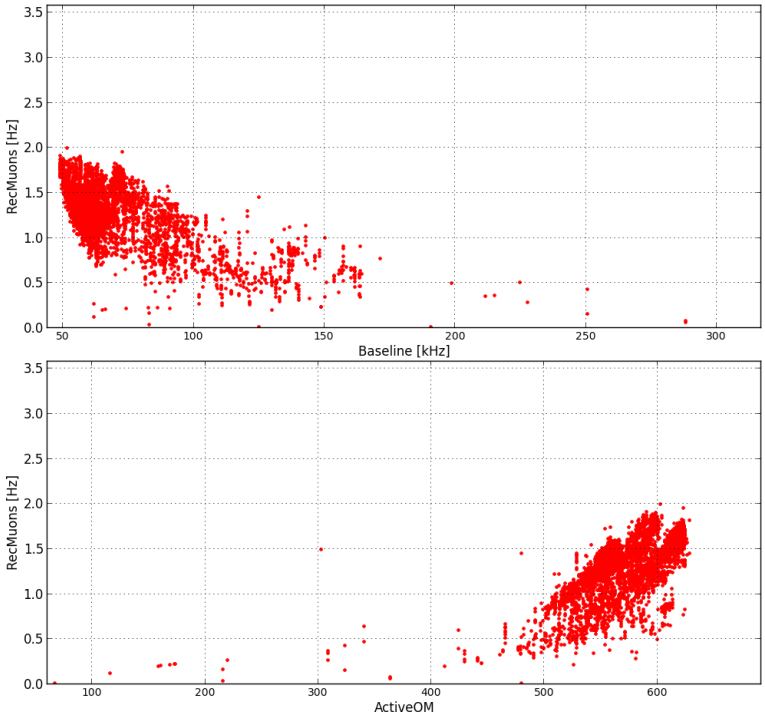

Muon rate for TimeSlice 5, with λ-cut -6.6

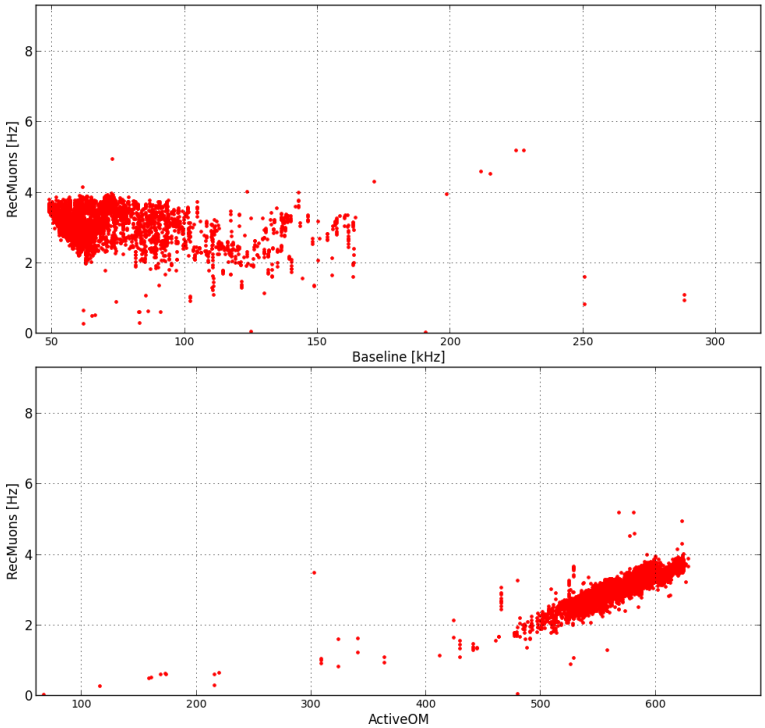

Muon rate for TimeSlice 5, with λ-cut -7.1

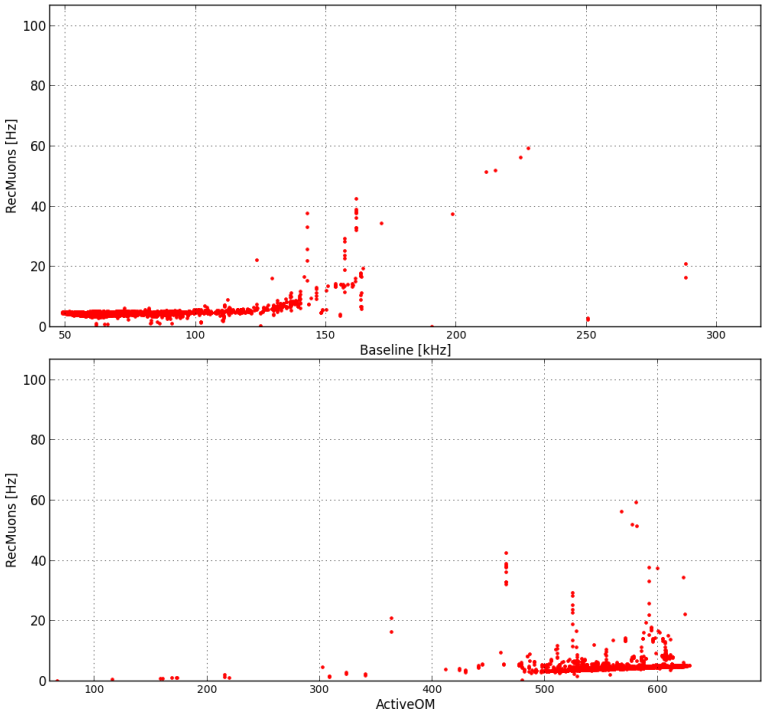

Muon rate for TimeSlice 6, with λ-cut -6.1

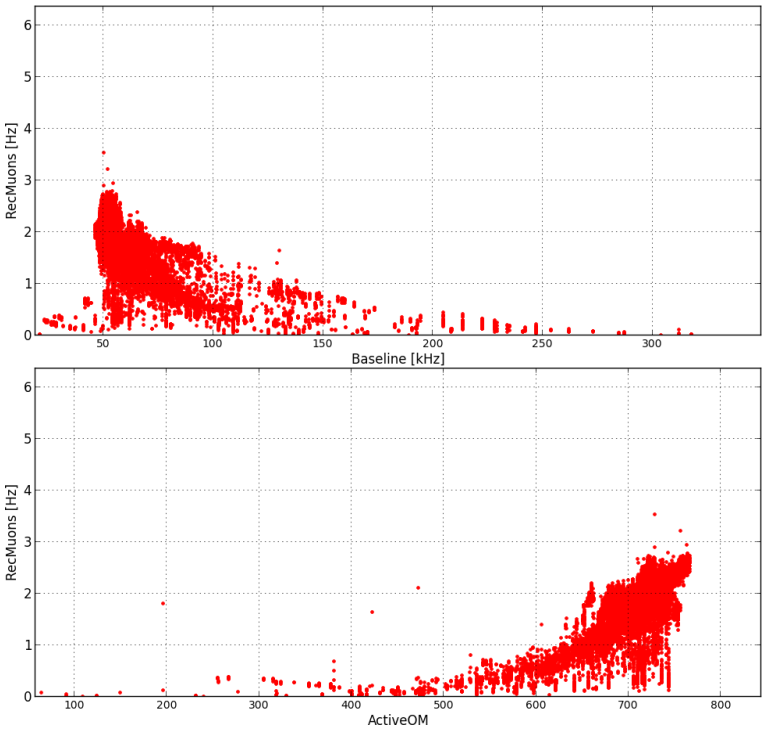

Muon rate for TimeSlice 6, with λ-cut -6.6

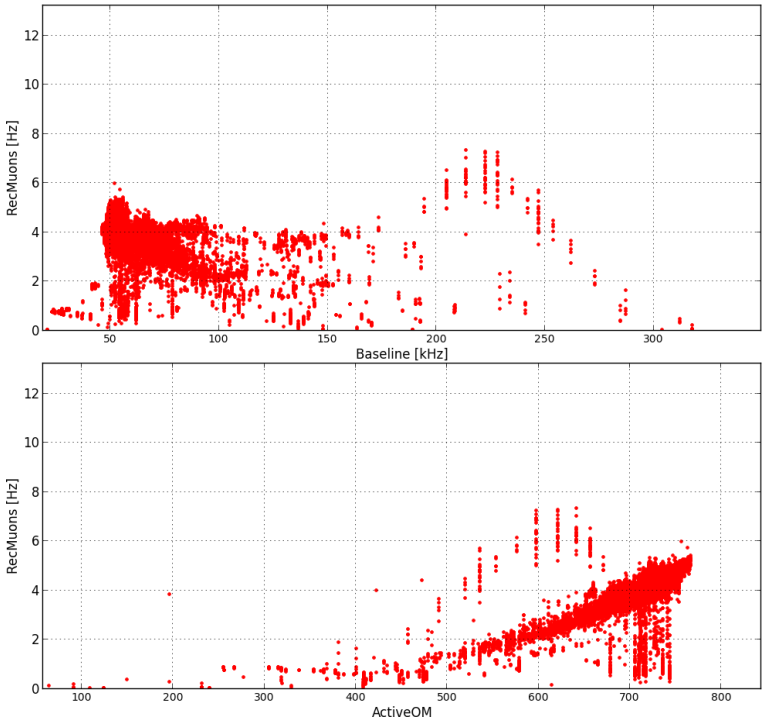

Muon rate for TimeSlice 6, with λ-cut -7.1

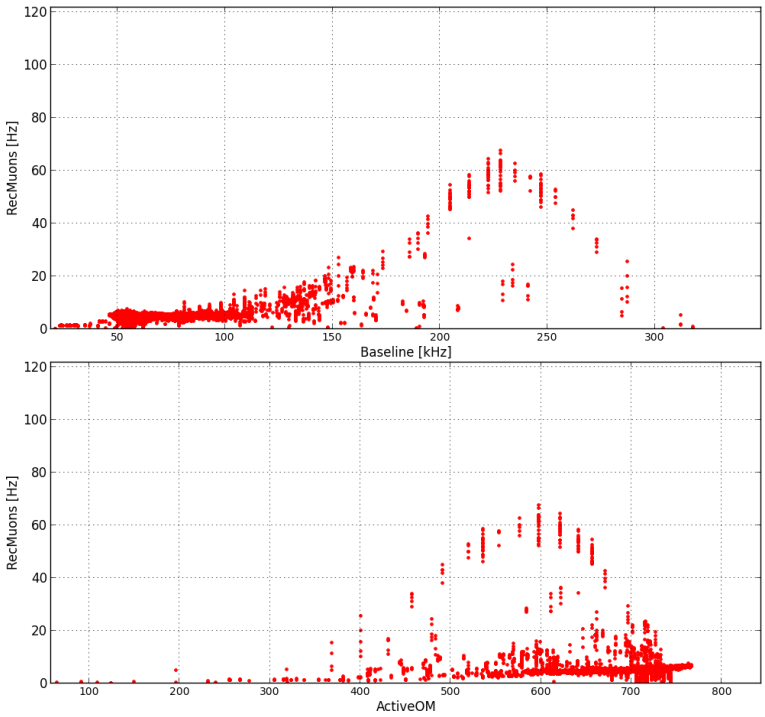

Muon rate for TimeSlice 7, with λ-cut -6.1

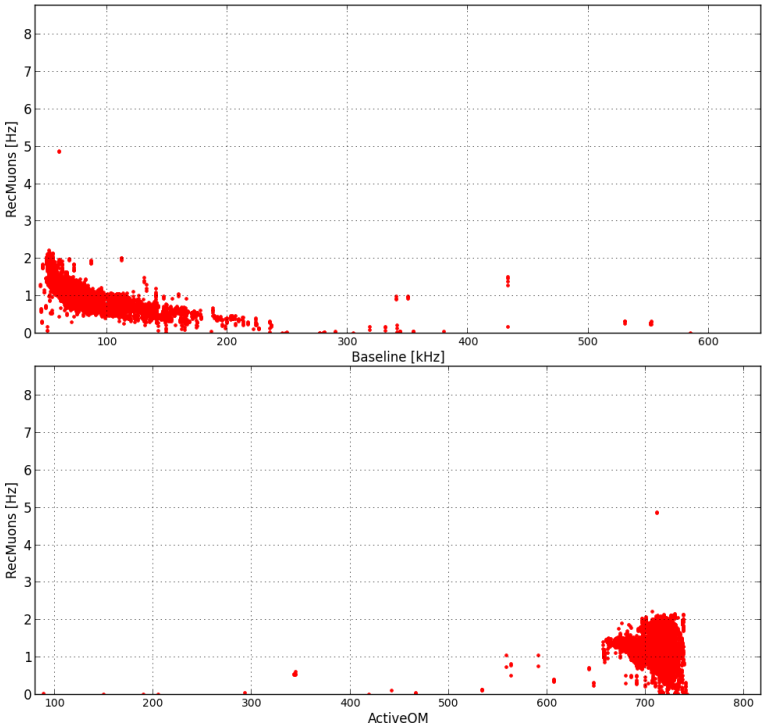

Muon rate for TimeSlice 7, with λ-cut -6.6

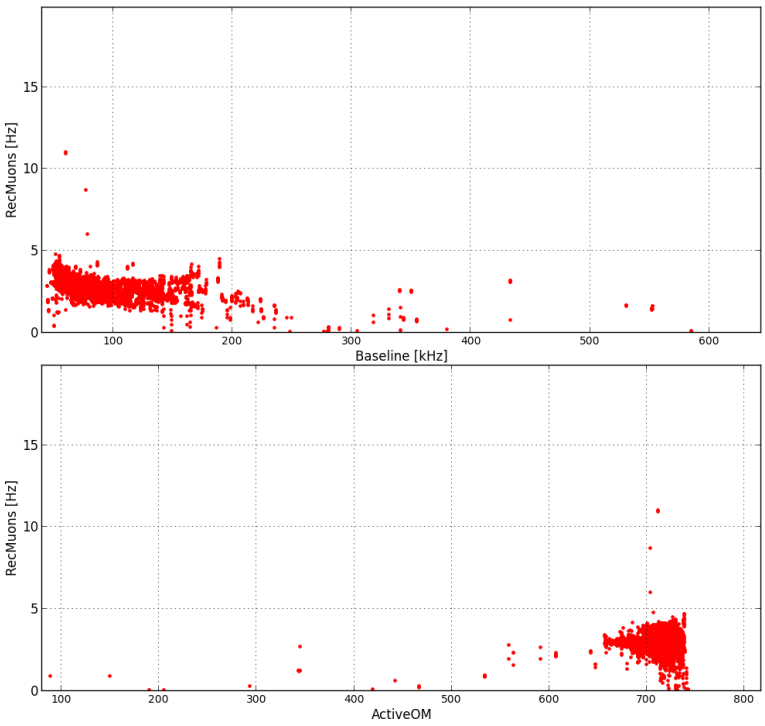

Muon rate for TimeSlice 7, with λ-cut -7.1

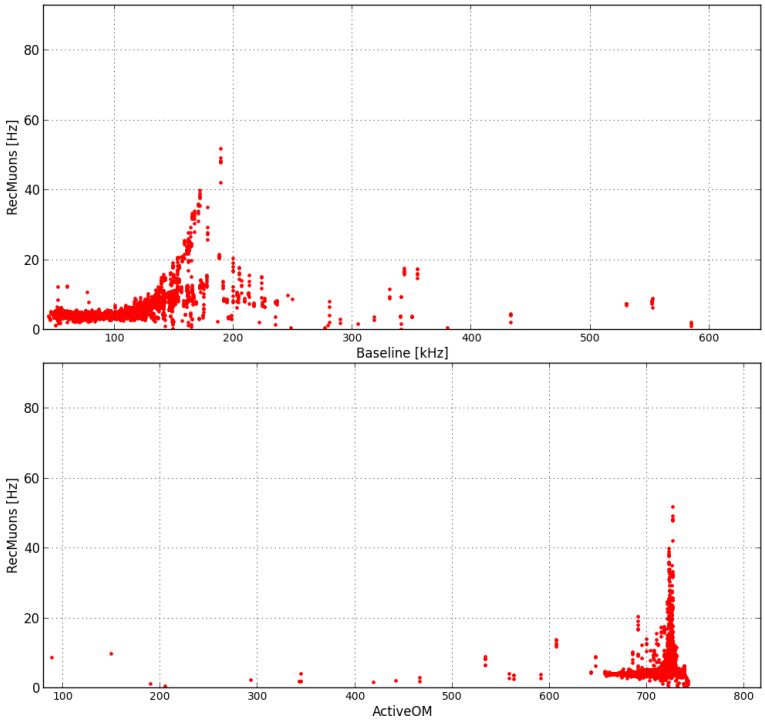

Muon rate for TimeSlice 8, with λ-cut -6.1

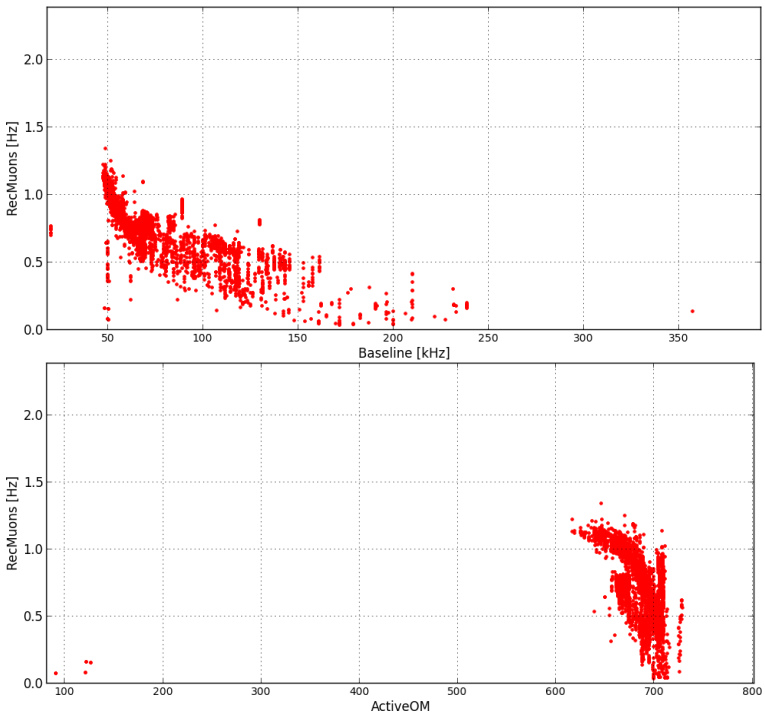

Muon rate for TimeSlice 8, with λ-cut -6.6

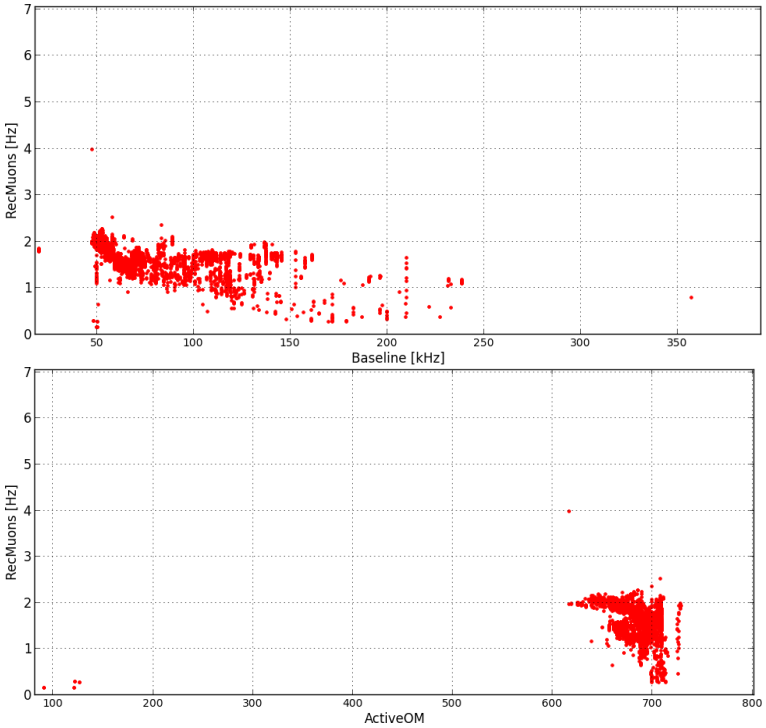

Muon rate for TimeSlice 8, with λ-cut -7.1

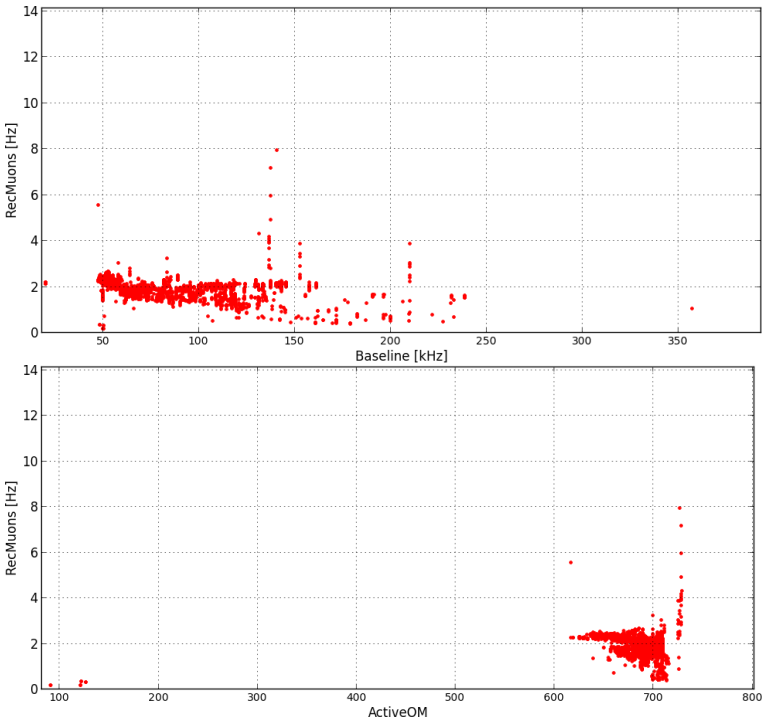

Appendix D

Muon rate versus baseline and number of active OM for run setups

Here the muon rate for reconstructed muons with zenith $< 60°$ is shown for different run setups used for TimeSlice6 versus the baseline and the number of active OM (see x-axis in plots). The λ-cut is set to -6.6 and -7.1 to show the influence on the spreading. The same plots where made for the other run setups and for the other TimeSlices but are not shown here. Weights are calculated based on that plots after some more single runs where rejected. See 8.2 for more information.

Run setup name: Line 1-12 Physics Trigger 3N+2T3+K40+TS0 Nov2010

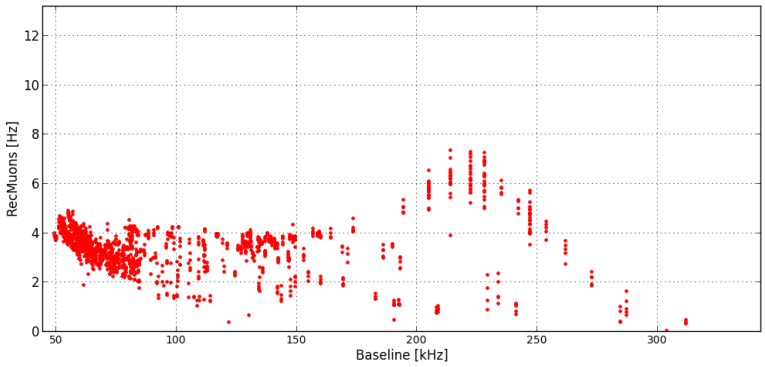

λ-cut: -6.6

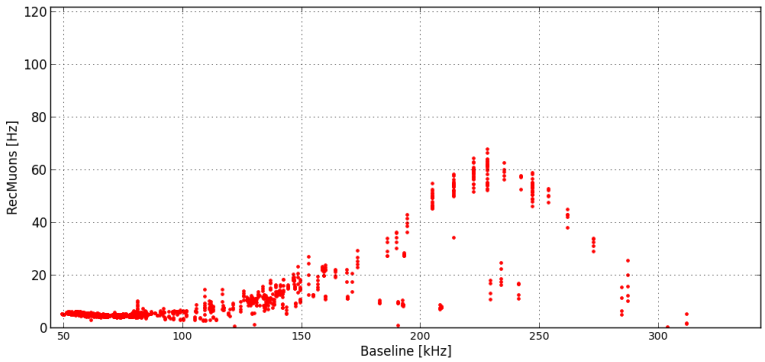

λ-cut: -7.1

Run setup name: Line 1-12 Physics Trigger 3N+2T3+K40+TS0 Nov2010

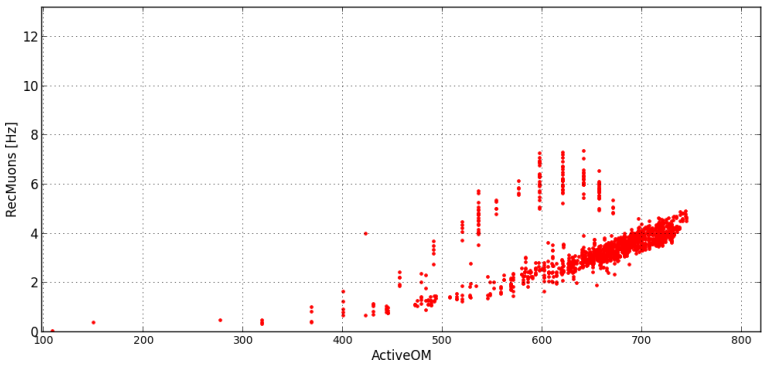

λ-cut: -6.6

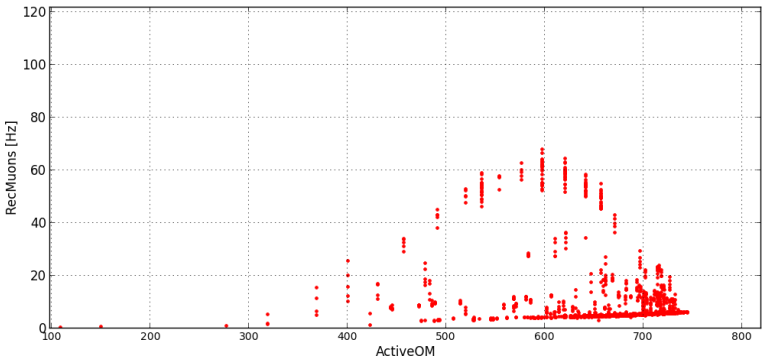

λ-cut: -7.1

Run setup name: Line 1-12 Physics Trigger 3N+2T3+K40+TS0 June2011

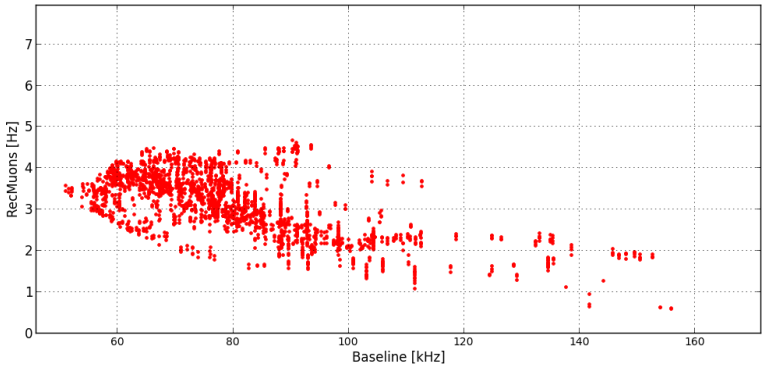

λ-cut: -6.6

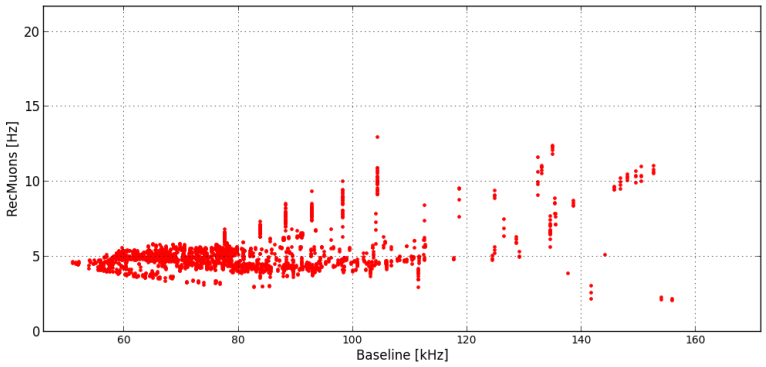

λ-cut: -7.1

Run setup name: Line 1-12 Physics Trigger 3N+2T3+K40+TS0 June2011

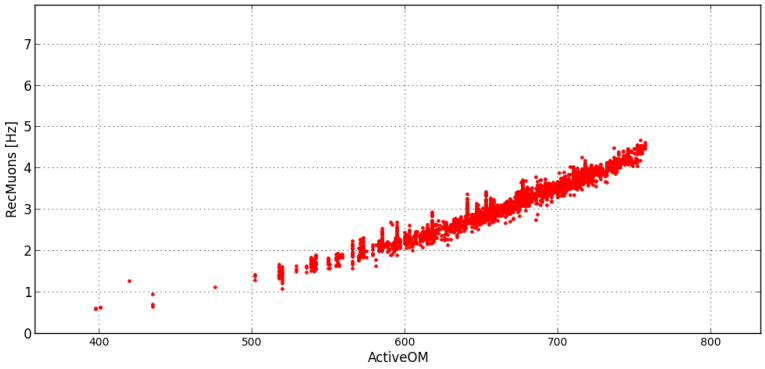

λ-cut: -6.6

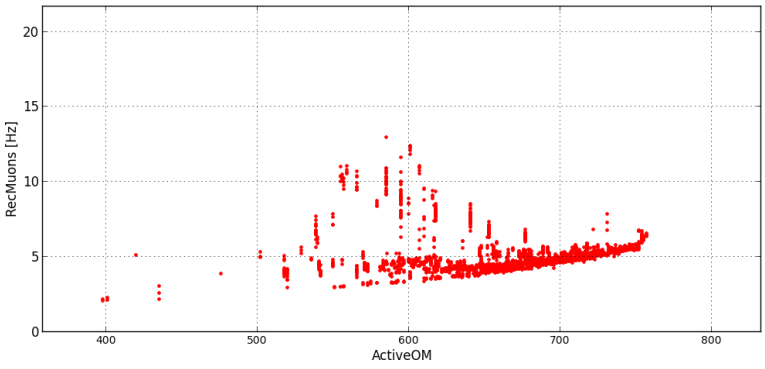

λ-cut: -7.1

Run setup name: Line 1-12 Physics Trigger 3N+2T3+K40+TS0 Dec2011

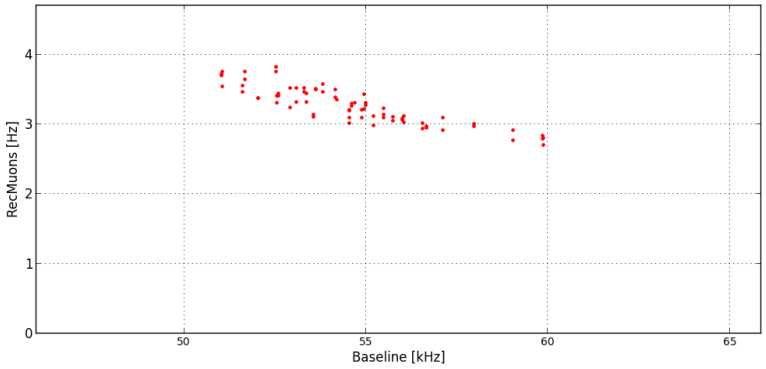

λ-cut: -6.6

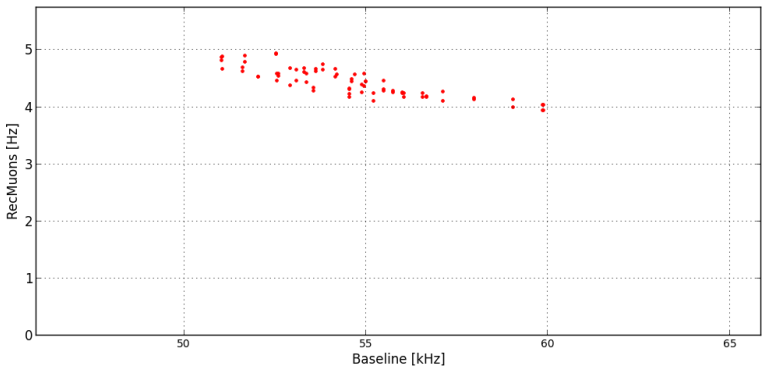

λ-cut: -7.1

Run setup name: Line 1-12 Physics Trigger 3N+2T3+K40+TS0 Dec2011

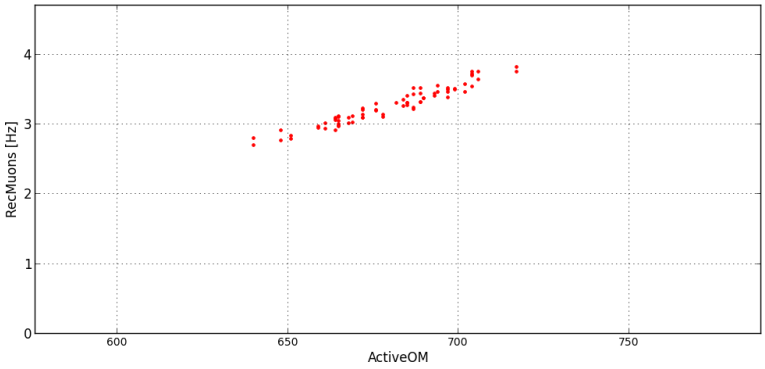

λ-cut: -6.6

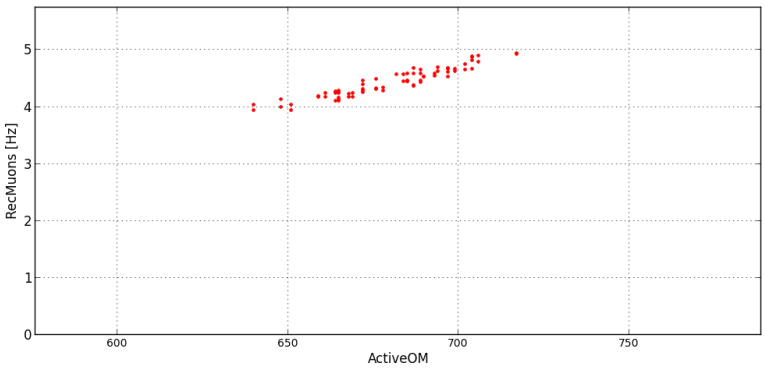

λ-cut: -7.1

Run setup name: Line 1-12 Physics Trigger 3N+2T3+GC+TQ+T2+K40+TS0 Nov2010

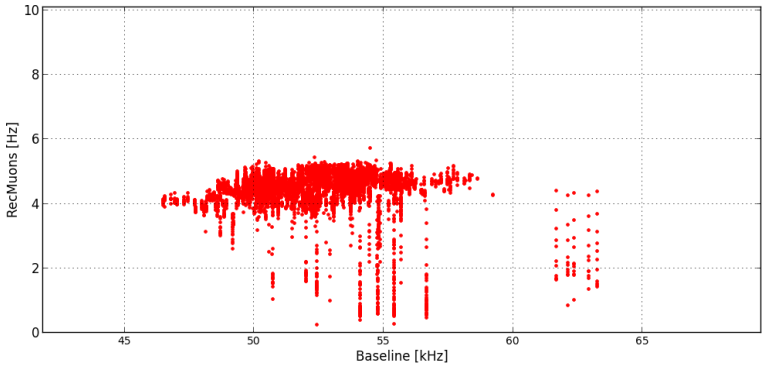

λ-cut: -6.6

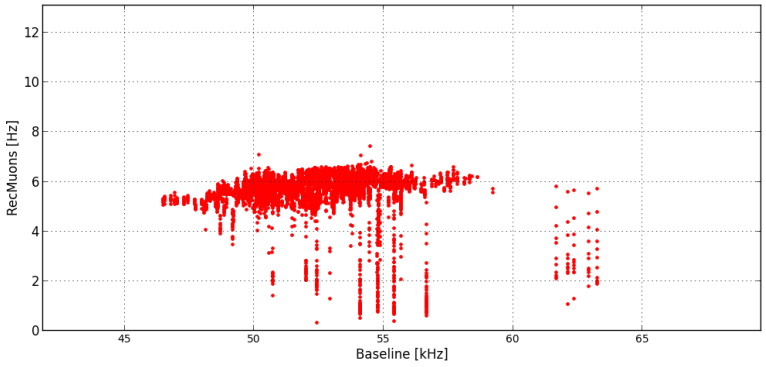

λ-cut: -7.1

Run setup name: Line 1-12 Physics Trigger 3N+2T3+GC+TQ+T2+K40+TS0 Nov2010

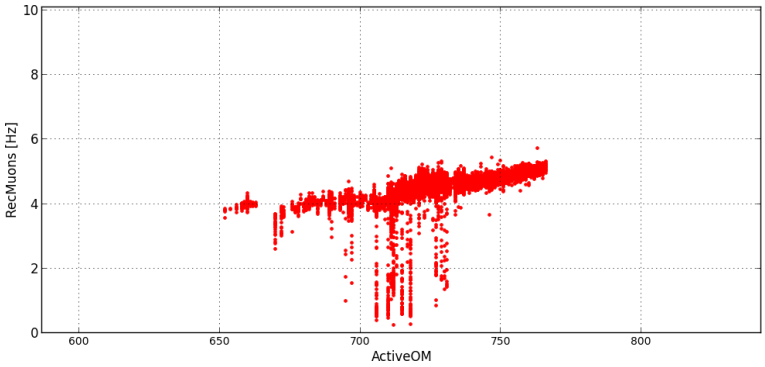

λ-cut: -6.6

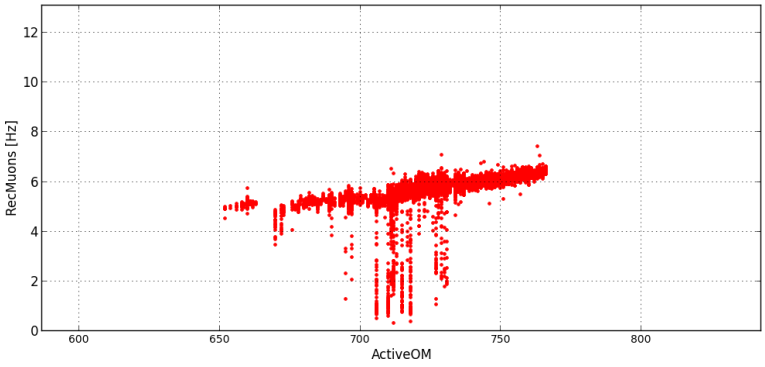

λ-cut: -7.1

Run setup name: Line 1-12 Physics Trigger 3N+2T3+GC+TQ+T2+K40+TS0 June2011

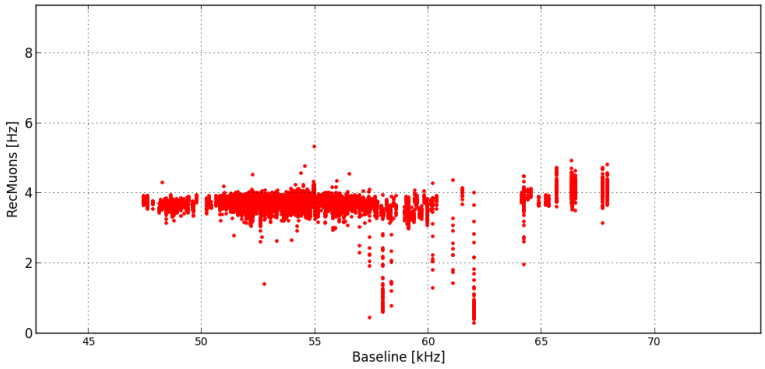

λ-cut: -6.6

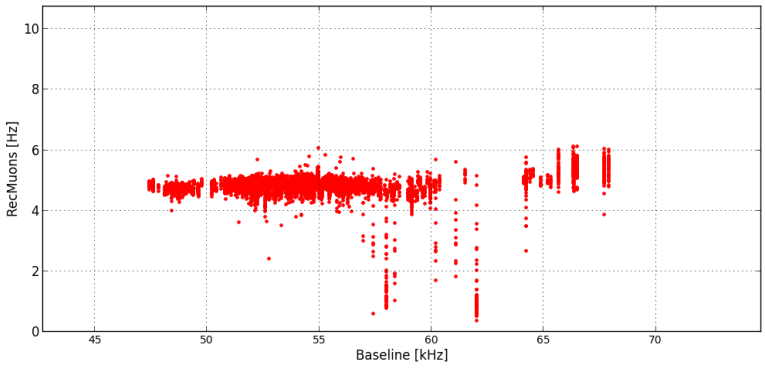

λ-cut: -7.1

Run setup name: Line 1-12 Physics Trigger 3N+2T3+GC+TQ+T2+K40+TS0 June2011

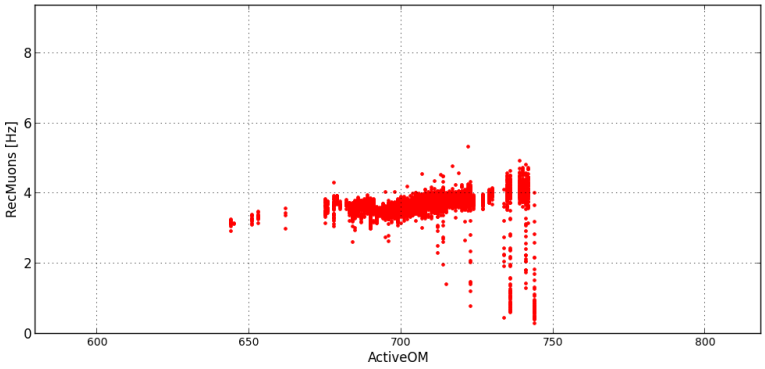

λ-cut: -6.6

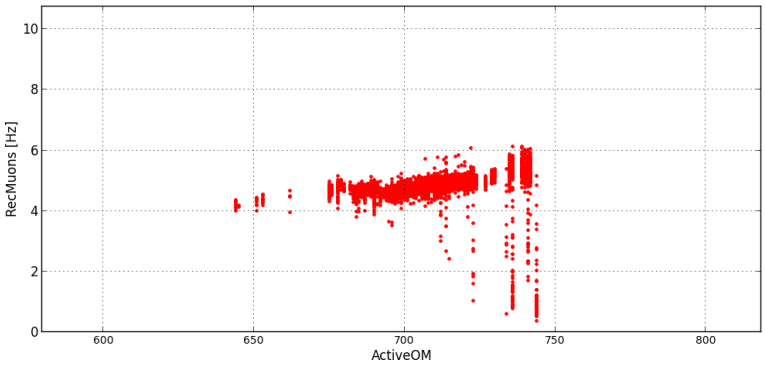

λ-cut: -7.1

Run setup name: Line 1-12 Physics Trigger 3N+2T3+GC+TQ+T2+K40+T0 Dec2011

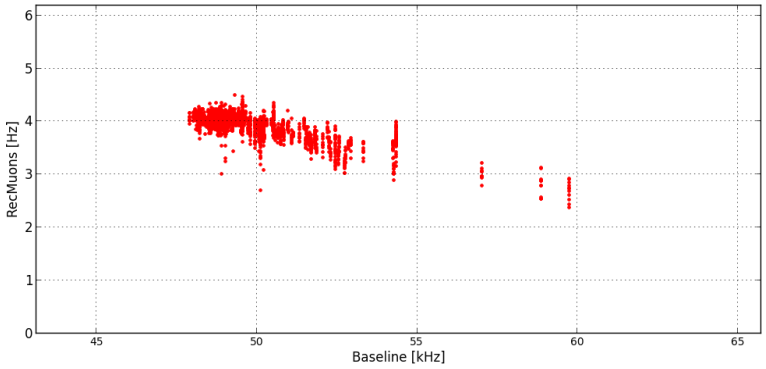

λ-cut: -6.6

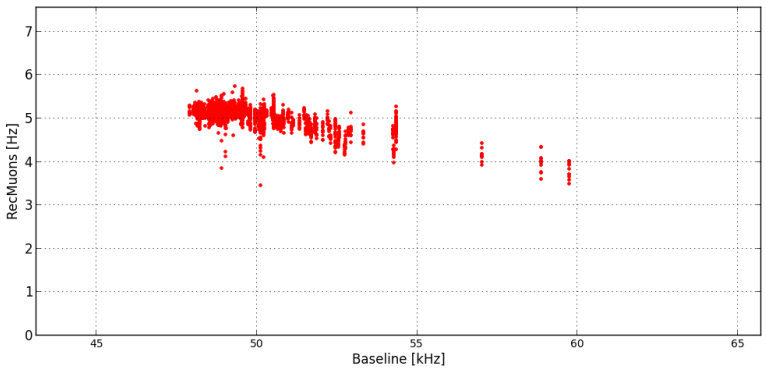

λ-cut: -7.1

Run setup name: Line 1-12 Physics Trigger 3N+2T3+GC+TQ+T2+K40+T0 Dec2011

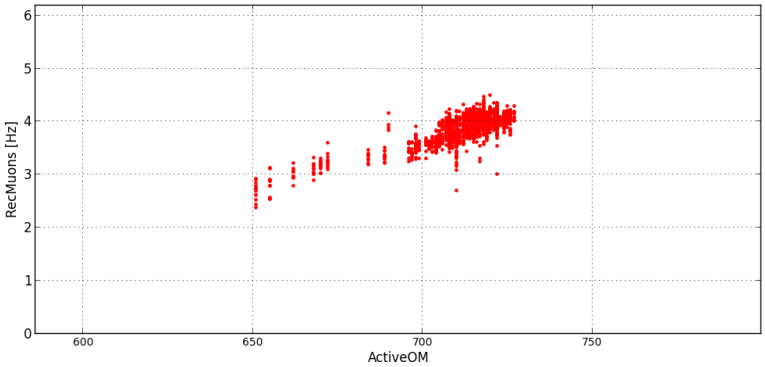

λ-cut: -6.6

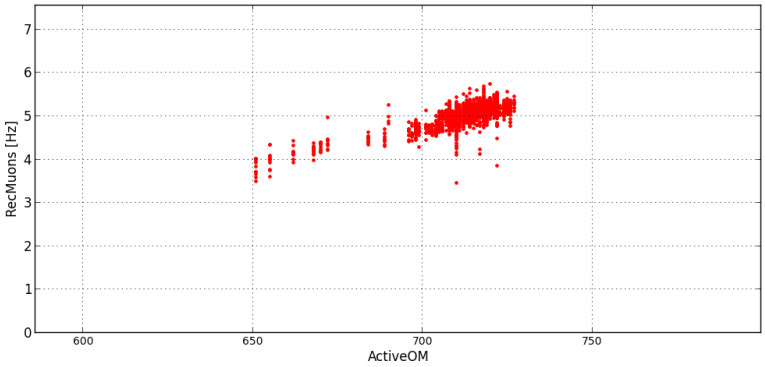

λ-cut: -7.1

Run setup name: Line 1-12 Physics Trigger 3N+2T3+GC+TQ+K40+TS0 Dec2011

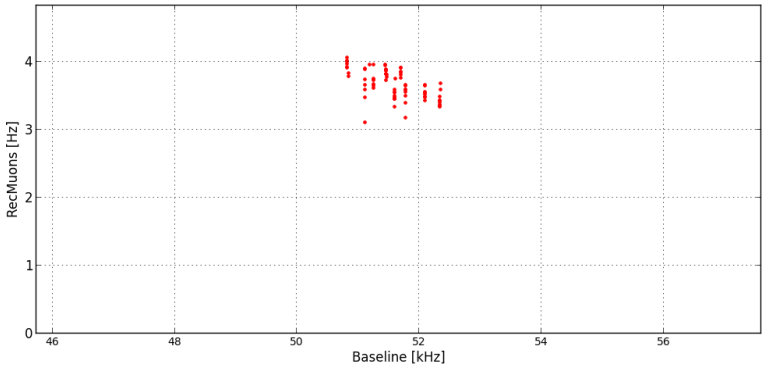

λ-cut: -6.6

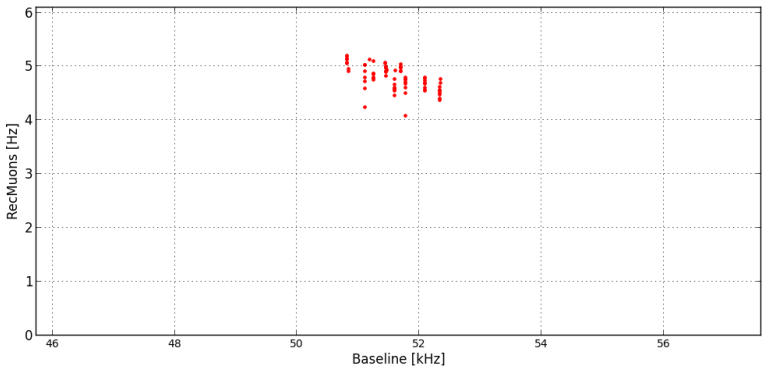

λ-cut: -7.1

Run setup name: Line 1-12 Physics Trigger 3N+2T3+GC+TQ+K40+TS0 Dec2011

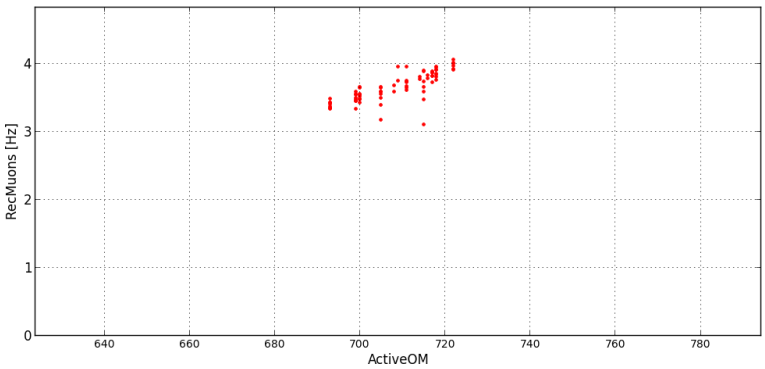

λ-cut: -6.6

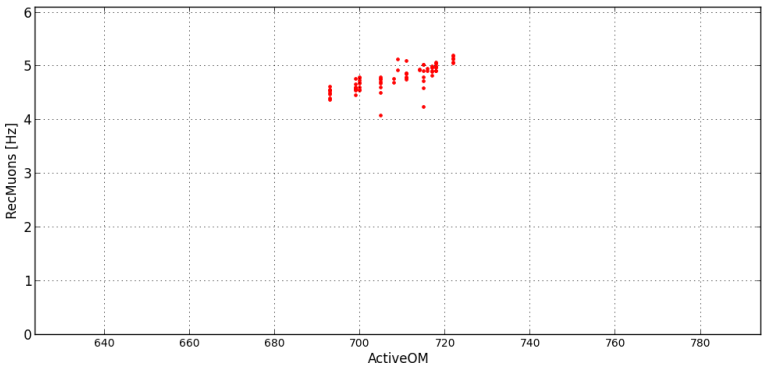

λ-cut: -7.1

Run setup name: Line 1-12 Physics Trigger 3N+2T3+GC+K40+TS0 Nov2010

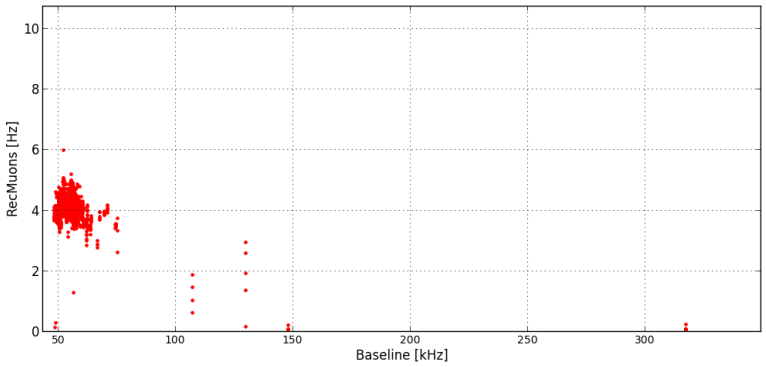

λ-cut: -6.6

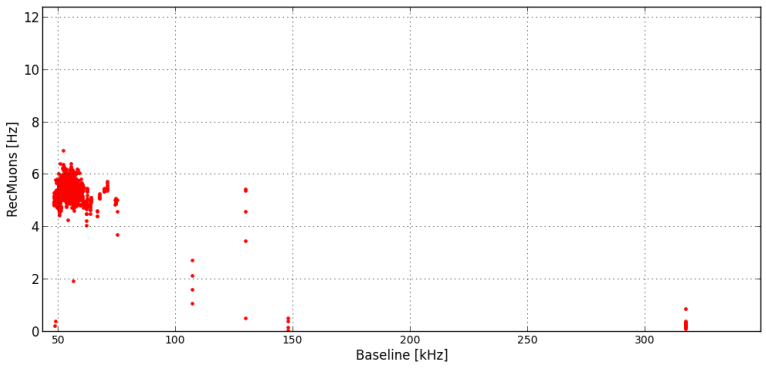

λ-cut: -7.1

Run setup name: Line 1-12 Physics Trigger 3N+2T3+GC+K40+TS0 Nov2010

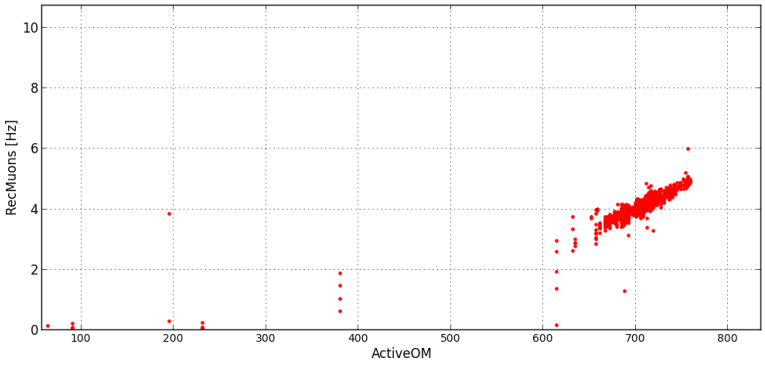

λ-cut: -6.6

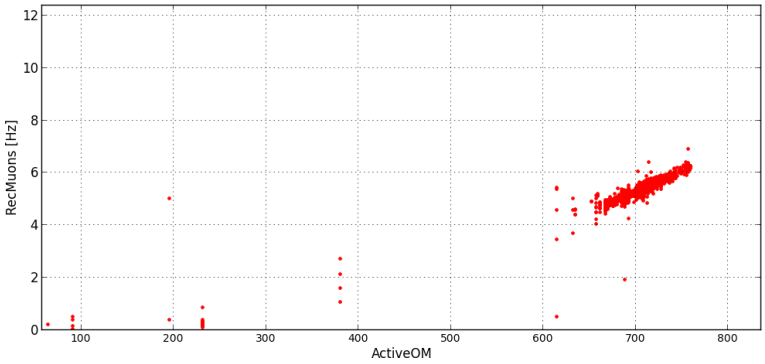

λ-cut: -7.1

Run setup name: Line 1-12 Physics Trigger 3N+2T3+GC+K40+TS0 June2011

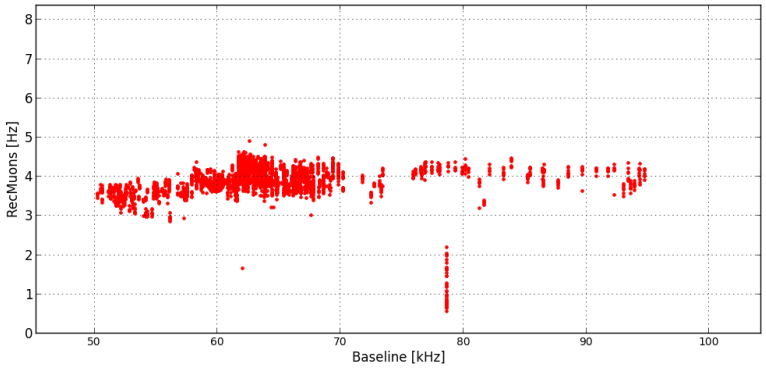

λ-cut: -6.6

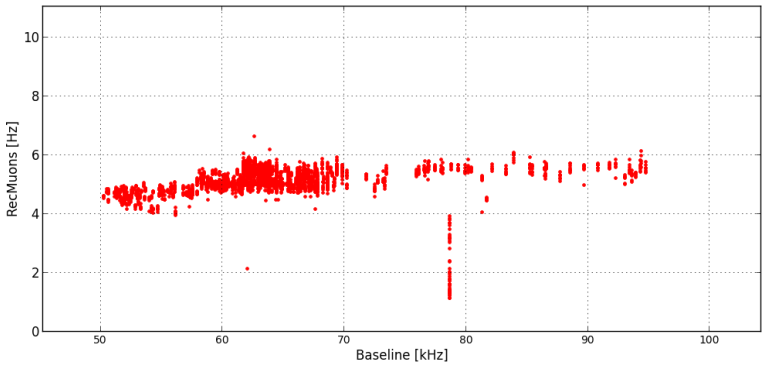

λ-cut: -7.1

Run setup name: Line 1-12 Physics Trigger 3N+2T3+GC+K40+TS0 June2011

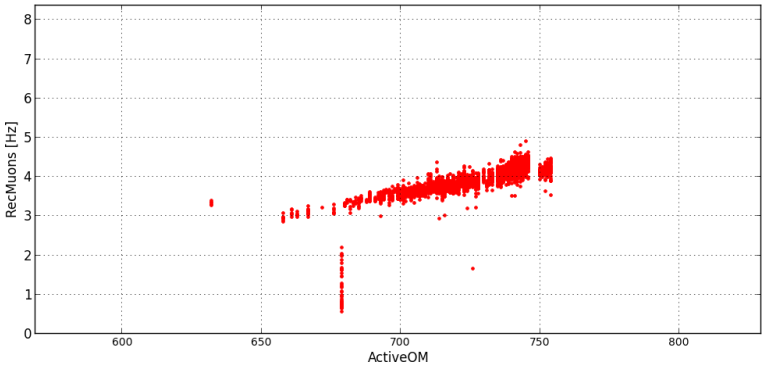

λ-cut: -6.6

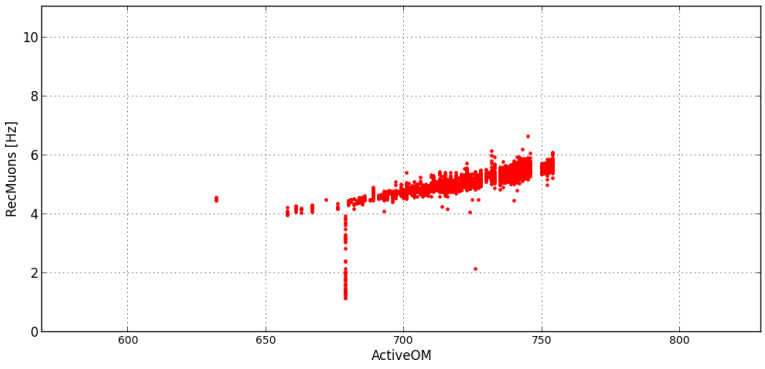

λ-cut: -7.1

Appendix E

Muon rate for run setups with different weights applied

These are plots of the muon rate over the baseline and the number of active OMs for the different run setups used in TimeSlice6. The weights compensating the decreasing efficiency of the detector over the time are applied to all data. The weights for the number of acitve OMs and baseline are applied afterwards and the result is shown (see text of the figures). The fit of the function $f(x) = ax^2 + bx + c$ (blue line) and the average of the muon rate (green line) are shown in the plots. The weights for the number of active OMs are calculated by the fit and the average value of the muon rate. The order is as follows: Weights for active OMs for each run setup are calculated only after the weights compensating the decreasing efficiency of the detector has been applied. The muon rate versus the baseline is shown as well but without fit (figures described by 'Weights for aging of the OMs applied').

After that the weights for the number of active OMs are applied to the data. A plot of the muon rate versus the number of active OM and the muon rate versus the baseline are shown. The first plot shows how the weights have changed the distribution of the muon rate in both plots. The figure showing the muon rate versus the baseline now shows the fit of the function $f(x)$ and the average muon rate. The plots for this step are identified by the text 'Weights for aging and active OM are applied'.

The last step is to apply the weights for the baseline calculated by the fit function and the average muon rate. Two more plots are shown viewing the muon rate versus active OM and baseline to show the difference. The text 'Weights for aging, active OM and baseline are applied' identifies these plots.

It can be seen that the muon rates of the run setups differ in the average muon rate and how the muon rate changes according to the baseline. Which makes it necessary to look at the run setups separately.

The steps are repeated for each run setup. The parameter of the fitted function and the average of the muon rate for all TimeSlices and run setups used can be found

in appendix F. The plots show the run setups used for TimeSlice6. The muon rate is calculated from the events reconstructed with AAFit and a λ-cut of -6.6. Histograms showing the distribution of the muon rates for all TimeSlices with different weights applied can be found in appendix G.

Line 1-12 Physics Trigger 3N+2T3+GC+K40+TS0 June2011:

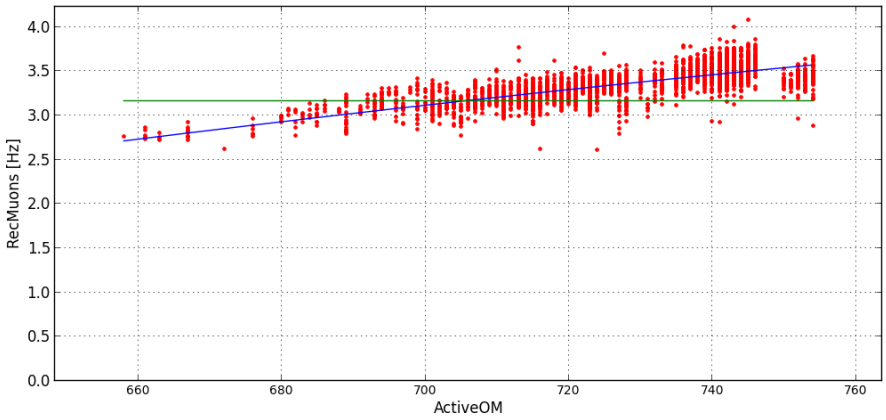

Weights compensating the decreasing efficiency over the time have been applied.

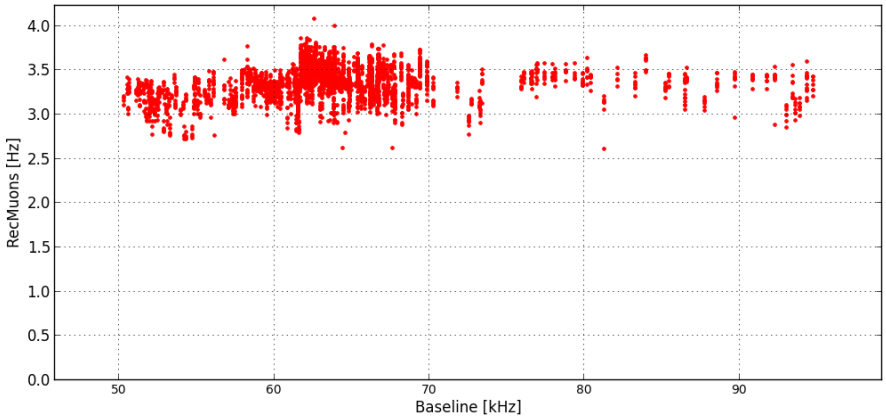

Weights compensating the decreasing efficiency over the time have been applied.

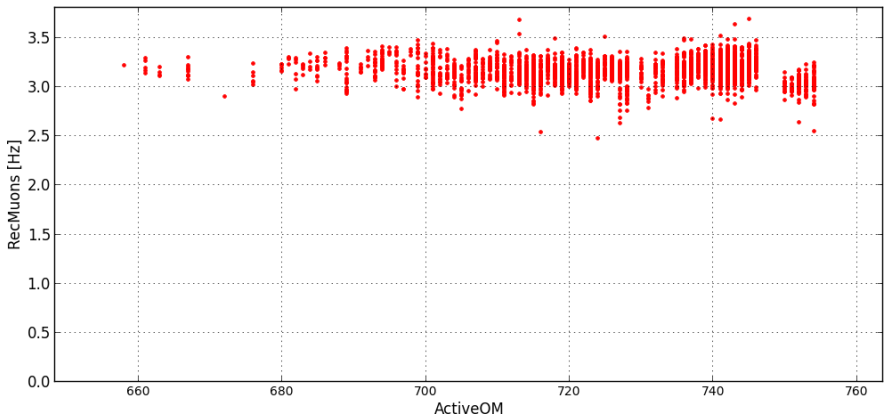

Weights compensating the decreasing efficiency over the time have been applied.

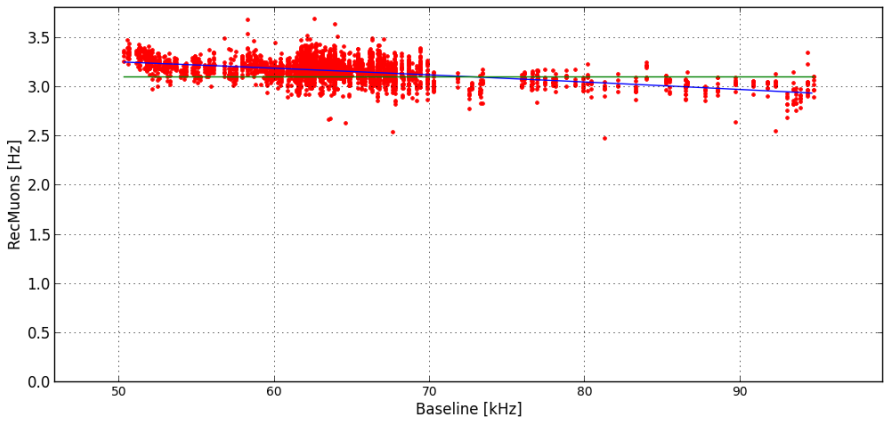

Weights compensating the decreasing efficiency over the time have been applied.

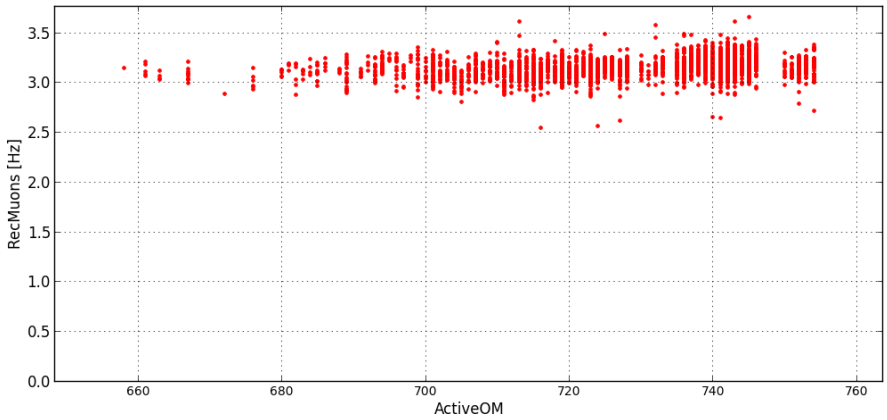

Weights compensating the decreasing efficiency over the time have been applied.

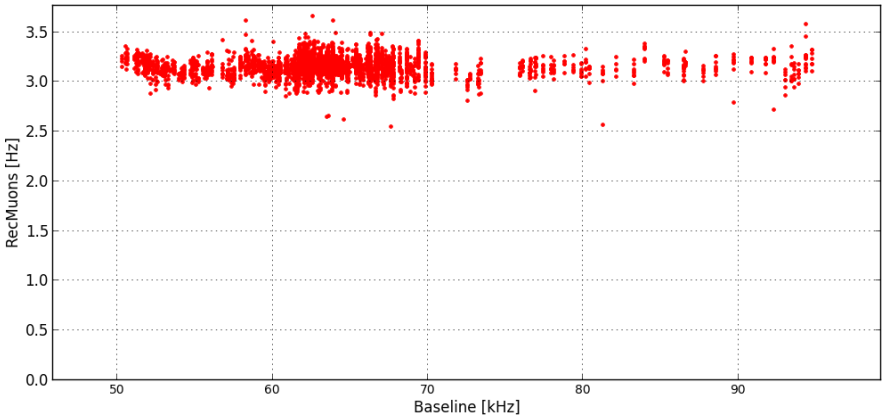

Weights compensating the decreasing efficiency over the time have been applied.

Line 1-12 Physics Trigger 3N+2T3+GC+K40+TS0 Nov2010:

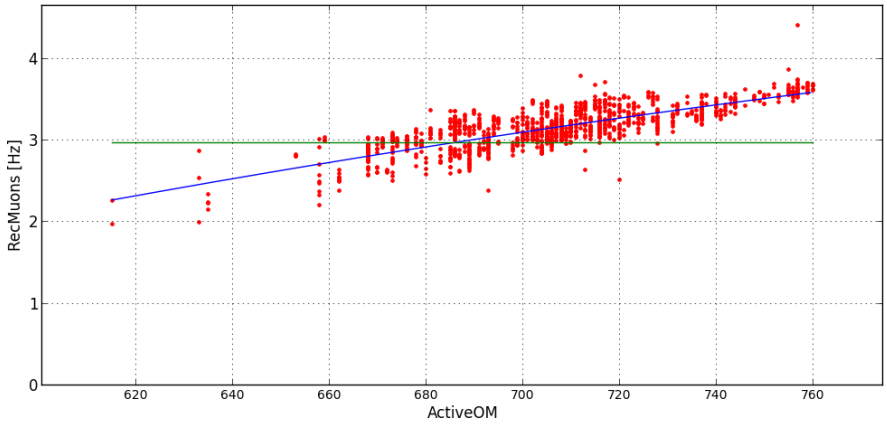

Weights compensating the decreasing efficiency over the time have been applied.

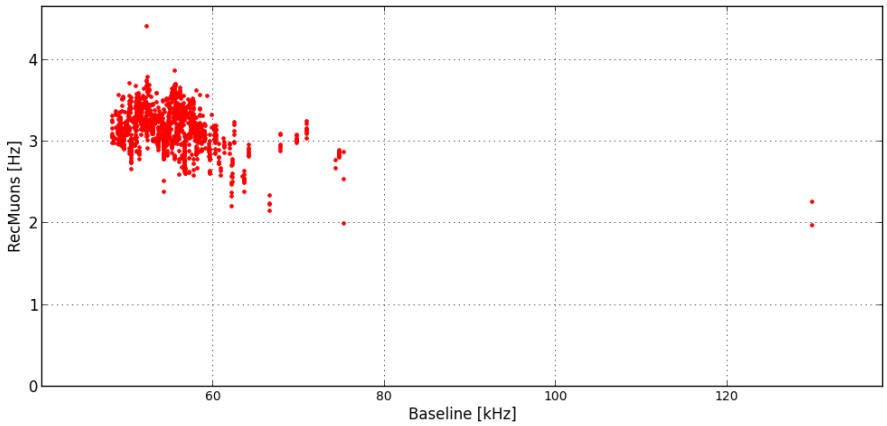

Weights compensating the decreasing efficiency over the time have been applied.

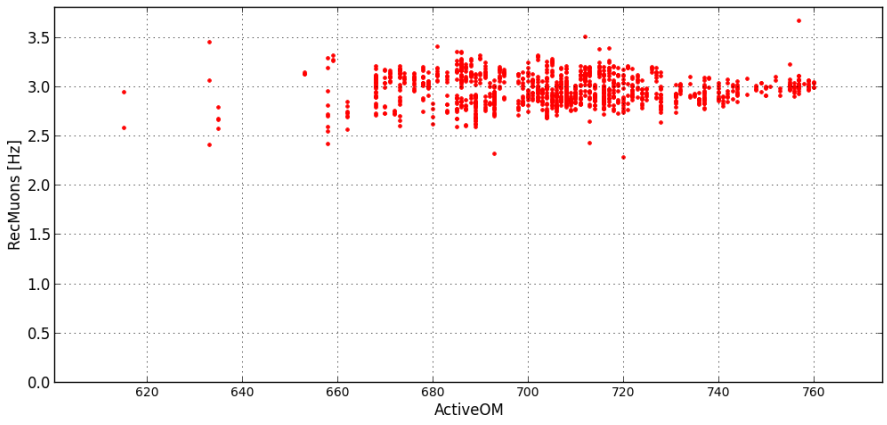

Weights compensating the decreasing efficiency over the time have been applied.

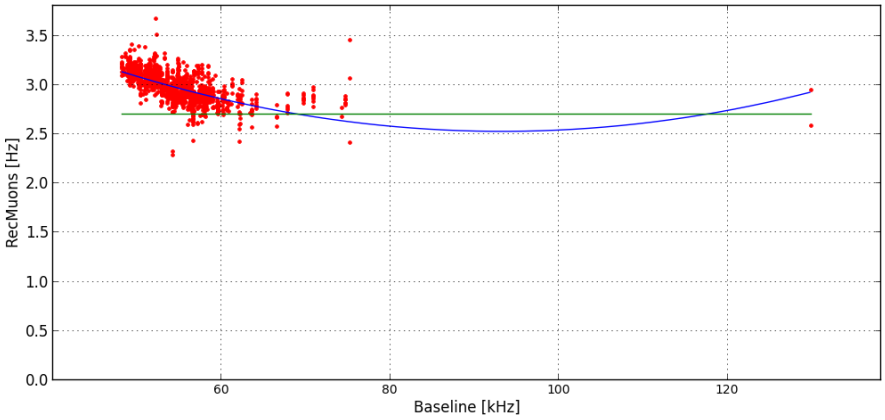

Weights compensating the decreasing efficiency over the time have been applied.

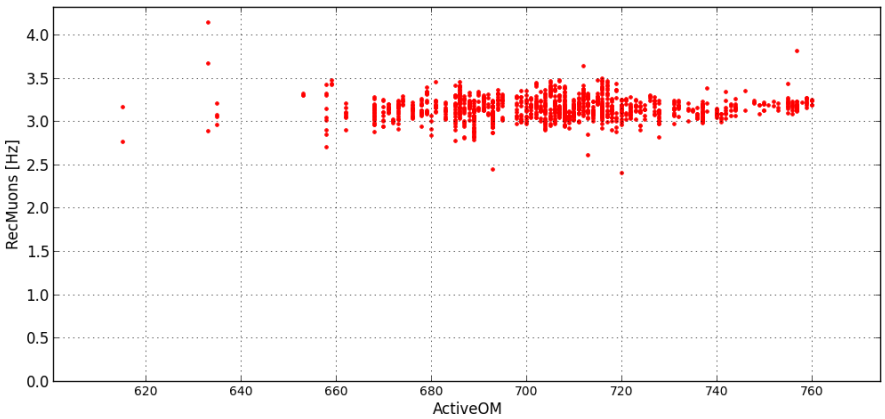

Weights compensating the decreasing efficiency over the time have been applied.

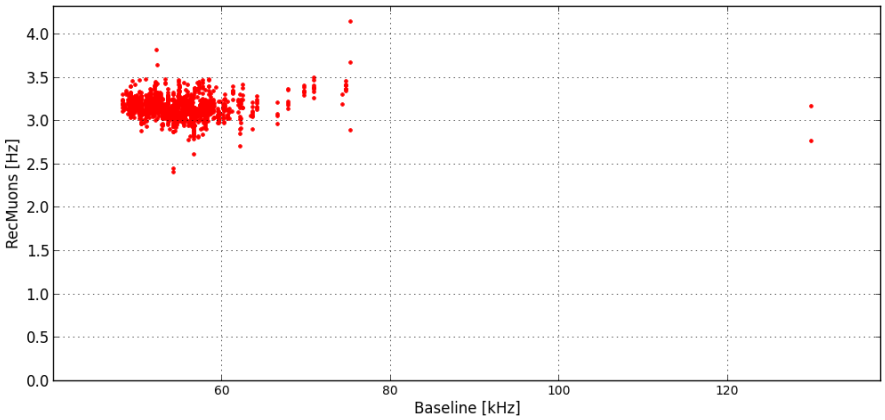

Weights compensating the decreasing efficiency over the time have been applied.

Line 1-12 Physics Trigger 3N+2T3+GC+TQ+K40+TS0 Dec2011:

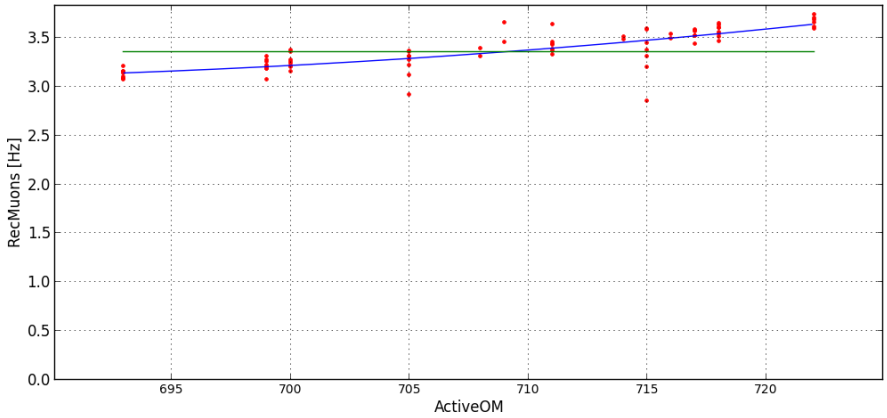

Weights compensating the decreasing efficiency over the time have been applied.

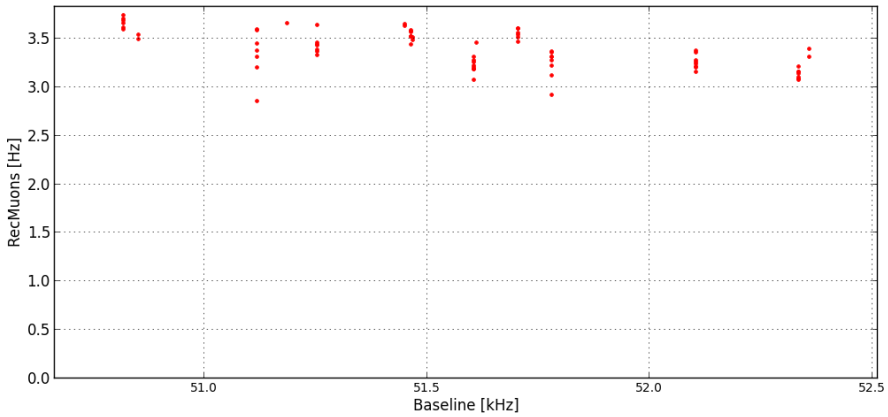

Weights compensating the decreasing efficiency over the time have been applied.

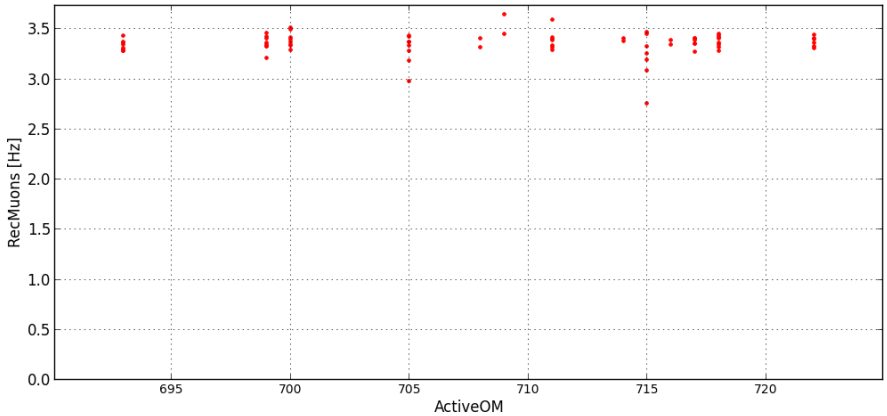

Weights compensating the decreasing efficiency over the time have been applied.

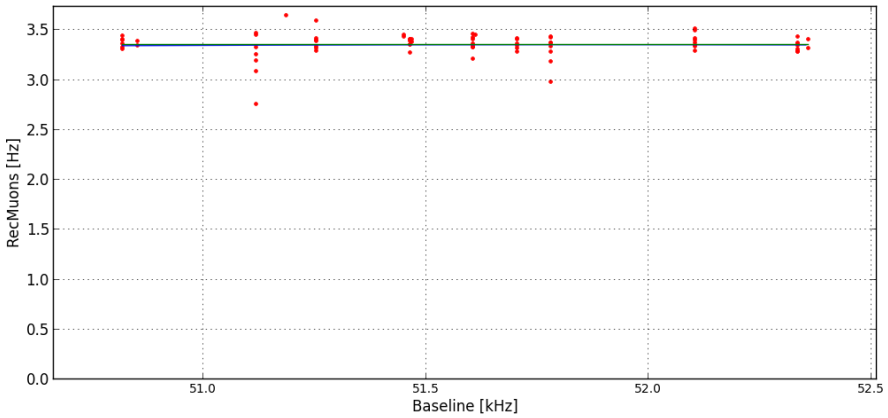

Weights compensating the decreasing efficiency over the time have been applied.

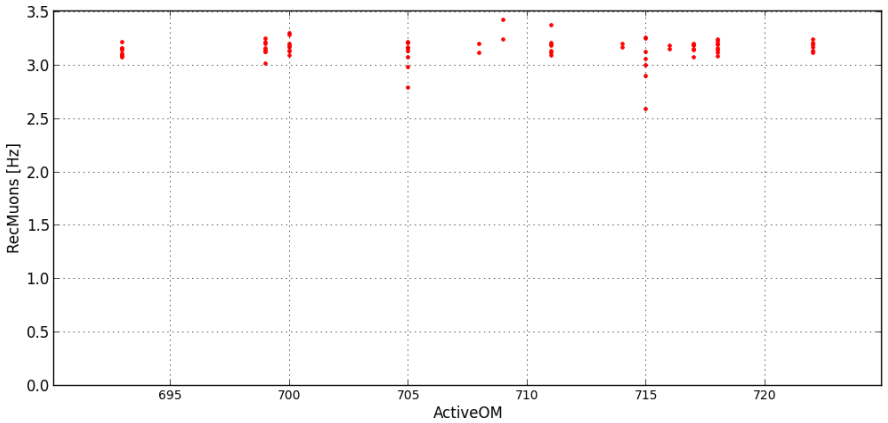

Weights compensating the decreasing efficiency over the time, active OM and baseline are applied.

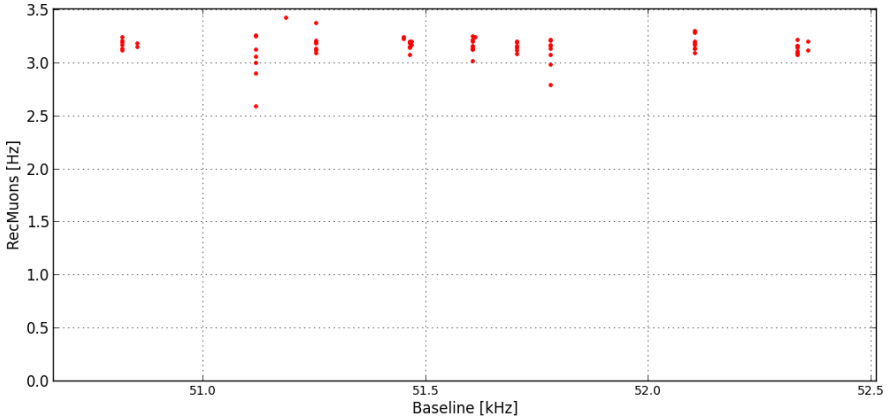

Weights compensating the decreasing efficiency over the time, active OM and baseline are applied.

Line 1-12 Physics Trigger 3N+2T3+GC+TQ+T2+K40+T0 Dec2011:

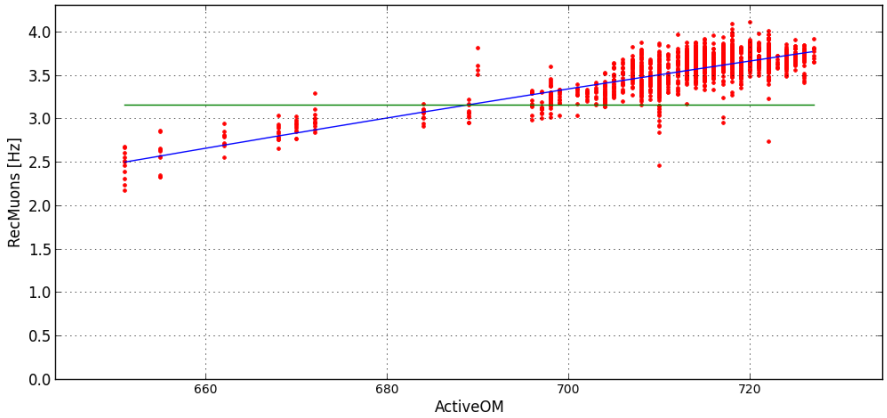

Weights compensating the decreasing efficiency over the time have been applied.

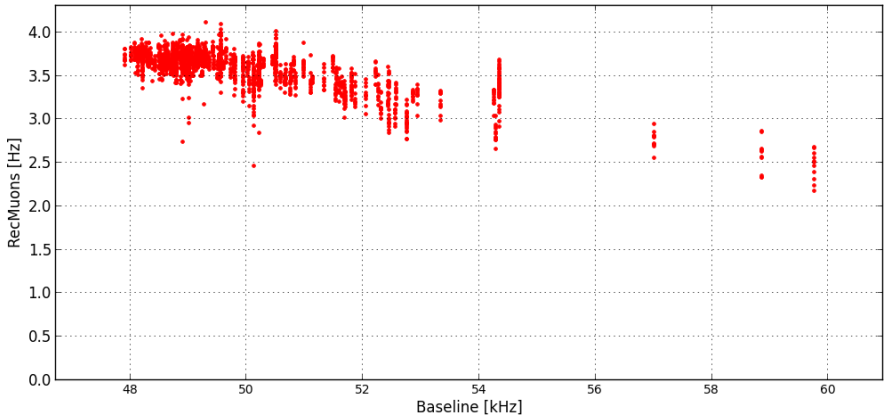

Weights compensating the decreasing efficiency over the time have been applied.

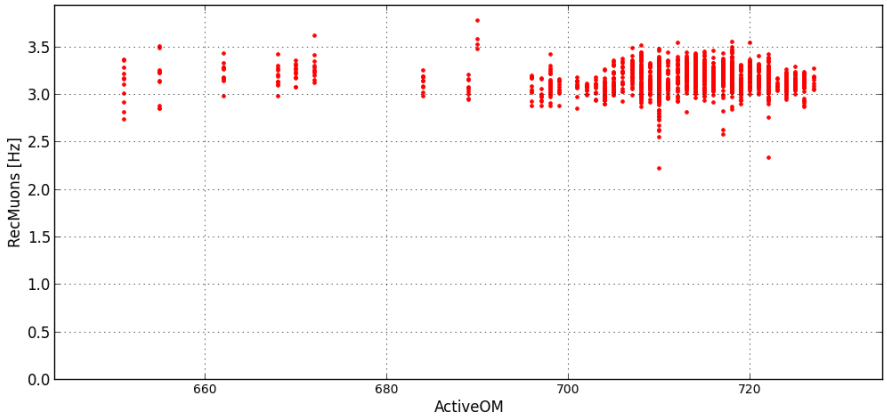

Weights compensating the decreasing efficiency over the time have been applied.

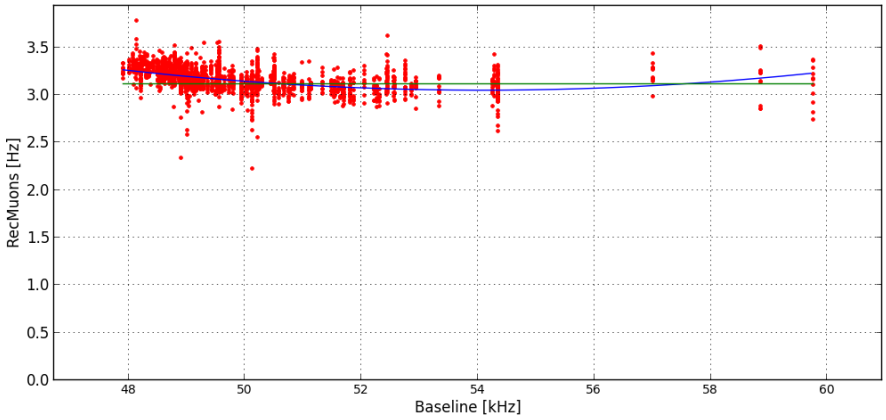

Weights compensating the decreasing efficiency over the time have been applied.

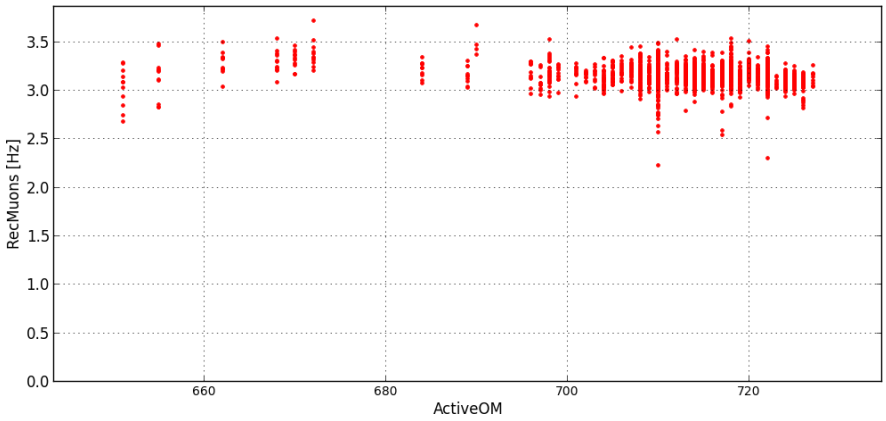

Weights compensating the decreasing efficiency over the time, active OM and baseline are applied.

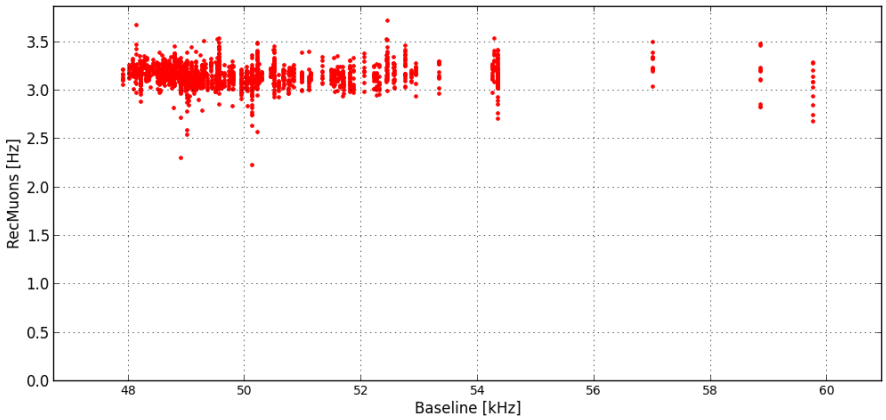

Weights compensating the decreasing efficiency over the time, active OM and baseline are applied.

Line 1-12 Physics Trigger 3N+2T3+GC+TQ+T2+K40+TS0 June2011:

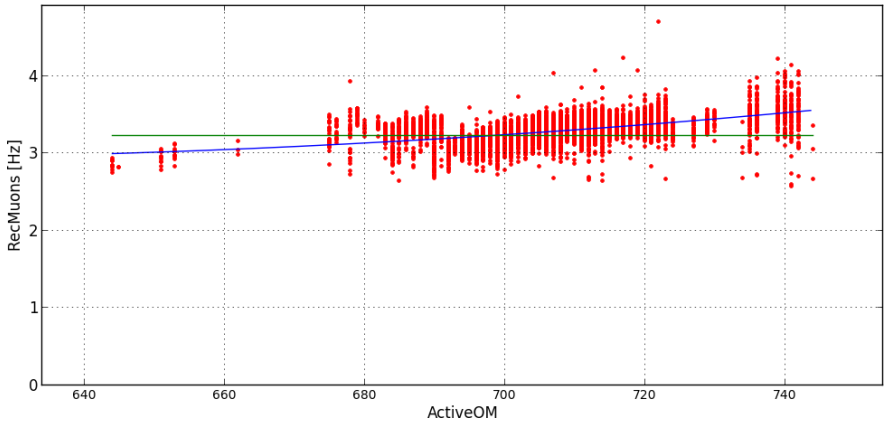

Weights compensating the decreasing efficiency over the time have been applied.

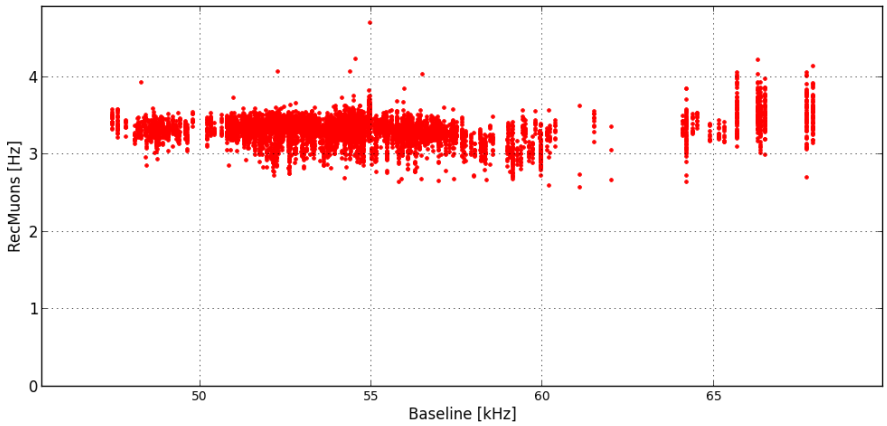

Weights compensating the decreasing efficiency over the time have been applied.

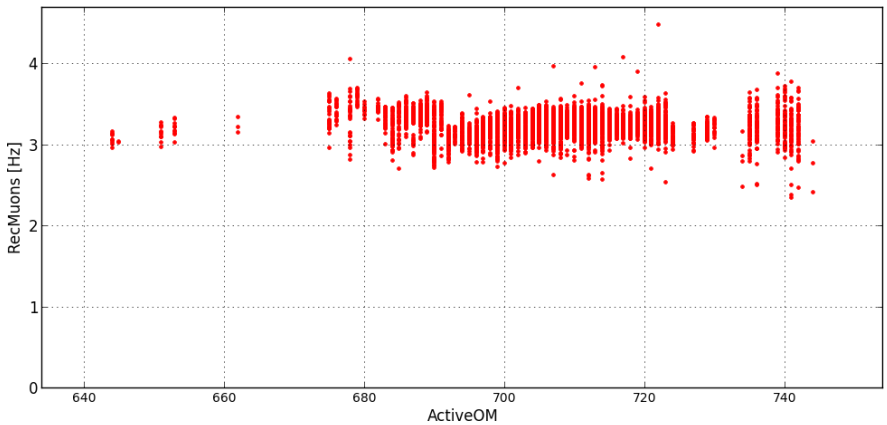

Weights compensating the decreasing efficiency over the time have been applied.

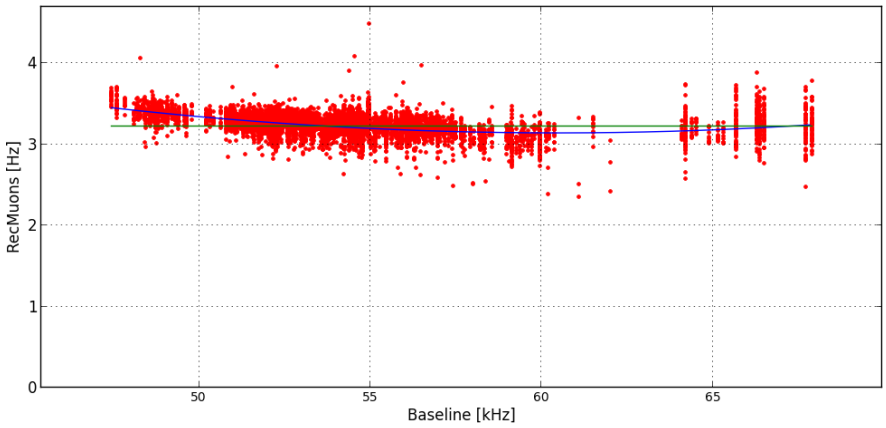

Weights compensating the decreasing efficiency over the time have been applied.

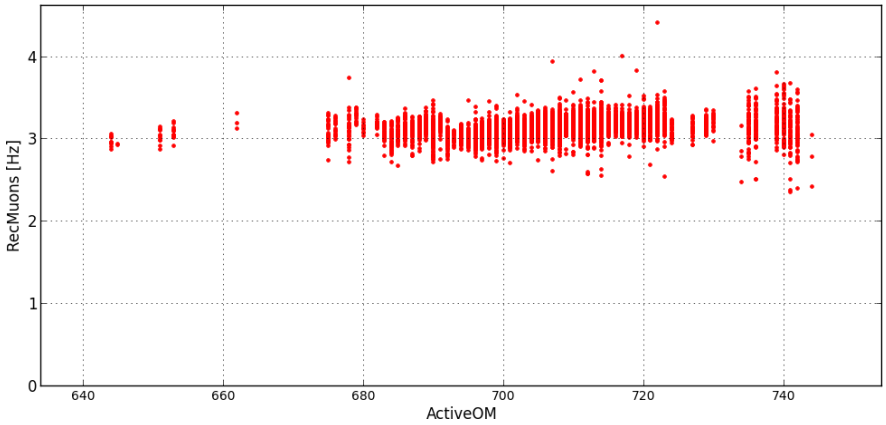

Weights compensating the decreasing efficiency over the time have been applied.

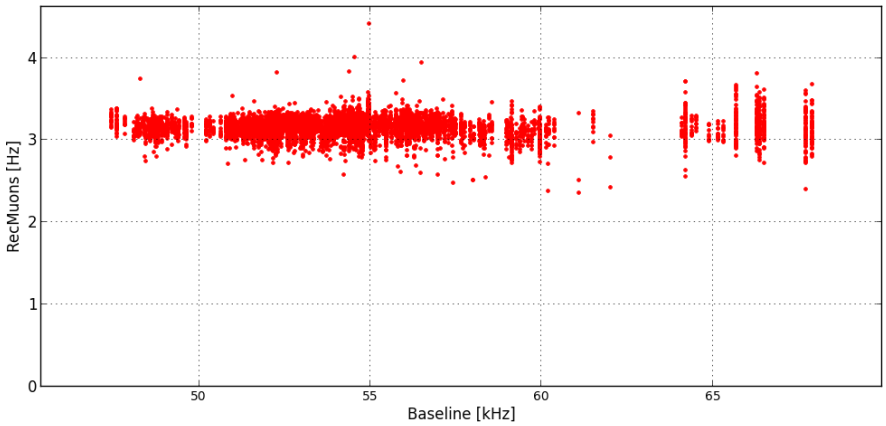

Weights compensating the decreasing efficiency over the time have been applied.

Line 1-12 Physics Trigger 3N+2T3+GC+TQ+T2+K40+TS0 Nov2010:

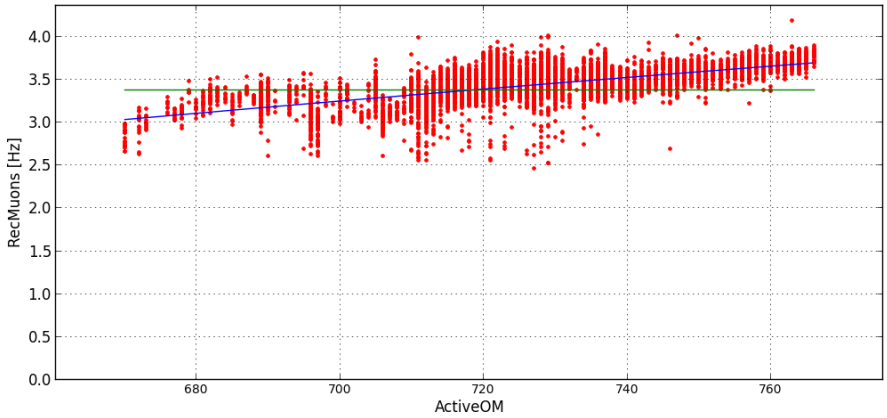

Weights compensating the decreasing efficiency over the time have been applied.

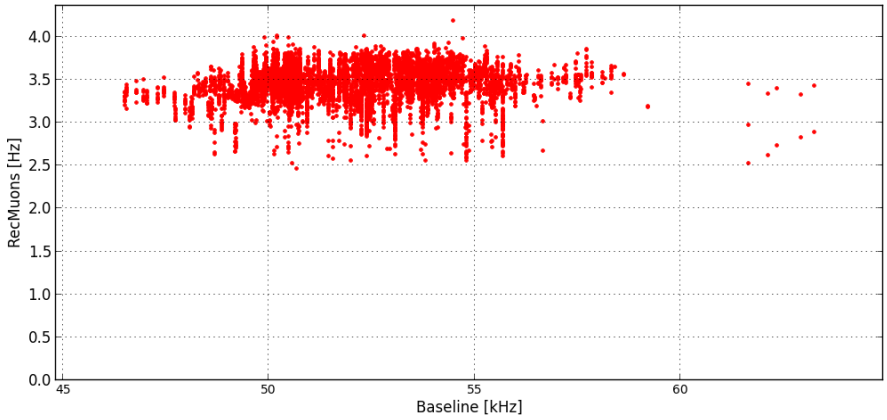

Weights compensating the decreasing efficiency over the time have been applied.

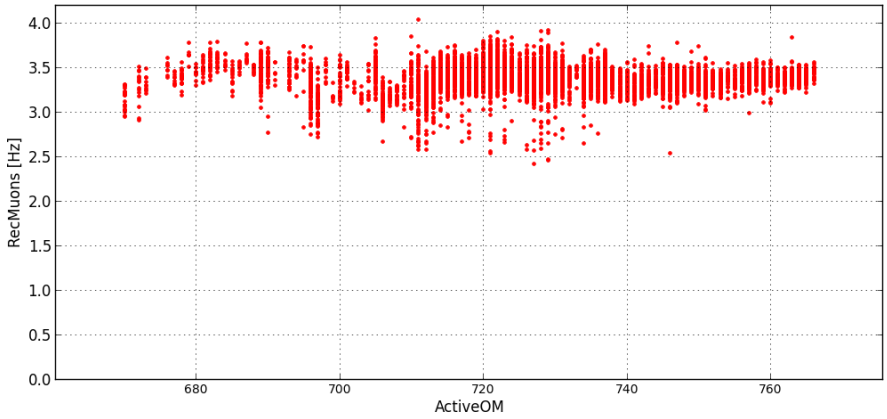

Weights compensating the decreasing efficiency over the time have been applied.

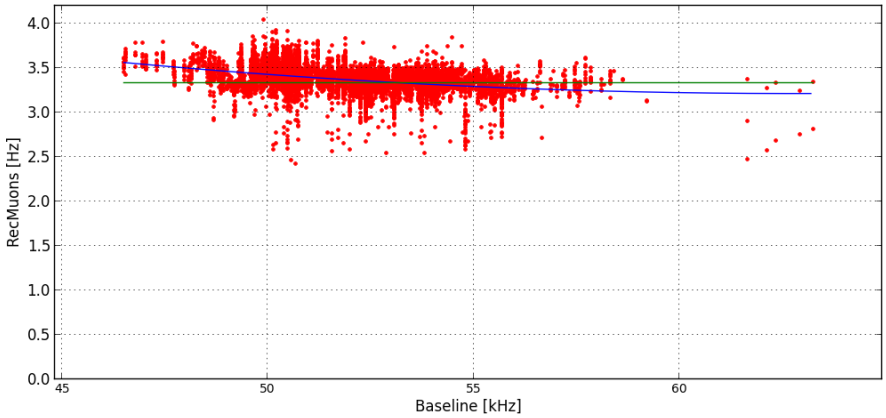

Weights compensating the decreasing efficiency over the time have been applied.

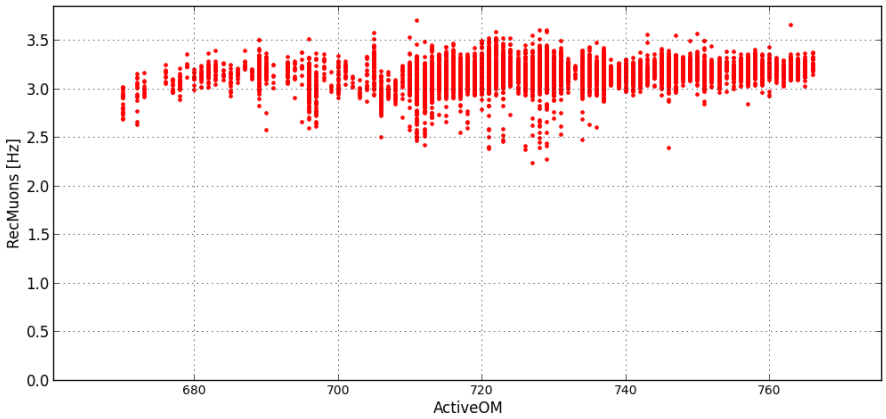

Weights compensating the decreasing efficiency over the time , active OM and baseline are applied.

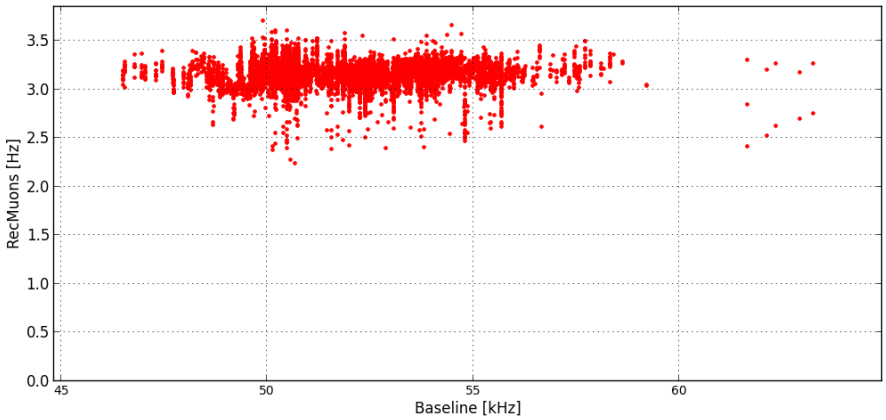

Weights compensating the decreasing efficiency over the time , active OM and baseline are applied.

Line 1-12 Physics Trigger 3N+2T3+K40+TS0 Dec2011:

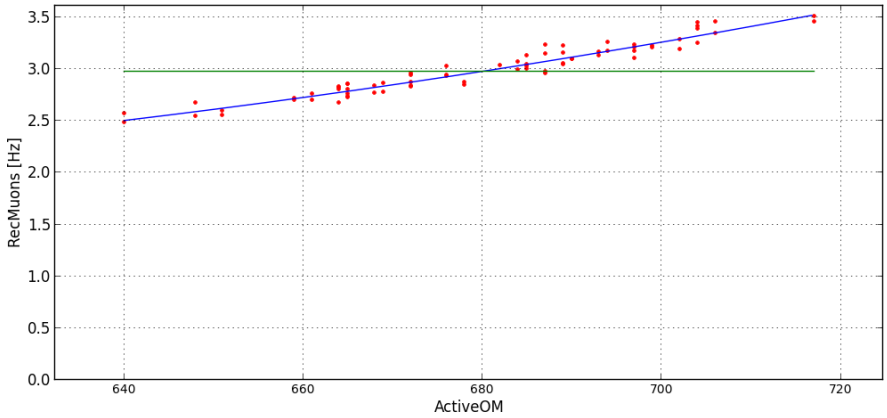

Weights compensating the decreasing efficiency over the time have been applied.

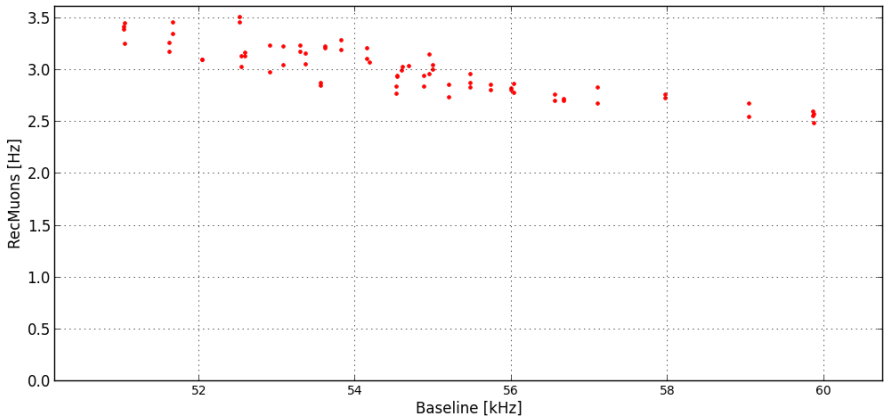

Weights compensating the decreasing efficiency over the time have been applied.

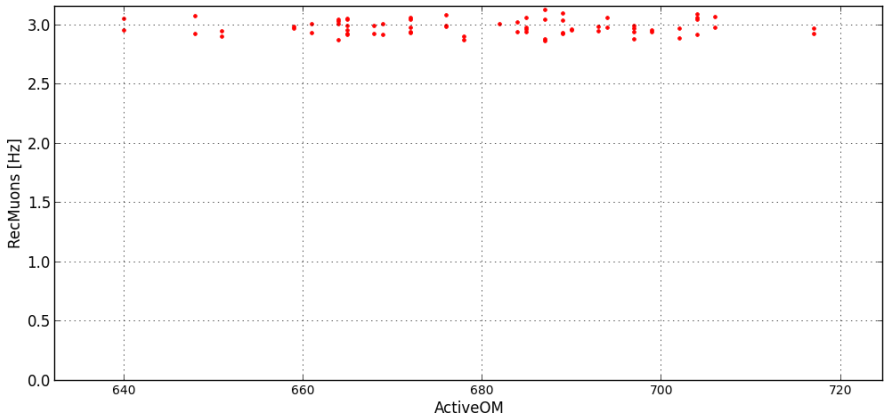

Weights compensating the decreasing efficiency over the time have been applied.

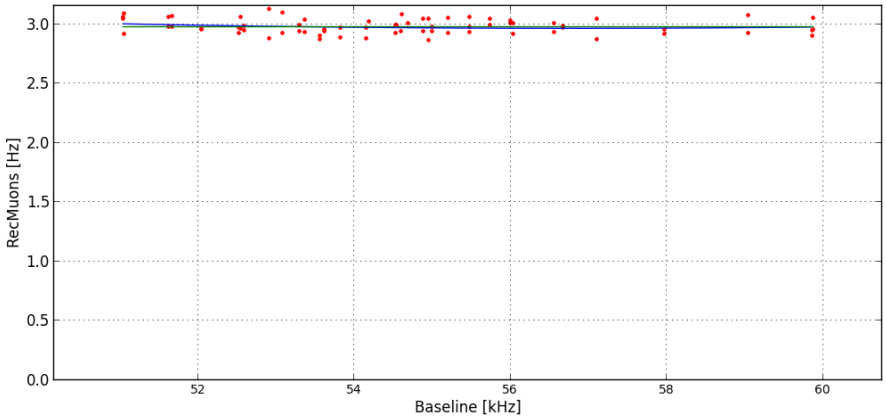

Weights compensating the decreasing efficiency over the time have been applied.

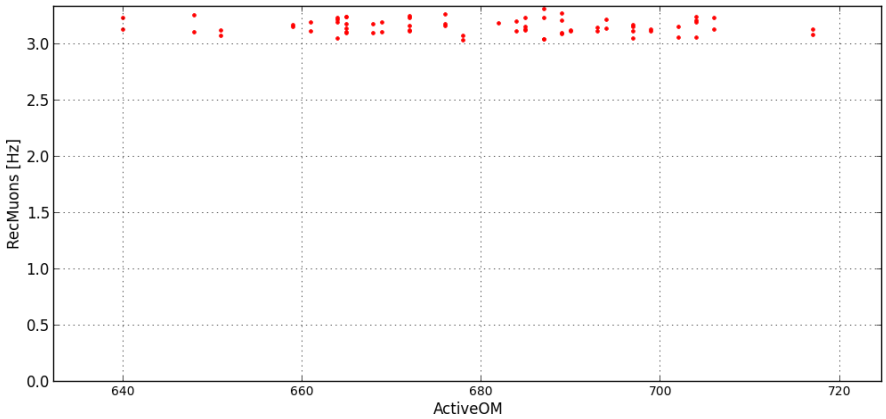

Weights compensating the decreasing efficiency over the time, active OM and baseline are applied.

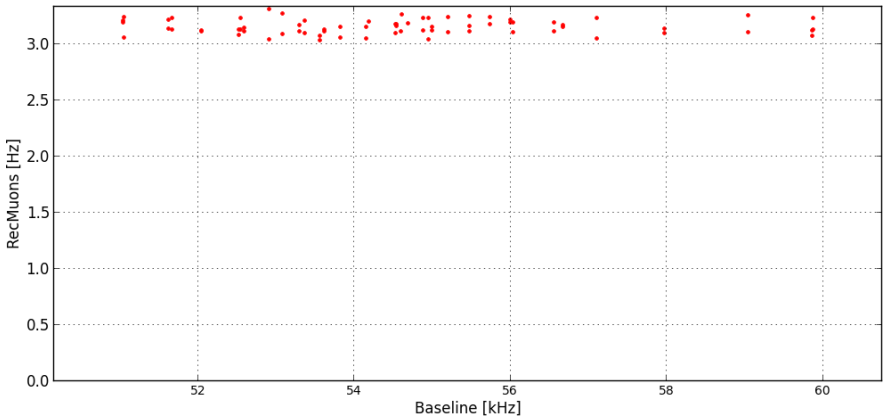

Weights compensating the decreasing efficiency over the time, active OM and baseline are applied.

Line 1-12 Physics Trigger 3N+2T3+K40+TS0 June2011:

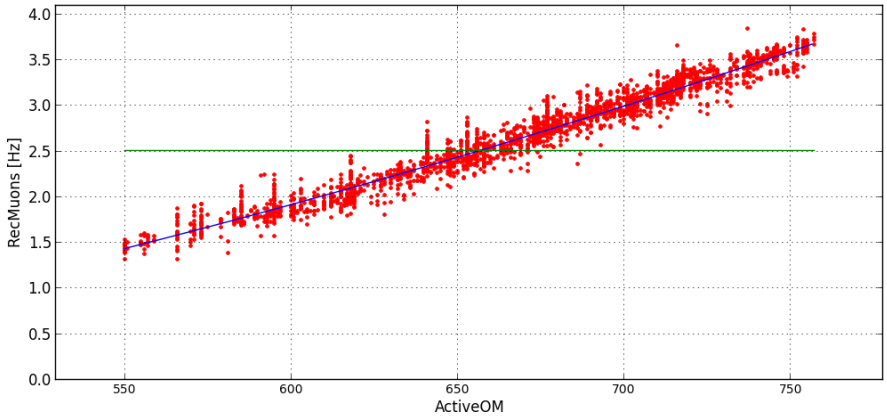

Weights compensating the decreasing efficiency over the time have been applied.

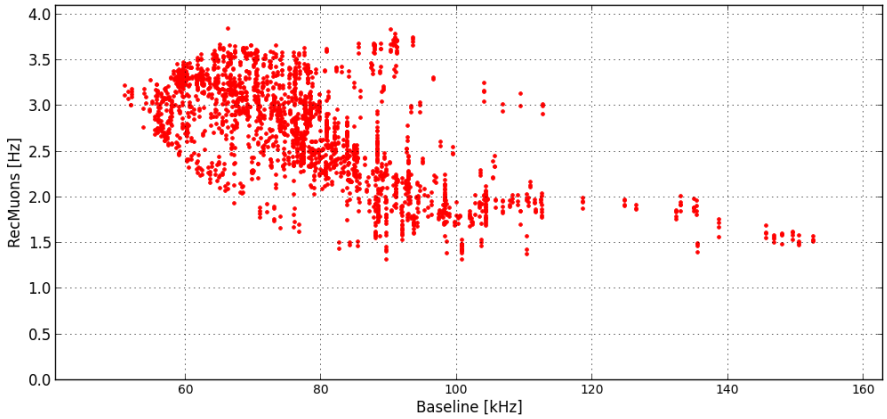

Weights compensating the decreasing efficiency over the time have been applied.

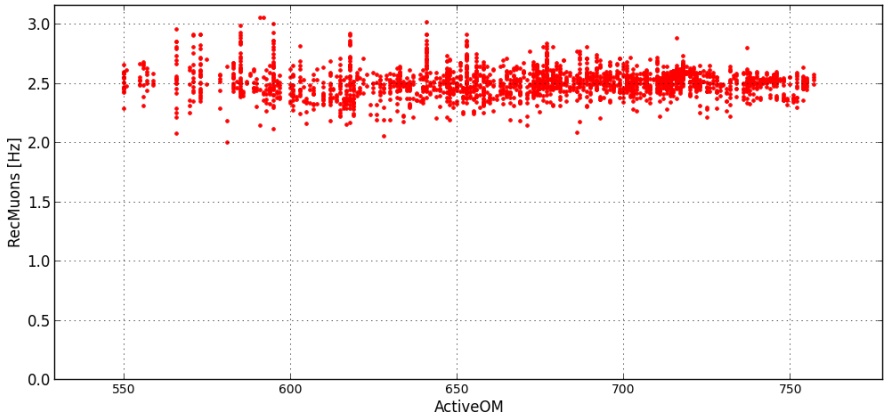

Weights compensating the decreasing efficiency over the time have been applied.

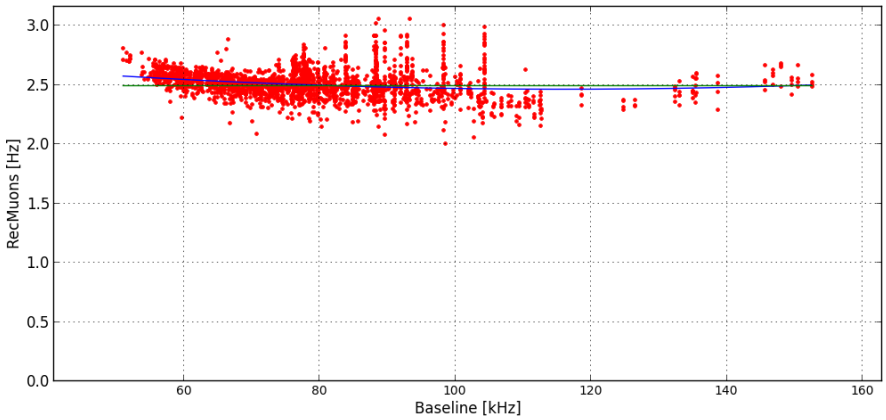

Weights compensating the decreasing efficiency over the time have been applied.

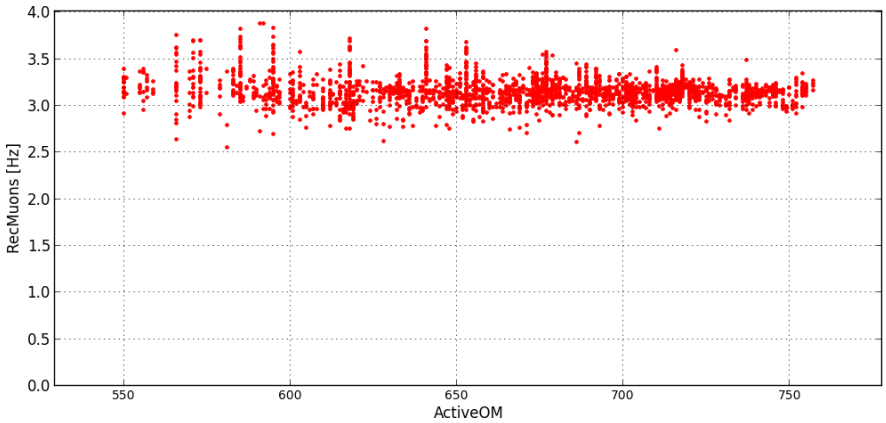

Weights compensating the decreasing efficiency over the time, active OM and baseline are applied.

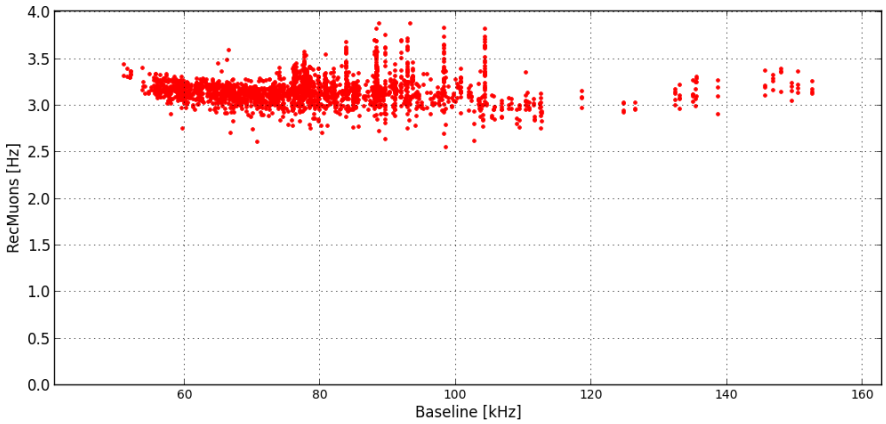

Weights compensating the decreasing efficiency over the time, active OM and baseline are applied.

Line 1-12 Physics Trigger 3N+2T3+K40+TS0 Nov2010:

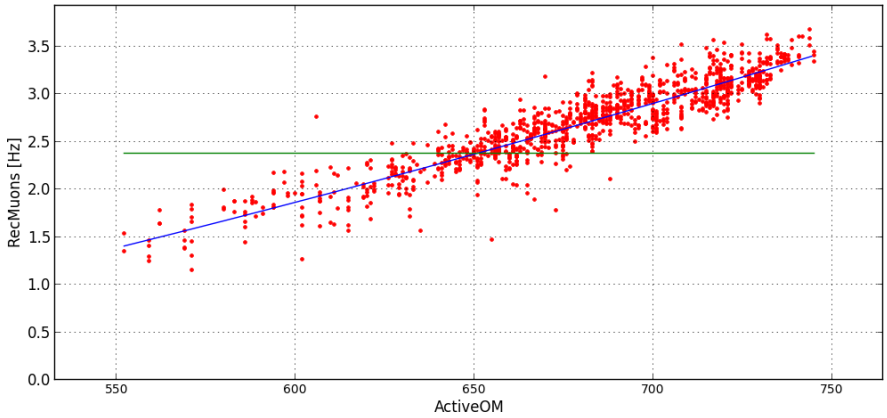

Weights compensating the decreasing efficiency over the time have been applied.

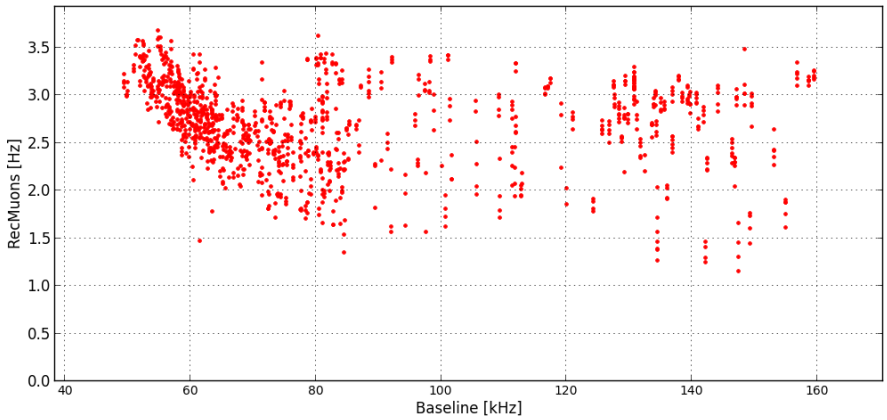

Weights compensating the decreasing efficiency over the time have been applied.

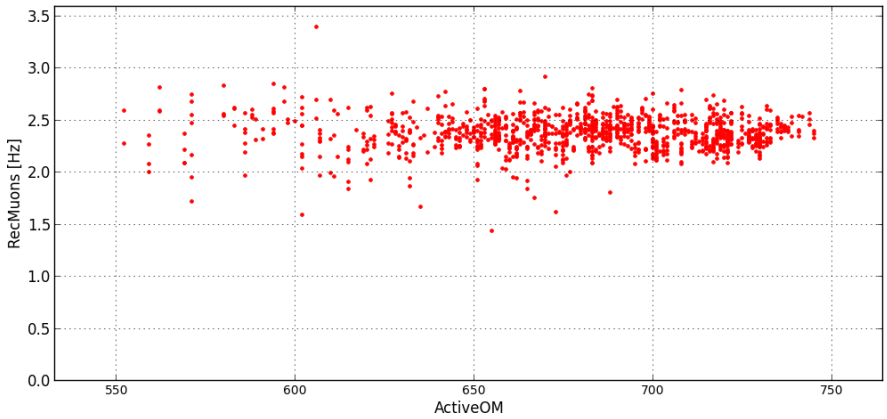

Weights compensating the decreasing efficiency over the time have been applied.

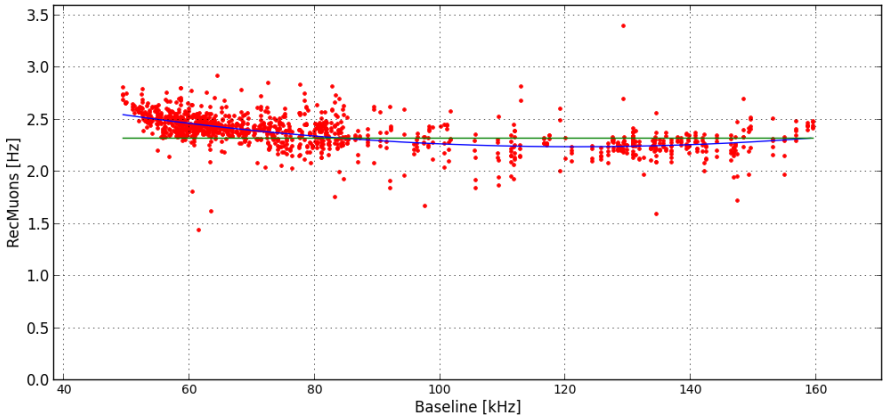

Weights compensating the decreasing efficiency over the time have been applied.

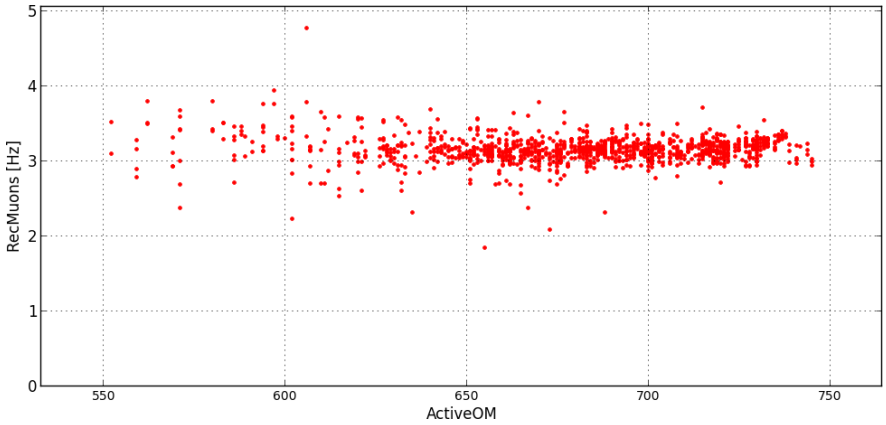

Weights compensating the decreasing efficiency over the time, active OM and baseline are applied.

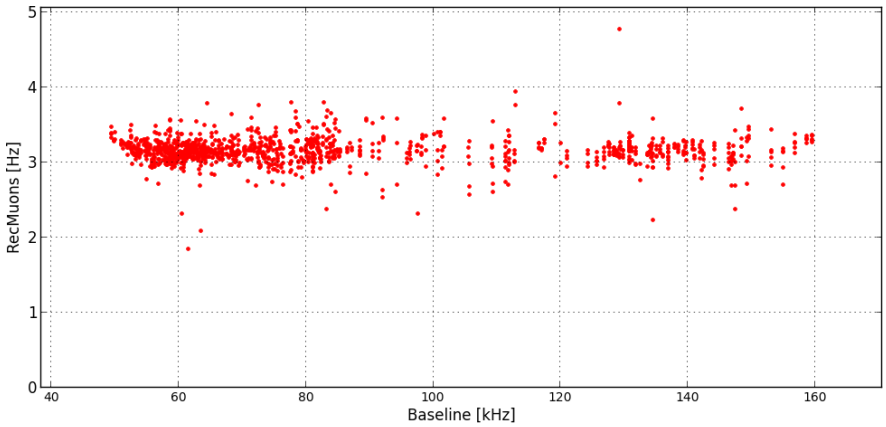

Weights compensating the decreasing efficiency over the time, active OM and baseline are applied.

Appendix F

Fit function and weights for active OM and baseline

The following tables give the parameter of the fitted functions to determine the weight depending on the baseline and the number of active optical modules. The functions were fitted to the muon rate for each run setup. The muon rates show different dependencies for the different run setups. The function used to fit the data is the polynom of second order: $f(x) = ax^2+bx+c$ where x is the baseline in kHz or the number of active optical modules. The parameters a, b and c where fitted and are listed below. The average of the muon rate was calculated and is given in the last column of the tables for each run setup. The weight for a given baseline or number of active OMs is calculated by: $W(x) = \frac{ax^2+bx+c}{<R>}$, where $< R >$ is the mean of the muon rate for that run setup. The parameters are given for the AAFit and BBFit reconstruction method using the trigger T3 and 3D and for the Monte Carlo data using AAFit.

The following tables list the parameter of the function used to calculate the weights for events triggered by the trigger T3 and reconstructed by AAFit.

Run setup for TimeSlice: 2008/05-2009/03, weights for baseline	a	b	c	Average
Physics Trigger - Noisy channels treated	1.5953e-03	-2.1371e-01	9.8545	2.793
Physics Trigger (th2 3pe, old L0 thresholds)	-6.3544e-03	8.1153e-01	-22.2346	3.271
Physics Trigger with GC	4.7216e-03	-5.3689e-01	17.6797	2.477
Physics Trigger (th2 3 p.e.)	1.4271e-03	-2.1196e-01	10.4591	2.752
Physics Trigger (th2 10 p.e.)	1.3462e-04	-2.7921e-02	3.4757	2.215
Physics Trigger - Noisy channels treated + Galactic center trigger	-5.2559e-04	2.7793e-02	3.2881	3.001

Run setup for TimeSlice: 2009/03-2009/07, weights for baseline	a	b	c	Average
Physics Trigger - Noisy channels treated	2.4077e-05	-1.0865e-02	3.6083	2.741
Physics Trigger with GC	1.6177e-04	-3.3741e-02	4.6288	2.971

Run setup for TimeSlice: 2009/07-2009/10, weights for baseline	a	b	c	Average
Physics Trigger 3N+2T3+GC 2009V3.0	6.1497e-04	-9.1006e-02	6.2969	2.971
Physics Trigger 3N+2T3 2009V3.0	-3.9889e-05	4.3439e-03	2.4941	2.581
Physics Trigger 3N+2T3+GC+K40 2009V3.0	1.8950e-02	-2.3035	72.9168	2.928
Physics Trigger with GC	2.2621e-04	-3.9065e-02	4.4286	2.771

Run setup for TimeSlice: 2009/11-2010/02, weights for baseline	a	b	c	Average
Physics Trigger 3N+2T3+GC+T2+TQ+K40 2009V3.1	3.6878e-05	-2.3960e-02	4.6643	3.475
Physics Trigger 3N+2T3+K40 2009V3.1	-2.7958e-04	1.8464e-02	3.1590	3.270
Physics Trigger 3N+2T3+GC+TQ+K40 2009V3.1	5.5709e-03	-6.6226e-01	23.2087	3.552
Physics Trigger 3N+2T3+GC+K40 2009V3.1	2.1688e-03	-2.5814e-01	10.9150	3.282

Run setup for TimeSlice: 2010/02-2010/10, weights for baseline	a	b	c	Average
Physics Trigger 3N+2T3+GC+TQ+T2+K40+TS0	8.4548e-05	-1.2486e-02	3.5409	3.099
Physics Trigger 3N+2T3+GC+TQ+T2+K40 2010V3.0	6.4225e-05	-1.3230e-02	4.2709	3.635
Physics Trigger 3N+2T3+K40 2009V3.1	8.0263e-05	-1.8696e-02	3.7905	2.792
Physics Trigger 3N+2T3+GC+T2+TQ+K40 2009V3.1	1.0350e-04	-2.1888e-02	3.8533	2.839
Physics Trigger 3N+2T3+K40 2010V3.0	4.1544e-05	-9.1366e-03	3.3164	2.838
Physics Trigger 3N+2T3+GC+K40 2010V3.0	3.7980e-05	-7.4925e-03	3.5057	3.150
Physics Trigger 3N+2T3+GC+K40 2009V3.1	1.2454e-04	-2.0990e-02	3.6883	2.840
Physics Trigger 3N+2T3+GC+K40+TS0	-1.0722e-03	1.3292e-01	-1.0241	3.056
Physics Trigger 3N+2T3+GC+TQ+K40 2009V3.1	-8.1312e-05	3.2057e-03	3.2812	3.082
Physics Trigger 3N+2T3+K40+TS0	1.8555e-04	-4.5326e-02	5.1992	2.880

Run setup for TimeSlice: 2010/11-2011/12, weights for baseline	a	b	c	Average
Physics Trigger 3N+2T3+GC+TQ+T2+K40+T0 Dec2011	5.5987e-03	-6.0568e-01	19.4297	3.115
Physics Trigger 3N+2T3+K40+TS0 June2011	2.6523e-05	-6.1373e-03	2.8187	2.492
Physics Trigger 3N+2T3+K40+TS0 Nov2010	5.8938e-05	-1.4337e-02	3.1104	2.315
Physics Trigger 3N+2T3+K40+TS0 Dec2011	1.1424e-03	-1.2977e-01	6.6518	2.976
Physics Trigger 3N+2T3+GC+TQ+K40+TS0 Dec2011	-9.5868e-03	9.9407e-01	-22.4149	3.352
Physics Trigger 3N+2T3+K40+TS0 not yet tuned	-2.1377e-04	2.6095e-02	1.9060	2.695

Run setup for TimeSlice: 2012/01-2012/12, weights for baseline	a	b	c	Average
Physics Trigger 3N+2T3+GC+TQ+K40+TS0 SNbuffer Feb2012	3.5866e-04	-7.5805e-02	6.5140	2.793
Physics Trigger 3N+2T3+K40+TS0 SNbuffer Dec2012	9.8131e-05	-2.3183e-02	4.4774	3.242
Physics Trigger 3N+2T3+K40+TS0 Dec2011	2.5985e-04	-5.8880e-02	5.1901	2.147
Physics Trigger 3N+2T3+GC+TQ+K40+TS0 Dec2011 noSNbuffer	-2.4459e-03	1.2544e-01	3.7337	3.340
Physics Trigger 3N+2T3+K40+TS0 SNbuffer Feb2012	9.2676e-05	-2.1357e-02	4.1001	2.970
Physics Trigger 3N+2T3+GC+K40+TS0 Dec2011 noSNbuffer	-3.1806e-03	3.5742e-01	-6.6320	3.362
Physics Trigger 3N+2T3+GC+K40+TS0 SNbuffer Nov2012	-1.1485e-03	1.6957e-01	-3.3443	2.896
Physics Trigger 3N+2T3+GC+K40+TS0 SNbuffer Feb2012	3.5147e-04	-4.9078e-02	4.9305	3.276

Run setup for TimeSlice: 2013/01-2013/12, weights for baseline	a	b	c	Average
Physics Trigger 3N+2T3+K40+TS0 SNbuffer Jun2013	-3.3342e-05	-1.0101e-02	4.3249	2.766
Physics Trigger 3N+2T3+GC+TQ+K40+TS0 SNbuffer Jun2013	-2.7318e-03	3.5442e-01	-8.1173	3.089
Physics Trigger 3N+2T3+GC+K40+TS0 SNbuffer Jun2013	-9.8789e-04	1.3399e-01	-1.2660	3.242
Physics Trigger 3N+2T3+K40+TS0 SNbuffer Dec2012	2.0950e-04	-6.7092e-02	6.6720	2.231
Physics Trigger 3N+2T3+GC+TQ+K40+TS0 SNbuffer Dec2012	-3.8935e-03	3.8890e-01	-6.3409	3.321
Physics Trigger 3N+2T3+K40+TS0 SNbuffer May2013	-2.7673e-05	4.7899e-03	3.0503	3.214
Physics Trigger 3N+2T3+GC+K40+TS0 SNbuffer Dec2012	2.3487e-03	-2.9212e-01	12.1626	3.155
Physics Trigger 3N+2T3+GC+K40+TS0 SNbuffer May2013	-1.0623e-04	1.5232e-02	2.7589	3.305

Run setup for TimeSlice: 2008/05-2009/03, weights for active OM	a	b	c	Average
Physics Trigger - Noisy channels treated	1.5953e-03	-2.1371e-01	9.8545	2.793
Physics Trigger (th2 3pe, old L0 thresholds)	-6.3544e-03	8.1153e-01	-22.2346	3.271
Physics Trigger with GC	4.7216e-03	-5.3689e-01	17.6797	2.477
Physics Trigger (th2 3 p.e.)	1.4271e-03	-2.1196e-01	10.4591	2.752
Physics Trigger (th2 10 p.e.)	1.3462e-04	-2.7921e-02	3.4757	2.215
Physics Trigger - Noisy channels treated + Galactic center trigger	-5.2559e-04	2.7793e-02	3.2881	3.001

Run setup for TimeSlice: 2009/03-2009/07, weights for active OM	a	b	c	Average
Physics Trigger - Noisy channels treated	2.4077e-05	-1.0865e-02	3.6083	2.741
Physics Trigger with GC	1.6177e-04	-3.3741e-02	4.6288	2.971

Run setup for TimeSlice: 2009/07-2009/10, weights for active OM	a	b	c	Average
Physics Trigger 3N+2T3+GC 2009V3.0	6.1497e-04	-9.1006e-02	6.2969	2.971
Physics Trigger 3N+2T3 2009V3.0	-3.9889e-05	4.3439e-03	2.4941	2.581
Physics Trigger 3N+2T3+GC+K40 2009V3.0	1.8950e-02	-2.3035	72.9168	2.928
Physics Trigger with GC	2.2621e-04	-3.9065e-02	4.4286	2.771

Run setup for TimeSlice: 2009/11-2010/02, weights for active OM	a	b	c	Average
Physics Trigger 3N+2T3+GC+T2+TQ+K40 2009V3.1	3.6878e-05	-2.3960e-02	4.6643	3.475
Physics Trigger 3N+2T3+K40 2009V3.1	-2.7958e-04	1.8464e-02	3.1590	3.270
Physics Trigger 3N+2T3+GC+TQ+K40 2009V3.1	5.5709e-03	-6.6226e-01	23.2087	3.552
Physics Trigger 3N+2T3+GC+K40 2009V3.1	2.1688e-03	-2.5814e-01	10.9150	3.282

Run setup for TimeSlice: 2010/02-2010/10, weights for active OM	a	b	c	Average
Physics Trigger 3N+2T3+GC+TQ+T2+K40+TS0	8.4548e-05	-1.2486e-02	3.5409	3.099
Physics Trigger 3N+2T3+GC+TQ+T2+K40 2010V3.0	6.4225e-05	-1.3230e-02	4.2709	3.635
Physics Trigger 3N+2T3+K40 2009V3.1	8.0263e-05	-1.8696e-02	3.7905	2.792
Physics Trigger 3N+2T3+GC+T2+TQ+K40 2009V3.1	1.0350e-04	-2.1888e-02	3.8533	2.839
Physics Trigger 3N+2T3+K40 2010V3.0	4.1544e-05	-9.1366e-03	3.3164	2.838
Physics Trigger 3N+2T3+GC+K40 2010V3.0	3.7980e-05	-7.4925e-03	3.5057	3.150
Physics Trigger 3N+2T3+GC+K40 2009V3.1	1.2454e-04	-2.0990e-02	3.6883	2.840
Physics Trigger 3N+2T3+GC+K40+TS0	-1.0722e-03	1.3292e-01	-1.0241	3.056
Physics Trigger 3N+2T3+GC+TQ+K40 2009V3.1	-8.1312e-05	3.2057e-03	3.2812	3.082
Physics Trigger 3N+2T3+K40+TS0	1.8555e-04	-4.5326e-02	5.1992	2.880

Run setup for TimeSlice: 2010/11-2011/12, weights for active OM	a	b	c	Average
Physics Trigger 3N+2T3+GC+TQ+T2+K40+T0 Dec2011	5.5987e-03	-6.0568e-01	19.4297	3.115
Physics Trigger 3N+2T3+K40+TS0 June2011	2.6523e-05	-6.1373e-03	2.8187	2.492
Physics Trigger 3N+2T3+K40+TS0 Nov2010	5.8938e-05	-1.4337e-02	3.1104	2.315
Physics Trigger 3N+2T3+K40+TS0 Dec2011	1.1424e-03	-1.2977e-01	6.6518	2.976
Physics Trigger 3N+2T3+GC+TQ+K40+TS0 Dec2011	-9.5868e-03	9.9407e-01	-22.4149	3.352
Physics Trigger 3N+2T3+K40+TS0 not yet tuned	-2.1377e-04	2.6095e-02	1.9060	2.695

Run setup for TimeSlice: 2012/01-2012/12, weights for active OM	a	b	c	Average
Physics Trigger 3N+2T3+GC+TQ+K40+TS0 SNbuffer Feb2012	3.5866e-04	-7.5805e-02	6.5140	2.793
Physics Trigger 3N+2T3+K40+TS0 SNbuffer Dec2012	9.8131e-05	-2.3183e-02	4.4774	3.242
Physics Trigger 3N+2T3+K40+TS0 Dec2011	2.5985e-04	-5.8880e-02	5.1901	2.147
Physics Trigger 3N+2T3+GC+TQ+K40+TS0 Dec2011 noSNbuffer	-2.4459e-03	1.2544e-01	3.7337	3.340
Physics Trigger 3N+2T3+K40+TS0 SNbuffer Feb2012	9.2676e-05	-2.1357e-02	4.1001	2.970
Physics Trigger 3N+2T3+GC+K40+TS0 Dec2011 noSNbuffer	-3.1806e-03	3.5742e-01	-6.6320	3.362
Physics Trigger 3N+2T3+GC+K40+TS0 SNbuffer Nov2012	-1.1485e-03	1.6957e-01	-3.3443	2.896
Physics Trigger 3N+2T3+GC+K40+TS0 SNbuffer Feb2012	3.5147e-04	-4.9078e-02	4.9305	3.276

Run setup for TimeSlice: 2013/01-2013/12, weights for active OM	a	b	c	Average
Physics Trigger 3N+2T3+K40+TS0 SNbuffer Jun2013	-3.3342e-05	-1.0101e-02	4.3249	2.766
Physics Trigger 3N+2T3+GC+TQ+K40+TS0 SNbuffer Jun2013	-2.7318e-03	3.5442e-01	-8.1173	3.089
Physics Trigger 3N+2T3+GC+K40+TS0 SNbuffer Jun2013	-9.8789e-04	1.3399e-01	-1.2660	3.242
Physics Trigger 3N+2T3+K40+TS0 SNbuffer Dec2012	2.0950e-04	-6.7092e-02	6.6720	2.231
Physics Trigger 3N+2T3+GC+TQ+K40+TS0 SNbuffer Dec2012	-3.8935e-03	3.8890e-01	-6.3409	3.321
Physics Trigger 3N+2T3+K40+TS0 SNbuffer May2013	-2.7673e-05	4.7899e-03	3.0503	3.214
Physics Trigger 3N+2T3+GC+K40+TS0 SNbuffer Dec2012	2.3487e-03	-2.9212e-01	12.1626	3.155
Physics Trigger 3N+2T3+GC+K40+TS0 SNbuffer May2013	-1.0623e-04	1.5232e-02	2.7589	3.305

The following tables list the parameter of the function used to calculate the weights for events triggered by the trigger 3DScan and reconstructed by AAFit.

Run setup for TimeSlice: 2008/05-2009/03, weights for baseline	a	b	c	Average
Physics Trigger - Noisy channels treated	1.1032e-03	-1.4044e-01	6.3886	1.958
Physics Trigger (th2 3pe, old L0 thresholds)	-4.3983e-03	5.6170e-01	-15.2133	2.440
Physics Trigger with GC	3.8407e-03	-4.3151e-01	13.7780	1.703
Physics Trigger (th2 3 p.e.)	1.5119e-03	-2.0844e-01	9.6828	2.564
Physics Trigger (th2 10 p.e.)	-3.0117e-04	4.0294e-02	5.3219e-02	1.384
Physics Trigger - Noisy channels treated + Galactic center trigger	6.3398e-05	-2.2436e-02	3.2650	2.132

Run setup for TimeSlice: 2009/03-2009/07, weights for baseline	a	b	c	Average
Physics Trigger - Noisy channels treated	-1.6307e-05	-6.3455e-04	2.2614	1.991
Physics Trigger with GC	8.4283e-05	-1.7887e-02	3.0548	2.164
Physics Trigger 3N only	-2.9626e-05	5.1299e-03	1.4962	1.678

Run setup for TimeSlice: 2009/07-2009/10, weights for baseline	a	b	c	Average
Physics Trigger 3N+2T3+GC 2009V3.0	-3.7136e-04	5.2199e-02	1.8723e-01	2.002
Physics Trigger 3N+2T3 2009V3.0	-3.4454e-04	4.9853e-02	-3.1658e-03	1.732
Physics Trigger 3N+2T3+GC+K40 2009V3.0	1.5462e-02	-1.8832	59.3530	2.026
Physics Trigger 3N only	7.1625e-05	-1.4342e-02	2.1184	1.428

Run setup for TimeSlice: 2009/11-2010/02, weights for baseline	a	b	c	Average
Physics Trigger 3N+2T3+GC+T2+TQ+K40 2009V3.1	-3.5219e-04	2.4234e-02	2.1597	2.436
Physics Trigger 3N+2T3+K40 2009V3.1	3.2363e-04	-4.6470e-02	3.8942	2.285
Physics Trigger 3N+2T3+GC+TQ+K40 2009V3.1	3.0264e-03	-3.5761e-01	13.0670	2.514
Physics Trigger 3N+2T3+GC+K40 2009V3.1	1.6116e-03	-1.9031e-01	7.8858	2.302

Run setup for TimeSlice: 2010/02-2010/10, weights for baseline	a	b	c	Average
Physics Trigger 3N+2T3+GC+TQ+T2+K40+TS0	4.3365e-05	-4.8264e-03	2.2503	2.117
Physics Trigger 3N+2T3+GC+TQ+T2+K40 2010V3.0	1.9102e-04	-2.8623e-02	3.5992	2.544
Physics Trigger 3N+2T3+K40 2009V3.1	4.4529e-05	-1.0036e-02	2.3031	1.784
Physics Trigger 3N+2T3+GC+T2+TQ+K40 2009V3.1	1.0395e-04	-1.6723e-02	2.5630	1.916
Physics Trigger 3N+2T3+K40 2010V3.0	-8.5689e-06	1.5420e-03	1.6999	1.764
Physics Trigger 3N+2T3+GC+K40 2010V3.0	4.7611e-05	-7.6057e-03	2.6334	2.342
Physics Trigger 3N+2T3+GC+K40 2009V3.1	5.6311e-05	-9.3351e-03	2.1632	1.830
Physics Trigger 3N+2T3+GC+K40+TS0	-9.8726e-04	1.2522e-01	-1.9132	2.026
Physics Trigger 3N+2T3+GC+TQ+K40 2009V3.1	-1.9229e-04	2.2144e-02	1.6404	2.209
Physics Trigger 3N+2T3+K40+TS0	1.9973e-04	-3.7566e-02	3.6287	1.959
Physics Trigger 3N+K40 2009V3.1	5.9886e-05	-1.5280e-02	2.9757	2.055

Run setup for TimeSlice: 2010/11-2011/12, weights for baseline	a	b	c	Average
Physics Trigger 3N+2T3+GC+TQ+T2+K40+T0 Dec2011	3.3462e-03	-3.6106e-01	11.8589	2.158
Physics Trigger 3N+2T3+GC+TQ+T2+K40+TS0 Nov2010	-5.9612e-04	3.9945e-02	1.8744	2.257
Physics Trigger 3N+2T3+GC+K40+TS0 Nov2010	8.9171e-04	-1.1545e-01	5.8689	2.194
Physics Trigger 3N+2T3+K40+TS0 June2011	-2.6245e-05	4.5529e-03	1.4905	1.659
Physics Trigger 3N+2T3+K40+TS0 Nov2010	2.1707e-05	-5.6477e-03	1.8044	1.473
Physics Trigger 3N+2T3+GC+TQ+T2+K40+TS0 June2011	1.5230e-03	-1.8087e-01	7.5382	2.226
Physics Trigger 3N+2T3+GC+K40+TS0 June2011	-2.6725e-05	-6.3324e-04	2.3685	2.178
Physics Trigger 3N+2T3+K40+TS0 Dec2011	5.3478e-04	-6.1225e-02	3.8360	2.089
Physics Trigger 3N+2T3+GC+TQ+K40+TS0 Dec2011	-1.1444e-02	1.1825	-28.2377	2.308
Physics Trigger 3N+K40+TS0 Nov2010	5.7344e-05	-1.2703e-02	2.7916	2.136

Run setup for TimeSlice: 2012/01-2012/12, weights for baseline	a	b	c	Average
Physics Trigger 3N+2T3+GC+TQ+K40+TS0 SNbuffer Feb2012	2.6684e-04	-5.5311e-02	4.5998	1.935
Physics Trigger 3N+2T3+K40+TS0 SNbuffer Nov2012	-1.1856e-04	1.7953e-02	8.7734e-01	1.501
Physics Trigger 3N+2T3+K40+TS0 SNbuffer Dec2012	5.9642e-05	-1.4577e-02	2.9985	2.201
Physics Trigger 3N+2T3+K40+TS0 Dec2011	1.8012e-04	-4.0696e-02	3.6679	1.571
Physics Trigger 3N+2T3+GC+TQ+K40+TS0 Dec2011 noSNbuffer	-4.5757e-03	3.9122e-01	-5.4449	2.303
Physics Trigger 3N+2T3+GC+TQ+K40+TS0 Dec2011	2.0260e-04	-3.1539e-02	3.4623	2.307
Physics Trigger 3N+2T3+K40+TS0 SNbuffer Feb2012	6.0174e-05	-1.4167e-02	2.8670	2.101
Physics Trigger 3N+2T3+GC+K40+TS0 Dec2011 noSNbuffer	-1.8892e-03	2.1213e-01	-3.6098	2.317
Physics Trigger 3N+2T3+GC+K40+TS0 SNbuffer Nov2012	-9.1004e-04	1.3421e-01	-2.9543	1.979
Physics Trigger 3N+2T3+GC+K40+TS0 SNbuffer Feb2012	2.8191e-04	-3.9506e-02	3.6375	2.300
Physics Trigger 3N+K40+TS0 SNbuffer Feb2012	-7.2731e-06	3.0391e-03	1.5048	1.767
Physics Trigger 3N+K40+TS0 SNbuffer Dec2012	5.0483e-06	-1.3759e-03	2.6123	2.531

Run setup for TimeSlice: 2013/01-2013/12, weights for baseline	a	b	c	Average
Physics Trigger 3N+2T3+K40+TS0 SNbuffer Jun2013	-3.3342e-05	-1.0101e-02	4.3249	2.766
Physics Trigger 3N+2T3+GC+TQ+K40+TS0 SNbuffer Jun2013	-2.7318e-03	3.5442e-01	-8.1173	3.089
Physics Trigger 3N+2T3+GC+K40+TS0 SNbuffer Jun2013	-9.8789e-04	1.3399e-01	-1.2660	3.242
Physics Trigger 3N+2T3+K40+TS0 SNbuffer Dec2012	2.0950e-04	-6.7092e-02	6.6720	2.231
Physics Trigger 3N+2T3+GC+TQ+K40+TS0 SNbuffer Dec2012	-3.8935e-03	3.8890e-01	-6.3409	3.321
Physics Trigger 3N+2T3+K40+TS0 SNbuffer May2013	-2.7673e-05	4.7899e-03	3.0503	3.214
Physics Trigger 3N+2T3+GC+K40+TS0 SNbuffer Dec2012	2.3487e-03	-2.9212e-01	12.1626	3.155

Run setup for TimeSlice: 2008/05-2009/03, weights for active OM	a	b	c	Average
Physics Trigger - Noisy channels treated	1.1032e-03	-1.4044e-01	6.3886	1.958
Physics Trigger (th2 3pe, old L0 thresholds)	-4.3983e-03	5.6170e-01	-15.2133	2.440
Physics Trigger with GC	3.8407e-03	-4.3151e-01	13.7780	1.703
Physics Trigger (th2 3 p.e.)	1.5119e-03	-2.0844e-01	9.6828	2.564
Physics Trigger (th2 10 p.e.)	-3.0117e-04	4.0294e-02	5.3219e-02	1.384
Physics Trigger - Noisy channels treated + Galactic center trigger	6.3398e-05	-2.2436e-02	3.2650	2.132

Run setup for TimeSlice: 2009/03-2009/07, weights for active OM	a	b	c	Average
Physics Trigger - Noisy channels treated	-1.6307e-05	-6.3455e-04	2.2614	1.991
Physics Trigger with GC	8.4283e-05	-1.7887e-02	3.0548	2.164
Physics Trigger 3N only	-2.9626e-05	5.1299e-03	1.4962	1.678

Run setup for TimeSlice: 2009/07-2009/10, weights for active OM	a	b	c	Average
Physics Trigger 3N+2T3+GC 2009V3.0	-3.7136e-04	5.2199e-02	1.8723e-01	2.002
Physics Trigger 3N+2T3 2009V3.0	-3.4454e-04	4.9853e-02	-3.1658e-03	1.732
Physics Trigger 3N+2T3+GC+K40 2009V3.0	1.5462e-02	-1.8832	59.3530	2.026
Physics Trigger 3N only	7.1625e-05	-1.4342e-02	2.1184	1.428

Run setup for TimeSlice: 2009/11-2010/02, weights for active OM	a	b	c	Average
Physics Trigger 3N+2T3+GC+T2+TQ+K40 2009V3.1	-3.5219e-04	2.4234e-02	2.1597	2.436
Physics Trigger 3N+2T3+K40 2009V3.1	3.2363e-04	-4.6470e-02	3.8942	2.285
Physics Trigger 3N+2T3+GC+TQ+K40 2009V3.1	3.0264e-03	-3.5761e-01	13.0670	2.514
Physics Trigger 3N+2T3+GC+K40 2009V3.1	1.6116e-03	-1.9031e-01	7.8858	2.302

Run setup for TimeSlice: 2010/02-2010/10, weights for active OM	a	b	c	Average
Physics Trigger 3N+2T3+GC+TQ+T2+K40+TS0	4.3365e-05	-4.8264e-03	2.2503	2.117
Physics Trigger 3N+2T3+GC+TQ+T2+K40 2010V3.0	1.9102e-04	-2.8623e-02	3.5992	2.544
Physics Trigger 3N+2T3+K40 2009V3.1	4.4529e-05	-1.0036e-02	2.3031	1.784
Physics Trigger 3N+2T3+GC+T2+TQ+K40 2009V3.1	1.0395e-04	-1.6723e-02	2.5630	1.916
Physics Trigger 3N+2T3+K40 2010V3.0	-8.5689e-06	1.5420e-03	1.6999	1.764
Physics Trigger 3N+2T3+GC+K40 2010V3.0	4.7611e-05	-7.6057e-03	2.6334	2.342
Physics Trigger 3N+2T3+GC+K40 2009V3.1	5.6311e-05	-9.3351e-03	2.1632	1.830
Physics Trigger 3N+2T3+GC+K40+TS0	-9.8726e-04	1.2522e-01	-1.9132	2.026
Physics Trigger 3N+2T3+GC+TQ+K40 2009V3.1	-1.9229e-04	2.2144e-02	1.6404	2.209
Physics Trigger 3N+2T3+K40+TS0	1.9973e-04	-3.7566e-02	3.6287	1.959
Physics Trigger 3N+K40 2009V3.1	5.9886e-05	-1.5280e-02	2.9757	2.055

Run setup for TimeSlice: 2010/11-2011/12, weights for active OM	a	b	c	Average
Physics Trigger 3N+2T3+GC+TQ+T2+K40+T0 Dec2011	3.3462e-03	-3.6106e-01	11.8589	2.158
Physics Trigger 3N+2T3+GC+TQ+T2+K40+TS0 Nov2010	-5.9612e-04	3.9945e-02	1.8744	2.257
Physics Trigger 3N+2T3+GC+K40+TS0 Nov2010	8.9171e-04	-1.1545e-01	5.8689	2.194
Physics Trigger 3N+2T3+K40+TS0 June2011	-2.6245e-05	4.5529e-03	1.4905	1.659
Physics Trigger 3N+2T3+K40+TS0 Nov2010	2.1707e-05	-5.6477e-03	1.8044	1.473
Physics Trigger 3N+2T3+GC+TQ+T2+K40+TS0 June2011	1.5230e-03	-1.8087e-01	7.5382	2.226
Physics Trigger 3N+2T3+GC+K40+TS0 June2011	-2.6725e-05	-6.3324e-04	2.3685	2.178
Physics Trigger 3N+2T3+K40+TS0 Dec2011	5.3478e-04	-6.1225e-02	3.8360	2.089
Physics Trigger 3N+2T3+GC+TQ+K40+TS0 Dec2011	-1.1444e-02	1.1825	-28.2377	2.308
Physics Trigger 3N+K40+TS0 Nov2010	5.7344e-05	-1.2703e-02	2.7916	2.136

Run setup for TimeSlice: 2012/01-2012/12, weights for active OM	a	b	c	Average
Physics Trigger 3N+2T3+GC+TQ+K40+TS0 SNbuffer Feb2012	2.6684e-04	-5.5311e-02	4.5998	1.935
Physics Trigger 3N+2T3+K40+TS0 SNbuffer Nov2012	-1.1856e-04	1.7953e-02	8.7734e-01	1.501
Physics Trigger 3N+2T3+K40+TS0 SNbuffer Dec2012	5.9642e-05	-1.4577e-02	2.9985	2.201
Physics Trigger 3N+2T3+K40+TS0 Dec2011	1.8012e-04	-4.0696e-02	3.6679	1.571
Physics Trigger 3N+2T3+GC+TQ+K40+TS0 Dec2011 noSNbuffer	-4.5757e-03	3.9122e-01	-5.4449	2.303
Physics Trigger 3N+2T3+GC+TQ+K40+TS0 Dec2011	2.0260e-04	-3.1539e-02	3.4623	2.307
Physics Trigger 3N+2T3+K40+TS0 SNbuffer Feb2012	6.0174e-05	-1.4167e-02	2.8670	2.101
Physics Trigger 3N+2T3+GC+K40+TS0 Dec2011 noSNbuffer	-1.8892e-03	2.1213e-01	-3.6098	2.317
Physics Trigger 3N+2T3+GC+K40+TS0 SNbuffer Nov2012	-9.1004e-04	1.3421e-01	-2.9543	1.979
Physics Trigger 3N+2T3+GC+K40+TS0 SNbuffer Feb2012	2.8191e-04	-3.9506e-02	3.6375	2.300
Physics Trigger 3N+K40+TS0 SNbuffer Feb2012	-7.2731e-06	3.0391e-03	1.5048	1.767
Physics Trigger 3N+K40+TS0 SNbuffer Dec2012	5.0483e-06	-1.3759e-03	2.6123	2.531

Run setup for TimeSlice: 2013/01-2013/12, weights for active OM	a	b	c	Average
Physics Trigger 3N+2T3+K40+TS0 SNbuffer Jun2013	-3.3342e-05	-1.0101e-02	4.3249	2.766
Physics Trigger 3N+2T3+GC+TQ+K40+TS0 SNbuffer Jun2013	-2.7318e-03	3.5442e-01	-8.1173	3.089
Physics Trigger 3N+2T3+GC+K40+TS0 SNbuffer Jun2013	-9.8789e-04	1.3399e-01	-1.2660	3.242
Physics Trigger 3N+2T3+K40+TS0 SNbuffer Dec2012	2.0950e-04	-6.7092e-02	6.6720	2.231
Physics Trigger 3N+2T3+GC+TQ+K40+TS0 SNbuffer Dec2012	-3.8935e-03	3.8890e-01	-6.3409	3.321
Physics Trigger 3N+2T3+K40+TS0 SNbuffer May2013	-2.7673e-05	4.7899e-03	3.0503	3.214
Physics Trigger 3N+2T3+GC+K40+TS0 SNbuffer Dec2012	2.3487e-03	-2.9212e-01	12.1626	3.155

The following tables list the parameter of the function used to calculate the weights for events triggered by the trigger T3 and reconstructed by AAFit using the run-by-run Monte Carlo.

Run setup for TimeSlice: 2010/11-2011/12, weights for baseline	a	b	c	Average
Physics Trigger 3N+2T3+GC+TQ+T2+K40+T0 Dec2011	2.1984e-03	-2.3768e-01	7.5612	1.162
Physics Trigger 3N+2T3+K40+TS0 June2011	3.9971e-05	-6.2483e-03	1.3892	1.157
Physics Trigger 3N+2T3+K40+TS0 Nov2010	1.3624e-05	-3.1907e-03	1.2999	1.129
Physics Trigger 3N+2T3+K40+TS0 Dec2011	9.3951e-04	-1.0414e-01	4.0164	1.138
Physics Trigger 3N+2T3+GC+TQ+K40+TS0 Dec2011	-1.5610e-02	1.6108	-40.3982	1.155
Physics Trigger 3N+2T3+K40+TS0 not yet tuned	-4.7013e-04	5.3862e-02	-3.6807e-01	1.169

Run setup for TimeSlice: 2010/11-2011/12, weights for active OM	a	b	c	Average
Physics Trigger 3N+2T3+GC+TQ+T2+K40+T0 Dec2011	2.1984e-03	-2.3768e-01	7.5612	1.162
Physics Trigger 3N+2T3+K40+TS0 June2011	3.9971e-05	-6.2483e-03	1.3892	1.157
Physics Trigger 3N+2T3+K40+TS0 Nov2010	1.3624e-05	-3.1907e-03	1.2999	1.129
Physics Trigger 3N+2T3+K40+TS0 Dec2011	9.3951e-04	-1.0414e-01	4.0164	1.138
Physics Trigger 3N+2T3+GC+TQ+K40+TS0 Dec2011	-1.5610e-02	1.6108	-40.3982	1.155
Physics Trigger 3N+2T3+K40+TS0 not yet tuned	-4.7013e-04	5.3862e-02	-3.6807e-01	1.169

The following tables list the parameter of the function used to calculate the weights for events triggered by the trigger T3 and reconstructed by BBFit.

Run setup for TimeSlice: 2008/05-2009/03, weights for baseline	a	b	c	Average
Physics Trigger - Noisy channels treated	1.0044e-03	-1.2287e-01	5.5508	1.825
Physics Trigger (th2 3pe, old L0 thresholds)	-3.5751e-03	4.5855e-01	-12.3147	2.171
Physics Trigger with GC	4.0090e-03	-4.4630e-01	13.9821	1.608
Physics Trigger (th2 3 p.e.)	7.2074e-04	-1.0875e-01	6.1775	2.175
Physics Trigger (th2 10 p.e.)	-1.4868e-05	-1.7467e-04	1.4605	1.381
Physics Trigger - Noisy channels treated + Galactic center trigger	1.7339e-04	-2.8684e-02	3.1564	2.057

Run setup for TimeSlice: 2009/03-2009/07, weights for baseline	a	b	c	Average
Physics Trigger - Noisy channels treated	-4.4934e-06	-3.6065e-04	1.9086	1.814
Physics Trigger with GC	6.0948e-05	-1.2673e-02	2.5960	1.975

Run setup for TimeSlice: 2009/07-2009/10, weights for baseline	a	b	c	Average
Physics Trigger 3N+2T3+GC 2009V3.0	3.1705e-04	-4.7094e-02	3.6130	1.886
Physics Trigger 3N+2T3 2009V3.0	-3.1165e-05	5.1270e-03	1.5044	1.711
Physics Trigger 3N+2T3+GC+K40 2009V3.0	5.9801e-03	-7.1876e-01	23.4166	1.826

Run setup for TimeSlice: 2009/11-2010/02, weights for baseline	a	b	c	Average
Physics Trigger 3N+2T3+GC+T2+TQ+K40 2009V3.1	-2.4261e-04	1.3925e-02	2.1702	2.210
Physics Trigger 3N+2T3+K40 2009V3.1	4.1122e-04	-5.7734e-02	4.0618	2.095
Physics Trigger 3N+2T3+GC+TQ+K40 2009V3.1	3.3971e-03	-4.0170e-01	14.1074	2.246
Physics Trigger 3N+2T3+GC+K40 2009V3.1	1.6897e-03	-2.0213e-01	8.1056	2.099

Run setup for TimeSlice: 2010/02-2010/10, weights for baseline	a	b	c	Average
Physics Trigger 3N+2T3+GC+TQ+T2+K40+TS0	1.2990e-04	-1.2458e-02	2.2442	1.963
Physics Trigger 3N+2T3+GC+TQ+T2+K40 2010V3.0	6.5694e-05	-9.5549e-03	2.6864	2.346
Physics Trigger 3N+2T3+K40 2009V3.1	6.0208e-05	-1.2124e-02	2.2577	1.707
Physics Trigger 3N+2T3+GC+T2+TQ+K40 2009V3.1	2.3160e-04	-3.3845e-02	2.9520	1.756
Physics Trigger 3N+2T3+K40 2010V3.0	-4.3921e-06	1.5256e-03	1.6249	1.732
Physics Trigger 3N+2T3+GC+K40 2010V3.0	-1.5560e-04	2.4080e-02	1.4098	2.328
Physics Trigger 3N+2T3+GC+K40 2009V3.1	9.6527e-05	-1.5936e-02	2.2833	1.718
Physics Trigger 3N+2T3+GC+K40+TS0	-1.1047e-03	1.4040e-01	-2.5488	1.877
Physics Trigger 3N+2T3+GC+TQ+K40 2009V3.1	-1.1101e-05	-3.4610e-03	2.2732	1.967
Physics Trigger 3N+2T3+K40+TS0	1.8716e-04	-3.1977e-02	3.1797	1.854

Run setup for TimeSlice: 2010/11-2011/12, weights for baseline	a	b	c	Average
Physics Trigger 3N+2T3+GC+TQ+T2+K40+T0 Dec2011	2.4642e-03	-2.6650e-01	9.1699	1.994
Physics Trigger 3N+2T3+GC+TQ+T2+K40+TS0 Nov2010	1.7207e-04	-3.5367e-02	3.4855	2.067
Physics Trigger 3N+2T3+GC+K40+TS0 Nov2010	6.6253e-04	-8.6003e-02	4.7432	1.999
Physics Trigger 3N+2T3+K40+TS0 June2011	-3.8605e-05	7.5028e-03	1.2804	1.611
Physics Trigger 3N+2T3+K40+TS0 Nov2010	1.6380e-05	-3.4217e-03	1.6016	1.439
Physics Trigger 3N+2T3+GC+TQ+T2+K40+TS0 June2011	1.1731e-03	-1.3938e-01	6.1367	2.041
Physics Trigger 3N+2T3+GC+K40+TS0 June2011	2.0506e-05	-4.9432e-03	2.2654	2.018
Physics Trigger 3N+2T3+K40+TS0 Dec2011	5.9225e-04	-6.7537e-02	3.8727	1.953
Physics Trigger 3N+2T3+GC+TQ+K40+TS0 Dec2011	2.5090e-02	-2.5904	68.9645	2.108

Run setup for TimeSlice: 2012/01-2012/12, weights for baseline	a	b	c	Average
Physics Trigger 3N+2T3+GC+TQ+K40+TS0 SNbuffer Feb2012	1.6343e-04	-3.3787e-02	3.4722	1.849
Physics Trigger 3N+2T3+K40+TS0 SNbuffer Nov2012	-1.2131e-04	1.8335e-02	8.2769e-01	1.462
Physics Trigger 3N+2T3+K40+TS0 SNbuffer Dec2012	4.3084e-05	-1.1054e-02	2.6668	2.040
Physics Trigger 3N+2T3+K40+TS0 Dec2011	1.4560e-04	-3.2747e-02	3.0992	1.419
Physics Trigger 3N+2T3+GC+TQ+K40+TS0 Dec2011 noSNbuffer	-9.5838e-04	2.0688e-02	3.7251	2.028
Physics Trigger 3N+2T3+GC+TQ+K40+TS0 Dec2011	1.4587e-04	-2.2448e-02	2.9475	2.137
Physics Trigger 3N+2T3+K40+TS0 SNbuffer Feb2012	3.7895e-05	-8.4463e-03	2.3189	1.887
Physics Trigger 3N+2T3+GC+K40+TS0 Dec2011 noSNbuffer	-2.1102e-03	2.3732e-01	-4.5868	2.055
Physics Trigger 3N+2T3+GC+K40+TS0 SNbuffer Nov2012	-1.1575e-03	1.7049e-01	-4.3753	1.884
Physics Trigger 3N+2T3+GC+K40+TS0 SNbuffer Feb2012	2.4212e-04	-3.3708e-02	3.2168	2.085

Run setup for TimeSlice: 2013/01-2013/12, weights for baseline	a	b	c	Average
Physics Trigger 3N+2T3+K40+TS0 SNbuffer Jun2013	-2.1923e-05	-5.0429e-03	2.6462	1.799
Physics Trigger 3N+2T3+GC+TQ+K40+TS0 SNbuffer Jun2013	-1.5011e-03	1.9471e-01	-4.2104	1.945
Physics Trigger 3N+2T3+GC+K40+TS0 SNbuffer Jun2013	-6.8194e-04	9.2716e-02	-1.0823	2.046
Physics Trigger 3N+2T3+K40+TS0 SNbuffer Dec2012	-1.5799e-04	2.4029e-02	1.1641	1.834
Physics Trigger 3N+2T3+GC+TQ+K40+TS0 SNbuffer Dec2012	-2.9409e-03	2.9444e-01	-5.1722	2.162
Physics Trigger 3N+2T3+K40+TS0 SNbuffer May2013	3.8328e-06	1.8601e-05	2.0995	2.137
Physics Trigger 3N+2T3+GC+K40+TS0 SNbuffer Dec2012	1.6985e-03	-2.1015e-01	8.5265	2.078

Run setup for TimeSlice: 2008/05-2009/03, weights for active OM	a	b	c	Average
Physics Trigger - Noisy channels treated	1.0044e-03	-1.2287e-01	5.5508	1.825
Physics Trigger (th2 3pe, old L0 thresholds)	-3.5751e-03	4.5855e-01	-12.3147	2.171
Physics Trigger with GC	4.0090e-03	-4.4630e-01	13.9821	1.608
Physics Trigger (th2 3 p.e.)	7.2074e-04	-1.0875e-01	6.1775	2.175
Physics Trigger (th2 10 p.e.)	-1.4868e-05	-1.7467e-04	1.4605	1.381
Physics Trigger - Noisy channels treated + Galactic center trigger	1.7339e-04	-2.8684e-02	3.1564	2.057

Run setup for TimeSlice: 2009/03-2009/07, weights for active OM	a	b	c	Average
Physics Trigger - Noisy channels treated	-4.4934e-06	-3.6065e-04	1.9086	1.814
Physics Trigger with GC	6.0948e-05	-1.2673e-02	2.5960	1.975

Run setup for TimeSlice: 2009/07-2009/10, weights for active OM	a	b	c	Average
Physics Trigger 3N+2T3+GC 2009V3.0	3.1705e-04	-4.7094e-02	3.6130	1.886
Physics Trigger 3N+2T3 2009V3.0	-3.1165e-05	5.1270e-03	1.5044	1.711
Physics Trigger 3N+2T3+GC+K40 2009V3.0	5.9801e-03	-7.1876e-01	23.4166	1.826

Run setup for TimeSlice: 2009/11-2010/02, weights for active OM	a	b	c	Average
Physics Trigger 3N+2T3+GC+T2+TQ+K40 2009V3.1	-2.4261e-04	1.3925e-02	2.1702	2.210
Physics Trigger 3N+2T3+K40 2009V3.1	4.1122e-04	-5.7734e-02	4.0618	2.095
Physics Trigger 3N+2T3+GC+TQ+K40 2009V3.1	3.3971e-03	-4.0170e-01	14.1074	2.246
Physics Trigger 3N+2T3+GC+K40 2009V3.1	1.6897e-03	-2.0213e-01	8.1056	2.099

Run setup for TimeSlice: 2010/02-2010/10, weights for active OM	a	b	c	Average
Physics Trigger 3N+2T3+GC+TQ+T2+K40+TS0	1.2990e-04	-1.2458e-02	2.2442	1.963
Physics Trigger 3N+2T3+GC+TQ+T2+K40 2010V3.0	6.5694e-05	-9.5549e-03	2.6864	2.346
Physics Trigger 3N+2T3+K40 2009V3.1	6.0208e-05	-1.2124e-02	2.2577	1.707
Physics Trigger 3N+2T3+GC+T2+TQ+K40 2009V3.1	2.3160e-04	-3.3845e-02	2.9520	1.756
Physics Trigger 3N+2T3+K40 2010V3.0	-4.3921e-06	1.5256e-03	1.6249	1.732
Physics Trigger 3N+2T3+GC+K40 2010V3.0	-1.5560e-04	2.4080e-02	1.4098	2.328
Physics Trigger 3N+2T3+GC+K40 2009V3.1	9.6527e-05	-1.5936e-02	2.2833	1.718
Physics Trigger 3N+2T3+GC+K40+TS0	-1.1047e-03	1.4040e-01	-2.5488	1.877
Physics Trigger 3N+2T3+GC+TQ+K40 2009V3.1	-1.1101e-05	-3.4610e-03	2.2732	1.967
Physics Trigger 3N+2T3+K40+TS0	1.8716e-04	-3.1977e-02	3.1797	1.854

Run setup for TimeSlice: 2010/11-2011/12, weights for active OM	a	b	c	Average
Physics Trigger 3N+2T3+GC+TQ+T2+K40+T0 Dec2011	2.4642e-03	-2.6650e-01	9.1699	1.994
Physics Trigger 3N+2T3+GC+TQ+T2+K40+TS0 Nov2010	1.7207e-04	-3.5367e-02	3.4855	2.067
Physics Trigger 3N+2T3+GC+K40+TS0 Nov2010	6.6253e-04	-8.6003e-02	4.7432	1.999
Physics Trigger 3N+2T3+K40+TS0 June2011	-3.8605e-05	7.5028e-03	1.2804	1.611
Physics Trigger 3N+2T3+K40+TS0 Nov2010	1.6380e-05	-3.4217e-03	1.6016	1.439
Physics Trigger 3N+2T3+GC+TQ+T2+K40+TS0 June2011	1.1731e-03	-1.3938e-01	6.1367	2.041
Physics Trigger 3N+2T3+GC+K40+TS0 June2011	2.0506e-05	-4.9432e-03	2.2654	2.018
Physics Trigger 3N+2T3+K40+TS0 Dec2011	5.9225e-04	-6.7537e-02	3.8727	1.953
Physics Trigger 3N+2T3+GC+TQ+K40+TS0 Dec2011	2.5090e-02	-2.5904	68.9645	2.108

Run setup for TimeSlice: 2012/01-2012/12, weights for active OM	a	b	c	Average
Physics Trigger 3N+2T3+GC+TQ+K40+TS0 SNbuffer Feb2012	1.6343e-04	-3.3787e-02	3.4722	1.849
Physics Trigger 3N+2T3+K40+TS0 SNbuffer Nov2012	-1.2131e-04	1.8335e-02	8.2769e-01	1.462
Physics Trigger 3N+2T3+K40+TS0 SNbuffer Dec2012	4.3084e-05	-1.1054e-02	2.6668	2.040
Physics Trigger 3N+2T3+K40+TS0 Dec2011	1.4560e-04	-3.2747e-02	3.0992	1.419
Physics Trigger 3N+2T3+GC+TQ+K40+TS0 Dec2011 noSNbuffer	-9.5838e-04	2.0688e-02	3.7251	2.028
Physics Trigger 3N+2T3+GC+TQ+K40+TS0 Dec2011	1.4587e-04	-2.2448e-02	2.9475	2.137
Physics Trigger 3N+2T3+K40+TS0 SNbuffer Feb2012	3.7895e-05	-8.4463e-03	2.3189	1.887
Physics Trigger 3N+2T3+GC+K40+TS0 Dec2011 noSNbuffer	-2.1102e-03	2.3732e-01	-4.5868	2.055
Physics Trigger 3N+2T3+GC+K40+TS0 SNbuffer Nov2012	-1.1575e-03	1.7049e-01	-4.3753	1.884
Physics Trigger 3N+2T3+GC+K40+TS0 SNbuffer Feb2012	2.4212e-04	-3.3708e-02	3.2168	2.085

Run setup for TimeSlice: 2013/01-2013/12, weights for active OM	a	b	c	Average
Physics Trigger 3N+2T3+K40+TS0 SNbuffer Jun2013	-2.1923e-05	-5.0429e-03	2.6462	1.799
Physics Trigger 3N+2T3+GC+TQ+K40+TS0 SNbuffer Jun2013	-1.5011e-03	1.9471e-01	-4.2104	1.945
Physics Trigger 3N+2T3+GC+K40+TS0 SNbuffer Jun2013	-6.8194e-04	9.2716e-02	-1.0823	2.046
Physics Trigger 3N+2T3+K40+TS0 SNbuffer Dec2012	-1.5799e-04	2.4029e-02	1.1641	1.834
Physics Trigger 3N+2T3+GC+TQ+K40+TS0 SNbuffer Dec2012	-2.9409e-03	2.9444e-01	-5.1722	2.162
Physics Trigger 3N+2T3+K40+TS0 SNbuffer May2013	3.8328e-06	1.8601e-05	2.0995	2.137
Physics Trigger 3N+2T3+GC+K40+TS0 SNbuffer Dec2012	1.6985e-03	-2.1015e-01	8.5265	2.078

Appendix G

Influence of different weights on the muon rate

The plots here show how the weighting reduce the spreading of the muon rate for all TimeSlices using the AAFit reconstruction algorithm with a λ-cut of -6.6. Only events that where triggered by T3 are used. The histograms show four different plots each. The yellow line shows the distribution of the muon rate without weights. The spreading is high in comparison to the other lines. After applying the weights that will compensate the decreasing efficiency of the detector over the time (green line), the weights for correcting the dependency of the number of active OMs to the muon rate are applied (red line). The last step is to apply the weights to correct the dependence of the muon rate to the value of the baseline (blue line).

The maximum of the yellow line can be located to higher and lower values compared to the blue line (all weights applied). This mainly comes from the decreasing efficiency of the detector over the time but the number of available lines too is important in this case.

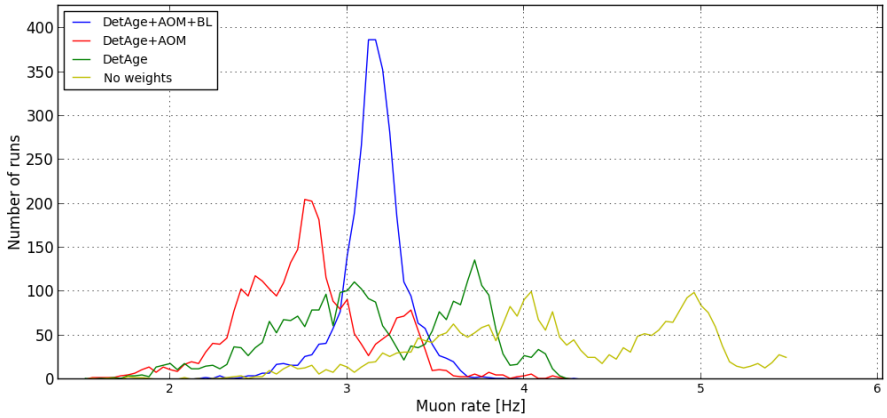

TimeSlice1

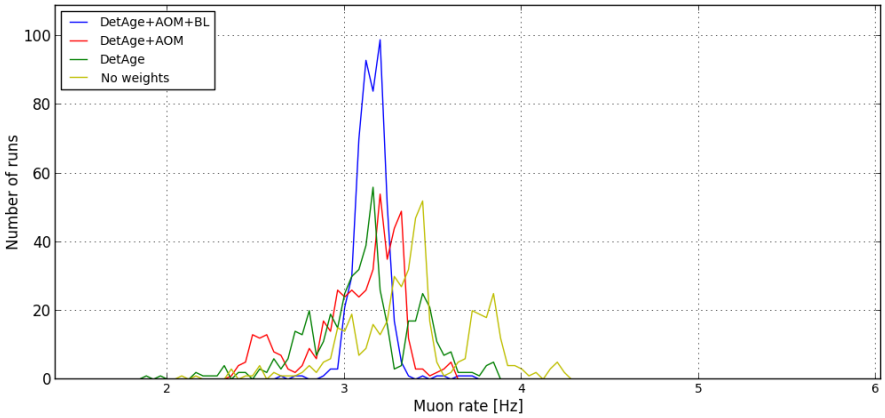

TimeSlice2

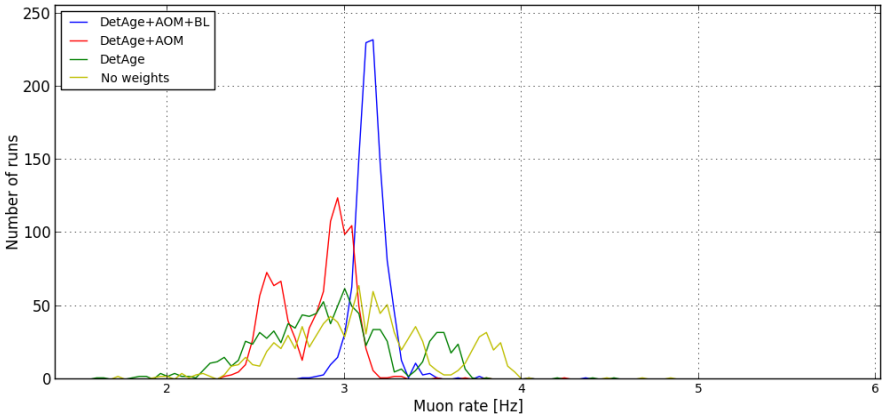

TimeSlice3

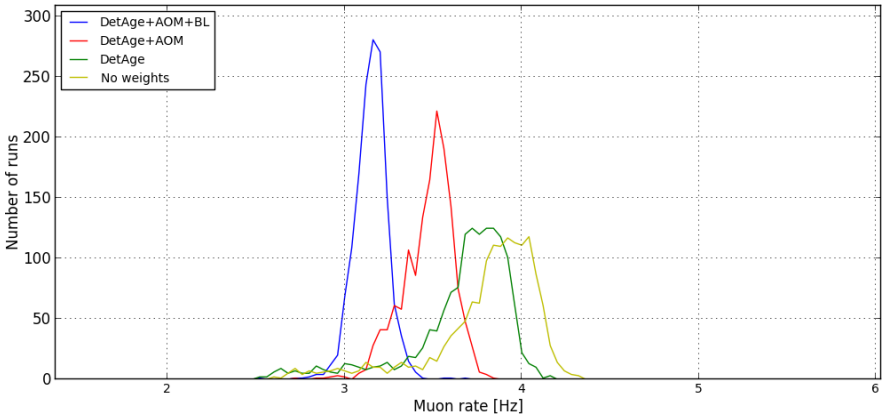

TimeSlice4

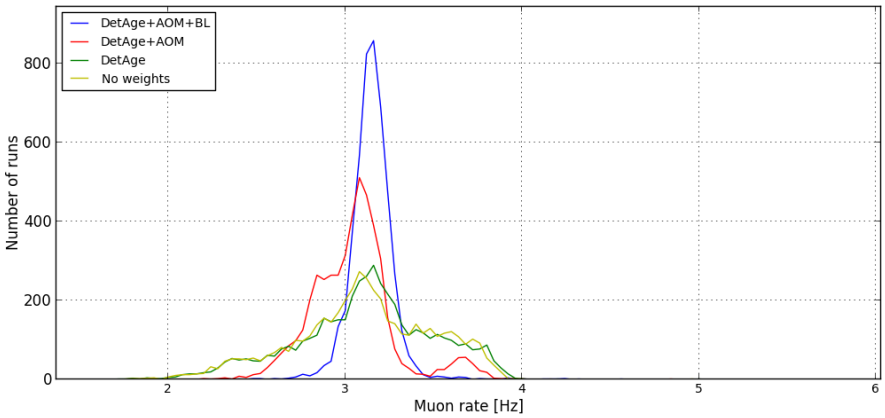

TimeSlice5

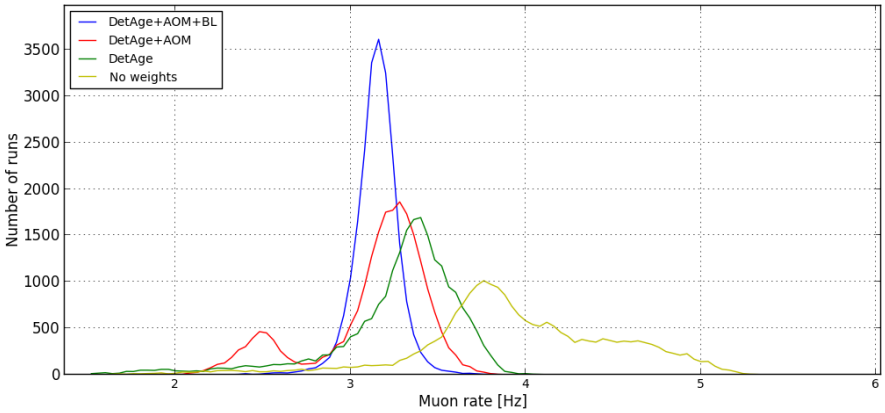

TimeSlice6

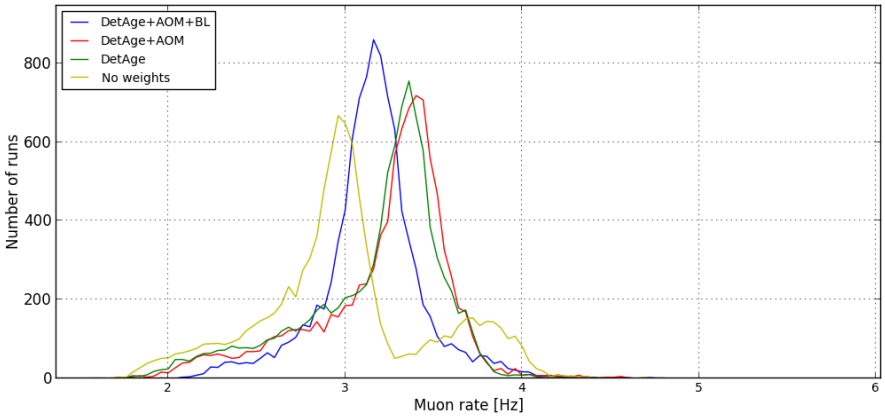

TimeSlice7

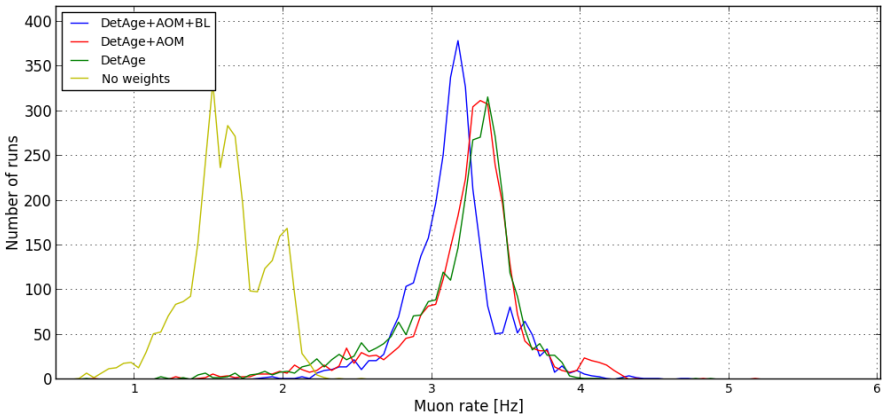
DetAge+AOM+BL
DetAge+AOM
DetAge
No weights
Number of runs
Muon rate [Hz]
0
50
100
150
200
250
300
350
400
1
2
3
4
5
6

TimeSlice8

Appendix H

Additional plots for trigger 3DScan with AAFit

Here some plots are shown which complete the usage of the datat selected by the trigger 3DScan and reconstructed by the AAFit algorithm. The procedure is the same as for the events triggered by T3 which is described in detail in the chapters 7 and 8.

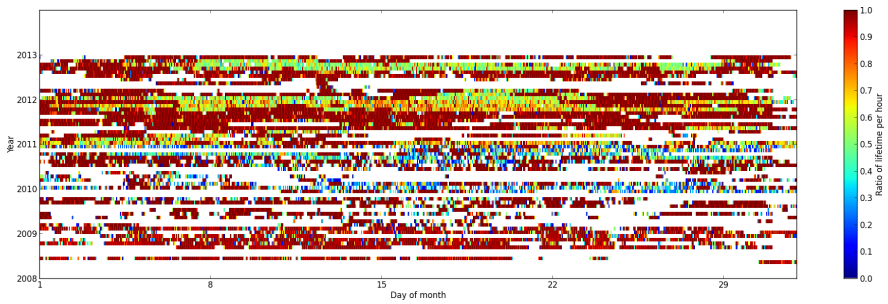

Figure H.1: This is the lifetime of the data used after the run selection. The ratio (color bar) gives the fraction of time for each hour used. Each line is a month starting with 1st January 2008 at the left bottom until December 2013 on the top. The columns are the hours in the specific month.

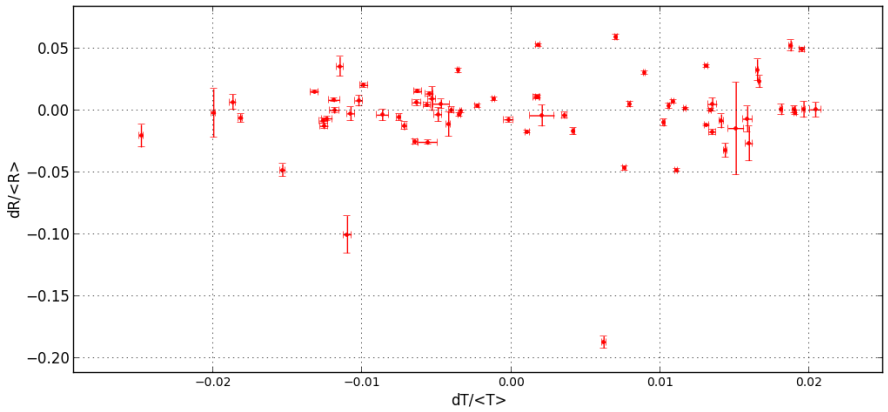

A plot of $dR/ < R >$ as a function of $dT_{eff}/ < T_{eff} >$ using the average over 21 days for the muon rate and the effective temperature as described in chapter 9.2. The lifetime of the data used is shown in figure H.1. No correlation can be seen. The weights for baseline and the number of active OMs where applied.

The following plots show how the weighting reduce the spreading of the muon rate

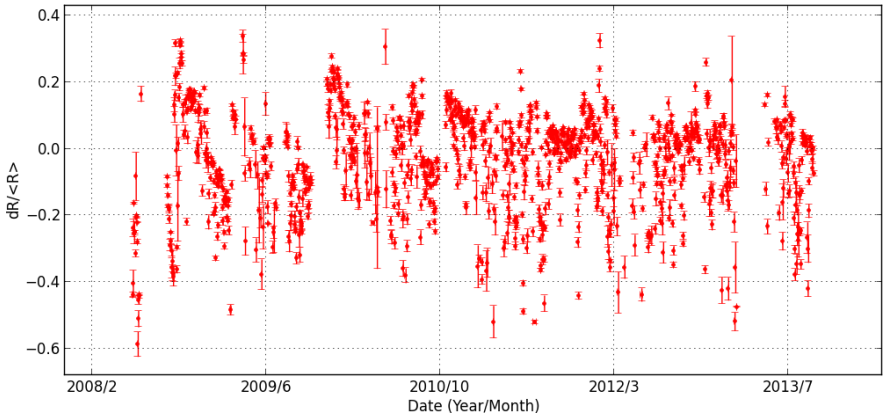

A plot of $dR/ < R >$ over the time using the average over 1 day for the muon rate. The lifetime of the data used is shown in figure H.1. No weights except for the decreasing efficiency of the detector over the time where applied. It can be seen, that the spreading is higher in comparison to figure 9.9. The weights have the desired effect and are reducing the spreading and the systematics of data taking with ANTARES. However, the spreading with weights applied to the data still is too high to see a relation of the effective temperature and the muon rate.

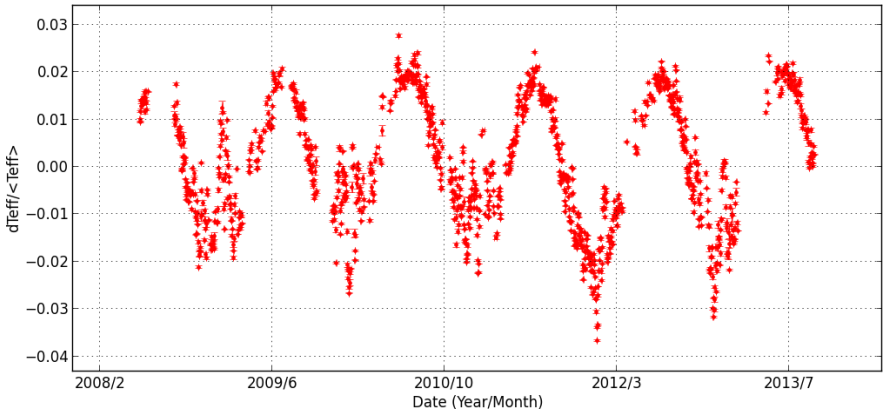

A plot of $dT/ < T >$ over the time using the average over 1 day for the effective atmospheric temperature. The muon rate shown in the former plot should follow the variation of the temperature for the case a correlation could have be seen.

for all TimeSlices using the AAFit reconstruction algorithm with a λ-cut of -6.6. Only events that where triggered by 3DScan are used. The histograms show four different plots each. The yellow line shows the distribution of the muon rate without weights. The spreading is high in comparison to the other lines. After applying the weights that will compensate the decreasing efficiency of the detector over time (green line), the weights for correcting the dependency of the number of active OMs to the muon rate are applied (red line). The last step is to apply the weights to correct the dependence of the muon rate to the value of the baseline (blue line).

The maximum of the yellow line can be located to higher and lower values compared to the blue line (all weights applied). This mainly comes from the decreasing efficiency of the detector over the time but the number of available lines too is important in this

case.

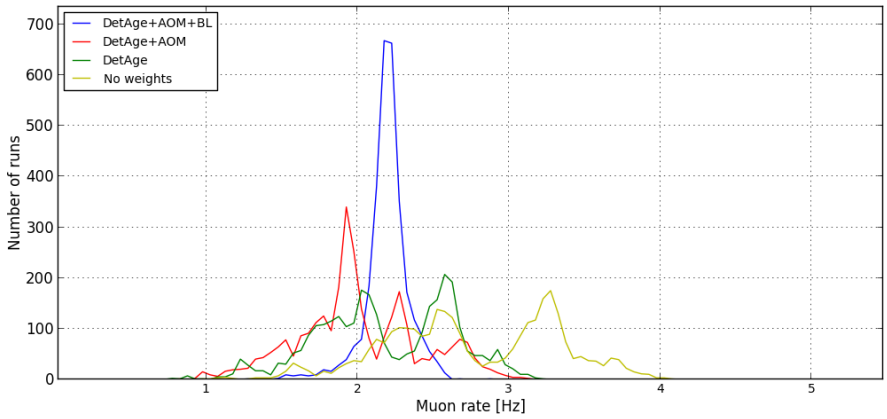

TimeSlice1

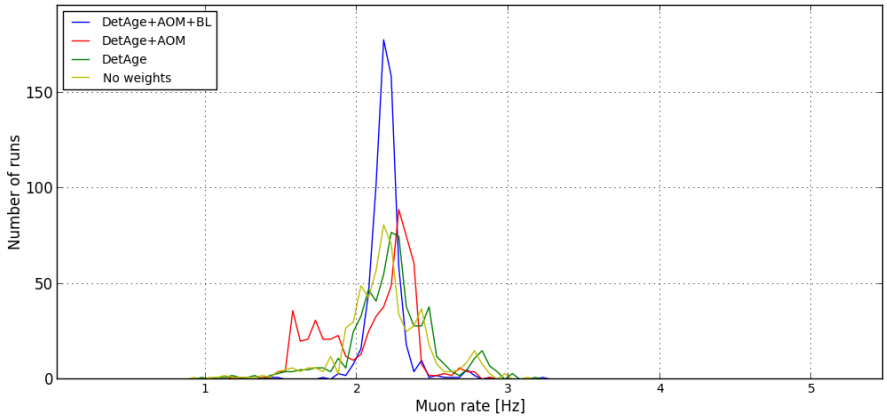

TimeSlice2

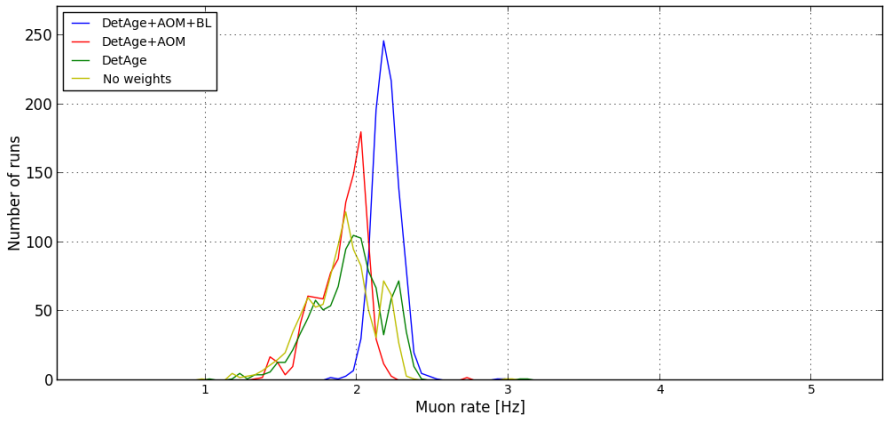

TimeSlice3

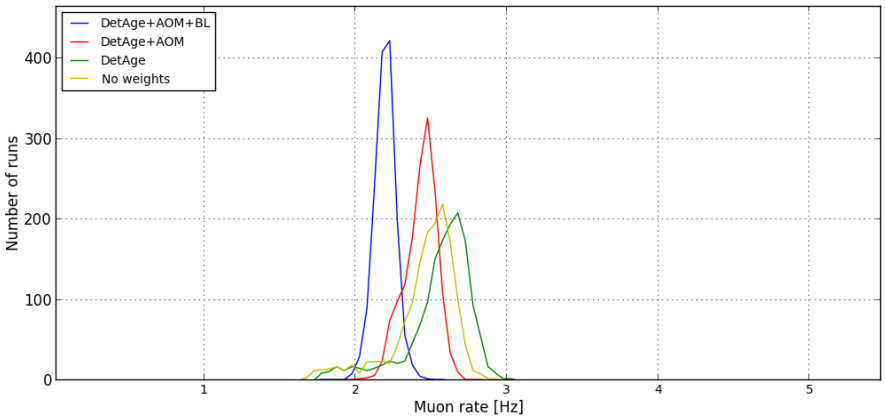

TimeSlice4

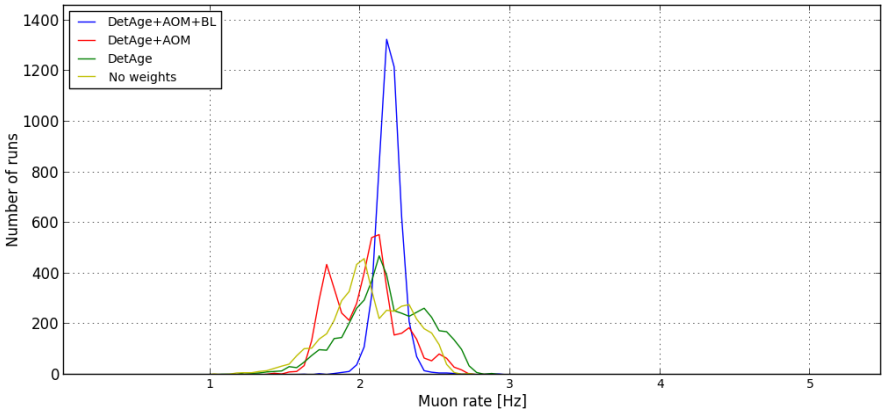

TimeSlice5

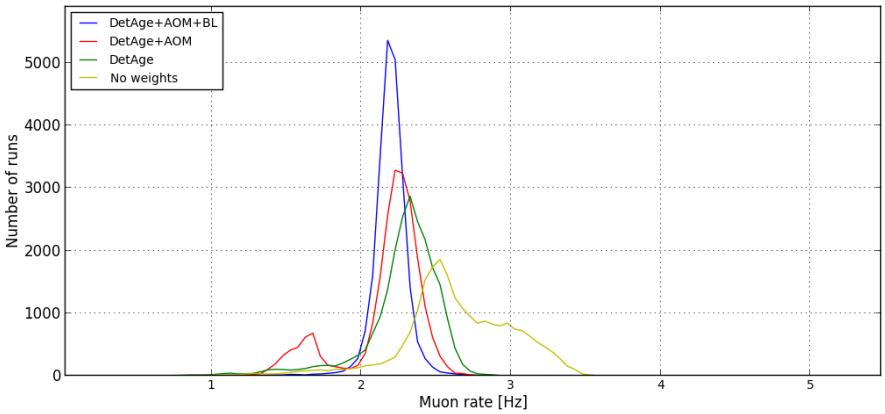

TimeSlice6

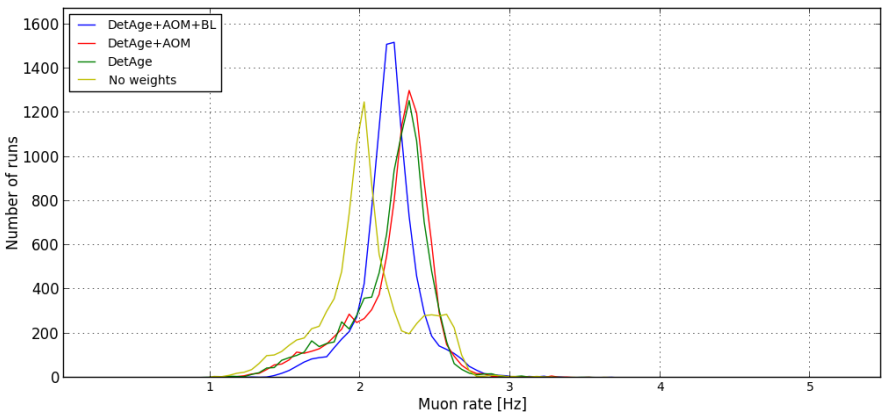
DetAge+AOM+BL
DetAge+AOM
DetAge
No weights
Number of runs
Muon rate [Hz]
0
200
400
600
800
1000
1200
1400
1600
1
2
3
4
5

TimeSlice7

Appendix I

Additional plots using BBFit reconstruction

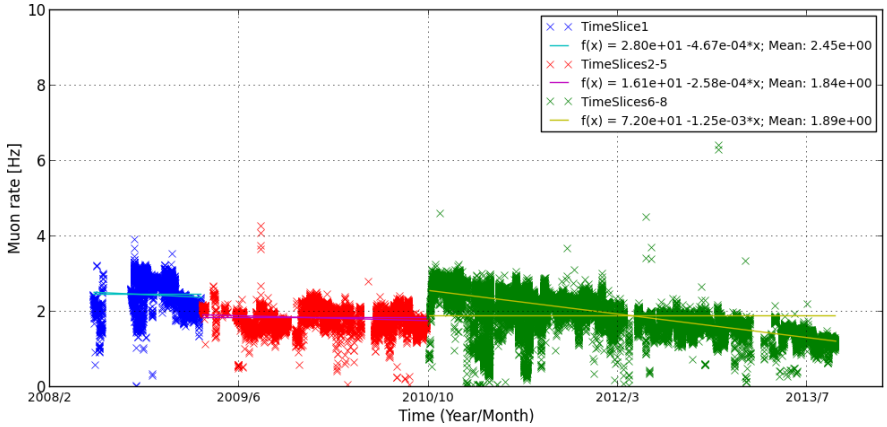

Figure I.1: This is the muon rate over the time. The rate is calculated using reconstructed events from BBFit only with a $T\chi^2$-cut of 35.0. This is the rate with no weights applied. Each cros stands for a calculated muon rate for one run. The different colors (blue, red and green) mark the time period the efficiency was calculated for. The solid lines (blue, purple and yellow) show the linear fit for the specific time period to the muon rate. The legend shows which TimeSlices where used and the fitted function is shown.

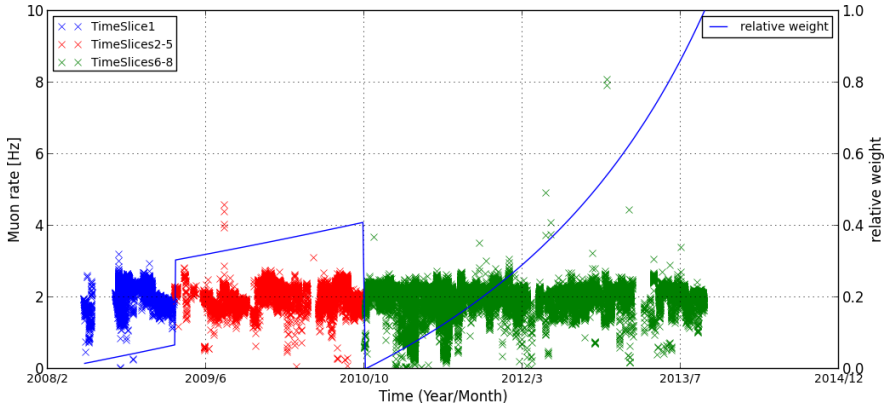

Figure I.2: This is the muon rate over the time after the weights calculated to compensate the decreasing efficiency over the time are applied. The solid line shows the relative weight that applied to the data calculated by the fitted functions of figure I.1.

The following pictures show the distribution of the muon rates and the effect of the weights for the efficiency of the detector (DetEff), the number of active OMs (AOM) and the baseline (BL) for all Timeslices.

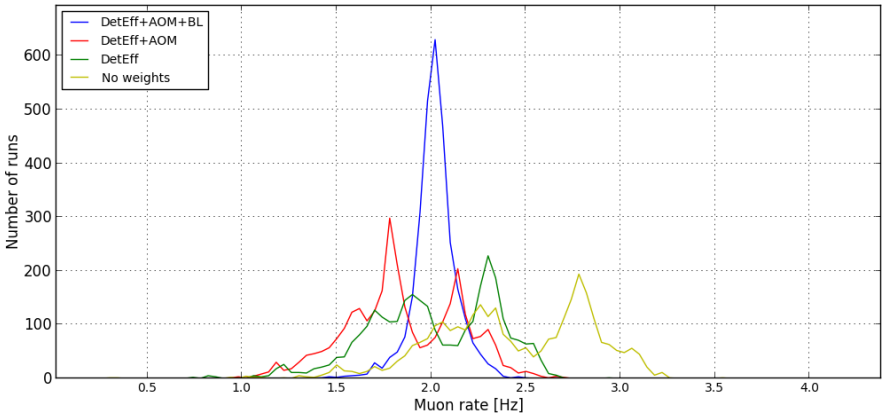

Figure I.3: TimeSlice1.

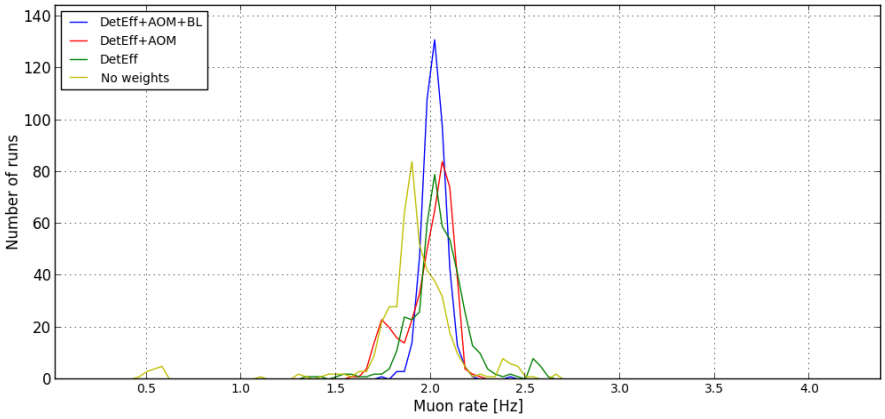

Figure I.4: TimeSlice2.

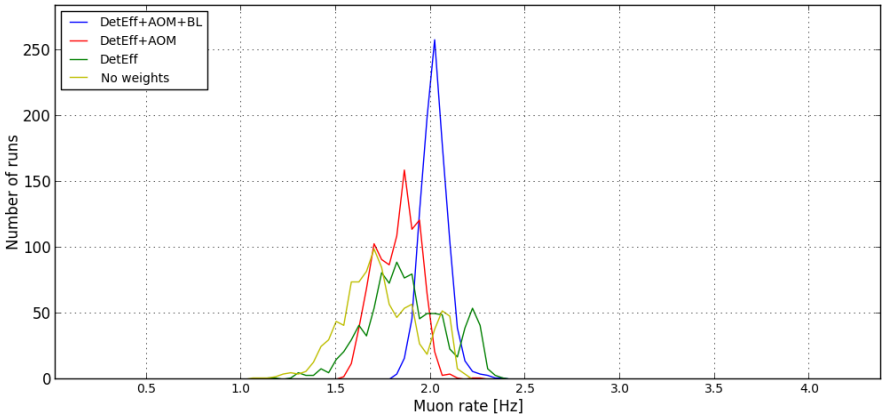

Figure I.5: TimeSlice3.

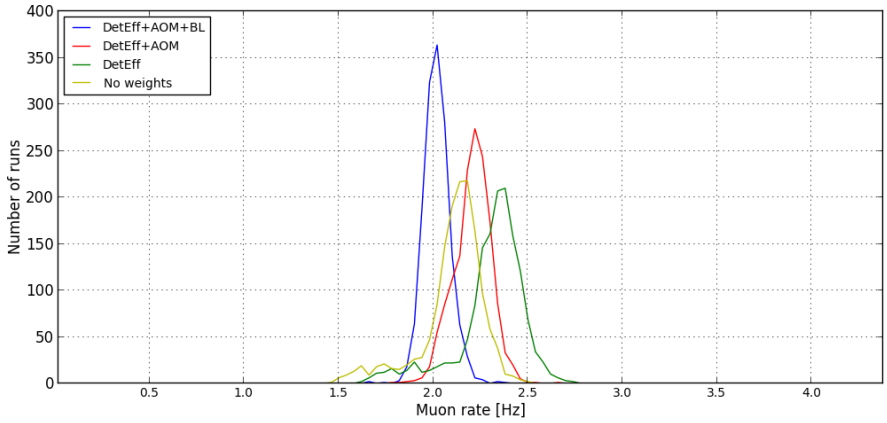

Figure I.6: TimeSlice4.

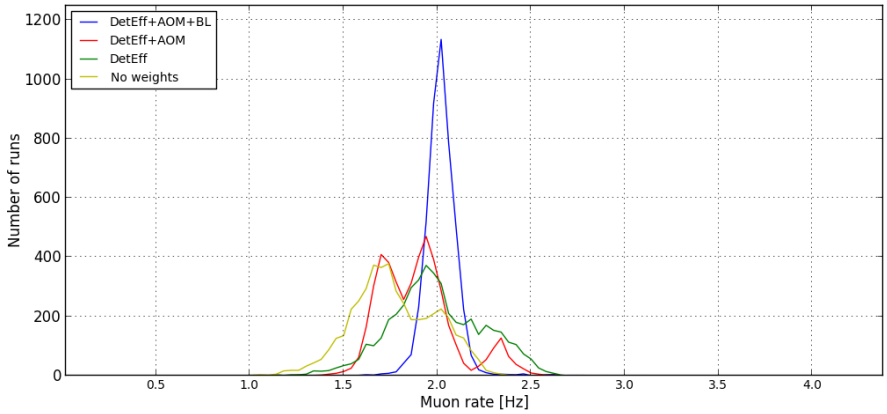

Figure I.7: TimeSlice5.

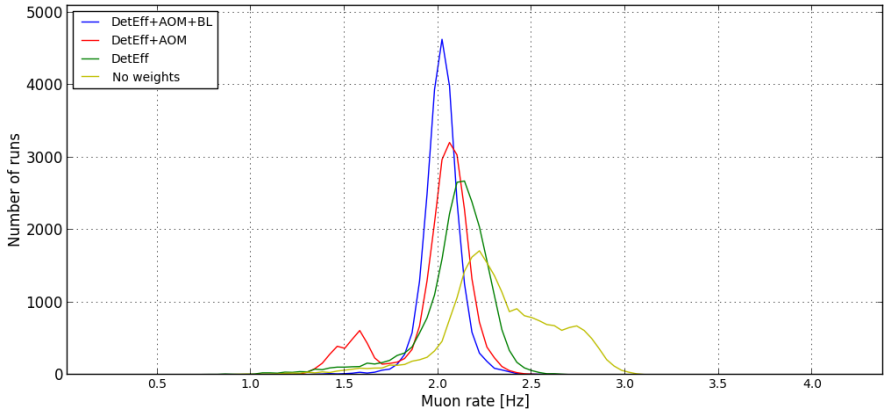

Figure I.8: TimeSlice6.

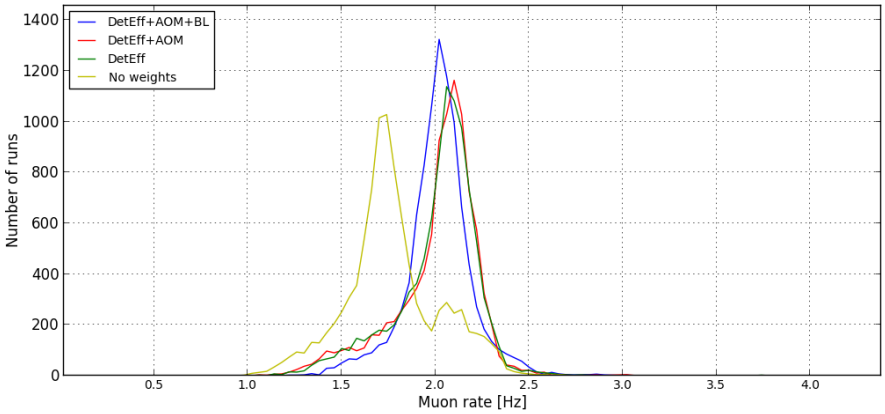

Figure I.9: TimeSlice7.

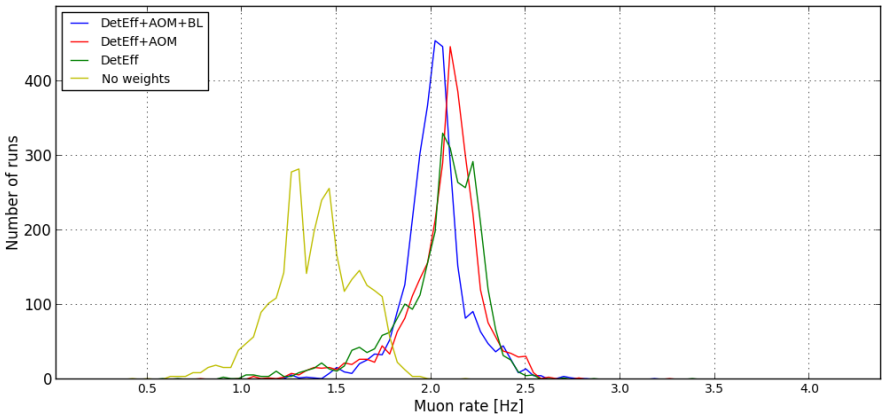

Figure I.10: TimeSlice8.

Appendix J

Examples for cuts on the hit rate of used OMs

These are more examples for cuts on the hit rate of the OMs used for reconstruction. The plots show the muon rate over the time as a six day average derived from the events that have survived the cuts. Cuts where made on the mean hit rate of all OMs within the frame, the number of OMs in status OK, and the mean rate of OMs in status high as described in section 9.6. In addition the hit rates of the OMs used for reconstruction is checked for different borders. In addition the mean of the atmospheric temperature is shown. The error bars show the statistical error.

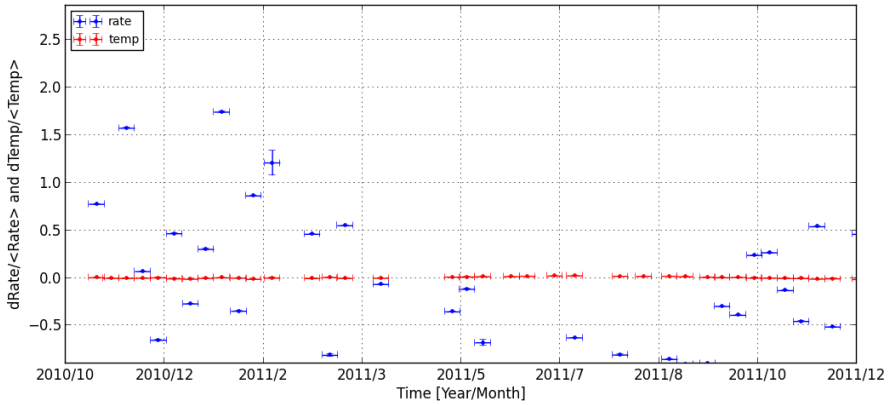

Figure J.1: 50 kHz < RateOK < 180 kHz
200 kHz < RateHigh < 300 kHz
680 < Number of OMs in status OK
10 kHz < hit rate for OMs used for reconstruction < 80 kHz
λ-cut: -6.6
mean muon rate: $\approx$ 0.2 Hz

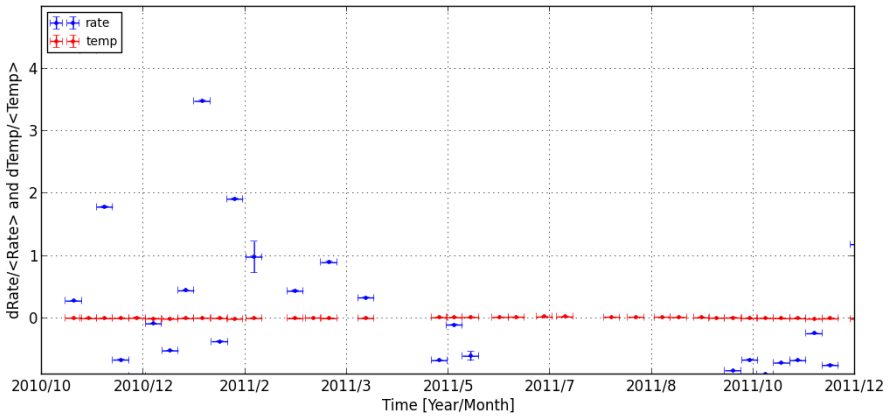

Figure J.2: 10 kHz < RateOK < 120 kHz
200 kHz < RateHigh < 300 kHz
680 < Number of OMs in status OK
10 kHz < hit rate for OMs used for reconstruction < 65 kHz
λ-cut: -6.6
mean muon rate: $\approx$ 0.06 Hz

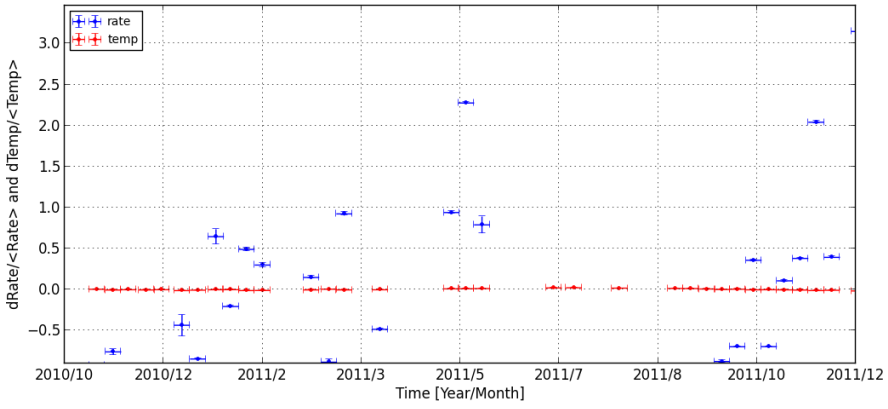

Figure J.3: 50 kHz < RateOK < 70 kHz
260 kHz < RateHigh < 380 kHz
680 < Number of OMs in status OK
10 kHz < hit rate for OMs used for reconstruction < 65 kHz
λ-cut: -6.6
mean muon rate: $\approx$ 0.3 Hz

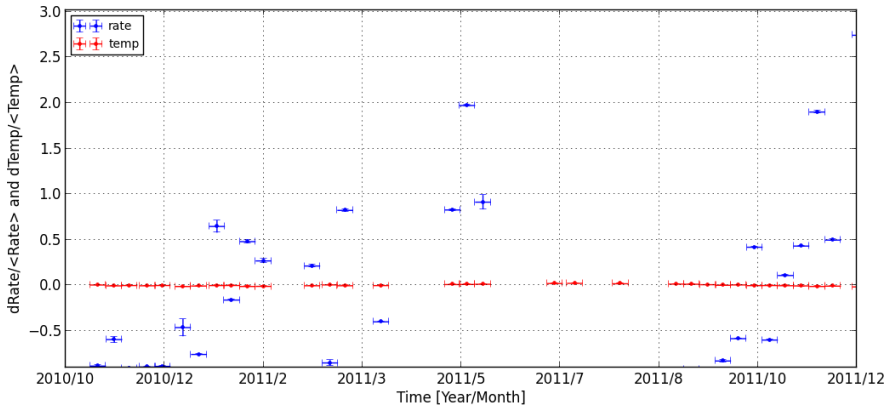

Figure J.4: 50 kHz < RateOK < 70 kHz
260 kHz < RateHigh < 380 kHz
680 < Number of OMs in status OK
10 kHz < hit rate for OMs used for reconstruction < 65 kHz
λ-cut: none
mean muon rate: $\approx$ 0.5 Hz

Bibliography

[1] Domenico D'Urso. Cosmic Ray Physics. 2014. arXiv:1411.4642 [astro-ph.HE].

[2] Esteban Roulet, for the Pierre Auger Collaboration. Latest results from the Pierre Auger Observatory. 2011. arXiv:1101.1825 [astro-ph.HE].

[3] IceCube Collaboration. First observation of PeV-energy neutrinos with IceCube. 2013. arXiv:1304.5356 [astro-ph.HE].

[4] Alessio Tamburro. Measurements of Cosmic Rays with IceTop/IceCube: Status and Results. 2012. arXiv:1210.1832 [astro-ph.HE].

[5] Paolo Desiati, for the IceCube Collaboration. Observation of TeV-PeV cosmic ray anisotropy with IceCube, IceTop and AMANDA. 2013. arXiv:1308.0246 [astro-ph.HE].

[6] Maurizio Spurio. *Particles and Astrophysics A Mulit-Messenger Approach.* Springer Cham Heidelberg New York Dordrecht London, 2015. ISBN: 978-3-319-08050-5.

[7] ECMWF/DWD/WDC-Climate 2009 ff: ERA-Interim. Website: `http://www.ecmwf.int/`.

[8] The MINOS Collaboration. Observation of muon intensity variations by season with the MINOS far detector. 2010. Available online at `http://arxiv.org/abs/hep-ex/0909.4012v3`.

[9] The MINOS Collaboration. Observation of muon intensity variations by season with the MINOS Near Detector. 2014. arXiv:1406.7019 [hep-ex].

[10] IceCube Collaboration. Atmospheric Variations as observed by IceCube. 2010. arXiv:1001.0776 [astro-ph.HE].

[11] *The Review of Particle Physics.* J. Beringer et al. (Particle Data Group), Phys. Rev. D86, 010001 (2012) and 2013 partial update for the 2014 edition.

[12] A. M. Hillas. Cosmic Rays: Recent Progress and some Current Questions. *arXiv:astro-ph/0607109v2*, 2006. Available online at `http://arxiv.org/abs/astro-ph/0607109`.

[13] Jörg R. Hörandel. Models of the Knee in the Energy Spectrum of Cosmic Rays. *arXiv:astro-ph/0402356v2*, 2004. Available online at `http://arxiv.org/abs/astro-ph/0402356`.

[14] T. K. Gaisser. *Cosmic rays and particle physics.* Cambridge University Press, 1990.

[15] High-energy cosmic-ray acceleration. *5th CERN-Latin American School of High-Energy Physics, Recinto Quirama (Medellin), Antioquia, Colombia, 15 - 28 Mar 2009*, 2009. Available online at `http://www.physics.adelaide.edu.au/astrophysics/hires/uhecr.html` Copyright © The University of Adelaide Copyright in this website and its contents is owned by, or licensed to, the University of Adelaide. You may download, display, print and reproduce this material in unaltered form (attaching a copy of this notice) for your personal, non-commercial use. The University of Adelaide reserves the right to revoke such permission at any time.

[16] Pierre Auger, P. Ehrenfest, R. Maze, J. Daudin, and Robley A. Fréon. Extensive Cosmic-Ray Showers. *Rev. Mod. Phys. 11, 288 – Published 1 July 1939*, 1939. Available online at `https://journals.aps.org/rmp/abstract/10.1103/RevModPhys.11.288`.

[17] The University of Adelaide. Air shower illustration. Website. Available online at `https://wiki.icecube.wisc.edu/index.php/Gulliver`.

[18] E. V. Bugaev, A. Misaki, V. A. Naumov, T. S. Sinegovskaya, S. I. Sinegovsky, N. Takahashi. Atmospheric Muon Flux at Sea Level, Underground, and Underwater. 10.1103/PhysRevD.58.054001. Available online at `arXiv:hep-ph/9803488v3`.

[19] Arthur H. Compton and Ivan A. Getting. An apparent effect of galactic rotation on the intensity of cosmic rays. *Phys. Rev.*, 47:817–821, Jun 1935.

[20] Marius Grigat. Large Scale Anisotropy Studies of Ultra High Energy Cosmic Rays Using Data Taken with the Surface Detector of the Pierre Auger Observatory. PHD Thesis.

[21] Renzo G.E. Ramelli. Search for Cosmic Rays Point Sources and Anisotropy Measurement with the L3+C Experiment. PHD Thesis.

[22] ICECUBE COLLABORATION. OBSERVATION OF ANISOTROPY IN THE GALACTIC COSMIC RAY ARRIVAL DIRECTIONS AT 400 TEV WITH ICECUBE. 2011. arXiv:1109.1017 [hep-ex].

[23] The MACRO Collaboration. Seasonal variations in the underground muon intensity as seen by MACRO. 1997.

[24] P.H. Barrett et al., Rev. Mod. Phys. 24 133. 1952.

[25] E.W. Grashorn. The atmospheric charged kaon/pion ratio using seasonal variation methods. 2010. Available online at http://arxiv.org/abs/0909.5382v3.

[26] Location of Antares. Website. Available online at http://www.ecap.nat.uni-erlangen.de/acoustics/research/amadeus_project/index.shtml.

[27] OpticalModule. Website. Available online at http://antares.in2p3.fr/Gallery/selected.htmls.

[28] OpticalModule. Website. Available online at http://antares.in2p3.fr/internal/dokuwiki/doku.php?id=figures_and_photos.

[29] Bettina Diane Hartmann. Reconstruction of Neutrino-Induced Hadronic and Electromagnetic Showers with the ANTARES Experiment. PHD Thesis.

[30] J.A. Aguilar et al. Transmission of light in the deep sea water at the site of the ANTARES neutrino telescope. 2005.

[31] Marco Bazzotti. Studies of the atmospheric muon flux with the ANTARES detector. PHD Thesis.

[32] Aart Heijboer, for the Antares Collaboration. Reconstruction of Atmospheric Neutrinos in Antares. 2009. arXiv:0908.0816v1 [astro-ph.IM].

[33] Imem Al Samarai. Search for neutrinos from transient sources with the ANTARES neutrino telescope and optical follow-up observations. PHD Thesis.

[34] J. Schuller. ANTARES: status report. Nuclear Physics B - Proceedings Supplements 150:177 - 180, 2006. Proceedings of the 9th Topical Seminar on Innovative Particle and Radiation Detectors. Available online at http://www.sciencedirect.com/science/article/pii/S0920563205008364.

[35] The ROOT team. ROOT - A data analysis framework. Website. Available online at http://root.cern.ch/.

[36] Internal Website of ANTARES. http://antares.in2p3.fr/internal/dokuwiki/doku.php?id=quality_flags.

[37] S. Escoffier. ANTARES internal note, ANTARES-SITE/2005-001 (2005).

[38] ANTARES collaboration. A Fast Algorithm for Muon Track Reconstruction and its Application to the ANTARES Neutrino Telescope. 2011. arXiv:1105.4116 [astro-ph.IM].

[39] A. Heijboer. PhD thesis. Universiteit van Amsterdam (2004).

[40] GENHEN used for ANTARES. Website: http://antares.in2p3.fr/internal/dokuwiki/doku.php?id=genhen.

[41] Mohamad-Ziad Charif. Indirect Search for Dark Matter with the ANTARES Telescope. PHD Thesis.

[42] J. Brunnerr. GEASIM, 2000. http://antares.in2p3.fr/internal/software/geasim.html.

[43] G.Carminati et al. Atmospheric MUons from PArametric formulas: a fast GEnerator for neutrino telescopes (MUPAGE), 2008. Comput. Phys. Commun., 179, 915.

[44] CORSIKA software package. Website: `https://web.ikp.kit.edu/corsika/`.

[45] GRIB file format Website. Website: `http://www.grib.us/`.

[46] edited by O. Fackler and J. Tran Thanh Van. *Tests of fundamental laws in physics.* Les Arcs, Savoie, France, 1989.

[47] The University of Michigan. Illustrations of coordinate systems. Website. Available online at `https://dept.astro.lsa.umich.edu/ugactivities/Labs/coords/index.html`.

[48] D. McNally. *Positional Astronomy.* Frederick Muller Ltd., 1974.

Acknowledgments

My thanks first go to Prof. Dr. Gisela Anton and Prof. Dr. Uli Katz for the opportunity to work an that topic, their advice and the possibility to take part of the working group.

Further I want to thank Dr. Thomas Eberl for his support, supervision and proofreading of my work.

I also want to thank all others of the ANTARES working group in Erlangen for the interesting discussions. Special thanks go to Florian Folger, Roland Richter, Jutta Schnabel, Thomas Seitz and Andreas Gleixner for their support and the comfortable working atmosphere.

Thanks go also to the whole ANTARES Collaboration with their help this work was possible.

I also acknowledge the ECMWF/DWD/WDC-Climate for providing the environmental data for this work.

Finally, I want to thank my family and friends that always have supported me.

Thank you.